Interaction Between Urban Tunnels and the Surrounding Environment

Lead Guest Editor: Xin-Jiang Wei
Guest Editors: Dongmei Zhang, Wanhuan Zhou, Chengwei Zhu, and Tom Iseley

Interaction Between Urban Tunnels and the Surrounding Environment

Interaction Between Urban Tunnels and the Surrounding Environment

Lead Guest Editor: Xin-Jiang Wei
Guest Editors: Dongmei Zhang, Wanhuan Zhou, Chengwei Zhu, and Tom Iseley

Zhaofei Chu, China
Wonseok Chung, Republic of Korea
Donato Ciampa, Italy
Gian Paolo Cimellaro, Italy
Francesco Colangelo, Italy
Romulus Costache, Romania
Liviu-Adrian Cotfas, Romania
Antonio Maria D'Altri, Italy
Bruno Dal Lago, Italy
Amos Darko, Hong Kong
Arka Jyoti Das, India
Dario De Domenico, Italy
Gianmarco De Felice, Italy
Stefano De Miranda, Italy
Maria T. De Risi, Italy
Tayfun Dede, Turkey
Sadik O. Degertekin, Turkey
Camelia Delcea, Romania
Cristoforo Demartino, China
Giuseppe Di Filippo, Italy
Luigi Di Sarno, Italy
Fabio Di Trapani, Italy
Aboelkasim Diab, Egypt
Thi My Dung Do, Vietnam
Giulio Dondi, Italy
Jiangfeng Dong, China
Chao Dou, China
Mario D'Aniello, Italy
Jingtao Du, China
Ahmed Elghazouli, United Kingdom
Francesco Fabbrocino, Italy
Flora Faleschini, Italy
Dingqiang Fan, Hong Kong
Xueping Fan, China
Qian Fang, China
Salar Farahmand-Tabar, Iran
Ilenia Farina, Italy
Roberto Fedele, Italy
Guang-Liang Feng, China
Luigi Fenu, Italy
Tiago Ferreira, Portugal
Marco Filippo Ferrotto, Italy
Antonio Formisano, Italy
Guoyang Fu, Australia
Stefano Galassi, Italy

Junfeng Gao, China
Meng Gao, China
Giovanni Garcea, Italy
Enrique García-Macías, Spain
Emilio García-Taengua, United Kingdom
DongDong Ge, USA
Khaled Ghaedi, Malaysia
Khaled Ghaedi, Malaysia
Gian Felice Giaccu, Italy
Agathoklis Giaralis, United Kingdom
Ravindran Gobinath, India
Rodrigo Gonçalves, Portugal
Peilin Gong, China
Belén González-Fonteboa, Spain
Salvatore Grasso, Italy
Fan Gu, USA
Erhan Güneyisi, Turkey
Esra Mete Güneyisi, Turkey
Pingye Guo, China
Ankit Gupta, India
Federico Gusella, Italy
Kemal Hacıefendioğlu, Turkey
Jianyong Han, China
Song Han, China
Asad Hanif, Macau
Hadi Hasanzadehshooiili, Canada
Mostafa Fahmi Hassanein, Egypt
Amir Ahmad Hedayat, Iran
Khandaker Hossain, Canada
Zahid Hossain, USA
Chao Hou, China
Biao Hu, China
Jiang Hu, China
Xiaodong Hu, China
Lei Huang, China
Cun Hui, China
Bon-Gang Hwang, Singapore
Jijo James, India
Abbas Fadhil Jasim, Iraq
Ahad Javanmardi, China
Krishnan Prabhakan Jaya, India
Dong-Sheng Jeng, Australia
Han-Yong Jeon, Republic of Korea
Pengjiao Jia, China
Shaohua Jiang, China

Chayut Ngamkhanong (iD), Thailand
Trung Ngo, Australia
Tengfei Nian, China
Mehdi Nikoo (iD), Canada
Youjun Ning (iD), China
Olugbenga Timo Oladinrin (iD), United Kingdom
Oladimeji Benedict Olalusi, South Africa
Timothy O. Olawumi (iD), Hong Kong
Alejandro Orfila (iD), Spain
Maurizio Orlando (iD), Italy
Siti Aminah Osman, Malaysia
Walid Oueslati (iD), Tunisia
SUVASH PAUL (iD), Bangladesh
John-Paris Pantouvakis (iD), Greece
Fabrizio Paolacci (iD), Italy
Giuseppina Pappalardo (iD), Italy
Fulvio Parisi (iD), Italy
Dimitrios G. Pavlou (iD), Norway
Daniele Pellegrini (iD), Italy
Gatheeshgar Perampalam (iD), United Kingdom
Daniele Perrone (iD), Italy
Giuseppe Piccardo (iD), Italy
Vagelis Plevris (iD), Qatar
Andrea Pranno (iD), Italy
Adolfo Preciado (iD), Mexico
Chongchong Qi (iD), China
Yu Qian, USA
Ying Qin (iD), China
Giuseppe Quaranta (iD), Italy
Krishanu ROY (iD), New Zealand
Vlastimir Radonjanin, Serbia
Carlo Rainieri (iD), Italy
Rahul V. Ralegaonkar, India
Raizal Saifulnaz Muhammad Rashid, Malaysia
Alessandro Rasulo (iD), Italy
Chonghong Ren (iD), China
Qing-Xin Ren, China
Dimitris Rizos (iD), USA
Geoffrey W. Rodgers (iD), New Zealand
Pier Paolo Rossi, Italy
Nicola Ruggieri (iD), Italy
JUNLONG SHANG, Singapore

Nikhil Saboo, India
Anna Saetta, Italy
Juan Sagaseta (iD), United Kingdom
Timo Saksala, Finland
Mostafa Salari, Canada
Ginevra Salerno (iD), Italy
Evangelos J. Sapountzakis (iD), Greece
Vassilis Sarhosis (iD), United Kingdom
Navaratnarajah Sathiparan (iD), Sri Lanka
Fabrizio Scozzese (iD), Italy
Halil Sezen (iD), USA
Payam Shafigh (iD), Malaysia
M. Shahria Alam, Canada
Yi Shan, China
Hussein Sharaf, Iraq
Mostafa Sharifzadeh, Australia
Sanjay Kumar Shukla, Australia
Amir Si Larbi (iD), France
Okan Sirin (iD), Qatar
Piotr Smarzewski (iD), Poland
Francesca Sollecito (iD), Italy
Rui Song (iD), China
Tian-Yi Song, Australia
Flavio Stochino (iD), Italy
Mayank Sukhija (iD), USA
Piti Sukontasukkul (iD), Thailand
Jianping Sun, Singapore
Xiao Sun (iD), China
T. Tafsirojjaman (iD), Australia
Fujiao Tang (iD), China
Patrick W.C. Tang (iD), Australia
Zhi Cheng Tang (iD), China
Weerachart Tangchirapat (iD), Thailand
Xiaxin Tao, China
Piergiorgio Tataranni (iD), Italy
Elisabete Teixeira (iD), Portugal
Jorge Iván Tobón (iD), Colombia
Jing-Zhong Tong, China
Francesco Trentadue (iD), Italy
Antonello Troncone, Italy
Majbah Uddin (iD), USA
Tariq Umar (iD), United Kingdom
Muahmmad Usman, United Kingdom
Muhammad Usman (iD), Pakistan
Mucteba Uysal (iD), Turkey

Ilaria Venanzi, Italy
Castorina S. Vieira, Portugal
Valeria Vignali, Italy
Claudia Vitone, Italy
Liwei WEN, China
Chunfeng Wan, China
Hua-Ping Wan, China
Roman Wan-Wendner, Austria
Chaohui Wang, China
Hao Wang, USA
Shiming Wang, China
Wayne Yu Wang, United Kingdom
Wen-Da Wang, China
Xing Wang, China
Xiuling Wang, China
Zhenjun Wang, China
Xin-Jiang Wei, China
Tao Wen, China
Weiping Wen, China
Lei Weng, China
Chao Wu, United Kingdom
Jiangyu Wu, China
Wangjie Wu, China
Wenbing Wu, China
Zhixing Xiao, China
Gang Xu, China
Jian Xu, China
Panpan, China
Rongchao Xu, China
HE YONGLIANG, China
Michael Yam, Hong Kong
Hailu Yang, China
Xu-Xu Yang, China
Hui Yao, China
Xinyu Ye, China
Zhoujing Ye , China
Gürol Yildirim, Turkey
Dawei Yin, China
Doo-Yeol Yoo, Republic of Korea
Zhanping You, USA
Afshar A. Yousefi, Iran
Xinbao Yu, USA
Dongdong Yuan, China
Geun Y. Yun, Republic of Korea

Hyun-Do Yun, Republic of Korea
Cemal YİĞİT, Turkey
Paolo Zampieri, Italy
Giulio Zani, Italy
Mariano Angelo Zanini, Italy
Zhixiong Zeng, Hong Kong
Mustafa Zeybek, Turkey
Henglong Zhang, China
Jiupeng Zhang, China
Tingting Zhang, China
Zengping Zhang, China
Zetian Zhang, China
Zhigang Zhang, China
Zhipeng Zhao, Japan
Jun Zhao , China
Annan Zhou, Australia
Jia-wen Zhou, China
Hai-Tao Zhu, China
Peng Zhu, China
QuanJie Zhu, China
Wenjun Zhu, China
Marco Zucca, Italy
Haoran Zuo, Australia
Junqing Zuo, China
Robert Černý, Czech Republic
Süleyman İpek, Turkey

Contents

Research Article

Measured Analysis on Surface Deformation and Influence of Cutter Torque for Twin Shield Tunnelling in Silty Sand

Yuqing Dong [ID],[1] Zhi Ding [ID],[1] Yexiang Jiang,[2] Chunlai Chen [ID],[1] Wenming Shen,[3] and Yinze Wang[1]

[1]*Department of Civil Engineering, Zhejiang University City College, Hangzhou 310015, China*
[2]*Hangzhou Metro Group Co., Ltd., Hangzhou 310017, China*
[3]*East China Surzey and Design Co., Ltd., China Railway Eryuan Engineering Group Co., Ltd., Hangzhou 310004, China*

Correspondence should be addressed to Chunlai Chen; chencl@zucc.edu.cn

In this study, the field measurement was conducted on the twin shield tunnelling in a shield section of Hangzhou Metro Line 6, where the surface deformation caused by twin shield tunnelling in the silty sand was obtained. The surface deformation law and the applicability of the twin-line Peck formula in the silt area were analyzed. The relationship between the cutterhead torque and the surface deformation in the silty sand was identified. Furthermore, the differences in surface deformation of twin shield tunnelling in the Hangzhou soft soil area were discussed. The results show that the settlement process caused by twin shield tunnelling in silty sand is faster than that of soft soil and has no rebound phenomenon. The twin-line Peck formula is suitable in silty sand, but the prediction of the latter line using this formula is slightly deviated because of the secondary disturbance effect. Due to the secondary disturbance of the soil caused by the construction of the latter line, the soil loss rate of the latter line is higher than that of the former line. Therefore, the reference ratio of the soil loss rate of the latter line and the former line is given. Furthermore, the cutterhead torque of the shield machine was found to be associated with the maximum instantaneous value of the surface deformation.

1. Introduction

In recent years, the development of subway tunnel engineering is very rapid, and tunnel engineering plays a very important role in the development of infrastructure constructions [1, 2]. Among the urban tunnel construction method, the shield method is widely used due to its fast construction speed and simple technology. However, it is inevitable to cause some disturbance to the surrounding soil. This can break the stress-balanced stress state of the original underground space and cause some deformation of the surrounding soil in the process of shield tunneling [3–5], which are particularly obvious in the double-line shield construction. The measurement and analysis of surface deformation is the most common method to study the disturbance of surrounding soil resulted from the shield construction, and the monitoring results can directly reflect

the actual surface deformation. Therefore, the measured analysis of ground deformation caused by shield construction has important engineering significance for ensuring construction safety and guiding soil reinforcement [6].

Many scholars have studied the surface deformation caused by shield construction, mainly based on the measurement analysis method [7–12] and the numerical simulation method [13–18]. The research on the deformation of surrounding soil caused by twin parallel shield tunneling mainly relies on the Peck empirical formula, which can be divided into two categories: (1) using the Peck formula to directly calculate the total deformation of surface deformation and (2) using the Peck formula to calculate the surface deformation caused by the former and latter tunnel excavation, respectively, and then the total surface settlement deformation is obtained by superposition. In terms of

field measurement and analysis, Ding et al. [19] measured and analyzed the surface settlement caused by twin shield tunnelling in the soft soil area and explored the law of surface deformation and the value of soil loss rate. Wei et al. [20] studied the relationship between surface deformation and cutterhead torque during shield tunneling through the statistical analysis of monitoring data and construction parameters of Hangzhou Metro Line 2 and obtained a suitable calculation method of cutterhead torque value for Hangzhou soft clay soil. Wan et al. [21] carried out research on the difficulties of cutterhead wear, blockage, and surface settlement encountered in the construction of shield machine in the typical water sand cobble layer. They found that the opening rate, maximum opening size, and opening position are the key factors affecting the geological adaptability of the shield machine.

The bearing capacity of silty sand is low, the permeability of the wall is high, and the internal friction angle is large [22]. Therefore, the rotary cutter working in silty sand is often bonded and worn, and even the working face collapses due to the cohesionless dispersion of silty sand material [23]. Moreover, liquefaction is easy to occur under the vibration of shield construction. To ensure the stable and efficient construction of shield in silty sand, it is necessary to reduce the disturbance to the stratum during tunneling and reduce the risk of spewing and blocking during soil discharge. However, at present, there are few studies on the influence of surface deformation and construction parameters caused by twin shield tunneling in silt sand. In addition, the influence of shield tunneling construction parameters on surface deformation is not considered in the abovementioned study. Therefore, it is of great engineering significance to explore the soil deformation caused by twin shield tunneling in silt sand.

Based on the statistical analysis of the measured data of a twin shield tunnel in Hangzhou Metro Line 6, this work studies the surface deformation in the process of twin shield construction in silt sand and makes a comparative analysis with the soft clay area. The application of Peck-based empirical formula and basic assumptions in the process of twin-line excavation in the silty sand area is investigated. The reference ratio between the soil loss rate in the former line and the latter line in the silty sand area is proposed. The relationship between shield construction parameters and surface deformation is discussed.

2. On-Site Monitoring Experiment

2.1. Project Overview. This study takes the double-track single-round shield section of Shuangpu station to Heshan Road Station of Hangzhou Metro Line 6 as the research object. The section line is located along Kehai Road, Shuangpu Town, Xihu District, Hangzhou, China, with a total length of 2486 m. The left and right lines of the section adopt a V-shaped slope, and the buried depth of the tunnel top is 9.0~15.5 m. Shi Chuan island shield machine is adopted, with an opening rate of 45%. As the shield machine in this section passes through the sandy soil, the cutterhead panel is cut off to become a spoke cutterhead. Increasing the

opening rate of the cutterhead is conducive to the slag entering the soil bin. The lining structure of the tunnel adopts prefabricated reinforced concrete segment lining, with an inner diameter of 5.5 m, an outer diameter of 6.2 m, and a width of 1.2 m, which is staggered joint assembly.

The distribution and parameters of the soil layer are shown in Table 1. In the table, W is the moisture content of soil layer, γ is the wet gravity, e is the void ratio, E_S is the compression modulus, ρ is natural density, K_0 is the static side pressure coefficient, ϕ_{cq} is internal friction angle, and V is Poisson's ratio. The geological section of shield tunneling is shown in Figure 1.

2.2. Layout of Measuring Points. In order to understand the surface deformation of the silty sand shield section in the process of tunneling, the monitoring points are arranged at the construction site. The layout of the monitoring points is as follows: several longitudinal monitoring points are arranged at intervals along the advancing direction of the tunnel on the central axis of the tunnel, and the transverse monitoring section is arranged perpendicular to the axis direction. A monitoring face is set every 35 meters on the tunnel axis and every 25 meters within 120 meters of the shield starting section. In special cases, a monitoring face is set, such as the place where the geological conditions change greatly and the places, where many buildings exist above the soil layer. Each monitoring surface is symmetrically arranged with the axis as the center to 1.5 m, 5 m, 7.5 m, 10 m, 13.5 m, 18.5 m, and L m (adjusted according to the tunnel buried depth). The layout of some monitoring sections is shown in Figure 2.

3. Analysis of Experiment Results

3.1. Analysis of Transverse Surface Deformation Law. Based on the measured data of surface deformation of each monitoring section, the variation trend of each monitoring cross section in the process of twin shield tunneling in the Hangzhou silty soil area is analyzed. It is found that the final settlement curve generally presents a "W" shape and is asymmetrical. Three typical sections were selected in this study. The former tunnel and the latter tunnel were located on the left and right sides of the middle line, respectively. As shown in Figures 3–5, the abscissa in the figure represents the amount of surface deformation, and the abscissa represents the horizontal distance between the monitoring point and the middle line of the tunnel. The maximum surface settlement above the latter line is obviously larger than that of the former line. The maximum surface deformation caused by the latter tunnel is larger than that of the former tunnel. The main reason is the superposition disturbance effect of the latter tunnel on the soil. There is a little difference in the secondary disturbance effect of each section.

Figure 6 shows the measured surface deformation curve of a section of Hangzhou Metro Line 2. The shield mainly passes through the soft soil layer. Compared to Figures 3–5, it is found that the final settlement trend of surface

TABLE 1: Parameters of soils.

Soil properties	W (%)	γ (kN/m³)	e	E_S (MPa^{-1})	ρ (g/cm³)	K_0	ϕ_{cq} (°)	V
③ 3 Sandy silt with silt	26.0	19.5	0.742	0.100	1.95	0.40	28.0	0.29
③ 31 Silt	25.4	19.6	0.716	0.083	1.96	0.34	30.0	0.29
③ 5 Sandy silt	25.3	19.7	0.706	0.100	1.97	0.37	29.0	0.29
③ 6 Silt	25.3	19.5	0.721	0.086	1.95	0.32	31.0	0.26
⑤ 33 Silt	23.5	19.7	0.687	0.096	1.96	0.32	31.5	0.26
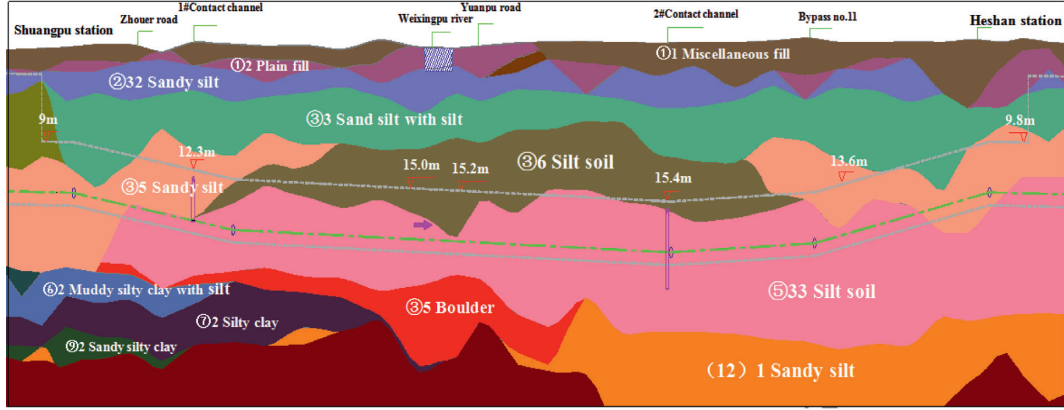
FIGURE 1: Geological profile of shield tunnel under construction.
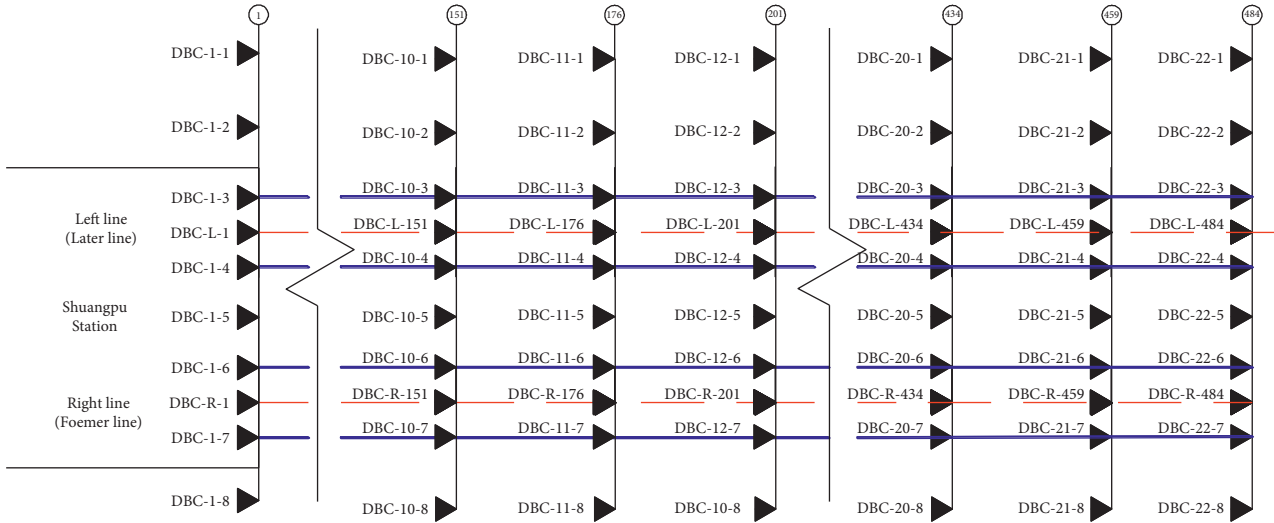
FIGURE 2: Layout of partial measuring points.

transverses deformation caused by twin shield tunneling in the soft soil area, which still conforms to the above rules. The average settlement of the latter line in the soft soil area is about 1.5 times bigger than that of the former line, while it is about 2 times in the silty sand area. It can be seen that the secondary disturbance effect produced by shield tunneling in silty soil area is stronger than that in soft soil, which indicates that the secondary disturbance phenomenon has a greater impact on silty soil than that in soft soil. Therefore, when the twin shield tunnelling is not properly controlled in the Hangzhou silt soil area, the surface deformation value is easy to exceed the alarm value, thus affecting the construction safety. The reason that the additional settlement caused by

the secondary disturbance effect of shield construction in silty soil area is more obvious than that in the soft soil area obtained from the field monitoring. This is related to the porosity and permeability of silty soil. Compared with soft soil, silty sand soil has larger void and lower cohesion [24]. Therefore, the self-stability of silty sand is worse and the effect of disturbance is greater.

3.2. Analysis of Surface Deformation with Time. In the process of shield construction, the surface will change with the different advancing stages. The measurement points with the largest deformation in the tunnel section during the
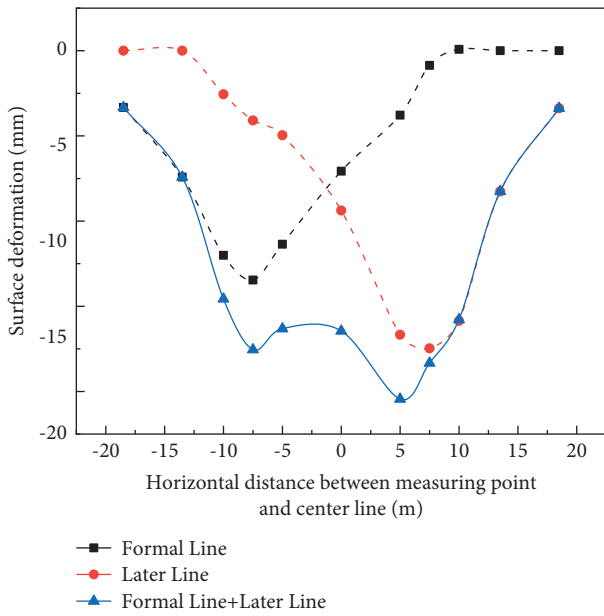
FIGURE 3: Surface deformation of section DBC10.
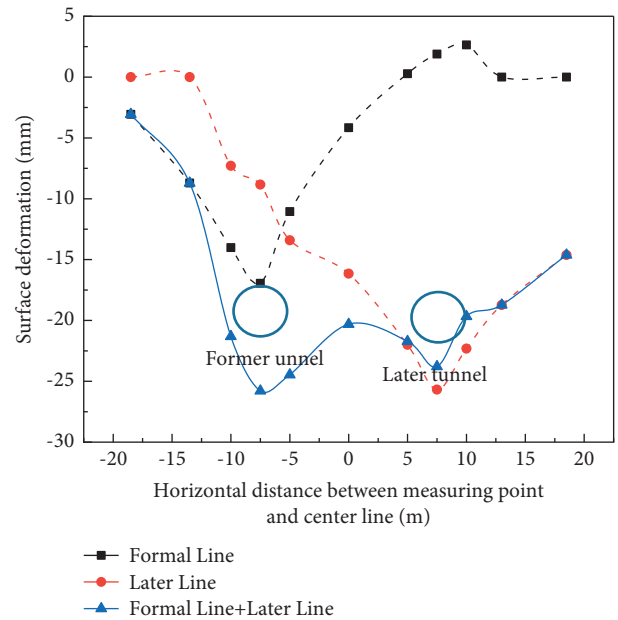
FIGURE 5: Surface deformation of section DBC35.
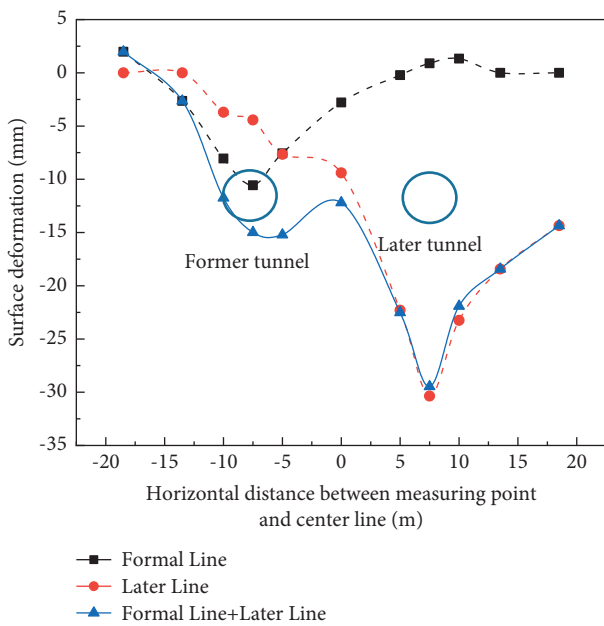
FIGURE 4: Surface deformation of section DBC26.
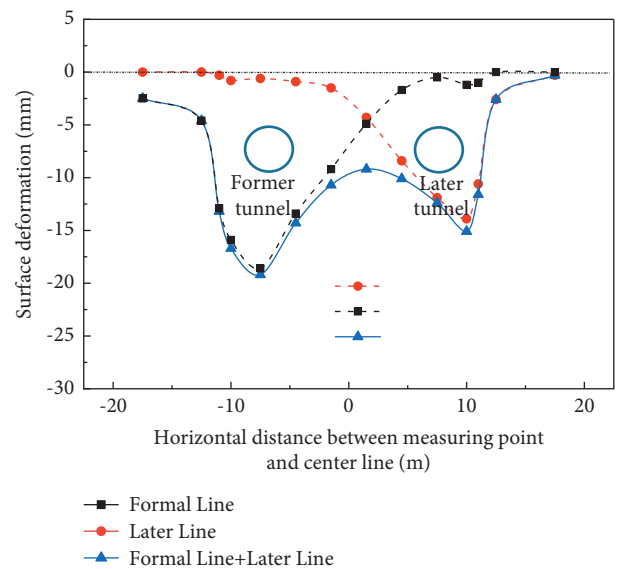
FIGURE 6: Measured curve of surface deformation of a section of Hangzhou Metro Line 2.

construction process are selected, respectively. As shown in Figures 7 and 8, the cumulative deformation curves of the largest deformation points in section DBC6 and section DBC26 are recorded. In the figures, the ordinate represents the amount of surface deformation, and the abscissa represents the time for the shield to pass through the monitored section. The negative value of the abscissa represents the days when the shield has not reached the monitoring section, and the positive value represents the days when the shield has crossed the monitoring section.

It can be seen from the analysis of Figures 7 and 8 that when the shield machine reaches the monitoring section,

the soil begins to settle rapidly. During the process of the shield machine passing through the monitoring section, the soil continues to settle, and the settlement speed gradually slows down after the shield tail passes through the monitoring section and finally tends to be stable. This is consistent with the stratum deformation law in the sandy silt area obtained from the research in literature [25–27]. Compared to Figure 9, different from the conclusion of [19] in the study of shield tunneling in soft soil areas, silty sand does not begin to settle one day earlier than soft soil, and there is no obvious rebound. The settlement in silty soil areas tends to be stable about 2 days
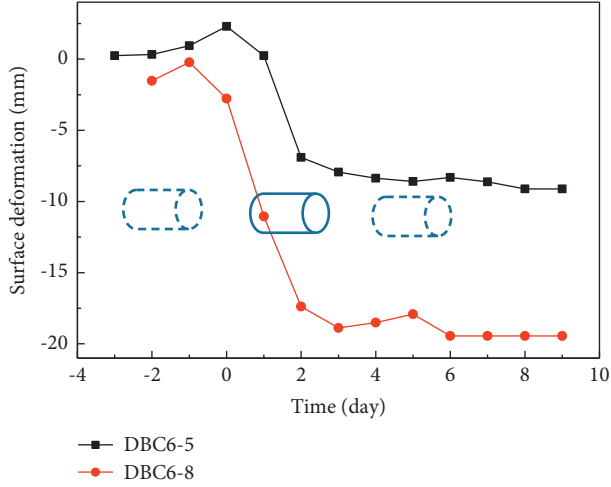
FIGURE 7: Deformation of monitoring points in section DBC6.
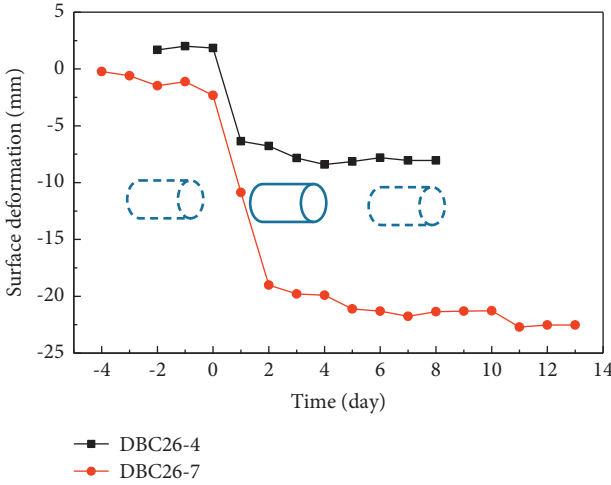
FIGURE 8: Deformation of monitoring points in section DBC26.
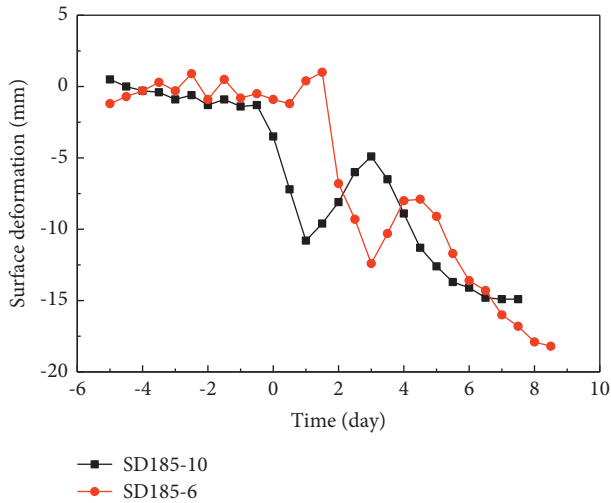
FIGURE 9: Accumulated deformation curve of SD185 section in Feng-Gu section of Hangzhou Metro Line 2.

after the shield machine reaches the cross section, while it tends to be stable in soft soil areas for a longer time. The reason is that the permeability coefficient of silty sand is larger and the pore water pressure dissipates faster after being disturbed by shield construction [28].

By comparing the cumulative surface deformation of the former line and the latter line in the process of shield tunneling in silty soil and soft soil, it is found that the soil deformation of the latter line is more obvious under the action of the second disturbance. As shown in Figures 7 and 8, the maximum settlement of the latter line of the monitoring section in the silty soil area is 2.11 times and 2.75 times that of the former line, which is significantly larger than that in the soft soil area about 1.5 times that of the former line [17]. Compared with soft soil, the seepage characteristics of silt soil are one of the potential causes of larger soil deformation and failure [29]. This is related to shear strain, sliding fraction, volumetric strain, particle displacement, and the cohesive failure zone of silt soil. From a microscopic point of view, the deformation characteristics of silt soil are affected by the pore size, distribution, shape, and arrangement of the silty clay at the bottom and side of the tunnel [30]. It proves the conclusion that the influence of secondary disturbance on silt soil is greater than that on soft soil. Therefore, special attention should be paid to the settlement of the latter line during construction. At the same time, the settlement of silty sand changes rapidly, so it is necessary to do a good job in the early prevention, which can provide a reference for construction and field monitoring.

4. Applicability Analysis of Peck Formula

Peck [7] statistically analyzed a large number of measured data of surface deformation caused by subway construction. Considering that the soil loss causes stratum movement, he proposed that the soil is in an undrained state during ground settlement, and the volume of soil loss is equal to the volume of the settlement tank. The surface settlement trough above the tunnel is in accordance with the normal distribution, and the horizontal settlement formula of the surface is obtained as follows:

$$S(x) = S_{max} \exp\left(-\frac{x^2}{2i^2}\right),$$

$$S_{max} = \frac{V_{loss}}{i\sqrt{2\pi}} = \frac{\pi R^2 \eta}{i\sqrt{2\pi}},$$

(1)

where x is the horizontal distance from the tunnel axis; $S(x)$ is the surface settlement at the location x; S_{max} is the maximum surface settlement above the tunnel axis; i is the width coefficient of the ground settlement tank; V_{loss} is the soil loss per unit length; R is the tunnel excavation radius; and η is the soil loss rate. On the basis of the Peck formula, Suwansawat and Einstein [31] studied the ground deformation formula of a double-line shield tunnel.

$$\delta(x) = \frac{\pi R^2 \eta_1}{\sqrt{2\pi} i_1} \exp\left(-\frac{(x - D/2)^2}{2i_1^2}\right)$$
$$+ \frac{\pi R^2 \eta_2}{\sqrt{2\pi} i_2} \exp\left(-\frac{(x + D/2)^2}{2i_2^2}\right), \tag{2}$$

where i_1 is the width coefficient of the ground settlement slot of the former tunnel; D is the soil loss rate of the former tunnel; D is the width coefficient of the ground settlement slot of the latter tunnel; η_2 is the soil loss rate of the latter tunnel; and D is the distance between the two tunnel axes.

Wei [32] summed up the value method of the width coefficient of the tunnel ground settlement trough based on a large number of literature studies. The value method of the width coefficient of the ground settlement trough is divided into three categories. According to the applicable conditions, three types of formulas suitable for silty sand are selected as follows:

$$i = (1 - 0.02\varphi)h, \tag{3}$$

$$i = 0.25(h + R), \tag{4}$$

$$i = kh. \tag{5}$$

In the formula, h is the depth from the tunnel axis to the ground; φ is the internal friction angle of the soil above the tunnel axis; and R is the outer radius of the tunnel, in which, in formula (3), φ takes 35° to 40° and in formula (5), k takes 0.2 to 0.3.

In this study, the surface deformation is predicted based on the condition of monitoring section DBC10. The i obtained by formulas (3) and (5) is 3~4.5, and the i obtained by formula (4) is 4.5. Therefore, i the former line takes 4.5, and if the value is assumed to be proportional to the final settlement, i the latter line takes 5.84. The predicted settlement curve is drawn by substituting it into the formula. The predicted results and measured surface deformation are shown in Figures 10 and 3.

Comparing the curves in Figures 10 and 3, it is found that the measured deformation curve and the predicted curve of section DBC10 present "W" shape, and the measured deformation curve and the predicted curve of other monitoring sections are basically similar in shape, with a high degree of coincidence, but there are some differences between the surface settlement values of the latter line of some sections and the predicted values. It can be seen that using the two-line Peck formula to predict the surface deformation caused by twin shield tunneling in the Hangzhou silt soil area has a certain reference value.

At present, there is no reasonable method to calculate the soil loss rate. In this study, according to the back analysis method described by Wei [33], combined with the measured data of surface settlement, formula (6) is used to calculate the value of η. When the back-calculation points are selected according to the measured data, only the sections whose measured surface deformation conforms to the prediction of the peck formula are selected.
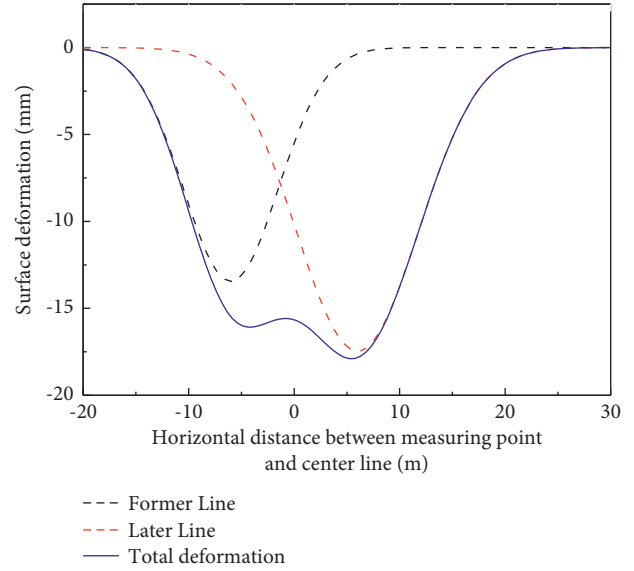
FIGURE 10: Prediction of surface deformation of section DBC10.

$$\eta = \frac{S_{\max} i \sqrt{2\pi}}{\pi R^2}. \tag{6}$$

The distribution of soil loss rate of each section is listed in Table 2, and the variation law of soil loss rate during double-line shield construction in silty soil area is analyzed. It can be seen from Table 2 that the main distribution range of soil loss rate of each effective monitoring section in this test is 0.2%~0.8%, accounting for 88.46% of the total, of which 0.2%~0.5% is the most, accounting for 57.69% of the total, which is similar to the situation of Hangzhou silt area. Further analysis shows that the average soil loss rate of the latter line is 1.83 times that of the former line, and 11.54% of the soil loss rate of the latter line reaches 0.8~1.2%, which is because the soil loss rate of the latter line is increased due to the influence of secondary disturbance. Therefore, when the two-line Peck formula is used to predict the surface deformation of silty soil area, it is suggested that the soil loss rate of the latter line should be 1.8 times that of the former line.

Table 3 shows the distribution of soil loss rate of shield construction in a soft soil section of Hangzhou Metro Line 2. Compared to the distribution of soil loss rate in the silty sand section in Table 2, the soil loss rate of the former line of silty sand is less than that of soft soil, and that of the latter line is close to or even greater than that of soft soil, which is consistent with the conclusion that silty sand is more affected by secondary disturbance.

In this study, the soil loss rate of each section of the former line and the latter line is drawn according to the ring number, as shown in Figure 11. The soil loss rate has no obvious change rule because the construction parameters in the process of shield tunneling have a great impact on the soil loss rate, and the slight change of construction parameters will greatly affect the soil loss rate.

TABLE 2: Distribution of loss rate in silt soil region in Hangzhou Metro Line 6.

Soil loss rate	0.2~0.5		0.5~0.8		0.8~1.2		Average value
Range (%)	Number	Proportion (%)	Number	Proportion (%)	Number	Proportion (%)	
Former line	9	34.62	5	19.23	0	0.00	0.42
Latter line	6	23.08	3	11.54	3	11.54	0.77
Total	15	57.69	8	30.77	3	11.54	0.6

TABLE 3: Distribution of loss rate in soft soil region in Hangzhou Metro Line 2.

Soil loss rate	0.2~0.5		0.5~0.8		0.8~1.2		Average value
Range (%)	Number	Proportion (%)	Number	Proportion (%)	Number	Proportion (%)	
Former line	7	58.33	4	33.33	1	8.33	0.49
Latter line	6	42.86	6	42.86	2	14.28	0.61
Total	13	50.00	10	38.46	3	11.54	0.55
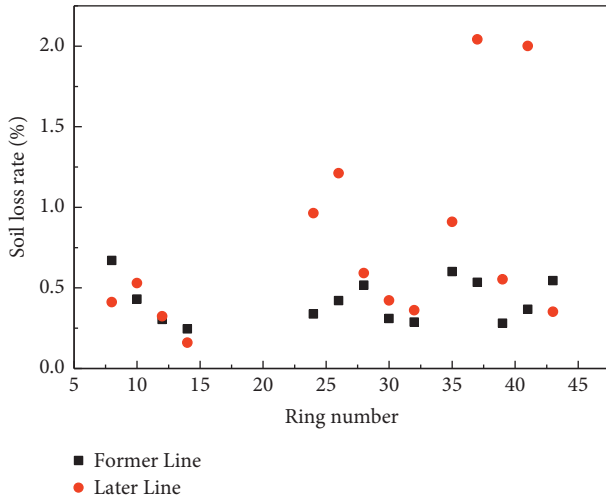
FIGURE 11: Loss rate of all sections.
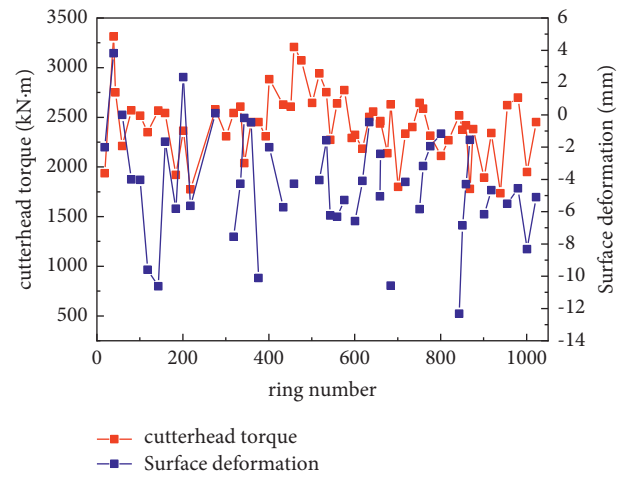
FIGURE 13: Relationship between displacement and torque of the latter line.

5. Correlation Analysis of Cutterhead Torque and Surface Deformation

The correlation between the instantaneous ground heave (the maximum deformation of the measuring point 12 hours after the shield machine passing) and the cutterhead torque of the shield machine is studied. The instantaneous deformation value and corresponding cutterhead torque value of each monitoring point at the arrival of the shield machine on the former line and the latter line are recorded, as shown in Figures 12 and 13.

Comparing Figures 12 and 13, it can be found that the absolute value of the maximum deformation value of the latter line is about 1.3 times bigger than that of the former line. At the same time, there is a similar proportion between the average torque of the former line and the latter line. The average torque of the latter line is 2645 kN·m, and the average torque of the former line is 2073 kN·m. This indicates that the maximum surface deformation value is related to

FIGURE 12: Relationship between displacement and torque of the former line.

TABLE 4: Maximum torque values of different cases.

Case	Cutterhead diameter (m)	Soil properties	Maximum torque (kN·m)
Hangzhou Metro line 6	6.2	Silty sand	3366
Metro Izmir, Turkey	6.52	Sandy gravel	5200
London Heathrow Airport Tunnel	9.15	London clay	18842
Hangzhou Metro line 2	6.17	Muddy silty clay	2082

the average torque during the shielding process. The main reason for the difference between the average torque of the former line and the latter line and the surface deformation is that the second disturbance is carried out during the driving process of the latter line, which increases the soil loss rate, especially for the silt soil. The porosity is higher. The pore size between the soil particles is uneven, and the influence of the construction disturbance is greater.

In this study, the cutterhead diameter and maximum torque of the shield machine in several engineering cases are selected for comparative analysis. It can be seen from Table 4 that the cutterhead excavation diameters of Hangzhou Metro Line 6 and Line 2 are basically the same. However, the soil layer changes from silty sand to muddy silty clay, and the maximum cutterhead torque is reduced to 0.62 times the original. The diameter of the London Heathrow Airport Tunnel is about 1.5 times bigger than that of the others, while the maximum torque is far more than that of other cases. It can be seen that the cutterhead excavation diameter and the excavation soil condition have a significant impact on the cutterhead torque, and the author speculates that the main reason is that the cutterhead diameter and the strength indexes of the shield tunneling soil are important parameters for calculating the cutterhead torque.

6. Conclusion

This study investigated and studies the surface deformation and the influence of cutterhead torque caused by twin shield tunneling in silt sand. The following results and conclusions are obtained as follows:

(1) The transverse deformation of the cross section of twin shield tunneling presents a "W" shape, whether in silt or soft soil. In the silty soil area, when the shield tunneling reaches the monitoring section, the soil settles sharply, which is different from the soft soil area. After the shield tail passes through, the soil continues to settle and the settlement speed slows down and finally becomes stable. In the silt soil stratum, the secondary disturbance effect of twin shield tunneling is stronger than that in the soft soil area, which should attract more attention in construction.

(2) By combining the measured data analysis with the theoretical formula, this work puts forward the hypothesis that the width coefficient of settlement slot of twin shield tunnel is related to the final settlement. The applicability of the two-line Peck formula in the Hangzhou silt soil area is verified.

(3) Compared to the soft soil area, the secondary disturbance effect produced by shield tunneling in silty soil area is more obvious, and the reference ratio of the soil loss rate of the latter line and the former line is proposed. In addition, the soil loss rate is difficult to be determined in the process of shield tunneling because of the variable construction parameters and great impact on the soil loss rate law.

(4) There is the same proportion between the ratio of the instantaneous maximum settlement and the average torque of the former line and the latter line. Through combining with the measured data and comparing with other cases, it is found that the cutterhead excavation diameter and soil conditions have a greater impact on the cutterhead torque, which should be paid attention to in shield construction.

Data Availability

The data used to support the findings of this study are available from the corresponding author upon request.

Conflicts of Interest

The authors declare that they have no conflicts of interest regarding the publication of this paper.

Acknowledgments

References

[1] Z. Ding, X.-j. Wei, and G. Wei, "Prediction methods on tunnel-excavation induced surface settlement around adjacent building," *Geomechanics and Engineering*, vol. 12, no. 2, pp. 185–195, 2017.

[2] K. Wu and Z. S. Shao, "Visco-elastic analysis on the effect offlexible layer on mechanical behavior of tunnels," *International Journal of Applied Mechanics*, vol. 11, no. 3, pp. 1–27, 2019.

[3] S.-M. Liao, J.-H. Liu, R.-L. Wang, and Z.-M. Li, "Shield tunneling and environment protection in Shanghai soft ground," *Tunnelling and Underground Space Technology*, vol. 24, no. 4, pp. 454–465, 2009.

[4] S.-M. Liao, C.-H. Cheng, and L.-S. Chen, "The planning and construction of a large underpass crossing urban expressway in Shanghai: an exemplary solution to the traffic congestions at dead end roads," *Tunnelling and Underground Space Technology*, vol. 81, pp. 367–381, 2018.

[5] M.-B. Liu and S.-M. Liao, "A case study on the underground rapid transport system (URTS) for the international airport hubs: Planning, application and lessons learnt," *Tunnelling and Underground Space Technology*, vol. 80, pp. 114–122, 2018.

[6] Z. Ding, X. Wei, X. Zhang, and X. Yin, "Analysis of the field monitoring data on soil movements and adjacent building settlement due to shield tunnelling," *Engineering Computations*, vol. 36, no. 4, pp. 1219–1237, 2019.

[7] R. B. Peck, "Deep excavations and tunneling in soft ground," in *Proceedings of the 7th International Conference on Soil Mechanics and Foundation Engineering*, pp. 225–290, Mexico, 1969.

[8] G. Wei, "Prediction of soil settlement caused by double-line parallel shield tunnel construction," *Disaster Advances*, vol. 6, no. 6, pp. 23–27, 2013.

[9] I. Ocak, "A new approach for estimating the transverse surface settlement curve for twin tunnels in shallow and soft soils," *Environmental Earth Sciences*, vol. 72, no. 7, pp. 2357–2367, 2014.

[10] Q. Fang, Q. Tai, D. Zhang, and L. N. Y. Wong, "Ground surface settlements due to construction of closely-spaced twin tunnels with different geometric arrangements," *Tunnelling and Underground Space Technology*, vol. 51, pp. 144–151, 2016.

[11] H. Park, J.-Y. Oh, D. Kim, S. Chang, and G. M. Venu, "Monitoring and analysis of ground settlement induced by tunnelling with slurry pressure-balanced tunnel boring machine," *Advances in Civil Engineering*, vol. 2018, pp. 1–10, 2018.

[12] J. Z. Lin, Y. X. Yang, and C. J. Yang, "Analysis and prediction of long-term settlement of Metro shield tunnel in saturated sand," *Geotechnical & Geological Engineering*, vol. 2021, pp. 1–12, 2021.

[13] N.-A. Do, D. Dias, P. Oreste, and I. Djeran-Maigre, "Three-dimensional numerical simulation of a mechanized twin tunnels in soft ground," *Tunnelling and Underground Space Technology*, vol. 42, pp. 40–51, 2014.

[14] N.-A. Do, D. Dias, and P. Oreste, "3D numerical investigation of mechanized twin tunnels in soft ground - influence of lagging distance between two tunnel faces," *Engineering Structures*, vol. 109, pp. 117–125, 2016.

[15] D. Z. Wu, K. P. Xu, and P. P. Guo, "Ground deformation characteristics induced by mechanized shield twin tunnelling along curved alignments," *Advances in Civil Engineering*, vol. 2021, Article ID 6640072, 2021.

[16] C. Zhang, Y. Cai, and W. Zhu, "Numerical study and field monitoring of the ground deformation induced by large slurry shield tunnelling in sandy cobble ground," *Advances in Civil Engineering*, vol. 2019, pp. 1–12, 2019.

[17] A. Naseem, K. Schotte, and X. M. Liu, "Ground settlements due to construction of triplet tunnels with different construction arrangements," *Advances in Civil Engineering*, vol. 2019, Article ID 8637837, 2019.

[18] K. Hang, Y. W. Sun, and X. Q. Huang, "Effects of different construction sequences on ground surface settlement and displacement of single long pile due to twin paralleled shield tunneling," *Advances in Civil Engineering*, vol. 2021, Article ID 5559233, 2021.

[19] Z. Ding, F. Y. Wang, and X. J. Wei, "Analysis and prediction of surface deformation of soft soil double-line shield construction," *Journal of Zhejiang University*, vol. 53, no. 1, pp. 61–68, 2019.

[20] X. J. Wei, F. Y. Wang, Z. Ding, and J. C. Fan, "Torque analysis of shield cutter in soft soil area and its influence on surface deformation," *Journal of Central South University*, vol. 49, no. 6, pp. 1491–1497, 2018.

[21] C. D. Wan, Z. Y. Jin, and G. C. Cai, "Adaptability of the cutter-head of the earth pressure balance (EPB) shield machine in water-rich sandy and cobble strata: a case study," *Advances in Civil Engineering*, vol. 10, Article ID 8847982, 2020.

[22] Y. Qian, F. Min, Z. Mo, X. Fan, and Q. Tang, "Experimental study of the influence of excavation surface stability and sand flowability caused by dense slurry-earth pressure balance shield tunneling in silty sand stratum," *Advances in Civil Engineering*, vol. 2020, no. 12, pp. 1–14, 2020.

[23] C.-H. Cheng, S.-M. Liao, X.-B. Huo, L.-S. Chen, and Z. S. Shao, "Experimental study on the soil conditioning materials for EPB shield tunneling in silty sand," *Advances in Civil Engineering*, vol. 2020, Article ID 8856569, 21 pages, 2020.

[24] X. Z. Ling, X. X. Kong, L. Tang et al., "Face stability of the slurry shield–driven tunnel with an impermeable filter cake in saturated medium sand," *Arabian Journal of Geosciences*, vol. 14, no. 15, 2021.

[25] F. B. Zhu, L. C. Yu, and L. S. Lin, "Experimental study on ground settlement induced by dynamic construction of shield tunnel," *China Safety Science Journal*, vol. 27, no. 11, pp. 116–120, 2017.

[26] H. T. Wang, H. Hui, B. X. Tu, and J. Y. Zhang, "Model test study on influence of subway shield tunnel construction on stratum settlement in sandy soil layer," *China Railway Science*, vol. 38, no. 6, pp. 70–78, 2017.

[27] G. Wei, Z. F. Yang, and L. L. Lin, "Research on ground settlement caused by shield construction in sandy silty area," *Journal of Wuhan University of Technology*, vol. 34, no. 12, pp. 93–96, 2012.

[28] Q. He, G. Jian, and W. X. Ning, "Numerical simulation of shield underneath passing a river in shallow water-rich sand layer," *Earth and Environmental Science*, vol. 634, no. 1, pp. 1755–1315, 2021.

[29] Z. Zhang, W. Xu, W. Nie, and L. Deng, "DEM and theoretical analyses of the face stability of shallow shield cross-river tunnels in silty fine sand," *Computers and Geotechnics*, vol. 130, Article ID 103905, 2021.

[30] H. Lei, Z. Cheng, S. Feng, J. Lou, and H. Zhong, "Investigation on the macro- and microdeformation characteristics of silty clay under different shield construction stress paths," *Bulletin of Engineering Geology and the Environment*, vol. 80, no. 12, pp. 9105–9125, 2021.

[31] S. Suwansawat and H. H. Einstein, "Describing settlement troughs over twin tunnels using a superposition technique," *Journal of Geotechnical and Geoenvironmental Engineering*, vol. 133, no. 4, pp. 445–468, 2007.

[32] G. Wei, "Study on the value of width coefficient of ground settlement trough in shield tunnel," *Industrial Construction*, vol. 39, no. 12, pp. 74–79, 2009.

[33] G. Wei, "Research on value and distribution of soil loss rate caused by shield tunnel construction," *Chinese Journal of Geotechnical Engineering*, vol. 28, no. 9, pp. 1354–1361, 2010.

Research Article

Research and Application of Intelligent Monitoring System Platform for Safety Risk and Risk Investigation in Urban Rail Transit Engineering Construction

Yong Wu [iD],[1,2] **Liang-Yun Zhao,**[3] **Ye-Xiang Jiang,**[3] **Wei Li,**[3] **Ye-Sheng Wang** [iD],[1,2] **Huan Zhao,**[4] **Wei Wu,**[4] **and Xiong-Jian Zhang**[4]

[1]*Powerchina Huadong Engineering Co. Ltd., Hangzhou 310014, China*
[2]*Engineering Research Center of Smart Rail Transportation of Zhejiang Province, Hangzhou 310014, China*
[3]*Hangzhou Metro Group Co. Ltd., Hangzhou 310020, China*
[4]*Zhejiang Huadong Mapping and Engineering Safety Technology Co. Ltd., Hangzhou 310014, China*

Correspondence should be addressed to Ye-Sheng Wang; wang_yc2@ecidi.com

In recent years, the construction scale of urban rail transit project is still in a high growth stage. In addition, the geology and surrounding environment of crossing lines are complex, and all kinds of safety accidents are still in a high incidence stage. Based on the investigation and summary of safety risk events and their causes in urban rail transit engineering construction at home and abroad, this paper fully combines the current national security management policies, introduces the "dual control" concept of safety risk classification and hidden danger investigation, and develops the intelligent monitoring system platform for urban rail transit engineering construction based on advanced technologies such as intelligent Internet of Things, 3D visualization, and artificial intelligence. It realizes the intelligent collection and analysis of engineering field monitoring data, the dynamic early warning management of engineering risk sources, the process embedding "dual control" mechanism of safety risk and hidden danger investigation, the real-time supervision of large equipment operations such as shield and hoisting, and the real-time control of high-risk operation sections such as contact channels. At the same time, the traceability and assessment management of the safety supervision process are strengthened. The parties involved in the project can realize the synchronous sharing of information through the platform and improve the efficiency of on-site safety and quality control.

1. Introduction

Urban rail transit is the main traffic in China. The development of urban rail transit is of great significance to relieve the pressure of urban public transport, promote urban construction and promote the economic development of related industries, improve the travel and living quality of citizens, and improve the urban environment. Because it is mostly constructed in the middle of prosperous area of city, affected by many factors, such as the ground environment, geological conditions, construction conditions, and construction technology, large-scale network construction means that it will be confronted with huge safety risks, vulnerabilities, and management issues. In view of this, the national construction department has issued a number of opinions and regulations, which further clarified the requirements of the dual prevention mechanism of safety risk control and risk investigation and management in engineering construction [1–5]. In addition, it was pointed out in the outline of the 13th Five-Year National Informatization Plan (in China) that it is necessary to improve the informatization level of construction industry, enhance the integrated application of BIM, big data, intelligence, real-time

communication, cloud computing, Internet of Things, and other information technologies, and build an integrated supervision platform. Based on the above requirements, in view of the safety supervision of rail transit engineering, the research and development of information intelligent supervision platform is imminent.

At present, in view of the construction and management of urban rail transit projects, it can greatly improve the efficiency of management by establish the risk management and governance system which is information-based, visual, and intelligent [6–8]. Many scholars and institutions at home and abroad have also carried out research and application in related fields. In terms of security risk management, based on cost of safety (COS) theory and analytic hierarchy process (AHP), Aminbakhsh et al. [9] proposed a priority assessment method for security risk in construction engineering. Yoo et al. [10] forecast and evaluated the impact of the expansion project of Seoul Metro Line 3 in South Korea on the surrounding environment and possible risks by GIS and artificial neural networks. Ding and Zhou [11] established an urban subway safety risk early warning platform which automatically realizes the identification, evaluation, and early warning of engineering safety risks by data fusion model and which has been applied to Wuhan City subway construction project management. Li et al. [12] put forward the subway construction safety risk identification system and early warning system by BIM platforms. Aiming at the risk in subway construction, Yang et al. [13] developed a subway construction dynamic safety risk management and control information system and a supporting mobile phone inspection APP. Shen et al. [14] developed the Chengdu shield construction safety risk management information system which integrates the construction parameters, monitoring data, and live video surveillance of shield at all working points in the city and which has automatic reminder functions and perfect early warnings and disposal and alarm working mechanism for significant risky sources in shield construction. Wei et al. [15] established a 2D/3D visualization web platform which makes use of sensors to collect data from different angles and visualizes geological parameters and TBM parameters to predict potential risks in TBM construction. In terms of risk investigation and management, Ding [16] proposed a risk management system based on the classification, investigation, evaluation, reporting, and governance of risk. Moreover, on the basis of the model, the Beijing rail engineering safety and quality risk management information platform was jointly developed. Zhou et al. [17] developed a risk detection information system based on wearable devices with risk identification function and Internet data transmission technology, and the system was used in Wuhan subway engineering. Based on the shortcomings of current risk management system, Gu et al. [18] constructed a risk management system according to the closed-loop management theory which classifies risk in accordance with level, grade, and profession and proposed a six-link

closed-loop management model. In addition, Tianjin, Nanning, Shenyang, Hefei, and other places have also carried out the research and application of the safety risk management information system for the construction of rail transit projects [19–25].

In the application, some shortcomings of the existing platform have gradually emerged, mainly as follows: the platform has single function, the specialization of data analysis and risk prediction is not enough, and the safety risk management system and hidden danger investigation system are independent of each other. In addition, existing platforms often focus on single construction task, single component, or single security risk status, and thus it cannot aggregate and integrate multisource information in real time, it has not yet realized the integrated control of construction, operation, and maintenance, and it lacks management and control of major safety risk nodes such as lifting and hoisting and refinement of big data analysis modules and key indicators; therefore, it is impossible to realize overall and dynamic security risk management and risk investigation. Currently, the dual prevention content of security risks and hidden danger inspection required by national policies, laws, and regulations has not yet been embedded. Combining the above deficiencies, on the basis of fully understanding the relevant policies of national security management and emergency management, the basic theory of risk control, and the rules of hidden danger investigation and management, the authors focus on the overall relevance and unity of security risk management and hidden danger investigation and management. Combined with the requirements of the State Council to implement the dual prevention mechanism in the field of high-risk industries, this paper studies the integration of safety risk intelligent assessment, hidden danger investigation and management, intelligent data monitoring, shield and large lifting equipment management, patrol and video monitoring, and key risk nodes and contact channel safety management and control.

2. Overall Design of the Platform's Operating Mechanism

2.1. Business Requirement Analysis. Based on the above analysis and the understanding of risk management theory, risk management mainly realizes the risk prediction before engineering construction, puts forward the process precontrol measures, and implements the precontrol measures in the construction process, namely, risk control. Hidden danger investigation mainly conducts regular investigation on the risk precontrol measures proposed before in the process of engineering construction to ensure that the measures are in place. The developer conducted in-depth research of the intelligent monitoring system platform of risk management and hidden danger control based on the underlying monitoring technology of IOT in order to improve the overall safety and quality of urban rail transport network construction.

2.2. Overall Design of Operating Mechanism. Based on the foresaid research, taking engineering risk control as the principal line, the overall operating mechanism of this platform has established the corresponding dual control for hidden danger detection and management. On the basis of the static risk rating evaluation in the preparatory stage of the construction, the major risk sources and their control were viewed as the key of hidden danger investigation. On top of that, all major risk sources were ensured to be under effective control with multidimensional monitoring information including supplementary data, construction parameters, and site inspection. In addition, the risk source level was dynamically adjusted for larger hidden danger and early warning alarm in the process of hidden danger detection and risk source monitoring. The specific dual control design of risk and hidden danger management is shown in Figure 1.

2.3. Integrated Design of Warning and Alarm Mechanism. Combined with the characteristics of rail transit construction and safety risk control, this platform developed and designed a four-color early warning and alarm mechanism for engineering risk monitoring based on multidimensional data sources. The blue warning corresponding project is in the state of concern, the yellow warning corresponding project is in the state of control, the orange warning corresponding project is in the state of alarm and has not been effectively controlled, and the red warning corresponding project is in the state of emergency. Among them, the judgment basis for the above warning is as follows:

(1) Red warning: monitoring data seriously exceed the standard or monitoring data have great mutations. Combined with the on-site and surrounding environmental inspection, it is comprehensively judged as an unacceptable risk, and the agency is in the critical state of emergency.

(2) Orange warning: the monitoring data reach the level of engineering alarm. Combined with the site and surrounding environmental inspection, it is comprehensively judged that the project is not willing to accept risks, and the project is in an unsafe state. The site must immediately take control measures.

(3) Yellow warning: the monitoring data reach the level of engineering alarm. Combined with the site and surrounding environmental inspection, it is comprehensively judged as an acceptable risk, and the site must take preventive measures.

(4) Blue warning: the monitoring data reach the level of monitoring warning and monitoring alarm. It is necessary to remind all parties to pay attention to the continuous change of the monitoring data. When necessary, preventive measures should be taken on the scene.

The explanation of the early warning "double control" index is as follows: when the cumulative change or two-day change rate exceeds 85% of the alarm value or when the on-site inspection is abnormal, the system starts early warning. Monitoring alarm: when one of the "double control" indicators (cumulative change and change rate) exceeds the alarm value or when the on-site inspection finds abnormalities. Engineering alarm: the monitoring data exceed the cumulative alarm value and are still not convergent (the change rate exceeds the alarm value for three consecutive days) or the cumulative value has exceeded the control value given by the design or when the abnormal situation is found in the field inspection.

This mechanism can realize the integrated early warning and alarm of monitoring data, patrol inspection, hidden danger investigation, video monitoring, large equipment monitoring, and quality defect monitoring. At the same time, the corresponding dynamic level adjustment of risk sources can be matched to truly realize the effective dynamic control of the whole process of key risk sources. Based on GIS map, the real-time adjustment and display function of dynamic level of risk sources in the whole network can be realized. The detailed design of early warning and alarm mechanism is shown in Figures 2 and 3.

3. Overall Design of the System's Framework

The framework design of the platform's system adopted the latest computer software development technology and mainstream framework design while ensuring the system scalability and easy maintenance and other requirements. Programming languages Java and .Net should be given preference. The framework was designed and developed with MVC model to realize the display separation of logic, data, and interface. The platform's software modules should adopt hierarchical framework and object-oriented concept to reduce the coupling between modules as much as possible, while the detailed design must consider the scalability. The overall design of the platform's technical framework is shown in Figure 4.

4. Overall Design of the System's Function

In view of the platform's overall requirements described in Section 2.1, the main considerations in terms of functional design of the platform's framework cover intelligent multidimensional supervisory measurement, large equipment safety monitoring (shield informational monitoring, crane hoisting monitoring, video monitoring, and so on), overall security risk control module, GIS map overview and information integration display module and other modules with their respective function of geographic information display, engineering information display, red and yellow cards, every project has a file, message transfer, and so on. The overall functional design of the systems' framework is shown in Figure 5.

5. System Development and Application

Based on the overall design of the platform's operation mechanism, framework, and function, the platform's
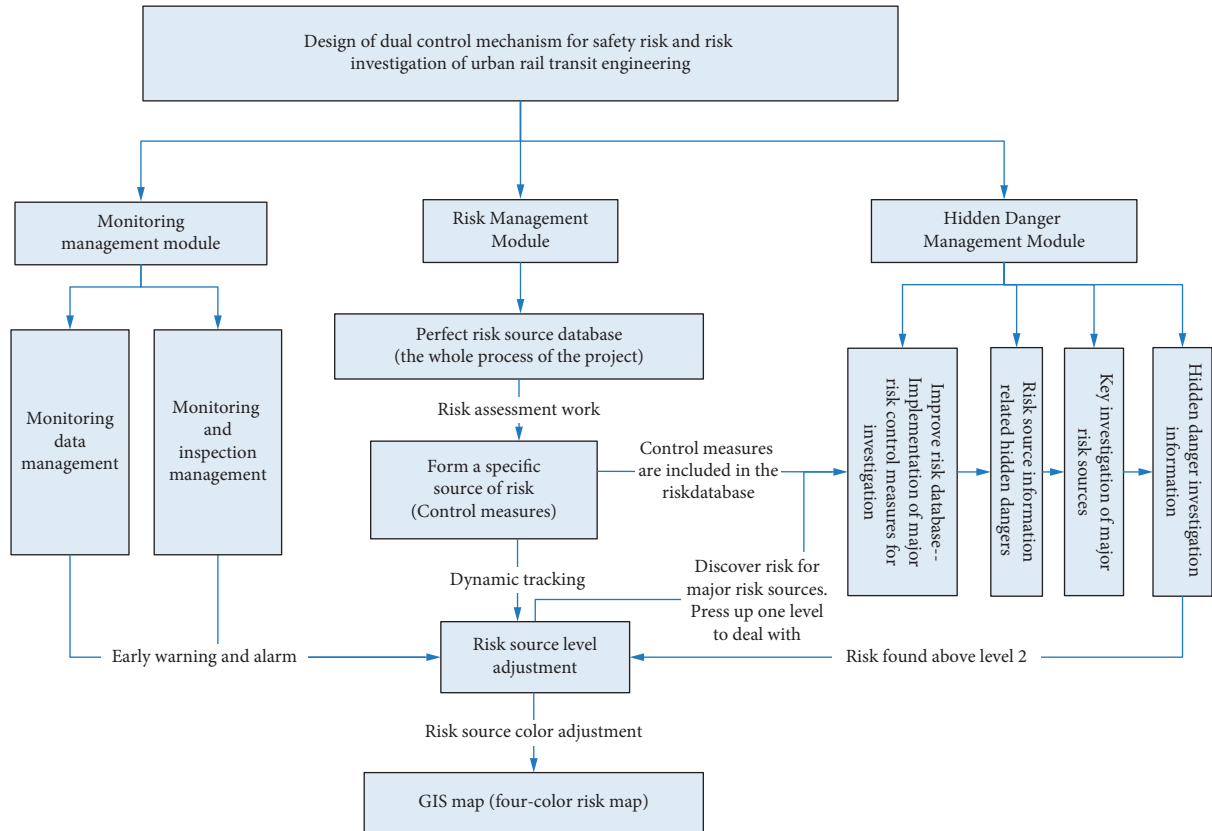
FIGURE 1: The design diagram of the dual management and control operation mechanism for the overall risk of the system platform.
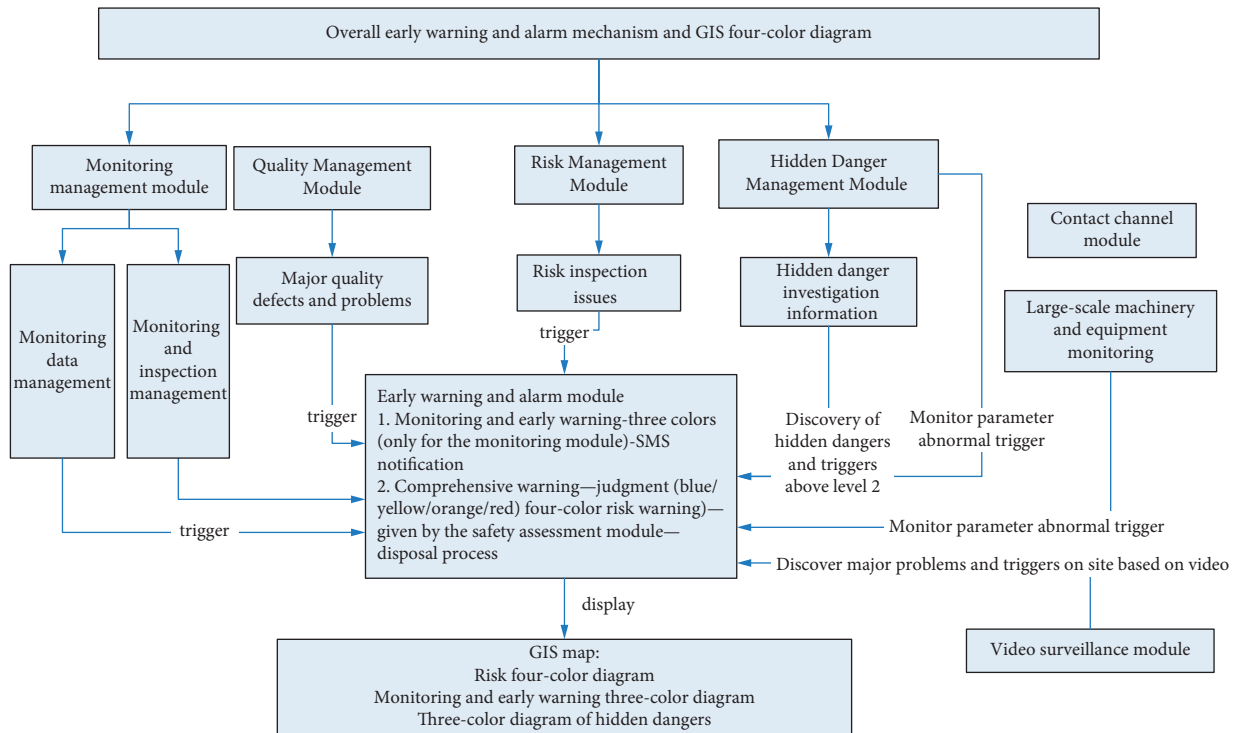
FIGURE 2: Design diagram of the overall early warning and alarm mechanism based on GIS four-color display.

FIGURE 3: Overall safety evaluation model of engineering early warning based on index analysis.

intelligent system of risk and hidden danger monitoring for urban rail transport project has been developed and formed on account of the full investigation and absorption of the advantage of the existing systems of major cities, and it was fully applied in the third-round project of Hangzhou subway construction, which achieved sound effect and economic benefits.

5.1. Portal Web and GIS. By integrating the basic data of each functional module, this module has realized info category display, model navigation, important message notification, task centralization, and other functions, so users need not switch back and forth between different functional modules.

Through GIS layer, it realized the multilayer display of more than five major themes in the same interface, such as construction state, risk tendency, hidden danger situation, warning alarm monitoring, and shield excavation, which can control the overall safety of urban rail transport construction.

Compared with other platforms, this module adds BIM 3D display (Figure 6) and engineering risk GIS 4D graph.

5.2. Intelligent Monitoring Measurement. Intelligent monitoring measurement module can realize at each work site the collection, integration, analysis, graphical display, trend forecast, and specified format report output of monitoring data.
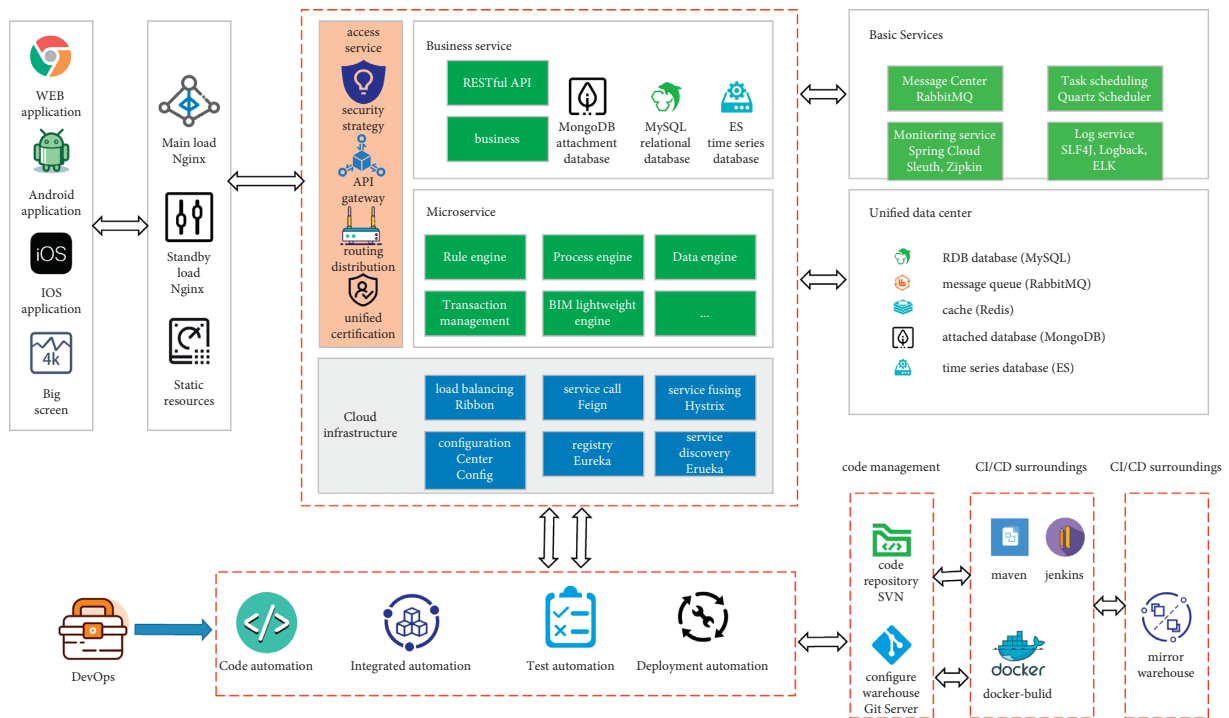
FIGURE 4: The architecture design drawing of the intelligent monitoring system for the investigation of safety risks and hidden dangers in urban rail transit engineering construction.
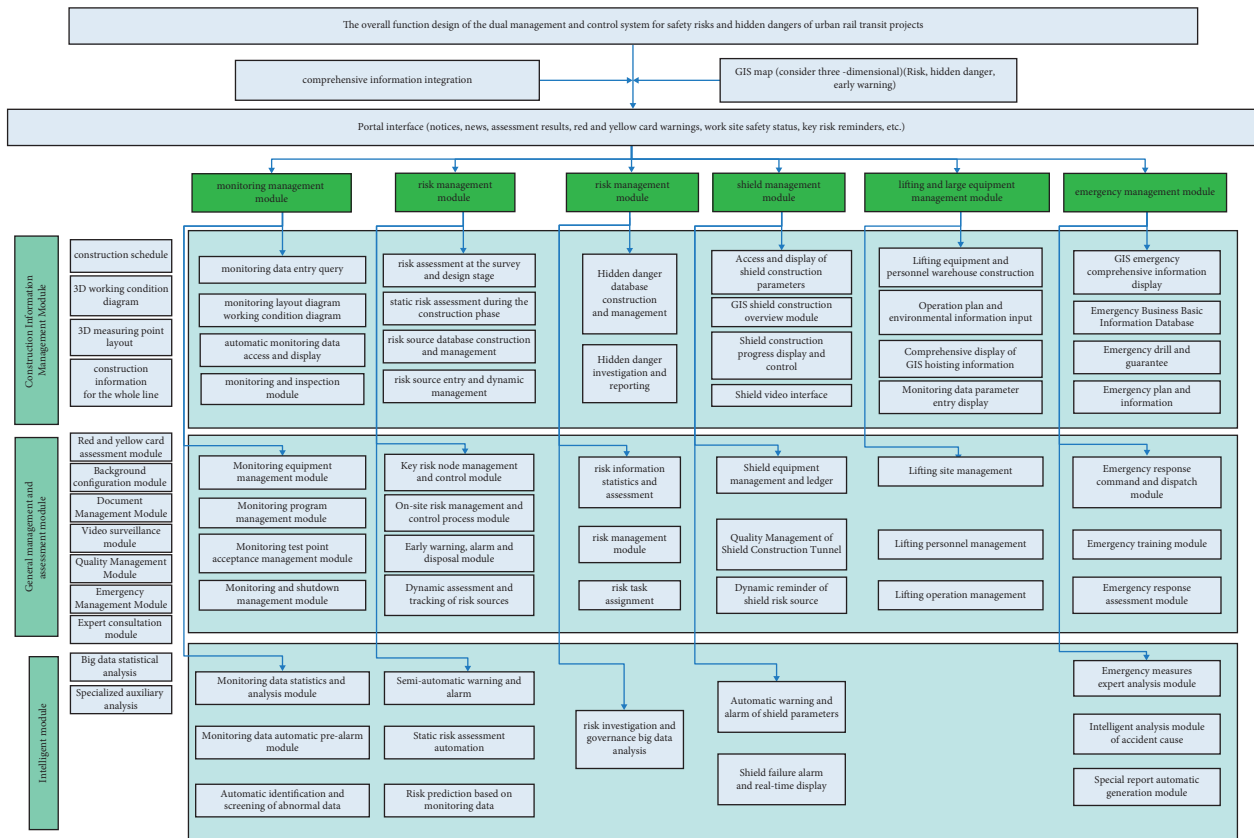
FIGURE 5: The architecture design of the intelligent monitoring system for the investigation of safety risks and hidden dangers in urban rail transit engineering construction.
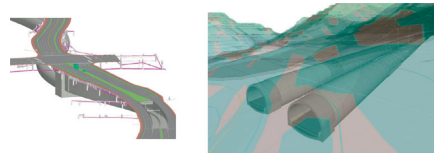
FIGURE 6: Engineering BIM 3D display model.
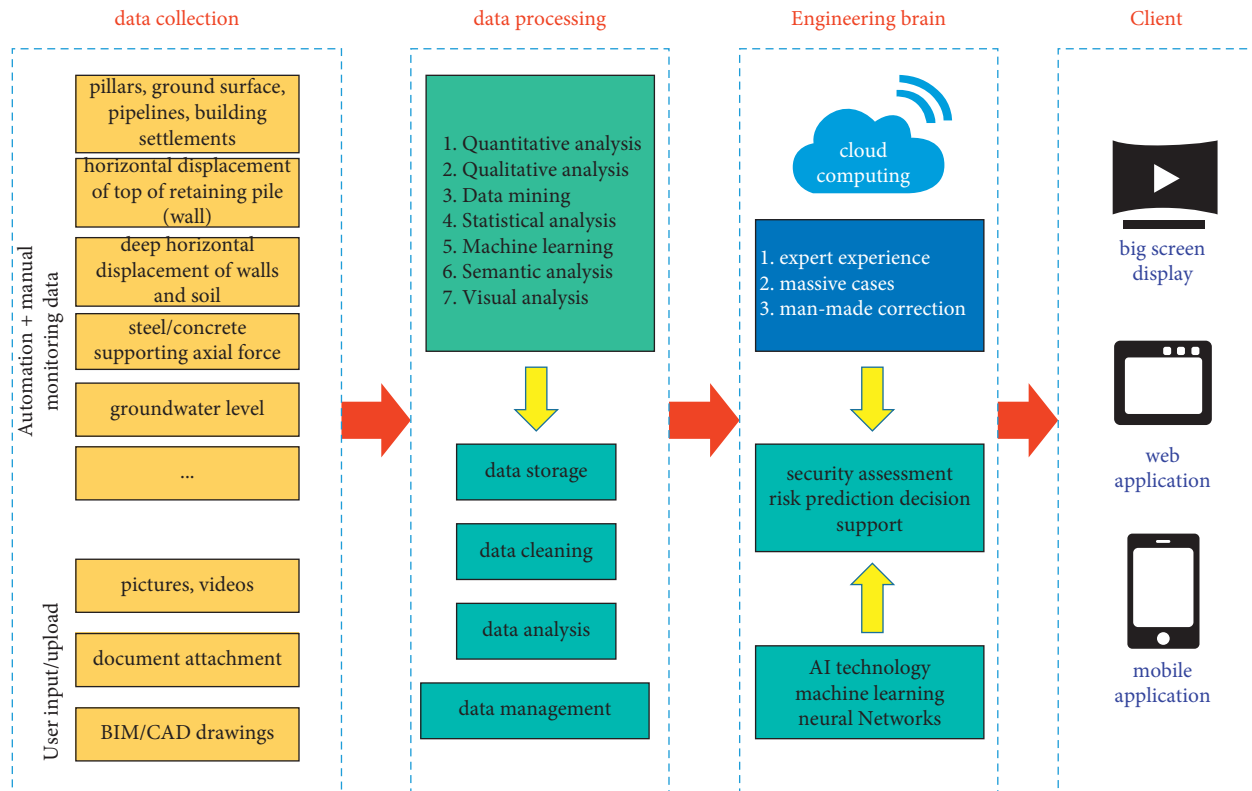
FIGURE 7: Monitoring and measurement module business flowchart.

The main idea is to integrate the IOT data in the safety monitoring system and manual monitoring data to analyze the relevant monitoring data at each work site in accordance with business needs using cloud computing, big data analysis, and other technologies, which can achieve data recording, graph drawing, automatic contrastive analysis of monitoring data, automatic warning for overrun, and the evaluation of the work site safety through monitoring data. The flowchart is shown in Figure 7. In the layer of data display, monitoring point data anomalies and their influence coverage are displayed in 3D visualization with BIM technology.

5.3. Intelligent Monitoring of Shield Machine.
Based on multiple heterogeneous data analysis and access technology to parameters of large shield tunneling machine of all brands, the module has acquired comprehensive access to PLC control parameters of well-known shield machines both at home and abroad, such as Herrenknecht, China Construction Tunneling Equipment, China Railway Engineering Equipment, Okumura, and Daye. While ensuring network information security, it can realize multilevel transmission stably and efficiently from LAN to Internet and has functions such as shield parameter online view, historical data review and statistical analysis, and so on. When the parameter exceeds the limit, it triggers automatic alarm and releases early warning notification in the form of SMS and APP. In addition, the shield module GIS can also achieve the dynamic display of shield machine tunneling path and real-time location through algorithms and correlate the major risk sources around the interval and the automatic release of risk forecast by the system during the traversal, which drew the attention of all parties.

5.4. Crane and Large Equipment Hoisting Monitoring.
This module mainly includes general information, library manager, hoisting log, safety control, and other submodules. It can realize the effective supervision of all kinds of crane and large equipment hoisting in the whole process.

5.5. Monitoring of Freezing Construction of Contact Channel.
The key risk point monitoring module of freezing engineering in contact channel can realize
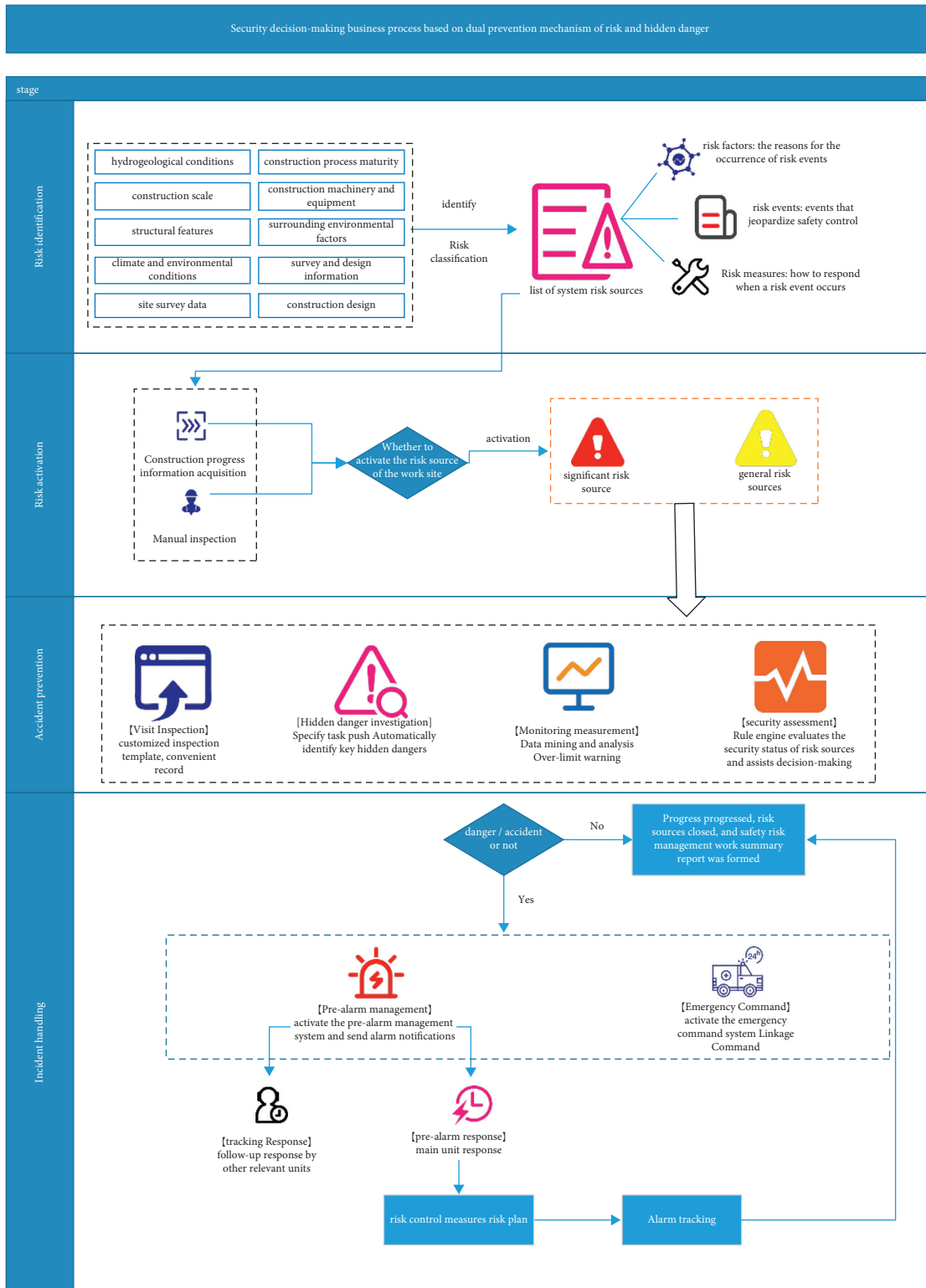
FIGURE 8: Security risk management and control process based on mechanism model.

automatic temperature data access, real-time temperature monitoring, automatic temperature abnormality pre-alarm, historical data query and statistics, aided safety assessment, freezing curtain calculation, and other functions.

5.6. Risk Management Module. This module is the core module of the system platform. Mainly based on the decision-making control of safety risk, it can identify and assess risks in the early stages of engineering construction, form control lists, and realize functions as dynamic risk control

and early warning management combined with the construction of a risk source database, and the security risk management and control process is shown in Figure 8.

5.6.1. Risk Source Management in Work Site.
The platform can form a project-wide dynamic risk source database according to the static risk assessment results, containing risk sources, factors, events, and measures. The work site risk source can form its control list based on the static risk assessment results and realize effective supervision of the work site risk sources through the system platform in the construction process.

5.6.2. Safety Assessment and Early Warning.
The safety assessment submodule allows daily risk assessments to be carried out to grasp the safety type of each work site. The page comprehensively displays information such as project overview, work condition diagram, and measuring point layout while associating risk source information according to construction progress.

Early warning submodule can show the warning information of each work site, including the warning level, time and status, and so on. The corresponding alarm report can be viewed in the attachment. In the search bar, you can filter searches according to the warning time and status as required.

5.7. Hidden Danger

5.7.1. Hidden Danger Investigation Module.
Integrated information module for hidden danger, through filtering time, can count the number of hidden dangers at all levels and form a pie chart and can compute the hidden danger rectification and form a bar chart so as to get detailed hidden danger statistics of each line according to the frequency of investigation below the chart.

5.7.2. Hidden Danger Investigation and Management Module.
The hidden danger check screen allows participants to add a hidden danger investigation record by creating a new task. The top of the page displays the number of each investigation status by different colors, and we can filter the qualified records by unit, situation, frequency type, start time, and other information.

In the hidden danger management module, the top of the page displays the status and quantity of hidden danger list by different colors, and we can filter the qualified lists by unit, hidden danger level, start time, and other information. One can check the specific information of the list and the progress of rectification through the "operation" button, and the hidden danger will be shut after the rectification is completed.

The hidden danger statistics module can count the number of various hidden danger levels by filtering lines and times and form the corresponding bar chart and pie chart.

5.7.3. Hidden Danger Assessment.
In the hidden danger assessment module, the rules of deducting points in the hidden danger management of Metro Group are inputted to the system to realize automatic assessment on the platform. You can select the work site to view the score through the left navigation tree. The system will show the total score and the reasons for points deduction in detail, and the specific deduction of points will pop up when you click on the button.

5.8. Overall Operation of the System.
As of December 31, 2020, the platform has been widely used in the third-round project of Hangzhou subway construction. At present, the monitoring module has reached a daily average processing of more than 50,000 monitoring data, with a total of 594 early warning messages; the video monitoring module has accessed a total of 261 work sites, with a total number of 1,783 videos; the crane hoisting module has recorded a total of 2,979 sets of equipment and 2,312 operators; the shield information module has accessed 332 shield machines and monitored nearly 120 shield constructions at the same time during the peak period of construction; the hidden danger investigation and management module rectifies and shuts more than 3,000 hidden dangers on average per month. When the platform was applied in the actual construction, the system has given full play to its role in improving the quality and efficiency of safety management in the process of intelligent multidimensional monitoring of engineering safety, static risk assessment and dynamic risk source control, hidden danger investigation and management of risk unit, comprehensive multidimensional information forewarning, and real-time information delivery. At the same time, it gave an excellent model and demonstration to the dual preventive work mechanism of risk rating control and hidden danger management for domestic rail transport projects, which brought about significant economic and social benefits and high promotion and application value.

6. Summary

The platform for the first time integrated and embedded into the system the dual control mechanism of safety risk control and hidden danger management, realizing the intelligent integration of multidimensional data based on the information of engineering safety monitoring, inspection, hidden danger investigation, major key points monitoring, shield and large equipment safety control, dynamic contact channel freezing temperature field, video and access control, engineering hidden danger investigation and management, etc. It has also realized the functions of prediction and prevention of key risk sources from the early stage of construction, of early warning and alarm, and of dynamic rating and control of the process risk, ensuring the whole process safety in the construction. The platform design generally reflected the concept of high security and data modelling, considered the overall information integration, achieved the automatic collection system, and realized the management process embedding, the 3D display, the

information-based work condition display, the project profile display, and other functions, which has great economic and social benefits.

Data Availability

No data were used to support this study.

Conflicts of Interest

The authors declare that they have no conflicts of interest.

Acknowledgments

References

[1] F. R. Luo and W. F. Cao, *Safety Risk Management System of Beijing Rail Transit Project*, China Railway Publishing House, Beijing, China, 2013.

[2] G. W. Liu, "Research and application on security and risk management information system for guangzhou metro project construction," *Railway Computer Application*, vol. 21, no. 5, pp. 29–33, 2012.

[3] Z. H. Shi, "Strengthening the development and operation management of urban rail transit projects," *Urban Rapid Rail Transit*, vol. 30, no. 1, pp. 1–3, 2017.

[4] P. Lyu, "Present situation and development of security technology for urban rail transit construction," *Urban Rapid Rail Transit*, vol. 30, no. 1, pp. 7–11, 2017.

[5] L. Q . Wang, "Research and practice on informatization of safety management for urban rail transit project in Guangzhou," *Journal of Safety Science and Technology*, vol. 12, no. 6, pp. 169–174, 2016.

[6] X.-S. Chen, Z.-H. Xu, B. Xiao-hua, X. Wang, and Y. Fu, "Challenges and technological breakthroughs in tunnel construction in China," *China Journal of Highway and Transport*, vol. 33, no. 12, pp. 1–14, 2020.

[7] Q. H. Qian and X. L. Rong, "State, issues and relevant recommendations for security risk management of China's underground engineering," *Chinese Journal of Rock Mechanics and Engineering*, vol. 27, no. 4, pp. 649–655, 2008.

[8] Q. Qian and P. Lin, "Safety risk management of underground engineering in China: progress, challenges and strategies," *Journal of Rock Mechanics and Geotechnical Engineering*, vol. 8, no. 4, pp. 423–442, 2016.

[9] S. Aminbakhsh, M. Gunduz, and R. Sonmez, "Safety risk assessment using analytic hierarchy process (AHP) during planning and budgeting of construction projects," *Journal of Safety Research*, vol. 46, pp. 99–105, 2013.

[10] C. Yoo, Y.-W. Jeon, and B.-S. Choi, "IT-based tunnelling risk management system (IT-TURISK) - development and implementation," *Tunnelling and Underground Space Technology*, vol. 21, no. 2, pp. 190–202, 2006.

[11] L. Y. Ding and C. Zhou, "Development of web-based system for safety risk early warning in urban metro construction," *Automation in Construction*, vol. 34, pp. 45–55, 2013.

[12] M. Li, H. Yu, H. Jin, and P. Liu, "Methodologies of safety risk control for China's metro construction based on BIM," *Safety Science*, vol. 110, pp. 418–426, 2018.

[13] C.-C. Yang, N. Wang, and Y. Lei, "Construction of information system of dynamic risk management for subway Construction," *Safety and Environmental Engineering*, vol. 24, no. 5, pp. 115–119, 2017.

[14] W.-P Shen, J. Zhang, and B. Yuan, "Research of safety risk management information system for shield tunneling construction in Chengdu metro based on intelligent interconnection technology," *Chinese Journal of Rock Mechanics and Engineering*, vol. 38, no. S2, pp. 3822–3832, 2019.

[15] L. J. Wei, M. Khan, O. Mehmood et al., "Web-based visualisation forlook-ahead ground imaging in tunnel boring machines," *Automation in Construction*, vol. 105, Article ID 102830, 2019.

[16] S. K. Ding, "Detection and treatment of hidden construction quality risks in urban rail transit," *Urban Rapid Rail Transit*, vol. 25, no. 6, pp. 43–47, 2012.

[17] C. Zhou, T. Ye, and L. Xing-gui, "Wearable devices for hidden danger identification and controlling in subway tunneling construction," *Journal of Civil Engineering and Management*, vol. 33, no. 2, pp. 30–35, 2016.

[18] X. Gu, D. Li, L. Zhang, and L. Ma, "Establishment and execution of potential safety hazard control system in Beijing subway," *Urban Mass Transit*, vol. 18, no. 7, pp. 9–13, 2015.

[19] C. Zhou, *Study on the Design and Application for Safety Control System in Metro Construction Project*, Huazhong University of Science and Technology, Wuhan, Hubei, China, 2007.

[20] G. Liu and H.-B. Cui, "Analysis and construction of safety-risk-management information system for metro construction based on GIS," *Architectural Technology*, vol. 42, no. 6, pp. 554–556, 2011.

[21] Y-Z. Wang, *Research on the Application of Security Risk Contorl Information Technology in Hefei Metro Line 2*, Lanzhou Jiaotong University, Lanzhou, China, 2018.

[22] W.-j. Zhu, R. H.. Weng, H. Q. Li, and X. Xi, "Development of metro hidden hazard investigation system based on mobile internet," *Urban Mass Transit*, vol. 22, no. 11, pp. 67–70, 2019.

[23] Z. Ding, X.-j Wei, and G. Wei, "Prediction methods on tunnel-excavation induced surface settlement around adjacent building," *Geomechanics and Engineering*, vol. 12, no. 2, pp. 185–195, 2017.

[24] Z. Ding, X.-j Wei, X. Zhang, and X.-s Yin, "Analysis of the field monitoring data on soil movements and adjacent building settlement due to shield tunnelling," *Engineering Computations*, vol. 36, no. 4, pp. 1219–1237, 2019.

[25] X. Yin, R. Chen, F. Meng et al., "Face stability of slurry-driven shield with permeable filter cake," *Tunnelling and Underground Space Technology*, vol. 111, Article ID 103841, 2021.

Research Article

Deformation Characteristics of Existing Twin Tunnels Induced by Double Shield Undercrossing with Prereinforcement: A Case Study in Hangzhou

Xinjiang Wei [iD],[1] **Mobao Zhang** [iD],[1,2,3] **Shaojun Ma,**[3] **Chang Xia,**[4] **Xingwang Liu,**[3] **and Zhi Ding** [iD][1]

[1]*Department of Civil Engineering, Zhejiang University City College, Hangzhou 310015, China*
[2]*College of Civil Engineering and Architecture, Zhejiang University, Hangzhou 310058, China*
[3]*Zhejiang Province Architectural Design and Research Institute, Hangzhou 310006, China*
[4]*Fuzhou Planning & Design Research Institute Group Co., Ltd., Fuzhou 350108, China*

Correspondence should be addressed to Zhi Ding; dingz@zucc.edu.cn

This paper is based on the case of the earth pressure balance (EPB) shield tunnelling project of the new Metro Line 2 undercrossing the existing Metro Line 1 in the soft soil urban area of Hangzhou. Because the EPB shield must break through a plain concrete wall before undercrossing the existing tunnels, the pipe roof prereinforcement was adopted to stabilize the soil between the existing tunnels and the new shield tunnel. The deformation characteristics of the existing tunnels in the process of double shield undercrossing were discussed. According to the variation of shield position, the settlement development could be divided into three stages: shield approaching subsidence, shield crossing heave, and shield leaving subsidence. The horizontal displacement shows a back and forth variation characteristic consistent with the direction of shield tunnelling. At the junction of tunnel and station, the shield undercrossing caused considerable differential settlement between the existing tunnel and the station. The construction of pipe roof prereinforcement will lead to the presettlement of the existing tunnels. The settlement of the existing tunnels caused by the attitude deviation of pipe roof and grouting disturbance should be reduced in reasonable ranges. In addition, the maximum longitudinal settlement of the existing tunnel during the shield second undercrossing was also discussed. It was considered that the influence of wall breaking is greater than the sequence of shield undercrossing. The driving parameters of shield tunnelling should be optimized before the second crossing.

1. Introduction

With the continuous advancement of urbanization, the metro system in Chinese major cities is developing rapidly, and the new shield tunnel crossing the existing metro tunnel is increasing frequently [1–4]. Especially in the city, underground space is increasingly complex nowadays, and the dangerous conditions such as small clearance, narrow space, and multiline staggered bring new challenges to shield crossing construction [5–7]. The disturbance of the shield tunnelling changes the stress and pore pressure of the surrounding soil, resulting in the soil deformation. The soil will transfer the deformation to the adjacent existing tunnel to have an impact on it [8, 9]. Shield undercrossing resulting in structural damage such as track bed detachment, segment cracking, and joint leakage, which will affect the safety of metro operation [10–12]. Due to the high requirements for deformation control of metro tunnels, certain prereinforcement measures were often adopted in engineering to ensure the operation of the metro tunnels [13, 14].

At present, scholars mainly use theoretical analysis, numerical simulation, model tests, and field measurement approaches to conduct a large number of studies on the impact of shield crossing on existing tunnels. For theoretical

analysis, the two-stage method is usually adopted, and the constant perfection in the foundation and tunnel model improved the accuracy and breadth of analysis [15–17]. For numerical simulation, many scholars have analyzed the interaction between shield machine, soil, and existing tunnel or carried out influence prediction based on the finite simulation approach [18–21]. For model test, the influencing factors analysis, such as soil condition, clear distance, intersection angle, and crossing type and the interaction evaluation of complex engineering condition, such as multiline overlapping, have received more and more extensive attention in recent years [22–24].

The field measurement data are the most direct expression of the impact of shield undercrossing [25–27]. The tunnelling of Heathrow Express tunnels at the CTA in the UK caused the maximum settlement of the existing Piccadilly Line tunnels to reach 63 mm. Three years later, the settlement reached 80 mm, the maximum cross section torsion was 0.15°, and a large number of cracks appeared [10]. Shenzhen existing Metro Line 1 undercrossed by four closely spaced tunnels of new Metro Line 7 and Line 9, with a minimum net distance of only 2.8 m [6]. The underground passage of Hangzhou Wenyi Road new tunnels undercrossed the existing Metro Line 2, resulting in a 23.5 mm uplift of the existing tunnels [27]. Mohamad et al. [28] used a distributed optical fibre strain sensing system and measured the stress and strain changes in the existing tunnel crossed by Thameslink shield in oblique angle of 21°. Li and Yuan [29] analyzed the influence of double shield undercrossing on the double-decked tunnel based on field measurement, considering that the superposition effect of double shield crossing would cause asymmetry longitudinal settlement of the existing tunnel, which was different from the deformation pattern of single shield crossing.

In addition, some prereinforcement measures are often adopted in engineering to reduce the adverse impact of shield undercrossing on the existing tunnels, such as in-tunnel grouting reinforcement [13, 30], spoil discharge jet grouting (SDJG) reinforcement [31, 32], steel segments reinforcement [14, 33], and pipe roof prereinforcement [34]. Pipe roof prereinforcement has been proved to be an effective technique to provide a temporary support for the soil before excavation face [35]. Luo et al. [36] analyzed the deformation mechanism of pipe roof and deduced the deformation calculation formula of pipe roof in the process of tunnel excavation. Yang et al. [37] obtained the relationship between the effective length of pipe roof and the height of excavation face. Wang et al. [38] reported a case study of ground surface settlement in the construction process of large-diameter shallow-buried tunnel prereinforced pipe roof in soft soil geological conditions. Li et al. [39] observed the project of tunnel construction under an operation airport runway and analyzed the runway movement caused by pipe-screen reinforcement and in-pipe grouting. It can be found that there were few reports about the engineering cases of using pipe roof to improve the soil between new and existing tunnels in soft soil urban areas, and the record of the influence of pipe roof construction on the existing tunnels was very limited. The effect of shield undercrossing on the existing tunnels under the prereinforcement of pipe roof also needed to be further evaluated.

This paper presents a case study of Hangzhou Metro Line 2 undercrossing Line 1 in soft soil urban area and aims to investigate the influence of double earth pressure balance (EPB) shield undercrossing and pipe roof prereinforcement construction on the existing twin tunnels. The project is located in the typical soft soil layer of Hangzhou Bay. The new and existing tunnels are closely crossed under the busy urban area, with a minimum clearance distance of 2.6 m. This paper describes and reports the process of pipe roof prereinforcement and the shield wall grinding. According to the monitoring data, the deformation characteristics of the existing twin tunnels during the first and second EPB shield undercrossing were compared, and the differential settlement between the tunnel and the station was reported.

2. Project Overview

2.1. Project Profile. Fengqilu Metro Station is located at the underground of the intersection of Yan'an Road and Fengqi Road in the urban area of Hangzhou and is connected with the Fengqi Road-Yan'an Road underpass. Fengqilu Metro Station is the interchange station for Metro Line 2 and Line 1, and the newly built Line 2 runs under Line 1. The plan and section view of the undercrossing area are shown in Figures 1 and 2.

The existing tunnel belongs to the section between Fengqi Road and Wulin Square of Hangzhou Metro Line 1, which is a circular-shaped shield twin tunnel in a north-south direction. The distance between the twin tunnels is 10.7 m and decreases slightly from south to north. The outer and inner diameters of the tunnel segment are 6.2 m and 5.5 m, respectively, and the single ring width is 1.2 m. The buried depth of the tunnel is about 9 m. Metro Line 1 began operation at the end of 2012.

The newly built Hangzhou Metro Line 2 is in east-west direction, and a twin tunnel with a circular shape is adopted. The horizontal distance between two tunnels is 9.8 m, and the buried depth of the tunnel is about 18 m. The intersection angle with the new and existing tunnel is 83°. The vertical distance between new tunnel and existing downline and upline tunnel is 2.8 m and 2.6 m, respectively. The downline of Metro Line 2 started from Fengqilu Station on April 11 and undercrossed Line 1 for the first time from April 19 to April 25, 2016. The undercrossing area of the new downline tunnel is from ring 7 to ring 30. Before undercrossing, there is a plain concrete wall of Underpass F that needs to be broken through. The upline of Metro Line 2 started from Zhonghe Road Station and passes through Line 1 for the second time from May 9 to May 13. The undercrossing area of the new upline tunnel is from ring 643 to ring 662. Two Japanese Mitsubishi EPB shields with a diameter of 6340 mm were used to construct the tunnel. The type and size of tunnel segments are consistent with those of Metro Line 1. The segments are connected by high strength bolts, and the joints are waterproof with EPDM (ethylene-propylene-diene monomer) rubber sealing strip, which has good processing performance and aging resistance [40, 41].
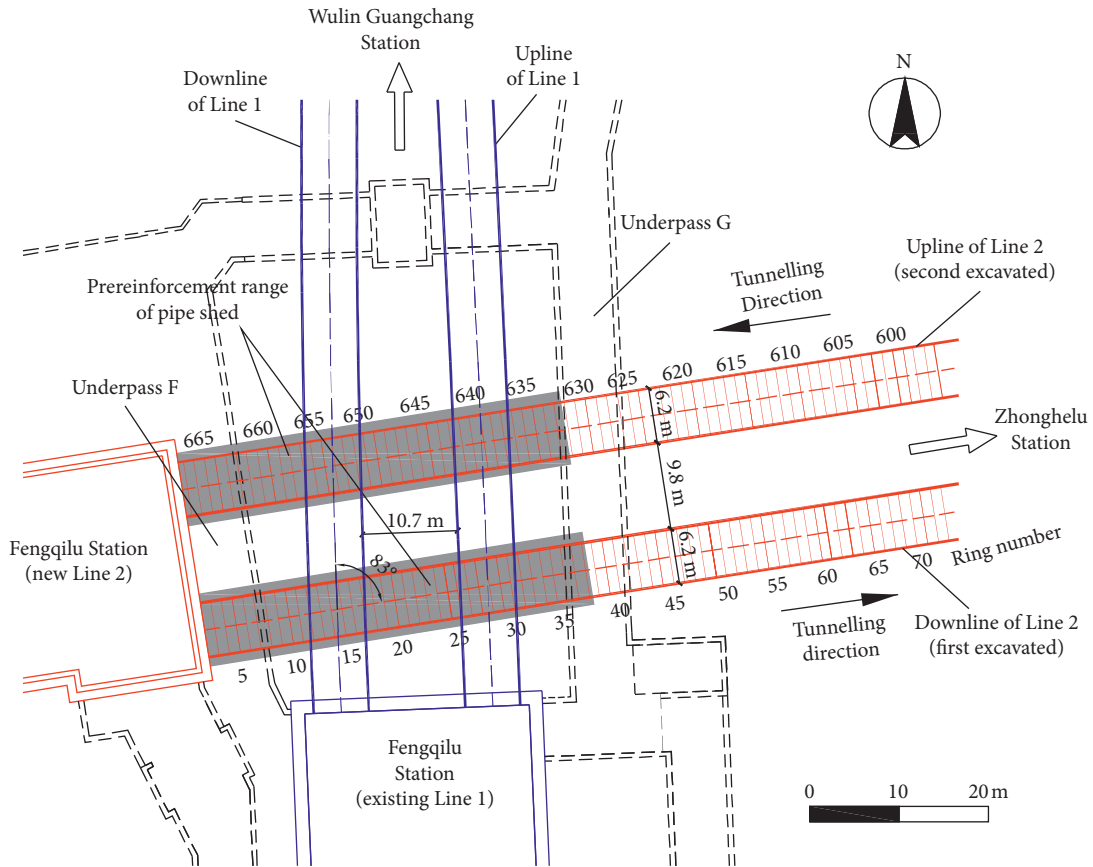
FIGURE 1: Plan view of new Metro Line 2 and existing Metro Line 1.
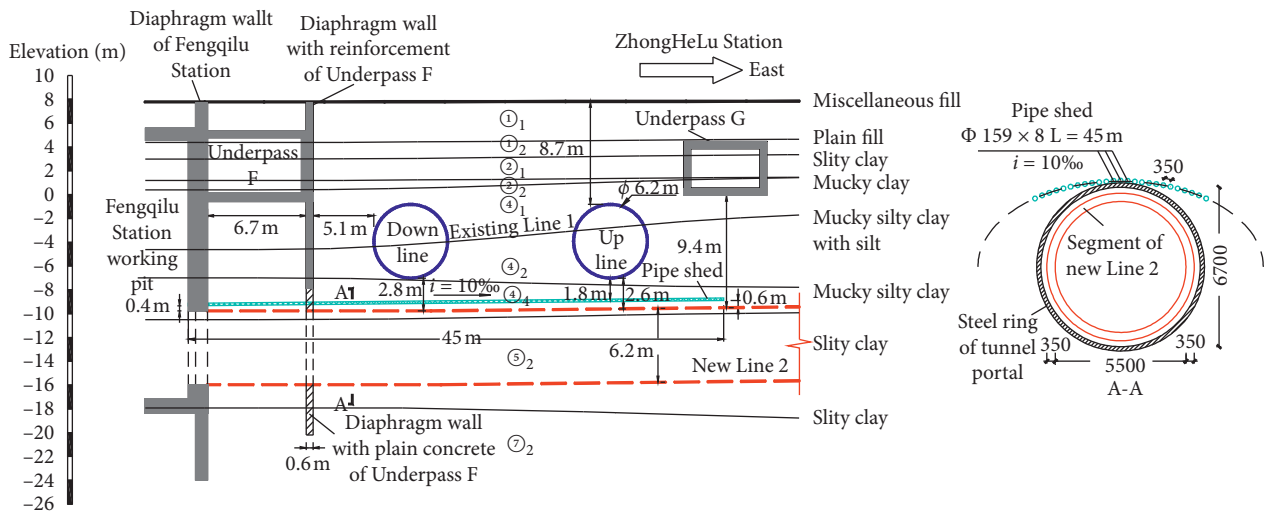
FIGURE 2: The sectional diagram of new Metro Line 2 and existing Metro Line 1 with typical geological profile.

2.2. Engineering Geology Conditions. According to the engineering geological investigation report, the undercrossing area is marine and continental intersedimentation strata, and the thickness of the quaternary strata is about 40 m. The surface of the site is filled with 0.7–5.0 m thick soil, and about 20 m below, it is mainly soft clay soil. The shallow groundwater of the site belongs to pore diving, mainly occurring in the surface fill and silty clay layer, and the buried depth of static water table is 2.1~3.6 m. Metro Line 1 is mainly located in the mucky silty clay layer, and Metro Line 2 is mainly located in the silty clay layer. The physical and mechanical parameters of soils are shown in Table 1.

TABLE 1: The physical and mechanical parameters of soils.

Layer number	Soil name	Unit weight γ (kN/m³)	Permeability coefficient (cm/s)		Water content ω (%)	Plastic limit W_p (%)	Cohesion c (kPa)	Friction angle φ (°)
			k_v	k_h				
②1	Silty clay	18.6	2.2×10^{-7}	6.7×10^{-7}	31.8	24.3	21.5	11.3
②2	Clayey silt	18.6	7.0×10^{-5}	1.0×10^{-4}	—	—	6.0	20.0
④1	Mucky clay	18.0	2.2×10^{-7}	3.1×10^{-7}	50.8	30.4	13.0	9.5
④2	Mucky silty clay with silt	18.1	3.0×10^{-6}	2.0×10^{-5}	34.5	21.4	14.0	10.0
④4	Mucky silty clay	17.4	2.5×10^{-7}	3.7×10^{-7}	41.3	25.5	13.0	9.0
⑤2	Silty clay	19.3	1.7×10^{-7}	3.0×10^{-7}	31.2	25.2	30.0	14.0
⑦2	Silty clay	18.5	1.8×10^{-7}	2.5×10^{-7}	30.3	24.2	31.3	16.3

3. Construction Progress of the New Metro Line 2

3.1. Pipe Roof Reinforcement. The new Line 2 is mainly located in the soft soil layer, and before the shield crosses the existing Line 1, it needs to break through the 600 mm thick plain concrete wall of Fengqilu Underpass F. In consideration of the disturbance of grind wall vibration to the soft soil layer and the super near net distance of 2.6 m, the pipe roof prereinforcement measures were adopted before the shield tunnelling of Line 2. Figures 1 and 2 show the layout of the pipe roof in plan and vertical section. The pipe roof prereinforcement was composed of 50 pieces of hot rolled seamless steel pipes. The elastic modulus of steel pipe is 2.06×10^5 MPa. 25 pieces were arranged in each arc direction above the upline and downline of Line 2. The outer diameter of the steel pipes was 159 mm and the thickness was 8 mm. The length of each steel pipe was 6 m, and both ends were preprocessed into external wire buckles for connection. The construction length of a single pipe roof was 45 m. The annular spacing of the pipe roof was 350 mm, and the longitudinal slope was 10‰. The vertical distance between the top of the pipe roof and Line 1 is about 1.8 m.

The construction steps of the pipe roof are shown in Figure 3: first, determine the location of each steel pipe and install the drill driver. Then, holes were drilled in the design position of the pipe roof to break the concrete and other obstacles. Thereafter, the pipe roof was driven into the soil by the drill inside the steel pipe sleeve, and the steel pipe was jacked in synchronously with the drill driver, as shown in Figures 4(a) and 4(b). The steel pipe was constructed from the middle to both sides, the construction of the next steel pipe needs to jump off an interval. In order to control the position of pipe roof jacking, a probe rod was installed in the drill pipe. When the steel pipe deviated, the wedge plate installed at the top of the auger bit was used to correct the jacking angle, as shown in Figure 4(c). Figure 5 is the site picture of the pipe roof after installation.

In order to enhance the overall stiffness of the pipe roof and further control the settlement of Metro Line 1 above, cement grout was filled inside the steel pipe after the installation of the pipe roof, and a certain pressure was maintained to make the grout flow out of the grouting hole on the steel pipe to infiltrate into the surrounding soil, so

that make each single concrete filled steel tube to form an integral arch shell. The cement grade used for grouting is PO 42.5, and the water-to-cement ratio was 0.8 : 1. The grouting pressure was controlled within 0.5~1.0 MPa. The construction and grouting of pipe roof for downline of Line 2 were from February 26 to March 10, 2016, for upline began on April 27 and finished on May 7, 2016.

3.2. Break through Plain Concrete Walls. As shown in Figure 2, the 0.6 m thick plain concrete wall needs to be broken before the downline of Line 2 crosses the existing Line 1. The tunnel portal of the Fengqilu Station is about 6.7 m away from the wall, and the downline of existing Line 1 is about 5.1 m away from the other side of the wall. The drilling core sample showed that the concrete strength of the wall is up to 34.4 MPa. If directly touching the concrete, the cutter head of the EPB shield was easy to get stuck. As shown in Figure 6, before the start of shield construction, four holes with a diameter of 0.18 m, corresponding to the position of the grouting hole outside the shield shell, were drilled from the tunnel portal of Fengqilu working pit, to drill through the plain concrete wall. On the one hand, it is convenient for the outside grouting hole to pass through the tunnel portal, and on the other hand, it can make the shield tunnel break the wall easier.

When the downline EPB shield cutter head was driving to the 7th ring, the rip teeth cutters touched the plain concrete wall. After that, the shield was suspended and the workers entered the earth chamber under normal pressure to drill some of the concrete manually where the previous hole had been. The diameter of the drill hole was controlled at 0.4~0.5 m and the depth is controlled at about 0.45 m, so as to ensure that enough thickness of concrete is left on the wall to prevent the soil from flowing in. Thereafter, the shield drove steadily and slowly, grinding through the plain concrete wall, as shown in Figure 7. The construction parameters of shield when grinding wall are shown in Table 2.

When the EPB shield is grinding 0.45 m into the concrete wall, enough pressure should be established in the earth chamber to maintain the earth pressure balance after the shield was driven into the natural soil. But at this time, the shield tail was still outside the portal, and no sealing system had been formed, so the pressure was difficult to establish. In
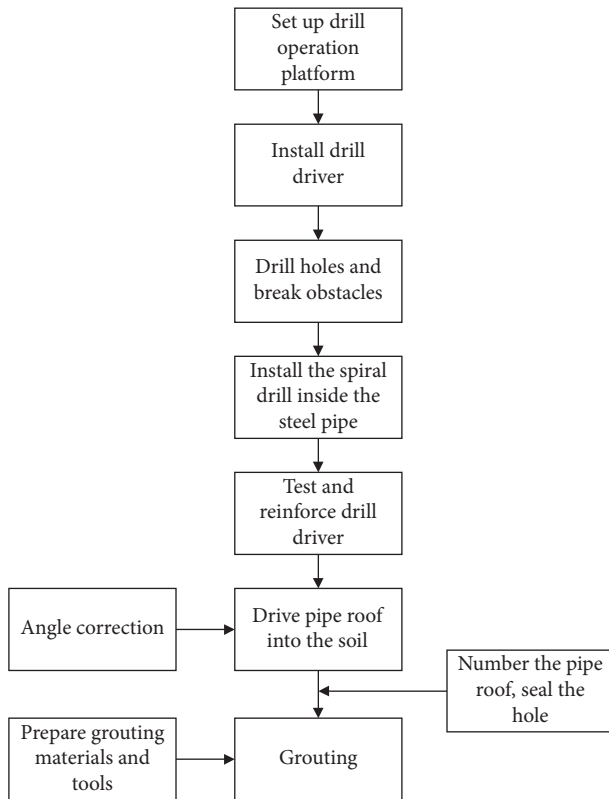
Figure 3: Construction steps of pipe roof construction.

order to fill the gap between the shield body and the surrounding soil, polyurethane was injected into the four corners of the shield to form a sealing ring. After that, steel sleeves were welded outside the portal to keep the EPB shield in a closed space so as to prevent soil loss and pressure relief, as shown in Figure 8.

3.3. Driving Parameters of EPB Shield.

Driving parameters of EPB shield will directly affect the soil around the shield and the adjacent existing tunnel, so it must be set accurately and adjusted in real time according to the monitoring feedback [42]. Before the downline shield of Metro Line 2 broke the wall, it was located in the reinforcement area of the tunnel portal, the EPB shield was half-empty or even empty excavated. The total thrust was about 5000–8000 kN, the cutter head torque was about 1000 kN·m, and the driving speed was stable at 10 mm/min.

When the EPB shield was grinding the wall, the total thrust increased to 18000 kN, the torque remained stable to about 1100 kN·m, the driving speed was set to 0.5 mm/min, and the pressure of 0.28 MPa was established in the earth chamber.

When the EPB shield entered the natural soil and crossed the existing Metro Line 1, the synchronous grouting of shield tail started, and the grouting volume per ring was 1.7 m^3. After the shield tail was discharged from the concrete wall, the grouting volume was adjusted to 3~3.5 m^3, the filling rate of grouting was 181%~212%, and the grouting pressure was 0.22~0.35 MPa. At this time, the earth chamber pressure was

set at 0.22~0.29 MPa, the total thrust was about 13500~15500 kN, the cutter head torque was about 1450~1550 kN·m, the driving speed was controlled at 15 mm/min, and the soil discharged per ring was about 40 m^3.

When the upline EPB shield of Metro Line 2 was undercrossing the existing Metro Line 1, the earth chamber pressure was set at 0.25~0.29 MPa, the total thrust was about 13500 kN, the torque of the cutter head was about 1000 kN·m, the driving speed was 20 mm/min, the synchronous grouting volume per ring was 2~3.5 m^3, and the filling rate of grouting was 121%~212%.

4. Deformation Monitoring and Analysis of Existing Metro Line 1

4.1. Monitoring Plan.

In order to reflect the influence of the EPB shield crossing process on Metro Line 1, a detailed monitoring plan has been made. The monitoring contents mainly involve track beds settlement, horizontal displacement, convergence deformation, and station settlement. As shown in Figure 9, 24 tunnel monitoring sections and 6 station monitoring sections were, respectively, arranged within the 150 m monitoring range of the existing Line 1. The text "US" and "DS" in Figure 9 represent the upline and downline monitoring sections of Line 1, respectively. The interval for the monitoring sections S7~S21 of the tunnel is 3.6 m, and the distance between monitoring sections S21~S30 is 6 m. The interval for the station monitoring section S1~S6 is 6 m.

Five monitoring points were set up in each tunnel monitoring section, as shown in Figure 10. The monitoring points P1 and P2 on the track beds were simultaneously used to measure the settlement and horizontal displacement of Line 1. P3 and P4, P1 and P5 were used to measure the horizontal and vertical convergence of the tunnel, respectively. In the station monitoring section, one monitoring point was installed on the track bed to measure the settlement of the track bed in the station. The monitoring points were monitored by an automatic measuring system composed of a Leica TS30 automatic total station and a reflecting prism, as shown in Figure 11. To focus on the deformation of the existing Line 1 caused by the shield crossing, the monitoring data of the existing tunnels returned to zero on April 5, 2016.

4.2. Settlement of the Existing Twin Tunnels of Line 1.

Figures 12 and 13 show the settlement development of some monitoring sections of the existing Line 1 in the process of double EPB shield tunnelling. The selected monitoring sections were located directly above the axis of the shield tunnelling. Positive values in the figure indicate tunnel heave and negative values indicate settlement.

As shown in Figure 12, the time of EPB shield tunnelling reflects the change of the relative position between the shield and existing Line 1. It can be divided into three stages: Stage 1 was the shield approaching stage, Stage 2 was the shield undercrossing stage, and Stage 3 was the shield away stage. When the shield passed through for the first time, the settlement of existing Line 1 showed an obvious stage change: first subsidence, then heave, and after that fall back.

(a)

(b)

(c)
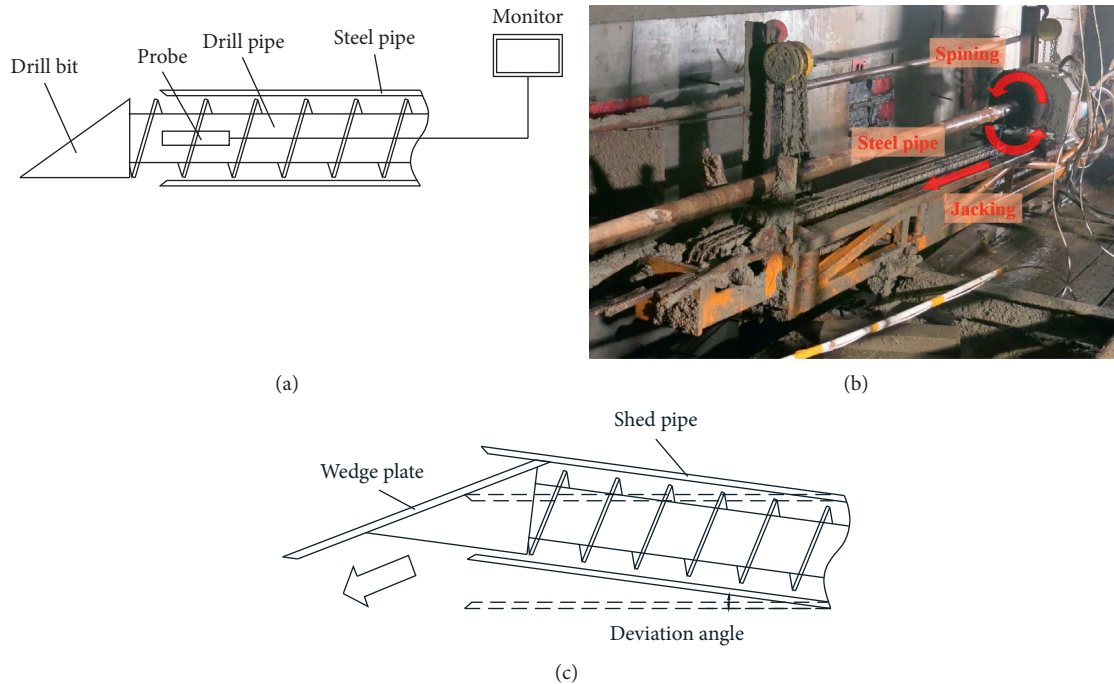
Figure 4: Pipe roof construction. (a) Pipe roof drill. (b) Drill driver. (c) Angle correction of drill bit.

Figure 5: Pipe roof installation.

Figure 6: The position of drill hole and grouting hole outside the shield shell.

The vibration of grinding wall caused the water loss of mucky silty clay with high water content behind the wall, which was the main reason for the settlement of the existing tunnel on Stage 1. After the wall was broken, the newly established pressure in the earth chamber, the rise of the total thrust, and the full grouting volume of the shield tail, coupled with the small number of shield tunnelling rings, the limited space for the grout diffusion, the undrained mucky silty clay layer, which is sensitive to disturbance, all of the above reasons made Line 1 show a rapid heave on Stage 2. After the shield tail protruded from the existing tunnel structural edge, the synchronous grouting continues to condense and the soil begins to consolidate resulting in the fall of heave of Line 1 on Stage 3.

As shown in Figure 13, during the second undercrossing, the settlement pattern of the existing Line 1 was different from that of the first undercrossing. On Stage 1, due to the less than one month from the first undercrossing, the pipe roof above upline of Line 2 was constructed from April 27 to May 7, and the settlement of existing Line 1 caused by the first undercrossing was not completely stable. Before the EPB shield passed through for the second time, the settlement of the upline of Line 1 developed steadily and the accumulated heave fell back to 2.1 mm, but the settlement of the downline developed rapidly and reached −6.5 mm. Therefore, on Stage 2, the earth chamber pressure and total thrust of the shield were not adjusted when passing through the upline of Line 1, and the heave of the upline was not large. When undercrossing the downline of Line 1, the earth chamber pressure was adjusted from 0.25 MPa to 0.29 MPa so that the heave of downline could offset the accumulated settlement. After the shield machine broke tunnel portal, the settlement of the existing tunnels on Stage3 fell back to stable.

(a)   (b)

FIGURE 7: Break through plain concrete walls. (a) Drill concrete manually. (b) EPB shield grinding.

TABLE 2: The variation of driving parameters during EPB shield grinding plain concrete wall.

Stroke (mm)	Length of shield cutter into the wall (cm)	Earth chamber pressure (MPa)	Total thrust (kN)	Torque (kN·m)	Advancing speed (mm/min)
1117	0	0.1	6727	180	0.5
1217	10	0.14	8146	180	0.5
1317	20	0.13	8388	1330	0.5
1420	30.3	0.14	12501	1100	0.5
1547	43	0.23	18360	1010	0.5
1590	47.3	0.23	18300	1100	0.5
1647	53	0.28	18420	1150	0.5
1747	63	0.28	18352	1110	0.5

FIGURE 8: Steel sleeve outside the tunnel portal.

Because of the existence of plain concrete wall and the different distance between the twin tunnels of Line 1 and the wall, the amount and trend of settlement of the existing twin tunnels of Line 1 were different. The settlement of the downline of Line 1 varies from −6.8 mm to 13.2 mm during the two undercrossing processes, while the settlement of the upline of Line 1 varies from −5.5 mm to 10.5 mm. According to *Technical Code for Protection of Urban Rail Transit Structures* DB33/T 1139-2017 (Zhejiang provincial standard) [43], the allowable cumulative value of tunnel vertical displacement is 15 mm (for structural safety condition: grade III). In this case, the tunnel heave had been close to this value. Daily inspection results showed that the existing tunnel structure remained intact and no new cracks and leakage appeared. In the range from 6 m before the cutter

head reaches the existing tunnel structure edge to 8 m after the shield tail leaves from the existing tunnel, the abrupt heave of the existing tunnel needs to focus on.

4.3. Horizontal Displacement of the Existing Twin Tunnels of Line 1. Figures 14 and 15 show the horizontal displacement variation of the monitoring sections that were above the axis of the EPB shield tunnelling. Positive values in the figure indicate that the existing tunnel moves to the Zhonghe Road Station (East) direction, while negative values indicate that the tunnel moves to the Fengqilu Station (West) direction. The variation of horizontal displacement of the existing tunnel could also be divided into three certain stages: Stage 1 was the displacement fluctuate stage when the shield was closing, Stage 2 was the displacement develop stage when the shield was passing, and Stage 3 was the displacement stable stage when the shield leaves. According to Figures 14(a) and 14(b), the vibration of grinding wall had little influence on the horizontal displacement of the existing tunnel. After the shield broke the wall, the cutter head pushed the soil forward and then caused the horizontal displacement of the twin tunnels of Line 1 in the same direction as the shield tunnelling on Stage 2. When the shield passed through the existing tunnel, the frictional effect of the shield shell caused the horizontal displacement developed rapidly eastward to 2.4–2.8 mm.

According to Figures 15(a) and 15(b), the horizontal displacement of Line 1 caused by the second crossing of the shield was similar to the first, but the absolute value of the
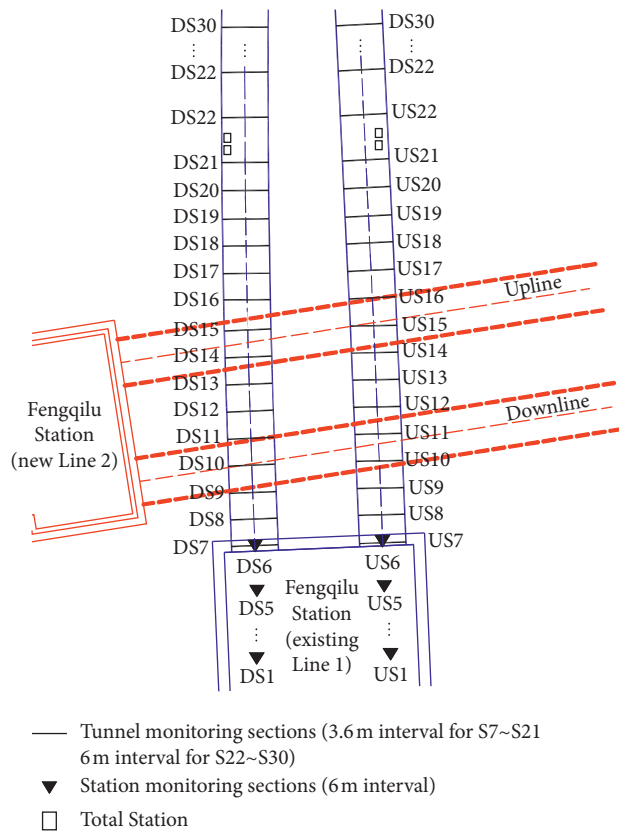
Figure 9: Layout of the monitoring sections of existing Line 1.

change was larger than first. The horizontal displacement was finally stabilized at 2.3 mm~3 mm westward. The magnitude and trend of horizontal displacement of upline and downline of Line 1 caused by shield crossing were similar, and there was no obvious relationship with the sequence of shield crossing and the distance from the wall. The horizontal displacement of the downline of Line 1 varies from −3.2 mm to 2.9 mm during the two crossing processes, and of the upline varies from −2.6 mm to 2.8 mm. It is far lower than the allowable cumulative value of 14 mm according to *Technical Code for Protection of Urban Rail Transit Structures* DB33/T 1139-2017 [43].

4.4. Differential Settlement at the Junction of Station and Tunnel of Line 1. Figure 16 shows the settlement development of Line 1 at the junction of the station and tunnel in the process of EPB shield crossing. The data in Figure 16(a) were from the station monitoring point DS6 and the tunnel monitoring section DS8. The data in Figure 16(b) were from the station monitoring point US6 and the tunnel monitoring section US8. The distance between DS6 and DS8 (US6 and US8) was about 4.2 m. As shown in Figure 16, the settlement between the existing tunnel and the station caused by shield crossing was significantly different. Influenced by the first shield undercrossing, due to the proximity of the shield tunnelling axis, the maximum heave of the tunnel monitoring section DS8 reached 9.0 mm. However, the settlement of station monitoring point DS6, which is 4.2 m away from

the DS8, was only −0.4 mm. The differential settlement reached 9.4 mm, and the average differential settlement was 2.2 mm per meter. After completion of the second shield crossing, the final differential settlement stabilized at about 1.9 mm.

For the upline of Line 1, the maximum heave of tunnel monitoring section US8 caused by the shield tunnelling for the first time was 2.0 mm, the settlement of station monitoring point US6 was −0.7 mm, and the differential settlement was 2.7 mm. The final differential settlement was about 1.8 mm.

In this project, the nearest horizontal distance between the shield tunnelling axis and the station edge of Line 1 was about 10 m. Influenced by shield crossing, the heave and settlement of the tunnel of Line 1 were very obvious within this range, but the settlement of the station was not as significant as that of the tunnel because of its large size and irregular structure. It should be emphasized that the differential settlement between the station and the tunnel will affect the running comfort of the train. The tunnel station stiffness difference and vehicle vibration may result in the further development of differential settlement, which lead to cracks, leakage, and other structure diseases at the junction. Therefore, the differential settlement caused by shield crossing at the interchange station area should be paid more attention to.

5. Discussion

5.1. Influence of Pipe Roof Construction. The settlement monitoring of the existing tunnel mentioned above excludes the existing tunnel heave caused by pipe roof construction itself. However, the construction of the pipe roof may also lead to the settlement of the existing tunnels. Figure 17 shows the settlement of the existing Line 1 before the departure of the downline of Line 2. Before shield tunnelling, the maximum settlement of the existing tunnel was 6.2 mm due to the construction of the pipe roof. The reasons can be attributed to two aspects: (1) The pipe roof has a length of 45 m, and the outer diameter of the steel pipe is 159 mm. However, the pipe roof was driven by a drill driver and guided by a wedge plate, so there were some difficulties in attitude control and it was easy to produce attitude deviation [39]. It can also be seen from Figure 17(b) that the upline of Line 1, which was far from the tunnel portal, appeared heave after the installation of the pipe roof, which proved that the attitude of the pipe roof was deviated, and the attitude at the far end was more difficult to control. (2) The stratum where the pipe roof was located in ④ mucky silty clay layer, and the pipe roof was connected as a whole by grouting. However, the grout was easy to be lost under such stratum conditions and further disturbed the soil, resulting in a certain degree of additional settlement of the soil [44].

5.2. Comparison of the Maximum Longitudinal Settlement of Existing Tunnels in Two Crossing Processes. In the process of double shield undercrossing, the downline and upline of existing Line 1 face the opposite crossing sequence, and both
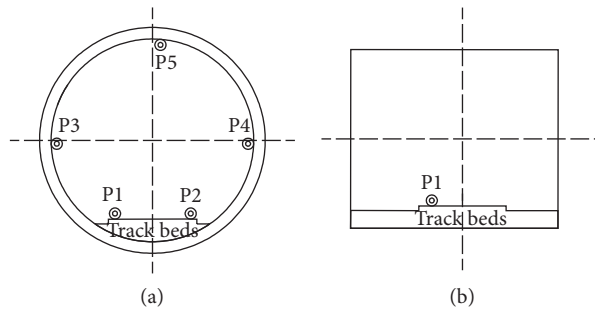
FIGURE 10: Arrangement of monitoring points for monitoring section.

FIGURE 11: Automatic total station and reflection prism.
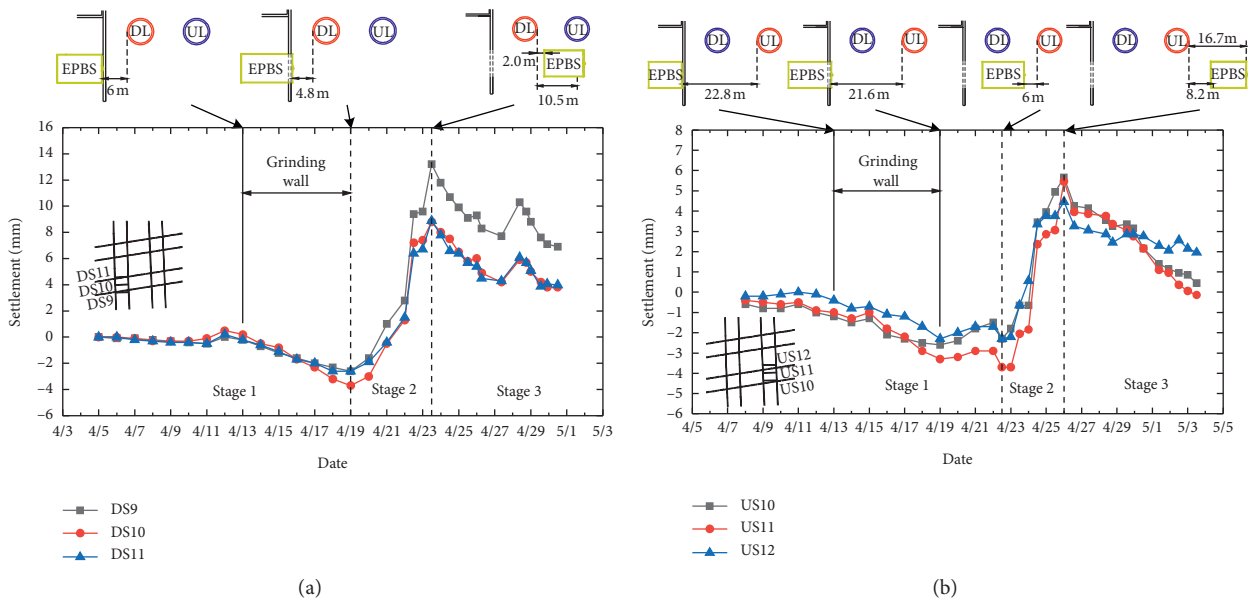
FIGURE 12: Development of settlement of the existing Line 1 during downline shield tunnelling of Line 2. (a) Downline of Line 1. (b) Upline of Line 1.

appear to a certain degree of heave phenomenon. The comparison of the maximum longitudinal settlement of the existing Line 1 is shown in Figure 18. First of all, on the first Stage 2, the shield crossing caused heave of the downline tunnel was larger than the upline. On the second Stage 2, the sequence of shield crossing was reversed, but the longitudinal heave of the two existing tunnels showed similar characteristics. Third, by comparing the heave of the upline of Line 1 on the first and second Stage 2, it was found that the size and distribution of tunnel heave were similar. Combined with the above three points, it could be concluded that the wall breaking of shield in a narrow space has a great

(a)

(b)
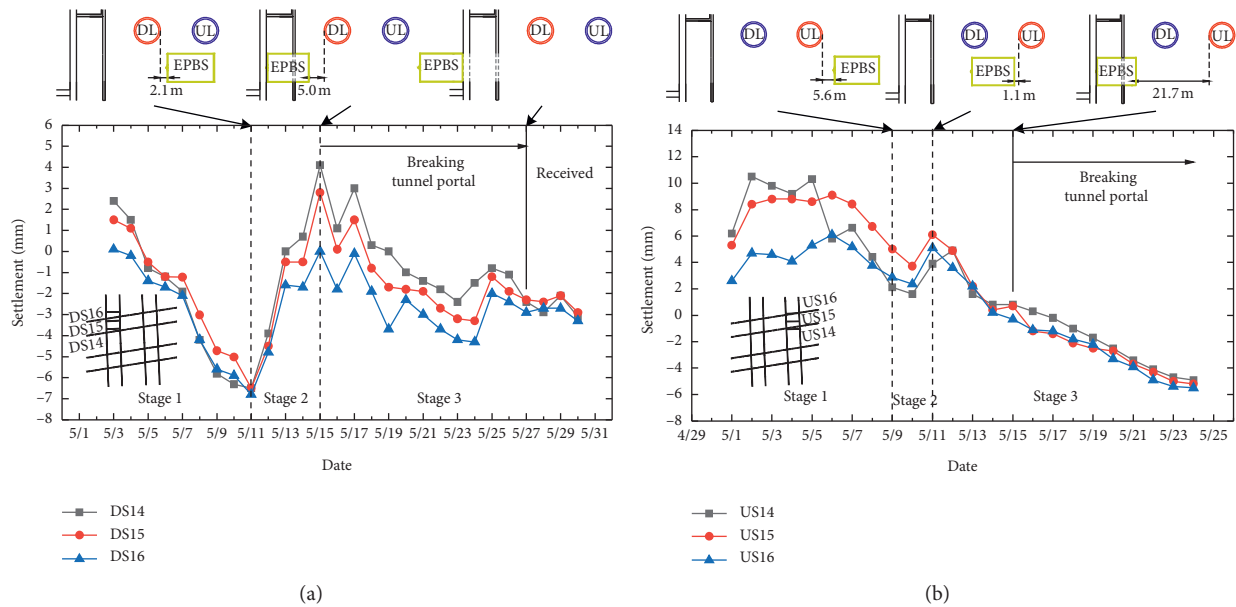
Figure 13: Development of settlement of the existing Line 1 during upline shield tunnelling of Line 2. (a) Downline of Line 1. (b) Upline of Line 1.

(a)

(b)
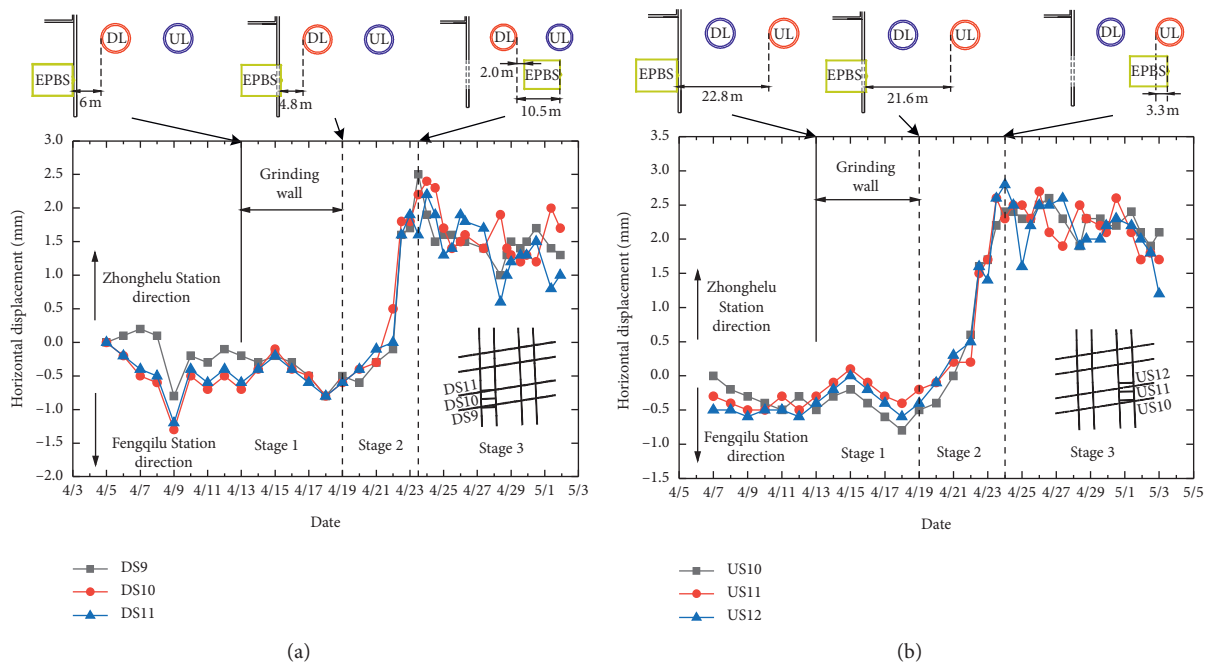
Figure 14: Development of horizontal displacement of the existing Line 1 during downline shield tunnelling of Line 2. (a) Downline of Line 1. (b) Upline of Line 1.

influence on the longitudinal deformation of the existing tunnel, while the effect of sequence of shield crossing is relatively insignificant.

In addition, the driving parameters of shield were adjusted in the second undercrossing (as shown in Table 3). It took 5 days for shield machine to cross under the existing tunnels in upline construction, but took 8 days for downline construction. Shorter construction time is more likely to

reduce the disturbance to the soil [45]. Smaller earth chamber pressure, total thrust, and grouting volume may also result in the less impact of superposition effect of the second shield crossing. Li and Yuan's study [29] pointed out that the shield driving parameters and monitoring results of the existing tunnel gathered in the first crossing could be fully studied and demonstrated before the second crossing, to provide reliable engineering experience for subsequent

(a)

(b)
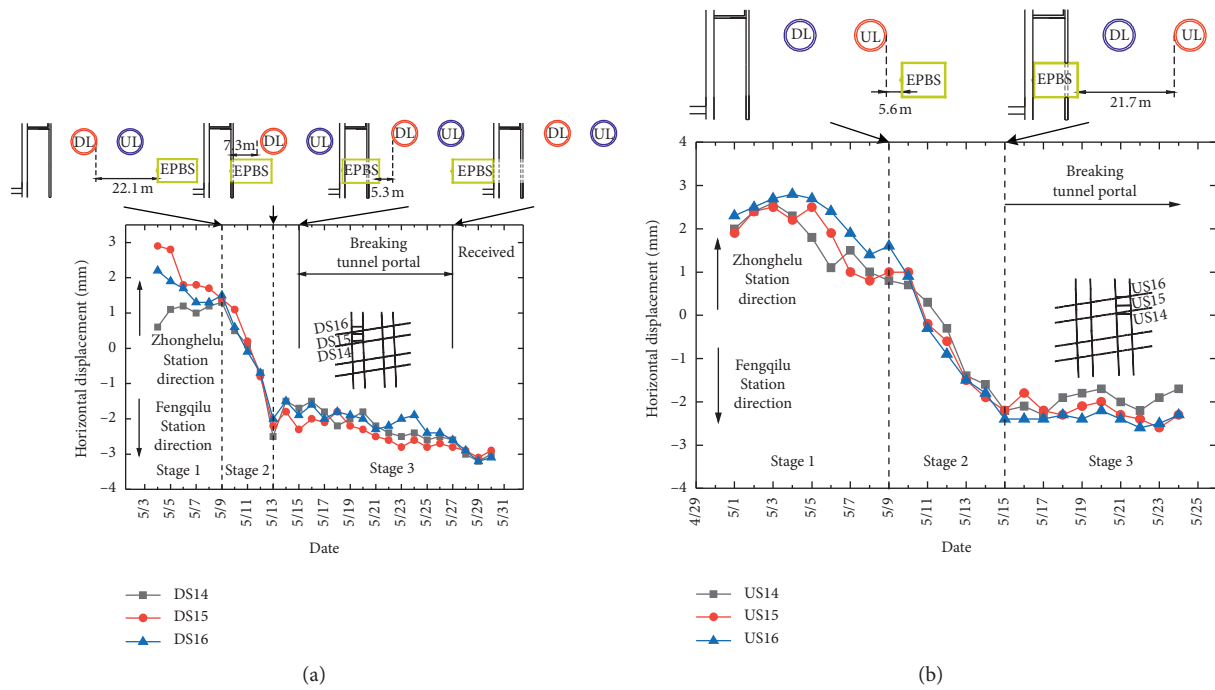
FIGURE 15: Development of horizontal displacement of the existing Line 1 during upline shield tunnelling of Line 2. (a) Downline of Line 1. (b) Upline of Line 1.

(a)

(b)
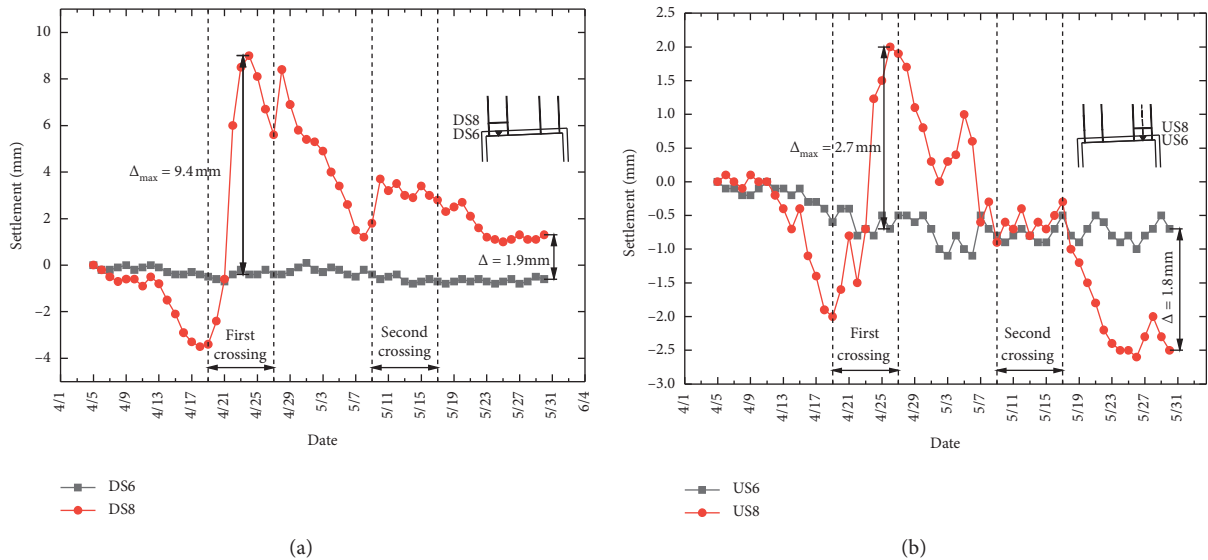
FIGURE 16: Settlement difference of the tunnel and station of existing Line 1 during shield tunnelling of Line 2. (a) Downline of Line 1. (b) Upline of Line 1.

(a)

(b)
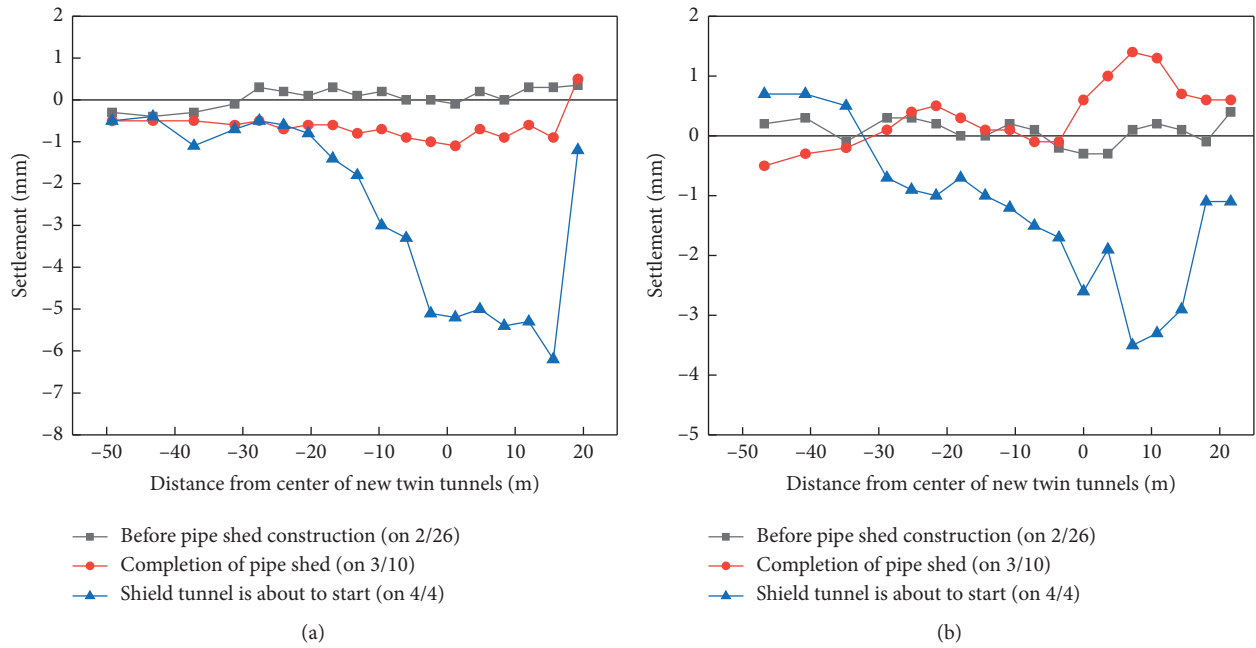
FIGURE 17: Longitudinal settlement of Line 1 before the shield tunnelling of the downline of Line 2. (a) Downline of Line 1. (b) Upline of Line 1.

(a)

(b)
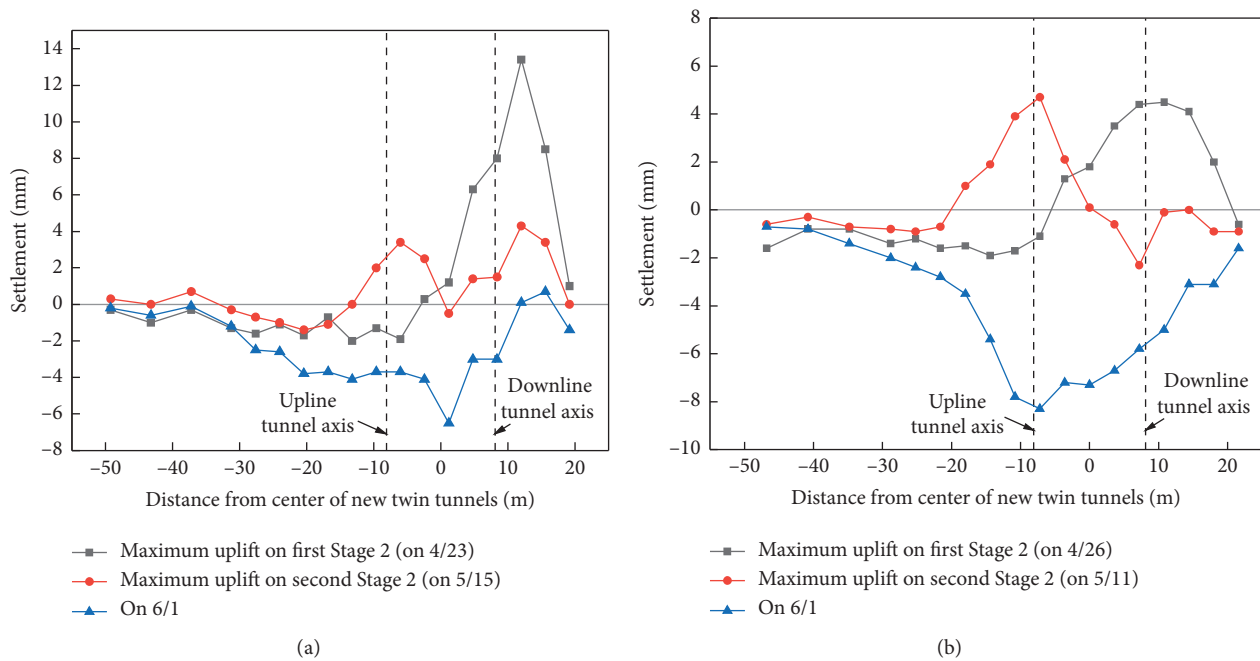
FIGURE 18: Maximum longitudinal settlement of Line 1 on typical stages. (a) Downline of Line 1. (b) Upline of Line 1.

TABLE 3: The driving parameters in double shield tunnelling process.

Newly built line	Shield tunnelling days	Crossing patterns	Earth chamber pressure (MPa)	Torque (kN·m)	Total thrust (kN)	Grouting volume per ring (m³)	Average advancing speed (mm/min)
Downline	Break through plain concrete wall: 6 days Undercrossing: 8 days Total: 14 days	First break through the wall, then undercrossing	0.22~0.29	1450~1550	13500~15500	3~3.5	15

TABLE 3: Continued.

Newly built line	Shield tunnelling days	Crossing patterns	Earth chamber pressure (MPa)	Torque (kN·m)	Total thrust (kN)	Grouting volume per ring (m³)	Average advancing speed (mm/min)
Upline	Undercrossing: 5 days Break through plain concrete wall: 2 days Total: 7 days	First undercrossing, then break through the wall	0.25~0.29	1000	13500	2~3.5	20

construction and reinforcement. Finally, on June 1, 5 days after the shield was received, the longitudinal heave of the downline and upline of Line 1 developed towards settlement and finally reached −6.5 mm and −8.3 mm, both of which were controlled within a reasonable range.

6. Conclusion

Based on the double EPB shield undercrossing the existing twin tunnel project in the soft soil area of Hangzhou, this paper introduced the measures of pipe roof reinforcement and shield wall grinding. The deformation of the existing twin tunnels was analyzed based on field monitoring. The main conclusion of this paper is summarized as follows:

(1) When the EPB shield undercrossing the existing tunnel under the complicated underground environment, it is a feasible method to use pipe roof to prereinforce the upper soil of the newly built tunnel. This case can be used as a reference for similar shield undercrossing existing tunnel projects in the future.

(2) The deformation of existing tunnel is closely related to the relative position of the EPB shield. The settlement development can be divided into three stages according to shield position change: shield approaching subsidence, shield crossing heave, and shield leaving subsidence. The horizontal displacement shows a back and forth variation characteristic consistent with the direction of shield tunnelling. Considerable differential settlement will occur at the junction of the tunnel and the station.

(3) Prereinforcement measures of pipe roof will cause early settlement of existing tunnels. It is necessary to carefully plan the installation and construction of long-distance and large-diameter pipe roof, control the pressure and flow rate of pipe roof grouting in soft soil area, and handle well of monitoring feedback, so as to minimize the tunnel settlement caused by attitude deviation and grouting disturbance during pipe roof construction.

(4) Break through the concrete wall in a narrow space will have a great impact on the existing tunnel. After the wall is broken by the EPB shield, the newly built earth chamber pressure, the rise of the total thrust, and the grouting, which is difficult to diffuse at shield tail, all the above will cause the heave of the existing tunnel near the wall. For shield undercrossing twin tunnels, the influence of the crossing sequence is less significant than that of wall breaking. After the optimization and adjustment of driving parameters, the influence of shield second undercrossing on the longitudinal heave of the existing tunnel can be well controlled.

Data Availability

The data used to support the findings of this study are available from the corresponding author upon request.

Conflicts of Interest

The authors declare that they have no conflicts of interest.

Acknowledgments

References

[1] S. Liao, J. Liu, R. Wang, and Z. Li, "Shield tunneling and environment protection in Shanghai soft ground," *Tunnelling and Underground Space Technology*, vol. 24, no. 4, pp. 454–465, 2009.

[2] Z. Huang, C. L. Zhang, and H. L. Fu, "Numerical study on the disturbance effect of short-distance parallel shield tunnelling undercrossing existing tunnels," *Advances in Civil Engineering*, vol. 2020, Article ID 8810658, 14 pages, 2020.

[3] Z. Ding, X. Wei, X. Zhang, and X. Yin, "Analysis of the field monitoring data on soil movements and adjacent building settlement due to shield tunnelling," *Engineering Computations*, vol. 36, no. 4, pp. 1219–1237, 2019.

[4] Z. Ding, X.-j. Wei, and G. Wei, "Prediction methods on tunnel-excavation induced surface settlement around adjacent building," *Geomechanics and Engineering*, vol. 12, no. 2, pp. 185–195, 2017.

[5] X. Liu, Q. Fang, and D. Zhang, "Mechanical responses of existing tunnel due to new tunnelling below without clearance," *Tunnelling and Underground Space Technology*, vol. 80, pp. 44–52, 2018.

[6] D. L. Jin, D. J. Yuan, S. Y. Liu, X. G. Li, and W. P. Luo, "Performance of existing subway tunnels undercrossed by four closely spaced shield tunnels," *Journal of Performance of*

Constructed Facilities, vol. 33, no. 1, 11 pages, Article ID 4018099, 2019.

[7] H. P. Lai, H. W. Zheng, R. Chen, Z. Kang, and Y. Liu, "Settlement behaviors of existing tunnel caused by obliquely under-crossing shield tunneling in close proximity with small intersection angle," *Tunnelling and Underground Space Technology*, vol. 97, Article ID 103258, 2020.

[8] Z. Zhang and M. Huang, "Geotechnical influence on existing subway tunnels induced by multiline tunneling in Shanghai soft soil," *Computers and Geotechnics*, vol. 56, pp. 121–132, 2014.

[9] X. J. Wei, M. B. Zhang, Z. Ding, and X. Zhang, "Research status and prospect of shield tunneling effect on preexisting metro tunnels and controlling technology," *Rock and Soil Mechanics*, vol. 41, no. 2, pp. 442–460, 2020, in Chinese.

[10] M. L. Cooper, D. N. Chapman, C. D. F. Rogers, and A. H. C. Chan, "Movements in the Piccadilly line tunnels due to the Heathrow express construction," *Géotechnique*, vol. 52, no. 4, pp. 243–257, 2002.

[11] H. Wu, S. Shen, J. Yang, and A. Zhou, "Soil-tunnel interaction modelling for shield tunnels considering shearing dislocation in longitudinal joints," *Tunnelling and Underground Space Technology*, vol. 78, pp. 168–177, 2018.

[12] X. Li, X. Lin, H. Zhu, X. Wang, and Z. Liu, "Condition assessment of shield tunnel using a new indicator: the tunnel serviceability index," *Tunnelling and Underground Space Technology*, vol. 67, pp. 98–106, 2017.

[13] X. Li and X. Chen, "Using grouting of shield tunneling to reduce settlements of overlying tunnels: case study in Shenzhen metro construction," *Journal of Construction Engineering and Management*, vol. 138, no. 4, pp. 574–584, 2012.

[14] Q. F. Zhang, "Field observation and theoretical study on an existing tunnel underpassed by new twin tunnels," *Advances in Civil Engineering*, vol. 2018, Article ID 1598672, 2018.

[15] R. Liang, T. Xia, Y. Hong, and F. Yu, "Effects of above-crossing tunnelling on the existing shield tunnels," *Tunnelling and Underground Space Technology*, vol. 58, pp. 159–176, 2016.

[16] L. Xiang, Q. Fang, D. L. Zhang, and Z. J. Wang, "Behaviour of existing tunnel due to new tunnel construction below," *Computers and Geotechnics*, vol. 110, pp. 71–81, 2019.

[17] P. Li, S. Du, S. Shen, Y. Wang, and H. Zhao, "Timoshenko beam solution for the response of existing tunnels because of tunneling underneath," *International Journal for Numerical and Analytical Methods in Geomechanics*, vol. 40, no. 5, pp. 766–784, 2016.

[18] X. Lin, R. Chen, H. Wu, and H. Cheng, "Deformation behaviors of existing tunnels caused by shield tunneling undercrossing with oblique angle," *Tunnelling and Underground Space Technology*, vol. 89, pp. 78–90, 2019.

[19] N.-A. Do, D. Dias, P. Oreste, and I. D. Maigre, "Three-dimensional numerical simulation of a mechanized twin tunnels in soft ground," *Tunnelling and Underground Space Technology*, vol. 42, pp. 40–51, 2014.

[20] V. Avgerinos, D. M. Potts, and J. R. Standing, "Numerical investigation of the effects of tunnelling on existing tunnels," *Géotechnique*, vol. 67, no. 9, pp. 808–822, 2017.

[21] K. Elbaz, S. Shen, A. Zhou, Z. Yin, and H. Lyu, "Prediction of disc cutter life during shield tunneling with AI via the incorporation of a genetic algorithm into a GMDH-Type neural network," *Engineering*, vol. 7, no. 2, pp. 238–251, 2021.

[22] C. W. W. Ng, T. Boonyarak, and D. Mašín, "Three-dimensional centrifuge and numerical modeling of the interaction between perpendicularly crossing tunnels," *Canadian Geotechnical Journal*, vol. 50, no. 9, pp. 935–946, 2013.

[23] P. Li, S. Du, X. Ma, Z. Yin, and S. Shen, "Centrifuge investigation into the effect of new shield tunnelling on an existing underlying large-diameter tunnel," *Tunnelling and Underground Space Technology*, vol. 42, pp. 59–66, 2014.

[24] T. Boonyarak and C. W. W. Ng, "Effects of construction sequence and cover depth on crossing-tunnel interaction," *Canadian Geotechnical Journal*, vol. 52, no. 7, pp. 851–867, 2015.

[25] D. Jin, D. Yuan, X. Li, and H. Zheng, "Analysis of the settlement of an existing tunnel induced by shield tunneling underneath," *Tunnelling and Underground Space Technology*, vol. 81, pp. 209–220, 2018.

[26] Q. Fang, D. Zhang, Q. Li, and L. N. Y. Wong, "Effects of twin tunnels construction beneath existing shield-driven twin tunnels," *Tunnelling and Underground Space Technology*, vol. 45, pp. 128–137, 2015.

[27] X. L. Gan, J. L. Yu, X. N. Gong, and M. Zhu, "Characteristics and countermeasures of tunnel heave due to large-diameter shield tunneling underneath," *Journal of Performance of Constructed Facilities*, vol. 34, no. 1, 13 pages, Article ID 04019081, 2020.

[28] H. Mohamad, P. J. Bennett, K. Soga, R. J. Mair, and K. Bowers, "Behaviour of an old masonry tunnel due to tunnelling-induced ground settlement," *Géotechnique*, vol. 60, no. 12, pp. 927–938, 2010.

[29] X. G. Li and D. J. Yuan, "Response of a double-decked metro tunnel to shield driving of twin closely under-crossing tunnels," *Tunnelling and Underground Space Technology*, vol. 28, pp. 18–30, 2012.

[30] D. Jin, D. Yuan, X. Li, and H. Zheng, "An in-tunnel grouting protection method for excavating twin tunnels beneath an existing tunnel," *Tunnelling and Underground Space Technology*, vol. 71, pp. 27–35, 2018.

[31] R. Chen, X. Lin, and X. Kang, "Deformation and stress characteristics of existing twin tunnels induced by close-distance EPBS under-crossing," *Tunnelling and Underground Space Technology*, vol. 82, pp. 468–481, 2018.

[32] H. N. Wu, P. Zhang, R. P. Chen, X. T. Lin, and Y. Liu, "Ground response to horizontal spoil discharge jet grouting with impacts on the existing tunnels," *Journal of Geotechnical and Geoenvironmental Engineering*, vol. 146, no. 7, 14 pages, Article ID 05020006, 2020.

[33] C. Chang, M. Wang, C. Chang, and C. Sun, "Repair of displaced shield tunnel of the Taipei rapid transit system," *Tunnelling and Underground Space Technology*, vol. 16, no. 3, pp. 167–173, 2001.

[34] J. Yu, Y. Hong, Y. Byun, and J. Lee, "Non-destructive evaluation of the grouted ratio of a pipe roof support system in tunneling," *Tunnelling and Underground Space Technology*, vol. 56, pp. 1–11, 2016.

[35] C. Yoo, "Finite-element analysis of tunnel face reinforced by longitudinal pipes," *Computers and Geotechnics*, vol. 29, no. 1, pp. 73–94, 2002.

[36] Y. B. Luo, J. X. Chen, B. Liu, L. J. Chen, and J. T. Xie, "Analysis of pipe-roof in tunnel exiting portal by the foundation elastic model," *Mathematical Problems in Engineering*, vol. 2017, Article ID 9387628, 12 pages, 2017.

[37] J. S. Yang, D. M. Gou, and Y. X. Zhang, "Field measurements and numerical analyses of double-layer pipe roof reinforcement in a shallow multiarch tunnel," *Transportation Research Record*, vol. 2050, no. 1, pp. 145–153, 2008.

[38] Z. Wang, W. Yao, Y. Cai, B. Xu, Y. Fu, and G. Wei, "Analysis of ground surface settlement induced by the construction of a large-diameter shallow-buried twin-tunnel in soft ground," *Tunnelling and Underground Space Technology*, vol. 83, pp. 520–532, 2019.

[39] X. Li, D. Yuan, D. Jin, J. Yu, and M. Li, "Twin neighboring tunnel construction under an operating airport runway," *Tunnelling and Underground Space Technology*, vol. 81, pp. 534–546, 2018.

[40] Z. N. Wang, S. L. Shen, A. Zhou, and H. M. Lyu, "Mechanical, flame-retarding, and creep-recovery proprieties of ethylene-propylene-diene monomer enhanced with nano-hydroxide for undersea tunnel sealing gasket," *Journal of Applied Polymer Science*, vol. 138, no. 10, Article ID 44946, 2021.

[41] Z. N. Wang, S. L. Shen, A. Zhou, and Y. S. Xu, "Experimental evaluation of aging characteristics of EPDM as a sealant for undersea shield tunnels," *Journal of Materials in Civil Engineering*, vol. 32, no. 7, 12 pages, Article ID 04020182, 2020.

[42] T. Yan, S. L. Shen, A. Zhou, and H. M. Lyu, "Construction efficiency of shield tunnelling through soft deposit in Tianjin, China," *Tunnelling and Underground Space Technology*, vol. 112, Article ID 103917, 11 pages, 2021.

[43] Department of Housing and Urban-Rural Development of Zhejiang Province, *Technical Code for Protection of Urban Rail Transit Structures (DB 33/T 1139-2017)*, Department of Housing and Urban-Rural Development of Zhejiang Province, Zhejiang, China, 2017.

[44] Z. Ding, X. Zhang, X. Yin, and J. Jiang, "Analysis of the influence of soft soil grouting on the metro tunnel based on field measurement," *Engineering Computations*, vol. 36, no. 5, pp. 1522–1541, 2019.

[45] Z. Wang, K. W Zhang, and G. Wei, "Field measurement analysis of the influence of double shield tunnel construction on reinforced bridge," *Tunnelling and Underground Space Technology*, vol. 81, pp. 252–264, 2018.

Research Article

Characteristics Analysis of Generalized Rock Quality Designation (RQD) Based on Degree of Joint Development

Lin Jun [ID],[1] **Sha Peng** [ID],[2] **Gao Shuyu**,[3] and **Ni Jiji** [ID][2]

[1]*Zhejiang Institute of Communications Co., Ltd., Hangzhou, Zhejiang 310000, China*
[2]*College of Civil Engineering, Shaoxing University, Shaoxing, Zhejiang 312000, China*
[3]*Key Laboratory of Rock Mechanics and Geohazards of Zhejiang Province, Shaoxing, Zhejiang 312000, China*

Correspondence should be addressed to Sha Peng; shapeng@usx.edu.cn

Rock quality designation (RQD) is widely adopted as a fundamental tool in characterizing rock masses since it was devised in 1964. Since the conventional RQD calculation is limited due to its dependence on the selected threshold, previous research introduced generalized RQD to adequately reflect the anisotropy and scale effect of RQD. However, the influence of the joint development inside rock mass on generalized RQD remains unclear. The objective of this work is to investigate characteristics of the generalized RQD in view of different development degrees of discontinuities in rock mass, including spacing (density) and trace length. Three-dimensional fracture network modelling is employed to simulate the actual rock mass of open-pit iron mine in China. Virtual scanlines are set to obtain RQD values in different directions. The results primarily show that the generalized RQD should be introduced to calculate the RQD with different thresholds to fully reflect the anisotropy of rock mass. The optimal threshold can be obtained based on an anisotropic coefficient, which is defined by (RQD_{max}-RQD_{min}). It is also indicated that the fracture spacing has a great influence on both the anisotropy of RQD and the selection of the optimal threshold. The optimal threshold of the generalized RQD increases with the increase in the fracture spacing. In addition, the scale effect of RQD in different models is discussed by changing the length of the scanlines. The longer the scanlines we set, the more stable RQD value can be obtained in the model. It is recommended to fit much longer scanline to get realistic RQD in heavily fractured rock mass.

1. Introduction

The presence of discontinuities plays an essential role in the strength and stability of rock masses, which controls the damage characteristics of rock mass [1–4]. Rock quality designation (RQD) is an important parameter in evaluating the quality of rock masses using drill core cataloging. This parameter was initially proposed by [5]. It provides a quite simple description of rock mass quality qualitatively [6]. At present, it has been widely employed as the foundational parameter in the rock mass classification system such as Rock Mass Rating (RMR) and the Rock Quality Tunneling Index (Q-system) [7–11]. RQD is internationally adopted in areas of mines, rock mechanics, and engineering geology

[12, 13]. The value of RQD is expressed as follows [14], where $\sum_{i=1}^{n} x_i$ is all pieces of core with length greater than 100 mm and X is the total length of the drilling borehole.

$$RQD = 100 \sum_{i=1}^{n} \frac{x_i}{X} \times 100\%. \quad (1)$$

However, three limitations in the aforementioned calculation principles are observed when obtaining RQD. First, the "threshold value of 10 cm" is used as the only criterion for judging rock quality. Whether this threshold can be used as the most reasonable threshold value for distinguishing rock mass has been questioned by many scholars [15–19]. Second, due to the geological survey level and engineering

cost, the value of RQD can be different for a given location when measured from cores with different drilling orientations [20, 21]. The conventional RQD cannot fully reflect the heterogeneity and anisotropy of the rock mass [22, 23]. Third, traditional methods often directly calculate the size of RQD based on the length of each section of the core in the borehole, ignoring the scale effect of RQD [24–26].

To overcome the aforementioned limitations, many domestic and foreign scholars have conducted relevant research. The authors in [27] found that RQD changes with the size of the scanline; that is, RQD has scale effect. Thus, the authors proposed corresponding empirical formulas as follows:

$$RQD = 100(1 + \lambda t)e^{-\lambda t}, \tag{2}$$

where λ is the density of structural surface (average number of structural surfaces per meter of scanline) and t is the selected threshold for calculation. Harrison believed that a reasonable selection of thresholds can expand the range of RQD change and proposed a corresponding equation [16]. Based on the relationship between threshold and RQD change, the generalized RQD was suggested in light of rock mass anisotropy [28]. The authors in [29] investigated the generalized RQD through in situ cataloging of discontinuities and 2D network simulation technology. The results pointed out the limitations in using 0.1 m as the only threshold. The authors in [30] conducted the three-dimensional fracturing network method to simulate rock slope of the Baihetan hydropower station. By arranging numerous scanlines, it is indicated that the generalized RQD has obvious spatial and scale effects.

The RQD index is influenced by different parameters which mainly include joint orientation, joint spacing, fracture frequency, and joint roughness [31]. Although predecessors have conducted extensive research on the limitations of the traditional method to calculate the generalized RQD, how the development of the discontinuities in rock mass will affect the characteristics of the generalized RQD remains unclear. Therefore, this study adopts 3D fracture network simulation [32, 33] to generate numerous models of an actual rock mass by considering different jointing degrees. A series of virtual scanlines were arranged in different directions in each model. The influence of joint development on the anisotropy of the generalized RQD is analyzed. The scale effect of generalized RQD is also studied by changing the length of the scanline, which provides a certain theoretical basis for selecting a reasonable drilling depth of rock projects.

2. Model Establishment of an Actual Rock Mass

2.1. Study Area and Geological Setting.
Practical investigations on RQD measurements were carried out at Anqian open-pit iron mine, which is located in southwest of Anshan, in Liaoning Province, China. The strata of this area were precipitated in medium and high metamorphic series with NW-SE trend. The major rock types at the open-pit slope are ferruginous quartzite, schist, and phyllite of the Anshan Group, which belongs to Precambrian.

We adopted the noncontact sampling method to conduct geological logging at Xudonggou stope using the ShapeMetriX3D system [34]. Four key discontinuity parameters of 258 discontinuities, i.e., orientation, number of sets, set spacing, and mean trace length, were collected and analyzed. Three sets of discontinuities intersect the rock mass of the stope: a bedding and two major joints, according to the variation range of dip angle (see Figure 1).

2.2. Model Parameters.
Gu [35] divided the joints of rock mass into five levels according to the scale of structures: I, II, III, IV, and V. Among them, the IV-grade structural planes extend from tens of centimeters to 20–30 m, with a large number distributed randomly, thereby affecting the integrity and mechanical properties of the rock mass. This issue is the subject of statistical analysis and simulation of structural planes. Studies have found that when the number of structural planes is constant, the development degree of discontinuities is mainly related to their spacing and ductility, and the occurrence and distribution type of structural planes have a minimal, even negligible, effect on it [36].

Regarding the quantitative description of structural plane spacing and ductility, the International Society for Rock Mechanics [37] proposed the ductility of structural planes into five levels (<1, 1–3, 3–10, 10–20, and >20; m) and the spacing into 7 levels (<20, 20–60, 60–200, 200–600, 600–2000, 2000–6000, and >6000; mm). Based on the preceding classification and the scale of the case study, this work only selects seven representative structural plane spacing values and five representative structural ductility ranges, which are tabulated in Table 1.

The discontinuities inside the rock mass are mainly divided into occurrence, ductility, and density (spacing). The accuracy of the above elements greatly determines the accuracy of the 3D joint network model [38]. Three sets of discontinuities at Xudonggou stope are developed in the rock mass. The distribution of occurrence follows the Fisher distribution [39], which contains only one parameter, the Fisher constant K. The spacing and trace length distribution obey the negative exponential distribution [40]. The specific parameters of 3D fracture network simulation are listed in Table 2. According to the result of [41], the value of CP3 is 2.0 for a uniform distribution of fracture orientation. For most fracture geometries, CP3 will vary between 1.0 and 3.0. Therefore, the value of CP3 is set to 2.0 here. Meanwhile, the density of the discontinuities can be calculated from the spacing presented in Table 1. The solution method is based on the work of [42]; and the calculation process is not mentioned in this study.

2.3. Model Generation and Scanline Layout.
The existence of discontinuities causes the rock mass to have an obvious scale effect. The parameters of rock mass change with the sampling scale [43]. With the increase in the sample to a certain critical value, the parameters of rock mass tend to be stable. The sampling size corresponding to the critical value is the

(a) (b)
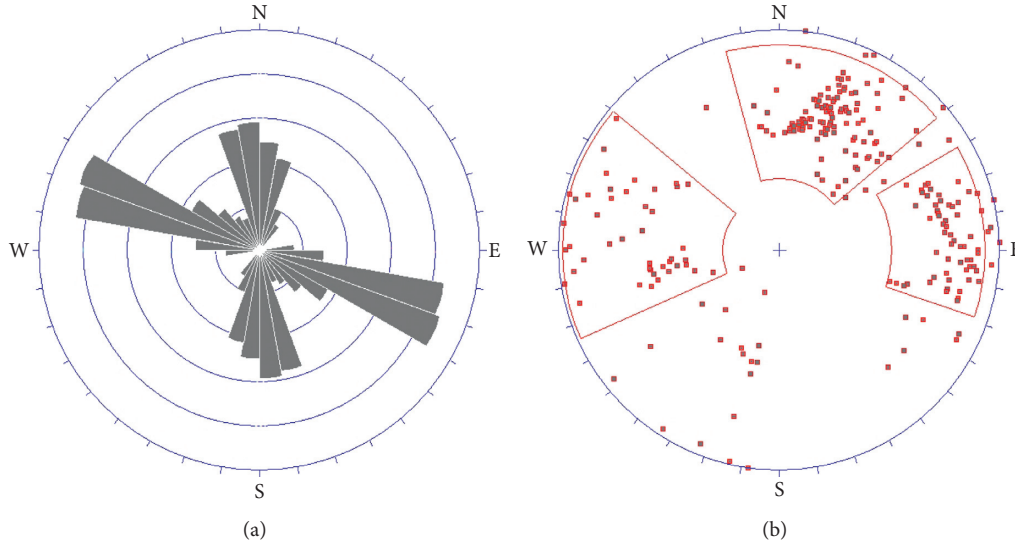
FIGURE 1: Joints distribution at Anqian open-pit iron mine: (a) rose diagram of joint and (b) pole distribution.

TABLE 1: Representative values of joint spacing and persistence.

Scalability (unit: m)	Extremely low	Low	Medium	High	Extremely high		
	1–3	3–8	8–14	14–20	20–30		
Spacing (unit: m)	Extremely dense	Very dense	Dense	Medium	Wide	Very wide	Extremely wide
	0.2	0.5	0.8	1	1.5	3	6

TABLE 2: Parameters of 3D fracture network.

Group	Structure occurrence			Spacing distribution	Volume density
	Occurrence	Distribution	K value		
Set 1	190°∠50°	Fisher	50	Negative index	
Set 2	238°∠37°	Fisher	20	Negative index	C_{p3}/S_f
Set 3	64°∠78°	Fisher	5	Negative index	

Note: C_{p3} is a constant and S_f is the spacing between structural planes.

representative elementary volume (REV). The authors in [44] introduced the index of the blockiness degree of fractured rock masses. The result indicated that the REV is 4–8 times of the spacing between discontinuities and no more than 8 times of the spacing. According to the selected maximum spacing of 6 m, the scale of the study area is set 50 m × 50 m × 50 m.

A total of 35 rock mass models with different structural plane development levels are generated using 3-Dimensional Distinct Element Codes (3DEC, Itasca Consulting [45]), as illustrated in Figure 2. To fully reflect the development of the discontinuities inside the rock mass, 5 cut planes are selected in each model. 18 scanlines are arranged on each cut plane at intervals of 10°. The directions of scanlines cover 0°–360°. Due to the symmetry of polar coordinates, we only calculate the scanlines in the range of 0°–180°. The selection of rock mass section and the layout of scanlines are displayed in Figure 3. According to the intersection of the internal structural plane of the model and the survey line, the program can automatically

calculate the line density in the survey line direction. Combining the Priest–Hudson formula (equation (2)), we can obtain the RQD value of the model in a certain direction.

3. Anisotropy of the Generalized RQD

Because of the discontinuous nature of rock masses, they are anisotropic, inhomogeneous [46, 47]. The values of RQD in different locations of the same rock mass should be inconsistent. That is, the distribution of RQD also has anisotropy. This section introduces the concept of the generalized RQD to analyze the anisotropy of RQD based on the degree of joints development.

3.1. Generalized RQD. Selecting a reasonable threshold can expand the variation range of RQD, which plays an important role in studying the heterogeneity and anisotropy of rock mass. Therefore, the concept of generalized RQD was

(a)

(b)

(c)

(d)
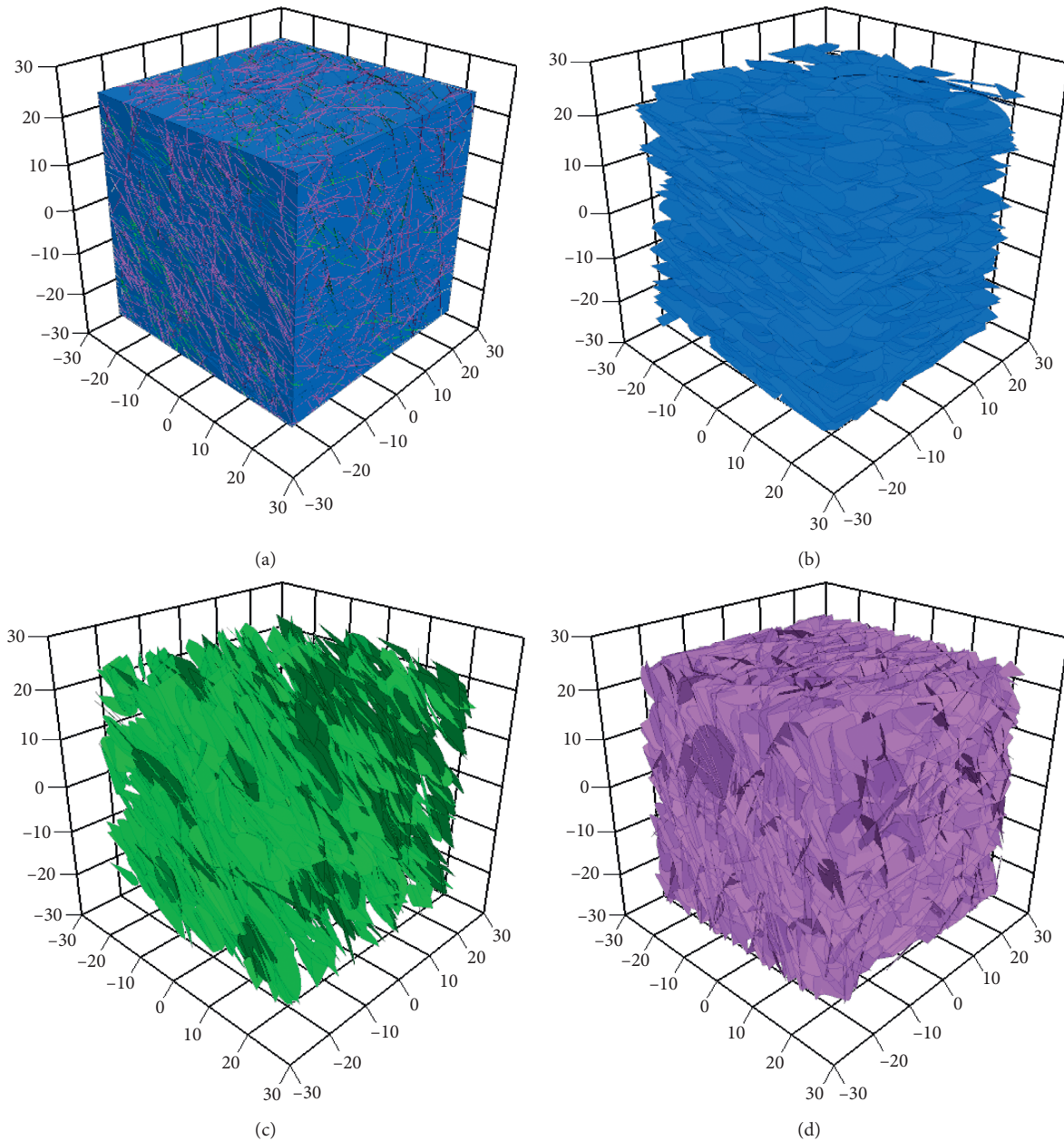
FIGURE 2: Illustration of 3D fractures (spacing: 1 m; trace length: 8–14 m): (a) 3D plane network model; (b) dominant group set 1; (c) dominant group set 2; (d) dominant group set 3.

introduced to maximize the variation range of the conventional RQD. For any threshold t, the percentage of the ratio of the sum of the length of the core length not less than t along a certain scanline (borehole) to the length of the scanline (borehole) is defined as the generalized RQD [48].

According to the arrangement in Figure 3, the scanlines of the selected section are set in each model with different thresholds. The average value can be calculated based on the measurement results from those scanlines with the same direction of each section. It is regarded as the RQD inside the rock mass in a certain direction. All calculation results are drawn into a 2D polar diagram. As shown in Figure 4, the angle in the figure indicates the direction of the scanline and

the polar radius indicates the magnitude of RQD. Due to constraints on length, Figure 4 only lists the RQD polar coordinate plane diagrams of nine models composed of extremely dense, medium dense, and extremely wide spacing with extremely low, medium, and high ductility, respectively.

3.2. Determination of Optimal Threshold. Figure 4 describes the RQD anisotropy under different structural plane development levels and different threshold conditions. As the distance remains the same, the polar coordinate plot changes within a narrow range with the ductility changes from 1–3 m

(a) (b)
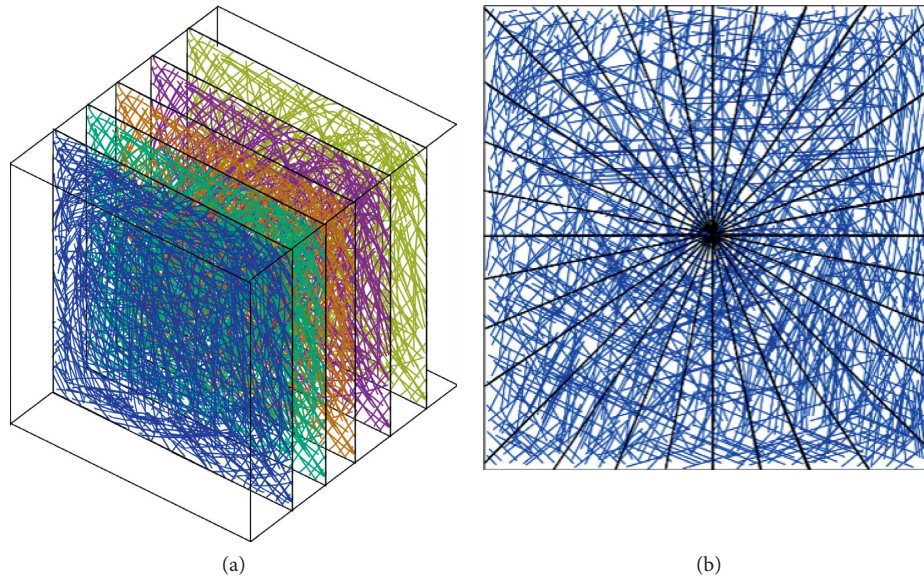
FIGURE 3: Schematic of scanline and section arrangement: (a) section's layout and (b) scanline's layout.

to 20–30 m. As the internal ductility remains the same, however, the polar coordinate plot changes significantly with the spacing changes from 0.2 m to 6 m. Hence, it is indicated that the RQD anisotropy is more sensitive to the spacing of the discontinuities. In addition, the polar coordinate plot in different models changes significantly with different thresholds, which shows that the threshold also has a greater impact on the RQD anisotropy. Therefore, the distance between the discontinuities within the model and the selected threshold are the main factors that affect the calculation results of RQD.

Since the anisotropy of the rock mass leads to the anisotropy of RQD, RQD anisotropy can reflect the anisotropy of rock mass. A reasonable threshold should be selected to maximize the variation range of RQD, which can reflect the anisotropy characteristics of rock mass. In this study, we define the optimal threshold of RQD as it can make the degree of RQD anisotropy reach the maximum in the model. Taking the model with a spacing of 1 m and a ductility of 8–14 m as an example, we set the thresholds from 0.1 m to 1.0 m. The degree of the RQD anisotropy can be characterized as the range of RQD (RQD_{max}-RQD_{min}). If the range of RQD reaches the maximum, the corresponding threshold can be considered as the optimal threshold.

It is illustrated in Figure 5 that the RQD range increases first with the increase in the threshold and then decreases when reaches a certain critical value. In this model, the RQD range reaches the maximum with the threshold of 0.7 m, which means the optimal threshold is 0.7 m. Therefore, the conventional RQD owes obvious limitation because the calculation with the only threshold of 0.1 m cannot adequately characterize the anisotropy of rock mass.

Furthermore, the optimal thresholds are not the same in different models. The degree of the discontinuity's development will affect the selection of the optimal threshold. Figure 6 presents the relationship between the optimal threshold and the development of the discontinuities (including spacing and ductility) among 35 different models. It shows that the optimal threshold of RQD increases with the increase in the spacing between the discontinuities, but the ductility has no significant effect on it. With the distance of 0.2–0.5 m, the threshold does not change with the ductility of the discontinuity. As the distance increases to 0.8–1.5 m, the optimal threshold changes slightly with the ductility. When the distance reaches 3–6 m, the optimal threshold starts to fluctuate with the change of the ductility.

Therefore, the influence of the ductility of the discontinuities on the optimal threshold of RQD is mainly related to the spacing of the discontinuities, which becomes remarkable with the increase in the spacing. Consequently, the distance between the discontinuities is the major factor for both the selection of the optimal threshold and the anisotropy of RQD.

4. Scale Effect of the Generalized RQD

Engineers usually calculate the RQD according to the length of the core in the borehole, ignoring the impact of the drilling depth on the RQD value. In fact, the true RQD of rock mass at any drilling depth (the length of the scanline) cannot be obtained [49, 50]. Thus, the issue is discussed using 3D fracture network simulation. The scale effect of the generalized RQD can be analyzed by changing the length of the scanlines.

Generally, engineering geological drillings are vertical because of the geological environment and drilling technology. Therefore, the scanlines are arranged as boreholes in the generated rock mass model, which are perpendicular to the *xoy* plane. A total of 121 scanlines are shown in Figure 7. The scanline is arranged every 5 m to get enough data.

Priest and Hudson [27] suggested a theoretical equation related to the calculation of the generalized RQD (equation

(a)

(b)

(c)
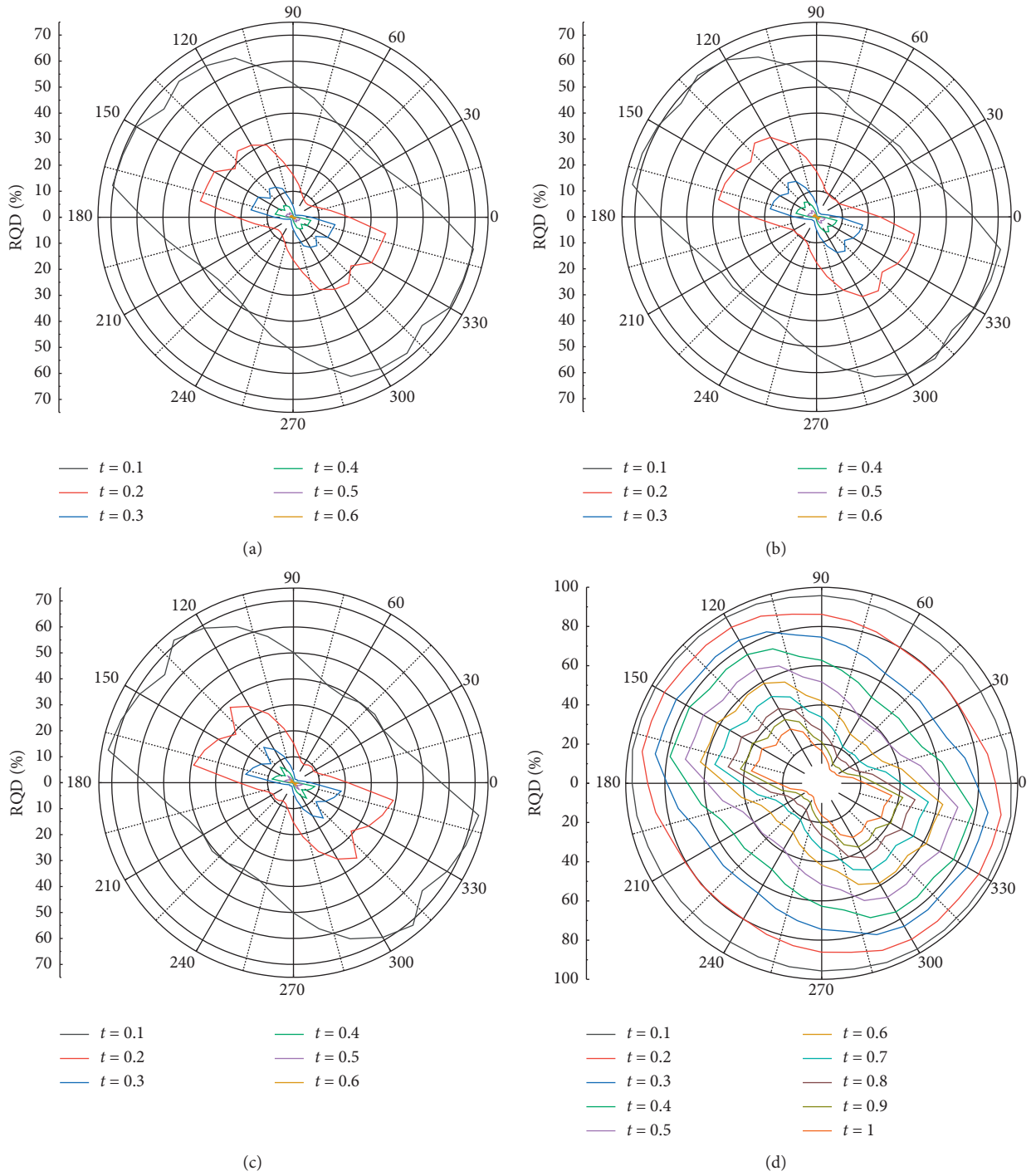
(d)

Figure 4: Continued.

(e)

(f)

(g)

(h)
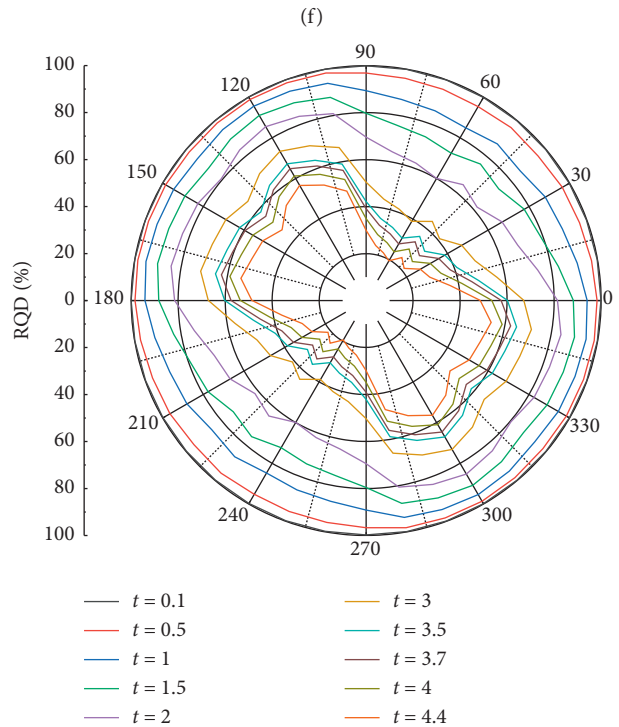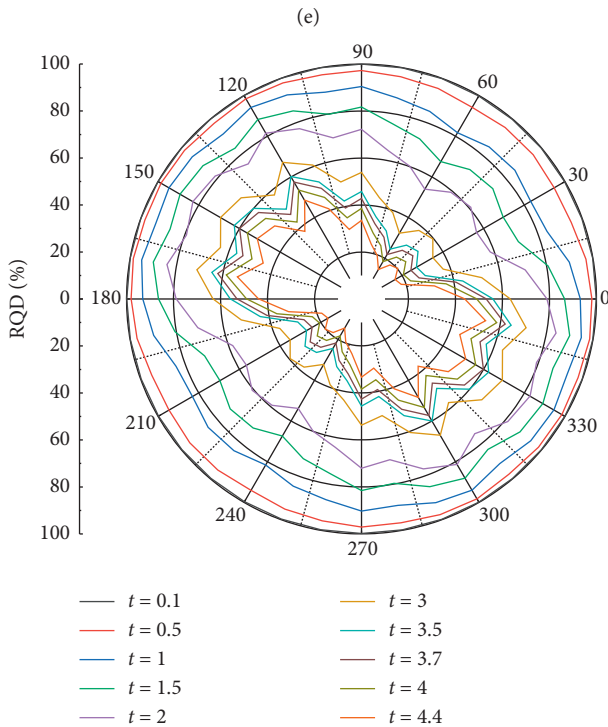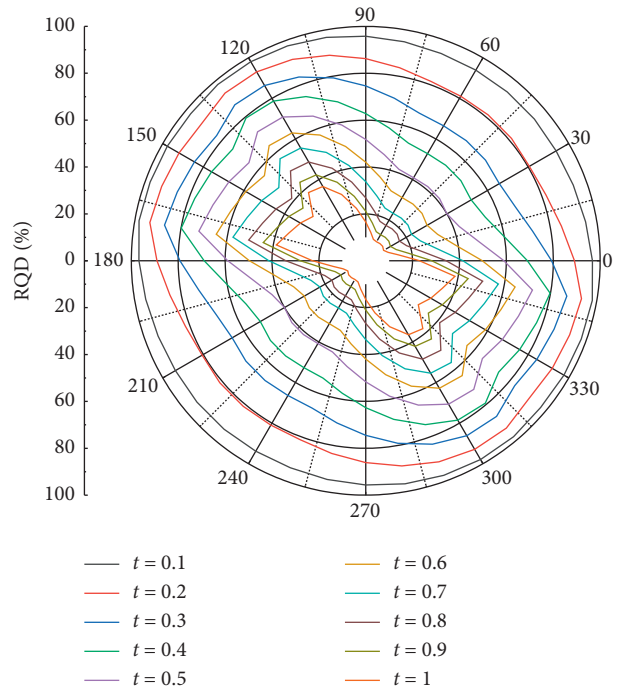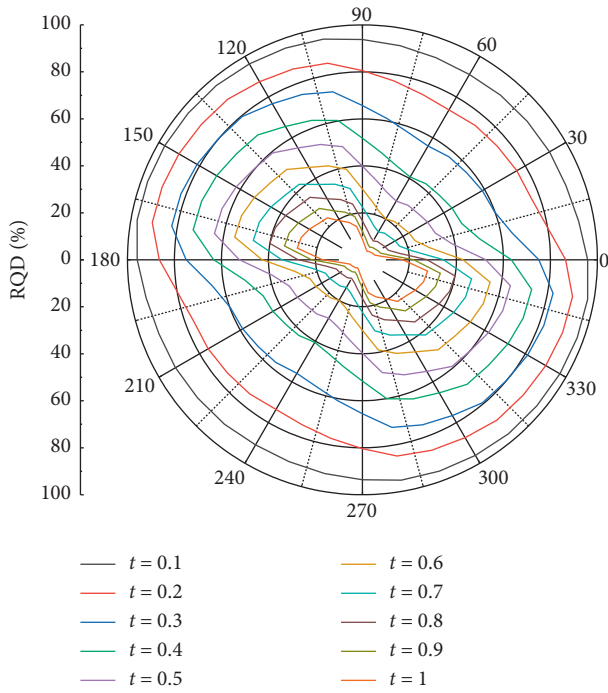
Figure 4: Continued.
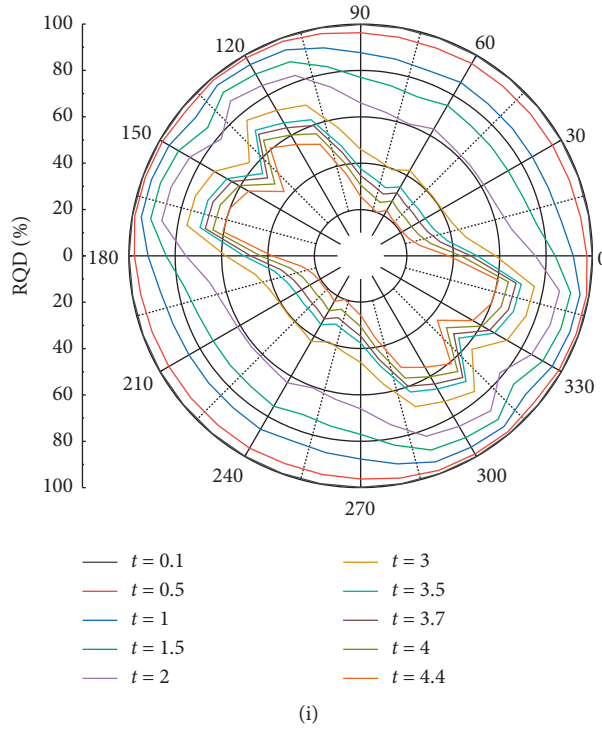
FIGURE 4: Generalized RQD with various thresholds in different directions of diverse models: (a) spacing 0.2, scalability: 1–3; (b) spacing 0.2, scalability: 8–14; (c) spacing 0.2, scalability: 20–30; (d) spacing 1, scalability: 1–3; (e) spacing 1, scalability: 8–14; (f) spacing 1, scalability: 20–30; (g) spacing 6, scalability: 1–3; (h) spacing 6, scalability: 8–14; (i) spacing 6, scalability: 20–30.
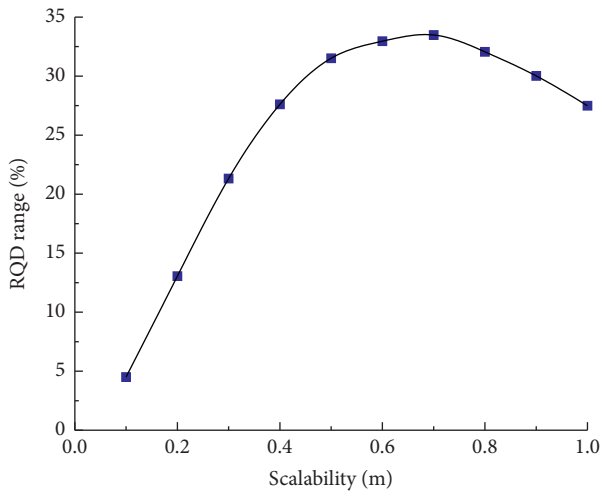
FIGURE 5: RQD range for different thresholds (spacing: 1 m; trance length: 8–14 m).

$$RQD = 100\left[(1 + \lambda t)e^{-\lambda t} - (1 + \lambda L)e^{-\lambda L}\right], \qquad (3)$$

$$RQD = \frac{100\left[(1 + \lambda t)e^{-\lambda t} - (1 + \lambda L)e^{-\lambda L}\right]}{1 - e^{-\lambda L} - \lambda L e^{-\lambda L}}. \qquad (4)$$

Five typical models with intervals of 0.2, 0.5, 0.8, and 1 m were selected as examples. The values of the generalized RQD with different lengths of the scanline are calculated according to equation (4) and the optimal thresholds of each model. The variation curves of the generalized RQD are plotted in Figure 8. It is assumed that the true RQD can be obtained under the full length of scanline, i.e., 50 m in this study. Then, the rate of RQD change is brought forward to compare the generalized RQD under each scanline length in different models with that corresponding to the scanline length of 50 m. The relationship between the rate of RQD change and the length of the scanline is shown in Figure 9.

The various models indicate that the generalized RQD converges with the increase in the scanline length, which has an obvious scale effect. The RQD result can represent the rock mass quality more accurately under the longer scanline. However, the convergence of the generalized RQD in different models is not consistent. When the spacing is 0.2 m, the RQD changes from large to small and then to converge as the length of the scanline increases. As the distance between the discontinuities increases, the change of RQD increases first and then decreases to convergence with the length of the scanline. The ductility of the discontinuities also affects the convergence of the RQD. The rate of the RQD change in

(3)), with respect to the hypothesis of negative exponential distribution of joint spacing. Equation (2) was proposed with regard to the effect of the scanline length. Another possible more realistic expression for the generalized RQD was also suggested by [51]. Compared with equation (3), the calculation of equation (4) is concerned more about the influence of short scanline on the RQD result. In these equations, λ is the density of the discontinuities, t is the calculation threshold, and L is the length of the scanline.
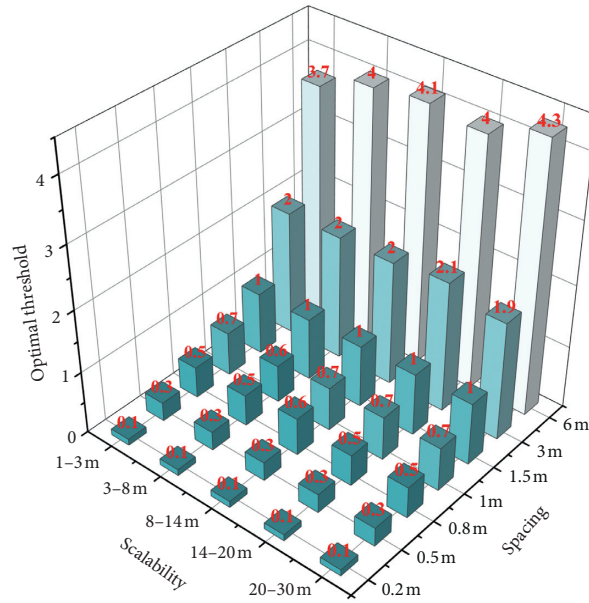
FIGURE 6: Optimal threshold in different models.
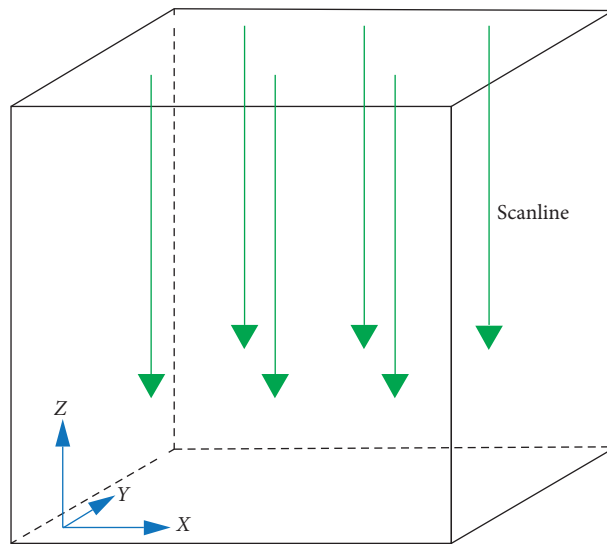
FIGURE 7: Schematic of vertical scanline setting.

each model increases as the ductility increases. It is indicated that the convergence length of scanline is positively associated with the ductility of the discontinuities.

For those rock masses without a recognizable structural pattern, it is difficult to determine the real RQD. When the number of scanlines is large enough, the average value of RQD can be close to the real RQD of rock mass infinitely. Therefore, the average RQD obtained from 121 scanlines with full length (50 m in this study) is assumed to be the real RQD. Subsequently, the average value obtained from different lengths of scanlines, which is recorded as $RQD^{\#}$, is regarded as the undetermined RQD of the rock mass. This study defines the variation rate of RQD as the difference between $RQD^{\#}$ and RQD. With respect to the engineering

requirement, it is considered to meet the research requirements when the variation rate of RQD is not greater than 2%, which is described in equation (5). We defined the $RQD^{\#}$ in a certain scanline satisfied the inequality as the convergence RQD value, and the corresponding scanline length is the convergence length of the scanline.

$$\left| \frac{RQD^{\#} - RQD}{RQD} \right| \leq 2\%. \tag{5}$$

Table 3 tabulates the shortest convergence length of the scanline and the convergence RQD value that meet equation (5) requirements of each model. The degree of joint development distinctly affects the convergence length of the

(a)

(b)

(c)

(d)
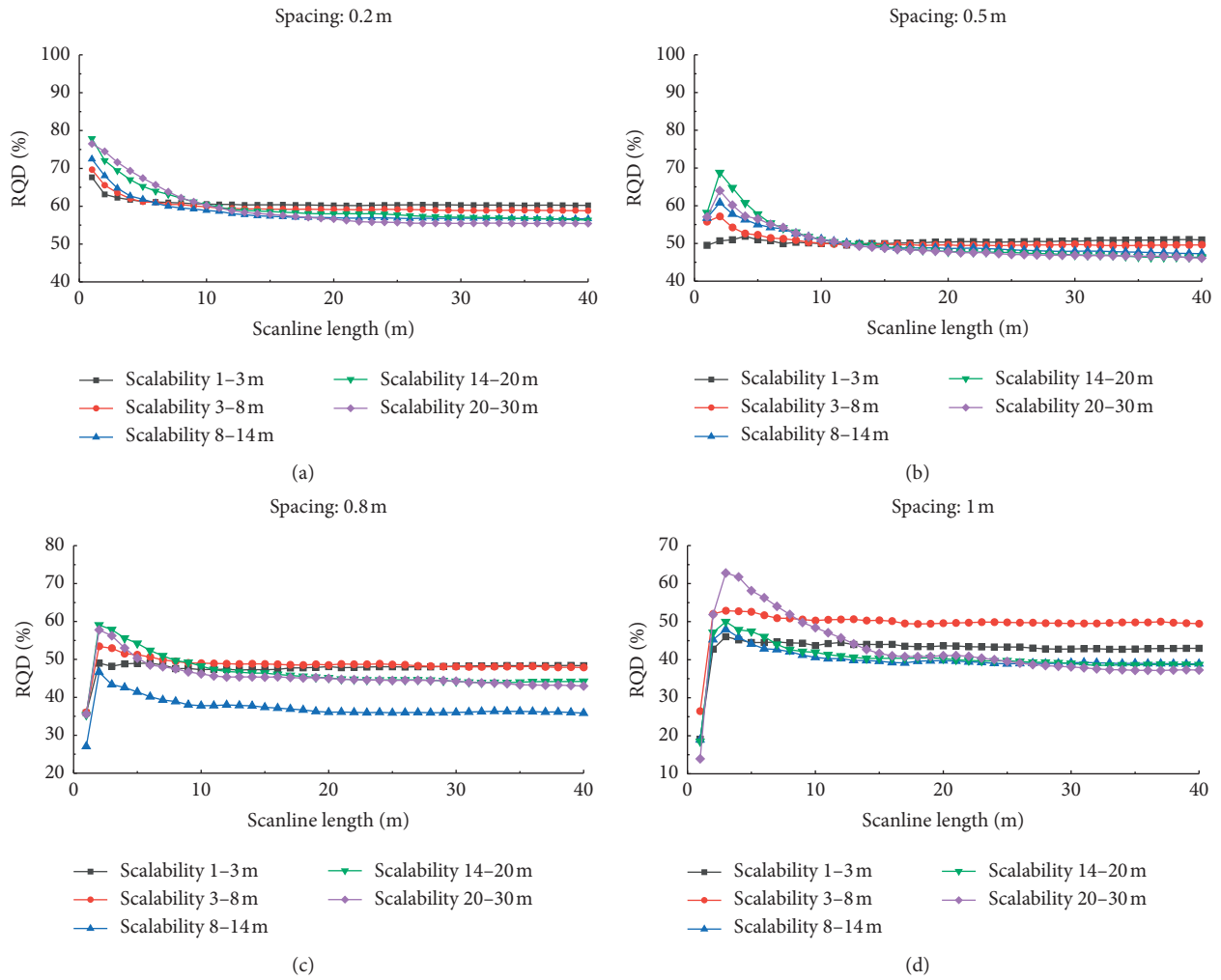
Figure 8: Variation of RQD values with scanline length.

(a)

(b)
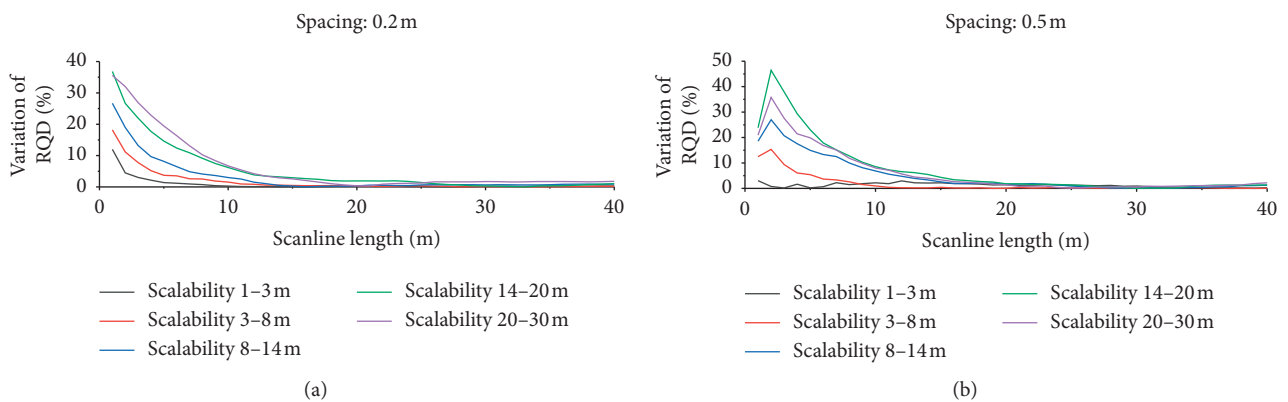
Figure 9: Continued.
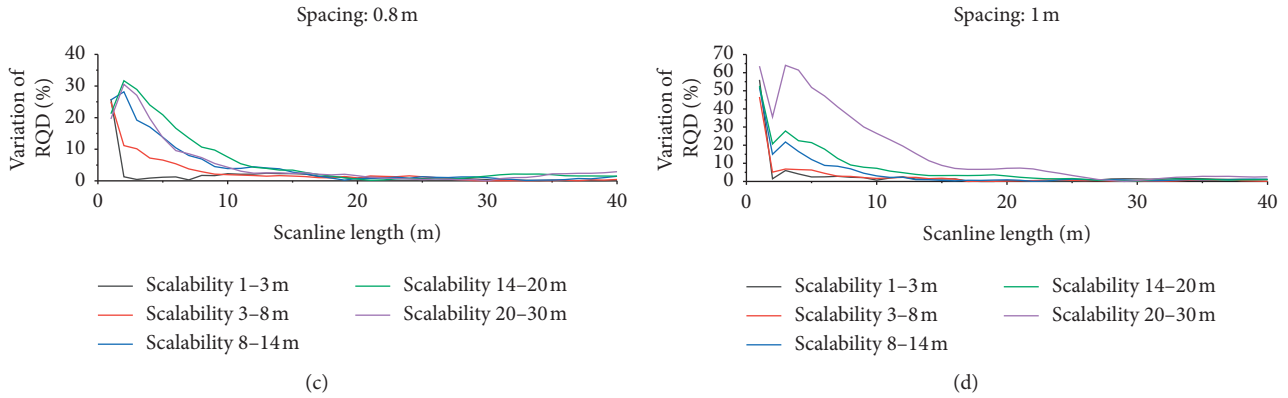
Figure 9: Variation rate of RQD values with scanline length.

Table 3: Convergence scanline lengths and convergence RQD values of different models.

Joint trace length	0.2 m		0.5 m		0.8 m		1 m	
	Convergence line length (L/m)	Convergence RQD (%)	Convergence line length (L/m)	Convergence RQD (%)	Convergence line length (L/m)	Convergence RQD (%)	Convergence line length (L/m)	Convergence RQD (%)
1–3 m	5	61.2	7	49.9	10	47.3	13	44
3–8 m	9	60.1	9	50.3	10	49	14	50.3
8–14 m	12	58	16	48.8	17	37	13	39.8
14–20 m	19	58	20	47.8	18	45.5	22	39.8
20–30 m	17	57.3	19	47.9	20	45	27	38.7

scanline. The convergence length generally exhibits a slight increase with the increase in the spacing. However, the increase is not uniform in each model. Compared with the spacing, the ductility greatly influences the convergence length of the scanline. With the same spacing, the convergence length in different models increases with the increase in ductility.

According to the combined results of Figures 7 and 8 and Table 3, the generalized RQD has an obvious scale effect. The RQD result is more stable with respect to the longer measuring line, and it can represent the quality of the entire rock mass more accurately. In addition, a longer scanline is needed to obtain a reliable RQD value for a heavily fractured rock mass.

5. Conclusions

This study used 3D structural plane network simulation technology to generate 35 rock mass models with different structural plane spacing and ductility, arranged survey lines inside the model instead of drilling holes, obtained enough values of the generalized RQD, and studied the relationship between the generalized RQD characteristics and the development of discontinuities. The specific conclusions are as follows:

(1) The traditional method using 0.1 m as the only threshold for RQD has significant limitations. It cannot fully reflect the anisotropy and scale effect of

the rock mass. The generalized RQD concept is introduced, and the optimal threshold is obtained based on the degree of RQD anisotropy. The results show that the degree of joint development affects the selection of the optimal threshold. The optimal threshold increases with the increase in the spacing, while of the discontinuities have a minimal influence on the selection of the optimal threshold. However, the influence degree of the ductility shows an increasing trend with the increase in the spacing.

(2) The degree of joint development has a significant effect on RQD anisotropy [52]. When the spacing is larger, the rock mass has higher anisotropy, while the ductility has a minimal effect on RQD anisotropy, which can even be ignored. Therefore, if the discontinuities with a larger spacing are encountered in the practical engineering, the number of drillings should be increased so that the RQD calculation can fully reflect the anisotropy of the rock mass.

(3) The generalized RQD has an obvious scale effect. The longer the scanline, the more stable the RQD obtained, and the more accurately it can represent the quality of the rock mass. In addition, when the discontinuities are highly developed in the rock mass, the scale effect of RQD is more obvious, and a longer scanline is needed to obtain a real RQD. Therefore, the sufficient length of the scanline is necessary to obtain stable and reliable RQD. Particularly, in heavily fractured rock masses, the length

of the scanline should be appropriately increased to ensure the accuracy of RQD [53].

Data Availability

The data used to support the findings of this study are included within the article.

Conflicts of Interest

The authors declare that there are no conflicts of interest in the publication of this article.

Acknowledgments

References

[1] H. Bao, Y. Zhai, H. Lan et al., "Distribution characteristics and controlling factors of vertical joint spacing in sand-mud interbedded strata," *Journal of Structural Geology*, vol. 128, Article ID 103886, 2019.

[2] H. Bao, X. Xu, H. Lan et al., "A new joint morphology parameter considering the effects of micro-slope distribution of joint surface," *Engineering Geology*, vol. 275, Article ID 105734, 2020a.

[3] M. Huang, C. Hong, J. Chen et al., "Prediction of the peak shear strength of rock joints based on BP neural network," *International Journal of Geomechanics*, vol. 21, no. 6, Article ID 04021085, 2021.

[4] X. Zhang, H. Lin, Y. Wang, and Y. Zhao, "Creep damage model of rock mass under multi-level creep load based on spatio-temporal evolution of deformation modulus," *Archives of Civil and Mechanical Engineering*, vol. 21, 2021.

[5] D. U. Deere, "Technical description of rock cores for engineering purposes," *Rock Mechanics and Engineering Geology*, vol. 1, no. 1, pp. 18–22, 1963.

[6] D. U. Deere, A. J. Hendron, F. D. Patton, and E. J. Cording, "Design of surface and near surface construction in rock," in *Proceedings of the 8th US Symposium Rock Mech Fail Break Rock*, pp. 237–302, Minneapolis, MN, USA, September 1966.

[7] Z. T. Bieniawski, "Engineering classification of jointed rock masses," *Transactions of the South African Institution of Civil Engineers*, vol. 15, no. 12, pp. 335–343, 1973.

[8] Z. T. Bieniawski, "Rock mass classification in rock engineering," in *Proceedings of the symposium on exploration and rock engineering*, vol. 2, pp. 97–106, Johannesburg, South Africa, November 1976.

[9] Z. T. Bieniawski, "The geomechanics classification in rock engineering applications," in *Proceedings of the 4th int congress on rock mechanics*, vol. 3, pp. 41–48, Montreux, Switzerland, September 1979.

[10] Z. T. Bieniawski, *The Rock Mass Rating (Rmr) System In Engineering Practice Rock Classification Systems for Engineering Purposes*, L. Kirkaldie, Ed., pp. 17–34, American Society for Testing Materials, Philadelphia, PA, 1988.

[11] N. Barton, R. Lien, and J. Lunde, "Engineering classification of rock masses for the design of tunnel support," *Rock Mechanics*, vol. 6, no. 4, pp. 189–236, 1974.

[12] E. Hoek and E. T. Brown, *Underground Excavations in Rock*, Institution of Mining and Metallurgy, London, England, 1980.

[13] E. Hoek and J. W. Bray, *Rock Slope Engineering*, The Institution of Mining and Metallurgy, London, England, 3rd edition, 1981.

[14] D. U. Deere, *Geological Considerations, Chapter 1, Rock Mechanics in Engineering Practice*, K. G. Stagg and O. C. Zienkiewicz, Eds., pp. 1–20, Wiley, London, England, 1968.

[15] J. A. Hudson and S. D. Priest, "Discontinuity frequency in rock masses," *International Journal of Rock Mechanics and Mining Science & Geomechanics Abstracts*, vol. 20, no. 2, pp. 73–89, 1983.

[16] J. P. Harrison, "Selection of the threshold value in RQD assessments," *International Journal of Rock Mechanics and Mining Sciences*, vol. 36, no. 5, pp. 673–685, 1999.

[17] J. P. Chen, J. H. Fan, and D. Liu, "Review and prospect on the application and research of RQD," *Rock and Soil Mechanics*, vol. 26, no. S2, pp. 249–252, 2005, in Chinese.

[18] P. Pells, Z. Bieniawski, S. Hencher et al., "RQD: time to rest in peace," *Canadian Geotechnical Journal*, vol. 54, pp. 825–834, 2017.

[19] Q. Chen, T. Yin, and H. Jia, "Selection of optimal threshold of generalized rock quality designation based on modified blockiness index," *Advances in Civil Engineering*, no. 1, pp. 1–11, 2019.

[20] S. Y. Choi and H. D. Park, "Variation of rock quality designation (RQD) with scanline orientation and length: a case study in Korea," *International Journal of Rock Mechanics and Mining Sciences*, vol. 41, no. 2, pp. 207–221, 2004.

[21] L. Li, S. Ouellet, and M. Aubertin, "An improved definition of rock quality designation, RQDc," in *Proceedings of the 3rd CANUS Rock Mechanics Symposium ROCKENG09*, M. Diederichs and G. Grasselli, Eds., pp. 1–10, Toronto, Canada, May 2009.

[22] B. Wang, H. M. Tang, W. X. Jian et al., "Application of 3d network modeling rock mass discontinuities to evaluating rock mass quality for dam foundation," *Rock and Soil Mechanics*, vol. 27, no. 4, pp. 594–596, 2006, in Chinese.

[23] J. Zheng, X. Yang, Q. Lü et al., "A new perspective for the directivity of Rock Quality Designation (RQD) and an anisotropy index of jointing degree for rock masses," *Engineering Geology*, vol. 240, pp. 81–94, 2018.

[24] Z. Sen and E. A. Eissa, "Rock quality charts for long-—normally distributed block size," *Int J Rock Mech Min Sci Geomech Abstr Pergamon*, vol. 29, no. 1, pp. 1–12, 1992.

[25] A. Palmström, "Measurements of and correlations between block size and rock quality designation (RQD)," *Tunnelling and Underground Space Technology*, vol. 20, no. 4, pp. 362–377, 2005.

[26] Y. Chen, H. Lin, X. Ding, and S. Xie, "Scale effect of shear mechanical properties of non-penetrating horizontal rock-like joints," *Environmental Earth Sciences*, vol. 80, 2021.

[27] S. D. Priest and J. A. Hudson, "Discontinuity spacings in rock," *International Journal of Rock Mechanics and Mining Science & Geomechanics Abstracts*, vol. 13, no. 5, pp. 135–148, 1976.

[28] S. G. Du, S. F. Xu, S. F. Yang et al., "Application of rock quality designation (RQD) to engineering classification of rocks," *Journal of Engineering Geology*, vol. 8, no. 3, pp. 351–356, 2000, in Chinese.

[29] G. X. Wang, X. D. Wang, and S. F. Xiao, "Study on applying broad sense RQD to anisotropy of rock mass," *Journal of Jilin University (Earth Science Edition)*, vol. 32, no. 3, pp. 258–260, 2002a, in Chinese.

[30] W. Zhang, J. P. Chen, X. Q. Yuan et al., "Study of size effect and spatial effect of RQD for rock masses based on three-dimensional fracture network," *Chinese Journal of Rock Mechanics and Engineering*, vol. 31, no. 7, pp. 1437–1445, 2012a, in Chinese.

[31] A. Azimian, "A new method for improving the RQD determination of rock core in borehole," *Rock Mechanics and Rock Engineering*, vol. 49, no. 4, pp. 1559–1566, 2016.

[32] H. S. Lee and T. F. Cho, "Hydraulic characteristics of rough fractures in linear flow under normal and shear load," *Rock Mechanics and Rock Engineering*, vol. 35, no. 4, pp. 299–318, 2002.

[33] B. Noetinger and N. Jarrige, "A quasi-steady state method for solving transient Darcy flow in complex 3d fractured networks accounting for matrix to fracture flow," *Journal of Computational Physics*, vol. 231, no. 1, pp. 23–38, 2015.

[34] Austria Startup Company, *ShapeMetriX3D System Manuals. Shengyang*, Europe and China Co. LTD., Shengyang, China, 2008.

[35] D. Z. Gu, *Foundation of Engineering Geomechanics of Rock Mass*, Science Press, Beijing, China, 2008.

[36] B. H. Kim, M. Cai, P. K. Kaiser et al., "Estimation of block sizes for rock masses with non-persistent joints," *Rock Mechanics and Rock Engineering*, vol. 40, no. 2, pp. 169–192, 2006.

[37] ISRM, "Suggested methods for the quantitative description of discontinuities in rock masses," *International Journal of Rock Mechanics and Mining Science & Geomechanics Abstracts*, vol. 15, no. 6, pp. 319–368, 1978.

[38] W. Zhang, J. P. Chen, C. C. Niu et al., "Determination of RQD and number of optimum scanlines based on three-dimensional fracture network," *Chinese Journal of Geotechnical Engineering*, vol. 35, no. 2, pp. 321–327, 2013, in Chinese.

[39] J. Zheng, J. Deng, X. Yang et al., "An improved Monte Carlo simulation method for discontinuity orientations based on Fisher distribution and its program implementation," *Computers and Geotechnics*, vol. 61, pp. 266–276, 2014.

[40] F. Wu, J. Wu, H. Bao, B. Li, Z. Shan, and D. Kong, "Advances in statistical mechanics of rock masses and its engineering applications," *Journal of Rock Mechanics and Geotechnical Engineering*, vol. 13, no. 1, pp. 22–45, 2021.

[41] W. S. Dershowitz, *Rock Joint Systems*, Ph.D. Dissertation, Ph.D. Dissertation Submitted to Massachusetts Institute of Technology, Cambridge, MA, USA, 1984.

[42] W. S. Dershowitz and H. Herda, "Interpretation of fracture spacing and intensity," in *Proceedings of the 33" US Rock Mechanics Symposium*, vol. 33, pp. 757–766, NM, USA, June 1992.

[43] Y. H. An and Q. Wang, "Analysis of representative element volume size based on 3d fracture network," *Rock and Soil Mechanics*, vol. 33, no. 12, pp. 3775–3780, 2013, in Chinese.

[44] L. Xia, X. F. Liu, and Q. C. Yu, "Determining representative elementary volume of fractured rock mass based on blockiness analysis," *Rock and Soil Mechanics*, vol. 31, no. 12, pp. 3991–3996, 2010, in Chinese.

[45] Itasca Consulting Group, Inc, *Distinct Element Method*, 2017, http://www.itascacg.com/software/products/3dec/distinct-element-method>.

[46] H. Bao, K. Zhang, C. Yan et al., "Excavation damaged zone division and time-dependency deformation prediction: a case study of excavated rock mass at Xiaowan hydropower station," *Engineering Geology*, vol. 272, Article ID 105668, 2020b.

[47] F. Wu, Y. Deng, J. Wu et al., "Stress–strain relationship in elastic stage of fractured rock mass," *Engineering Geology*, vol. 268, Article ID 105498, 2020.

[48] M. Haftani, H. A. Chehreh, A. Mehinrad et al., "Practical investigations on use of weighted joint density to decrease the limitations of RQD measurements," *Rock Mechanics and Rock Engineering*, vol. 49, no. 4, pp. 1551–1558, 2015.

[49] W. Zhang, Q. Wang, J. P. Chen et al., "Determination of the optimal threshold and length measurements for RQD calculations," *International Journal of Rock Mechanics and Mining Sciences*, vol. 51, no. 1, pp. 1–12, 2012b.

[50] J. S. Li and S. S. Zuo, "Spatial variation of rock quality designation (RQD) in fractured rock masses," *Journal of Jilin University (Earth Science Edition)*, vol. 44, no. 3, pp. 946–953, 2014, in Chinese.

[51] Z. Senz and A. Kazi, "Discontinuity spacing and RQD estimates from finite length scanlines," *International Journal of Rock Mechanics and Mining Science & Geomechanics Abstracts*, vol. 21, no. 4, pp. 203–212, 1984.

[52] E. Hoek and E. T. Brown, "The Hoek–Brown failure criterion and GSI – 2018 edition," *Journal of Rock Mechanics and Geotechnical Engineering*, vol. 11, no. 3, pp. 445–463, 2019.

[53] G. X. Wang, S. F. Xiao, and J. P. Chen, "Study on application of 3d network of discontinuities to RQD," *Chinese Journal of Rock Mechanics and Engineering*, vol. 21, no. 12, pp. 1761–1764, 2002b, in Chinese.

Research Article

Freezing Temperature Field of FSPR under Different Pipe Configurations: A Case Study in Gongbei Tunnel, China

Yin Duan [ID],[1,2] **Chuanxin Rong** [ID],[1,2] **Hua Cheng,**[1,2] **Haibing Cai** [ID],[1,2] **and Wei Long** [ID][1,2]

[1]*State Key Laboratory of Mining Response and Disaster Prevention and Control in Deep Coal Mine, Huainan, China*
[2]*School of Civil Engineering and Architecture, Anhui University of Science and Technology, Huainan 232001, China*

Correspondence should be addressed to Chuanxin Rong; chxrong@aust.edu.cn

As a new tunnel presupport construction technology, the freeze-sealing pipe roof method (FSPR) has been successfully applied to the Gongbei Tunnel Project for the first time in China. To overcome the practical difficulties of this new method in the freezing construction process, such as welding difficulties of the profiled freezing tube, refrigerant leakage, and long construction period, based on the principle of an equal cooling capacity, an improved design of freezing tube was proposed. By designing three different pipe configurations and using scaled model tests and numerical simulation, the feasibility of the improvement and the difference in the freezing temperature field were studied. The research results show that the improved design with double circular freezing tubes exhibited a lower temperature and a higher cooling rate during the test, and the time required to meet the freezing design requirements was significantly shortened. Finally, a composite structure of "pipe roof and frozen soil curtain" with a better carrying capacity and water sealing performance was formed. It was recommended to strengthen the temperature monitoring at the pipe wall in the preliminary stage of the freezing construction to ensure the water sealing effect between the pipes. In the later stage, attention should be paid to monitoring the thickness of the frozen curtain and reducing excessive frost heave through technical means such as cooling capacity control. The improvement and configurations proposed in this research could effectively replace profiled freezing tubes in the original project, better adapt to horizontal freezing projects of similar curved tunnels, achieve the freezing goal faster, and provide a reference for the promotion of the FSPR.

1. Introduction

The construction and expansion of urban underground structures, especially underground traffic tunnels, is the key to alleviating the pressure on urban surface traffic, promoting urban economic development, improving urban ecological environments and urban structures, and achieving sustainable development [1, 2]. Short-distance urban underground large-section traffic tunnels mostly adopt shallow-buried and concealed construction methods [3, 4]. In the southern and coastal areas of China, this method mainly faces the problem of complex saturated soft soil layers. As a common presupport method in these areas, the pipe roof method (PRM) uses a combination of multiple steel jacking pipes as the load-bearing structure and installs water-stop locks between the jacking pipes to achieve the goal of controlling ground subsidence and sealing

water [5–9]. The artificially ground freezing method (AGF) has also been widely used in more than 220 municipal and subway freezing projects in the water-bearing soft ground of China [10–15].

As shown in Figure 1, the Gongbei Tunnel serves as a key project for the Zhuhai connecting line of the Hong Kong-Zhuhai-Macao Bridge, which passes through the Gongbei Port of Zhuhai City. It is a typical shallow-buried tunnel with a length of 255 m, a buried depth of 4-5 m, and a cross-sectional area of 345 m^2, and its design line consists of a gentle curve and a circular curve ($R = 890$ m) [16, 17]. The geology of the tunnel site is extremely complex, which is composed of a large number of unevenly developed water-rich soft sandy soil layers and silt clay layers. Numerous ground buildings have been developed along the line, most of which were pile foundations, and the closest distance

Figure 1: Schematic diagram of the Gongbei Tunnel.

between the pipe roof and the structural pile foundation was only 0.46 m, making the tunnel construction extremely difficult. The pipe roof method has poor adaptability to curved tunnels and cannot guarantee the water sealing effect between the jacking pipes, leading to higher construction risks. The artificially ground freezing method also has the effect of frost heaving and thaw settlement of the ground, causing an adverse impact on nearby structures of the tunnel. After repeated demonstrations, the freeze-sealing pipe roof method (FSPR) which combines the advantages of the pipe roof method and the artificially ground freezing method has been proposed. The principle of this new method is that, firstly, several sections of large-diameter and closely arranged steel pipes were jacked into the stratum to form a pipe roof, and then the artificially ground freezing was carried out by installing freezing tubes inside the pipe wall to form a certain thickness of frozen soil curtain around the pipe roof, finally forming a supporting system with both bearing capacity and water sealing performance.

As in Figure 2, 18 concrete pipes (filled with concrete) and 18 hollow pipes with a diameter of 1.6 m were alternately arranged around the tunnel excavation section, and the average distance between jacking pipes was about 357 mm. The circular freezing tubes were installed on the left and right sides of the inner wall of the concrete pipes (odd-numbered pipes) to freezing soil layers, and the limiting tube in the concrete pipe controls the thickness of frozen soil by circulating hot saltwater in the later period of freezing. The profiled freezing tubes (made of 125 mm × 125 mm × 8 mm angle iron) were directly welded on the inner wall of the hollow pipes (even-numbered pipes) to strengthen freezing between the pipes (Figure 3). These hollow pipes were not filled with concrete and were mainly used as passages for freezing monitoring during the construction process. To ensure the water sealing effect while avoiding excessive frost heave, the thickness range of the frozen soil curtain was set to 2–2.6 m. The actual freezing time established by the freezing construction plan was 180 days, of which the active freezing period lasted for the first 90 days.

Based on the engineering characteristics of the Gongbei Tunnel, Hu et al. [18, 19] established a temperature field calculation model for the FSPR through theoretical derivations and numerical simulations and obtained an analytical solution of the steady-state temperature field. Moreover, the feasibility of this method has been verified through model tests [20, 21] and field measurements [22]. Ren et al. [23] performed numerical simulations and large-scale model tests to demonstrate the feasibility and reliability of the fine dynamic control freezing and sealing water design scheme. Ji et al. [24] proposed that it is necessary to carry out further investigations on technical issues of the FSPR, such as long-distance zoned horizontal freezing ground reinforcement mechanism, freezing parameters, and modes. Kang et al. [25] conducted numerical simulations on the excavation of the Gongbei Tunnel and pointed out that the change of the temperature field was the key factor for predicting the frozen wall thickness. Lu et al. [26] analyzed and predicted the overall temperature field of a freezing pipe circular arrangement and the change of the freezing curtain thickness with time through finite element numerical simulations. Zhang et al. [27] predicted the soil temperature change and surface frost heave displacement during an artificial freezing process based on a thermomechanical coupling method and compared the effects of two methods of controlling ground frost heave: soil pregrouting around the pipe roof and the application of limiting tubes. Ren et al. [28] analyzed and verified the pipe combination method through field temperature measurements based on the engineering design plan.

The abovementioned research played an important role in promoting the theoretical development and application of the FSPR. However, some practical problems were still encountered during the freezing construction period. In particular, the installation of the profiled freezing tube requires a large amount of overhead and arc welding, and all the works need to be completed in a narrow space inside the jacking pipe. These excessive welding difficulties cannot guarantee the installation quality and often lead to cracks
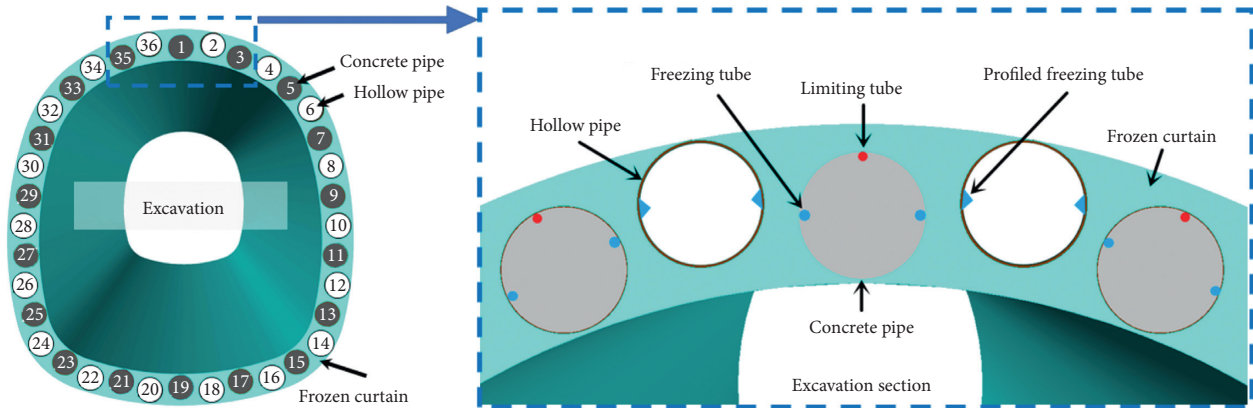
FIGURE 2: Principle diagram of FSPR method designed for Gongbei Tunnel.
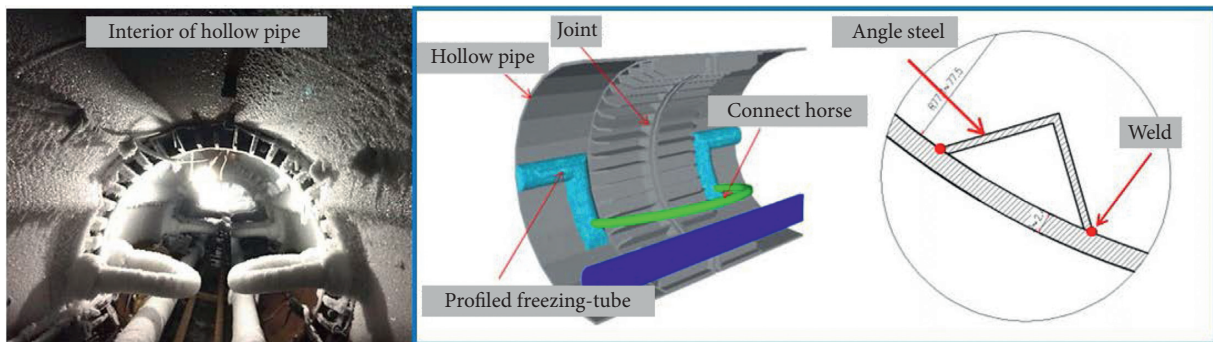
FIGURE 3: Diagrammatic sketch of hollow pipe with profiled freezing tube.

and refrigerant leakage, resulting in high maintenance costs. Furthermore, it not only affected the construction schedule but also brought about working environment problems, such as construction thermal disturbance and safety hazards.

In this study, to overcome the practical difficulties of FSPR in the freezing construction process, we took jacking pipes and freezing tubes as the research objects and proposed an improved design for the profiled freezing tubes based on previous research [29, 30]. The feasibility of the improvement and the difference in the freezing temperature field under different pipe configurations during the active freezing period was investigated through scaled model tests and numerical simulations to provide a certain reference for the promotion of this new construction method.

2. Scaled Model Test and Process

2.1. Scaling Laws and Test Materials.
Considering different test conditions, the geometric scaling law was first determined as $C_l = 1/10$. Other related scaling laws were obtained based on the Kosovich criterion and the Fourier criterion (Table 1) [31–33]. The test soil layer material was selected according to project site conditions. The diameters of the jacking pipe and the freezing tube, velocity and flow, and the physical parameters of the test materials through laboratory tests are presented in Tables 2–4, respectively.

2.2. Model Design and Test System.
Three types of jacking pipes were designed in this test: one concrete pipe and two hollow pipes. The concrete pipe was made by installing a freezing tube on each horizontal side of the inner wall of the steel pipe and filling it with C30 fine aggregate concrete. One of the hollow pipes has the same structure as the engineering prototype, and the other one is an improved design based on the principle of equal cooling capacity, which uses cement mortar (made of Ordinary Portland Cement, sand, and water) to wrap and fix the circular freezing tubes on the inner wall of the hollow pipe, instead of the welded profiled freezing tubes in the prototype (Figure 4). Due to the complexity of the pipe roof form in the actual project, it was appropriately simplified in the current test. Some of the concrete pipes and the hollow pipes were taken for the horizontal arrangement to design three different pipe configurations (Figure 5).

(1) Configuration A: The combination of a concrete pipe and a hollow pipe (including the profiled freezing tubes), and this configuration was consistent with the engineering prototype.

(2) Configuration B: The combination of a concrete pipe and a hollow pipe (including the improved double circular freezing tubes).

(3) Configuration C: The combination of two concrete pipes and three hollow pipes (including improved double circular freezing tubes).

TABLE 1: Scaling laws.

Scaling parameter	Geometry (mm)	Temperature (°C)	Thermal capacity (J·kg⁻¹·K)	Thermal conductivity (W·m⁻¹·K⁻¹)	Velocity of flow (m/min)	Rate of flow (m³/h)	Time (h)
Scaling law	1/10	1	1	1	10	1/10	1/100

TABLE 2: Diameters of jacking pipe and freezing tube.

Diameter	Prototype (mm)	Model (mm)
Jacking pipe	1600	160
Freezing tube	80	8

TABLE 3: Velocity and flow.

Parameter (single-tube)	Prototype	Model
Flow rate (m³/h)	5	0.5
Flow velocity (m/min)	16.6	166

TABLE 4: Physical parameters of test materials.

Material	Density (kg·m⁻³)		Thermal capacity (J·kg⁻¹·K)		Thermal conductivity (W·m⁻¹·K⁻¹)		Water content (%)	Freezing point (°C)
	ρ	ρ_{sat}	Unfrozen	Frozen	Unfrozen	Frozen		
Saturated sand	1436	2054	1370	1070	1.48	1.80	40.29	−0.5
C30 concrete	2455		920		1.64		—	—
Cement mortar	1910		845		1.29		—	—
Steel pipe	7840		319		62		—	—
Air	1.28		1005		0.02		—	—
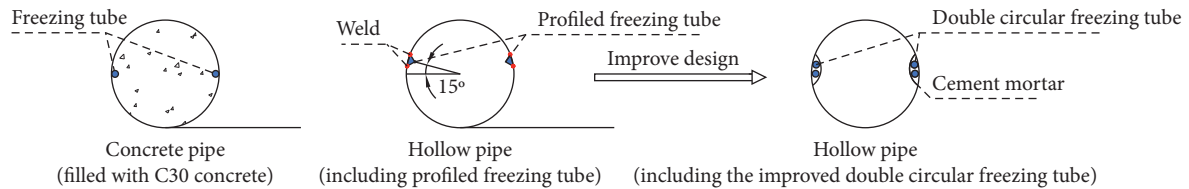
FIGURE 4: Three types of jacking pipes.

The horizontal distance between adjacent pipes and the distance between adjacent measurement points were both 50 mm. In Configurations A and B, temperature measurement points were arranged on the midline between the two pipes and in the vertical and horizontal directions of the hollow pipe. In Configuration C, considering that the pipes alternately formed the pipe roof, three rows of temperature measurement points were set in the vertical direction. All the red points in Figure 5 were control points, which were used to monitor whether the test results complied with the freezing design requirements.

The size of the model box was 1200 mm × 3900 mm × 1500 mm ($H \times W \times L$), which was welded by 6 mm thick steel plates and divided into three test areas. Insulation materials were laid on the inner wall of the box, and partitions were provided in adjacent test areas. All the jacking pipes were installed horizontally in the center of the box, and the height of the pipe center from the ground was 600 mm (Figure 6).

Two temperature monitoring systems were designed for this test (Figure 7(a)). A TML TDS-602 data logger with thermocouple sensors was used as the main monitoring system (Figure 7(b)) and the test data were based on it. The accuracy of the sensor was ±0.1°C and the range was from −80°C to +200°C. A CW-500 digital thermometer was used as the auxiliary monitoring system, which performed auxiliary acquisition during the test to guarantee the authenticity of the data. The plane of the measurement points of these two systems was symmetrical along the horizontal centerline of the model (Figure 7(a)). Each freezing tube had an independent valve and was connected with the main inlet and return pipes of the refrigeration system (Figure 7(c)). An SKLD-80F electromagnetic flowmeter was installed on the main freezing tube to monitor the total flow. Following the freezing construction organization of the Gongbei Tunnel, the temperature of the freezing system was controlled in the range of −25 to −28°C; hence, the freezing system temperature of this test was set to −25°C.
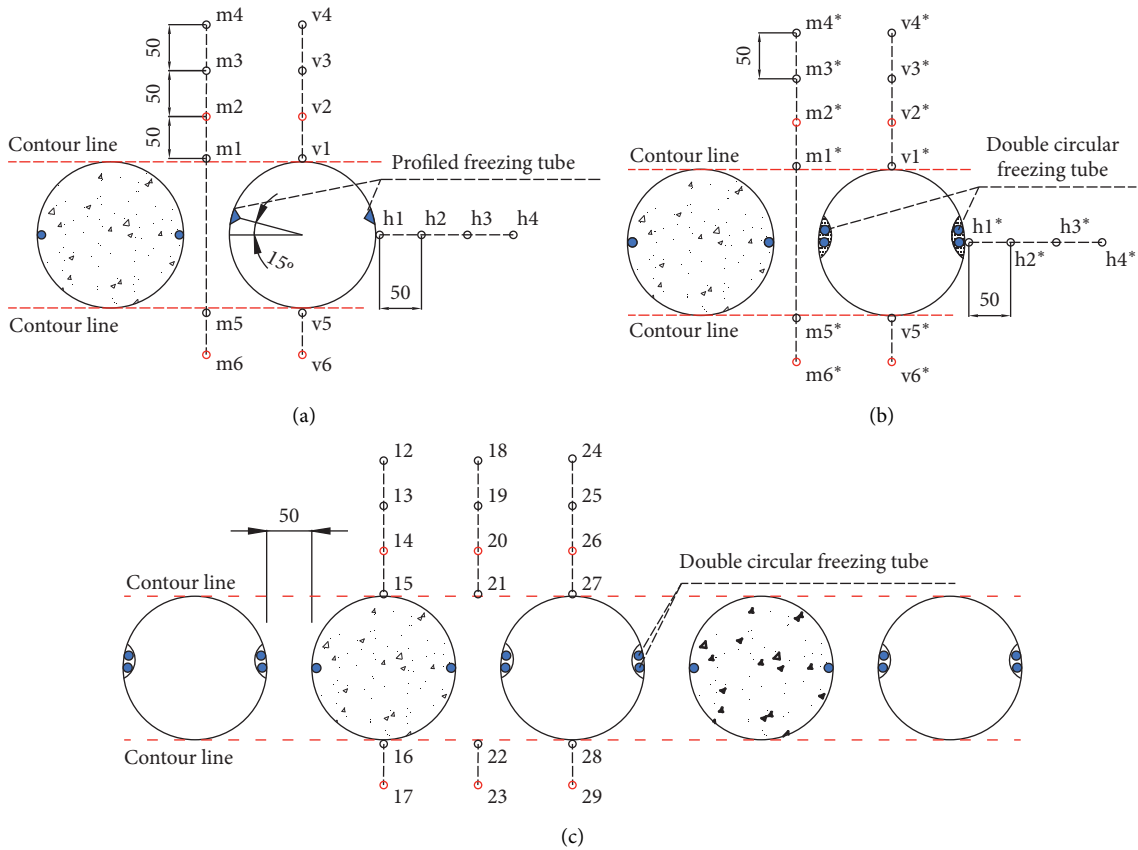
FIGURE 5: Three different pipe configurations with temperature measurement points (mm): (a) Configuration A. (b) Configuration B. (c) Configuration C.

2.3. Test Process

(1) Combining the active freezing period of the project (90 days) and the time scaling law (1/100), the converted freezing time of this test was set to 0.9 days (about 21 hours).

(2) Turn on the refrigeration system and reduce the saltwater temperature to the design value (−25°C).

(3) When the refrigeration system began to circulate, one-time freezing was conducted in all test areas. The system automatically monitors and collects the temperature data until the end of the test.

(4) The average thickness of the frozen soil curtain specified in the Gongbei Tunnel's freezing construction design data ranges from 2 to 2.6 m. Considering the geometric scaling law $C_l = 1/10$, it can be obtained that the freezing target of this test is to make the frozen wall thickness reach 260 mm, which means that the temperature of the red points in Figure 5 has reached the freezing point (−0.5°C).

3. Test Results and Discussion

3.1. Contrast Analysis of Improved Design.

Figures 8 and 9 display the "temperature-time" curves at midline points and vertical line points in Configurations A and B, respectively. The blue horizontal dotted line in each figure represents the freezing point (−0.5°C) baseline. In Tables 5–7, T_0 and T_{21} represent the initial temperature and final temperature of the test, respectively, V represents the average cooling rate in 21 hours, and ΔT and Δt represent temperature difference and time difference, respectively. It was noticeable that all curves manifested a general trend of decreasing first and then stabilizing. The curves of the symmetrical points basically coincide, and the temperature of the points on the contour line (Figure 5) was the lowest. The temperature at each point dropped sharply in the first 5 hours; however, the slope of the curve for Configuration B was greater. At 12 h, the temperature of m1 and m5 in Configuration A reached the freezing point, indicating that the thickness of the frozen soil between the pipes reached 160 mm; however, the corresponding time in Configuration B was only 5 hours. The temperatures at m2* and m6* had reached the freezing point at 14 h (7 hours earlier than Configuration A), which indicates that the thickness of the frozen soil between the two pipes reached 260 mm, and the freezing time was shortened by 33.3%. At 21 h, the average temperature at m2* and m6* was −4.4°C, which was 3.75°C lower than that of m2 and m6, and the average cooling rate increased by 25.5% (Table 5).

Compared with Configuration A, the temperatures at control points v2* and v6* in Configuration B had reached the freezing point at 16 h, and the average temperature was reduced by 4.65°C at 21 h, and the average cooling rate increased by 34.1% (Table 6). The temperature at h2* had reached the freezing point at 10 h (9 hours earlier than the
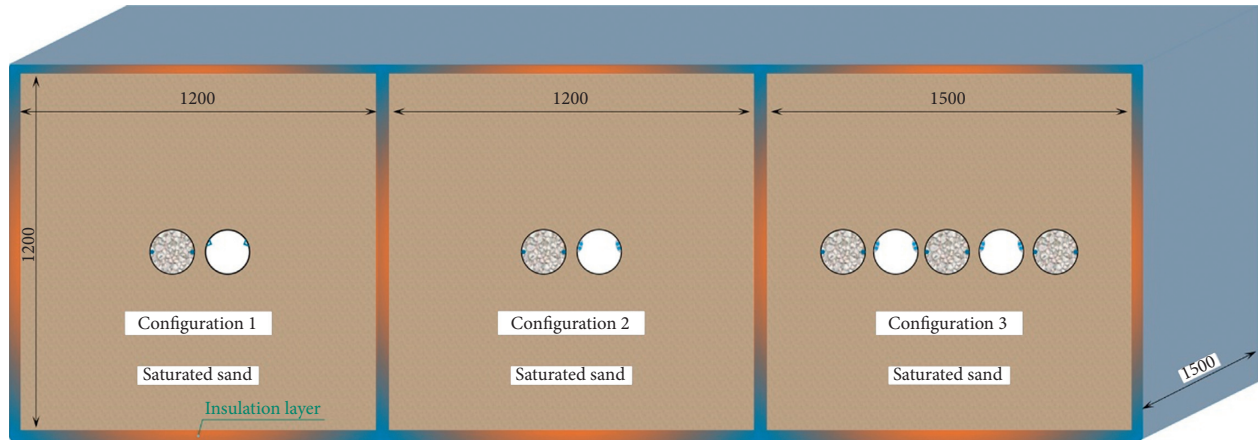
FIGURE 6: Test model box.
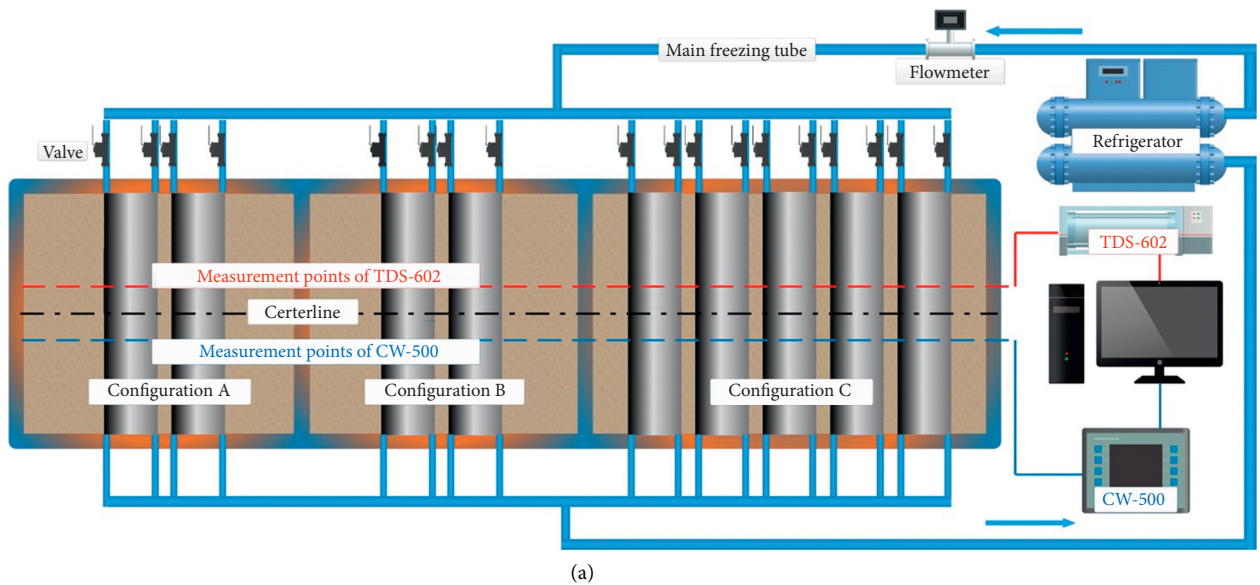
(a)

(b)

(c)

FIGURE 7: Layout of the test system: (a) Schematic plan of the test system. (b) TDS-602 data logger. (c) Freezing system.

time at h2, corresponding to a reduction of 47%) (Table 7). At 21 h, the temperature at h2* was 3°C lower than that at h2, and the average cooling rate increased by 13%, indicating that the improved design enhanced the vertical and horizontal freezing effect of the hollow pipe.

Although both configurations ultimately met test design requirements, it is obvious that the improved design yielded superior results and reflected a shorter freezing time and a higher cooling rate. The remaining points also supported these observations.
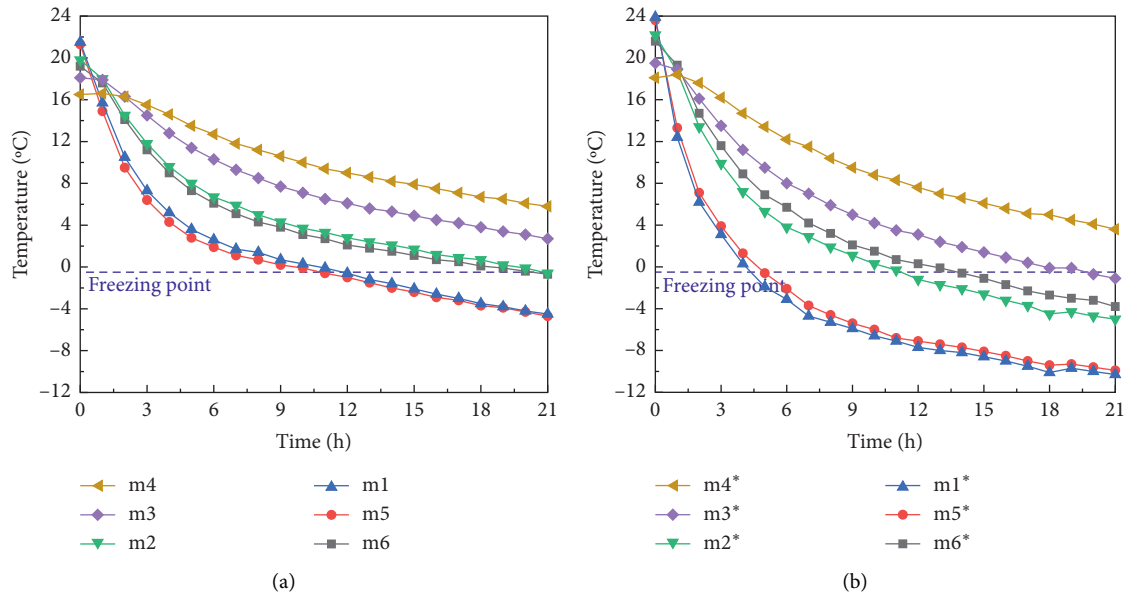
FIGURE 8: Temperature-time curves at midline points: (a) Configuration A. (b) Configuration B.
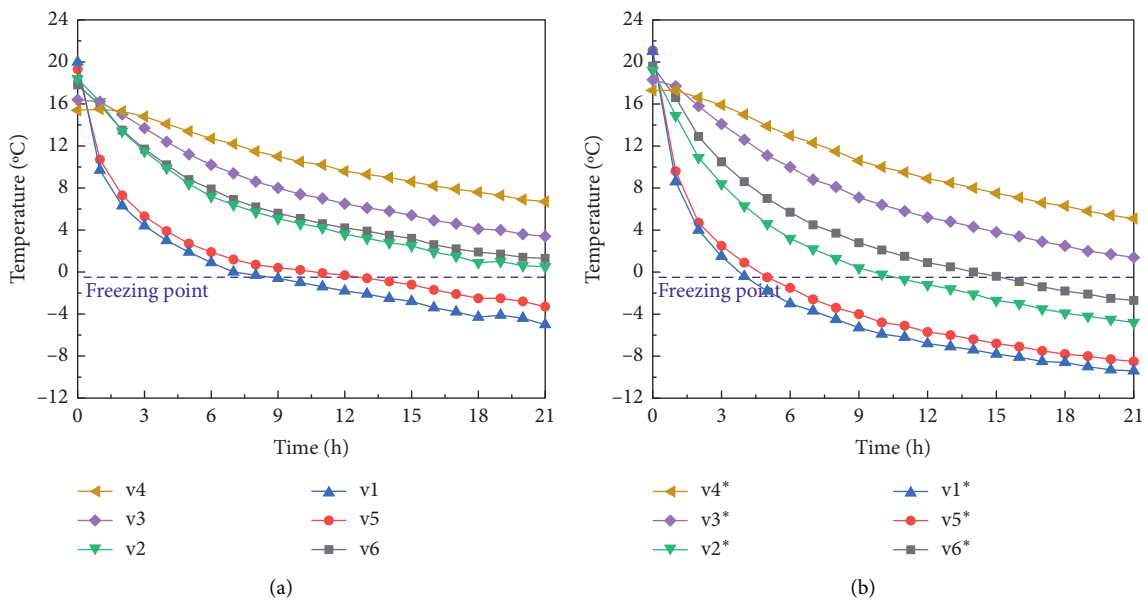
FIGURE 9: Temperature-time curves along the vertical line of hollow pipes: (a) Configuration A. (b) Configuration B.

3.2. Analysis of Test Results Based on Improved Pipe Roof.
It was clear from Figure 10(a) that, in comparison to Configuration B, as Configuration C used multiple jacking pipes to form the "pipe roof," the freezing effect was further improved in the middle and late stages of the test. The temperature curves at m1* and 21 measurement points coincided in the first four hours, indicating that, in the early freezing stage, temperature fields between jacking pipes changed in the same degree and the "group pipe effect" was not yet obvious. With the prolonged freezing time, the temperature curve at the measurement point 21 dropped

further, and the "group pipe effect" gradually improved the freezing effect. At the end of the test, the temperatures at m1* and 21 measurement points were −10.3°C and −13°C, respectively, and the other points conformed to the above rules.

It was observable from Figure 10(b) and Table 8 that the temperature curve at each measurement point 50 mm above the pipe contour line in Configuration C followed the same variation trend. In comparison to Configuration B, the "group pipe effect" in Configuration C was more evident. Temperatures at all measurement points dropped below the

TABLE 5: Contrast of temperature data of control points at midline.

Measuring point	T_0 (°C)	T_{21} (°C)	ΔT (°C)	V (°C/h)	Time of temperature below freezing point (h)	Δt (h)
m2	19.8	−0.6		−0.97	21	
m2*	22.2	−5.0	−4.4	−1.30	12	−9
m6	19.2	−0.7		−1.03	21	
m6*	21.6	−3.8	−3.1	−1.21	14	−7

TABLE 6: Contrast of temperature data of control points at vertical line.

Measuring point	T_0 (°C)	T_{21} (°C)	ΔT (°C)	V (°C/h)	Time of temperature below freezing point (h)	Δt (h)
v2	18.4	0.5		−0.85	—	
v2*	19.2	−4.8	−5.3	−1.14	12	—
v6	17.8	1.3		−0.79	—	
v6*	19.6	−2.7	−4.0	−1.06	16	—

TABLE 7: Contrast of temperature data at horizontal direction.

Measuring point	T_0 (°C)	T_{21} (°C)	ΔT (°C)	V (°C/h)	Time of temperature below freezing point (h)	Δt (h)
h2	19.9	−1.2		−1.00	19	
h2*	19.6	−4.2	−5.4	−1.13	10	9
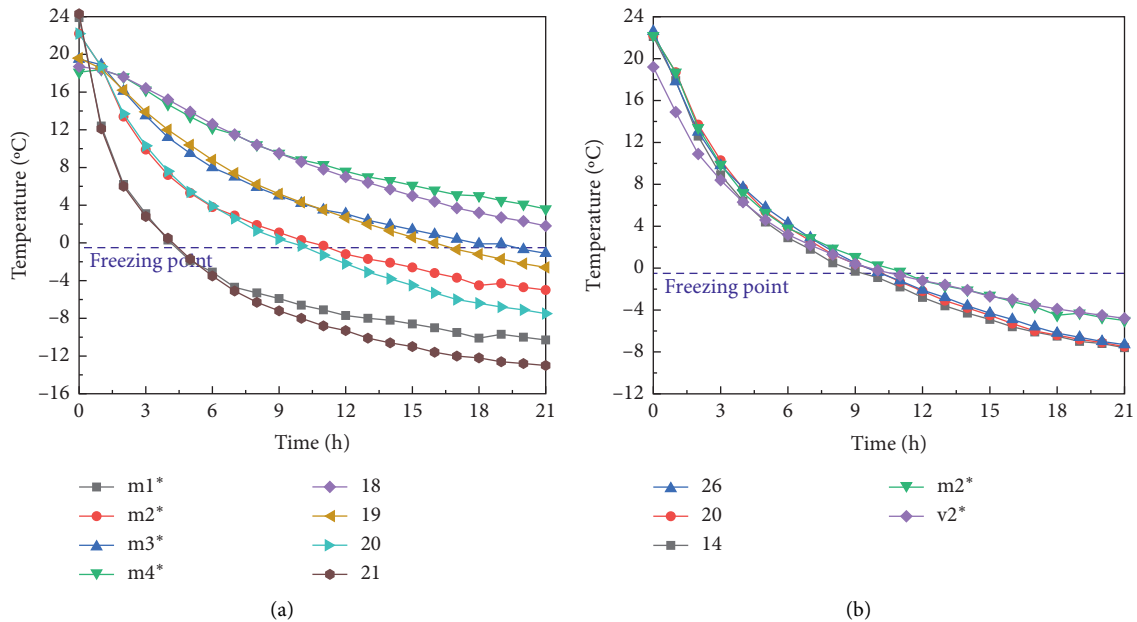
FIGURE 10: Comparison of "temperature-time" curves at measurement points in Configurations B and C. (a) Midline points between the pipes in Configurations B and C and (b) points at 50 mm above the pipe contour line in Configurations B and C.

freezing point at 11 h, and the time was shortened by 1 hour. Moreover, the average temperature at 21 h was −7.5°C, which was about 2.6°C (53%) lower than that of Configuration B, and the average cooling rate also increased by 16%. Therefore, by adopting the pipe roof form consisting of a hollow pipe with improved double circular freezing tubes and a concrete pipe, a frozen soil curtain with a certain thickness quickly formed in the soil layer, and the freezing target can be achieved earlier.

4. Numerical Simulation Results and Discussion

4.1. Model Establishment.
Numerical models were established for the three pipe configurations to study the development law and the differences of freezing temperature field. Taking Configuration C as an example, the two-dimensional temperature field of the test model was simulated in COMSOL Multiphysics® v. 5.4 (Figure 11). The

TABLE 8: Temperature data at measurement point 50 mm above the contour line in Configurations B and C.

Measuring point	T_0 (°C)	T_{21} (°C)	V (°C/h)	Time of temperature below freezing point (h)
14	22.1	−7.6	−1.41	10
20	22.2	−7.5	−1.41	11
26	22.6	−7.3	−1.42	11
m2*	22.2	−5	−1.30	12
v2*	19.2	−4.8	−1.14	12

(a)

(b)
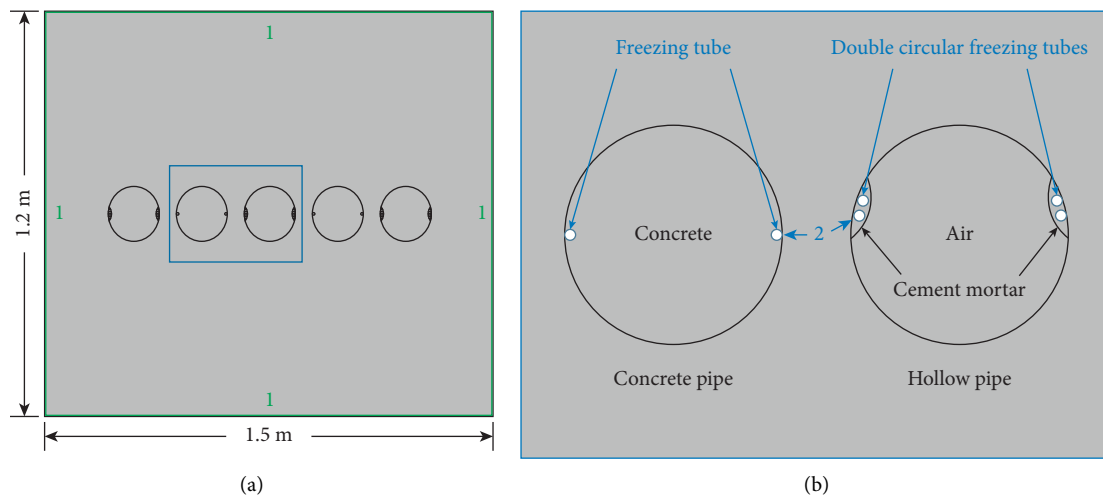
FIGURE 11: Numerical model of Configuration C.

calculation module adopted the porous medium heat transfer module, which can effectively simulate the heat transfer phenomena in the soil [34–36]. The computational domain grid system used nonstructural triangular elements, and the grid density was higher near the steel pipes and the freezing tubes (Figure 12). The minimum element size, average element mass, and minimum element mass of the numerical model were 0.42 mm, 0.8289, and 0.04317, respectively, indicating that the mesh element quality was good and the calculation results were convergent [37]. The numerical model had two boundaries (Figure 11): the first one was the soil layer boundary, which acted as an insulation layer, and the initial temperature of the soil layer was set to 20°C; and the second one was the freezing tube wall (−25°C), which followed the Dirichlet boundary condition.

The comparison between the simulation data and the test data of selected measurement points in Figure 13 shows that the numerical results are in good agreement with the test, which means that the numerical simulation method used in this paper has good accuracy. Therefore, it can conduct in-depth and comprehensive research on the variation law of freezing temperature field and the development of frozen soil curtain.

4.2. Validation of Improved Results. Figures 14 and 15 compare the 21-hour freezing temperature field distributions and the frozen soil wall thicknesses at different positions in Configurations A and B, respectively. As the freezing tubes were near the horizontal direction of the pipes, the

temperature in the horizontal direction was lower than that in the vertical direction, and the shape of the isotherm at a far distance was approximately elliptical. The average thicknesses of the frozen wall formed between the two pipes in Configurations A and B were 252 mm and 281 mm, respectively, which means that a reliable water sealing structure between the pipes was formed. However, in comparison to Configuration A, the average thickness of the frozen soil wall on the vertical line of the hollow pipe, the vertical line of the concrete pipe, and between the two pipes increased by 20%, 7%, and 12% in Configuration B, respectively.

4.3. Discussion on Development and Distribution Law of Freezing Temperature Field Based on Improved Design. Figure 16(a) exhibits the temperature field cloud diagram of Configuration C at 3 h, and the black line represented the boundary of the frozen soil wall. As the distance between the pipes was very small and the freezing tubes were close to the horizontal position on both sides of the pipes, the frozen soil wall of a certain thickness was initially formed between the pipes. Due to the alternating arrangement of the concrete pipes and hollow pipes, the shape of the frozen soil wall between the pipes was asymmetric, and the thickness near the concrete pipe was slightly larger, and the overall average thickness was about 123.2 mm. Although the frozen soil wall had a role in sealing water to a certain extent, it was limited by its thickness; thus, cracks and water flow passages may have appeared at the junction of frozen soil and the pipe wall

(a)

(b)
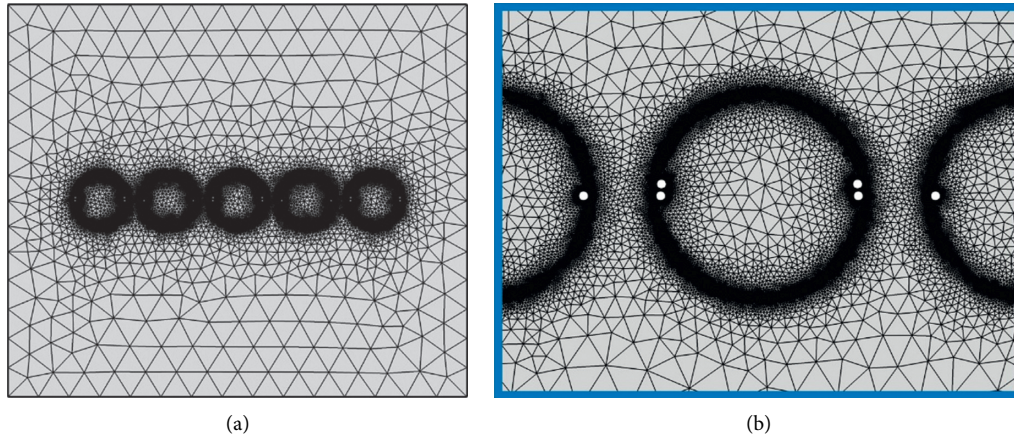
FIGURE 12: Grid system of Configuration C.

m2 (simulation)

m2 (test)

(a)

m2* (simulation)

m2* (test)

(b)
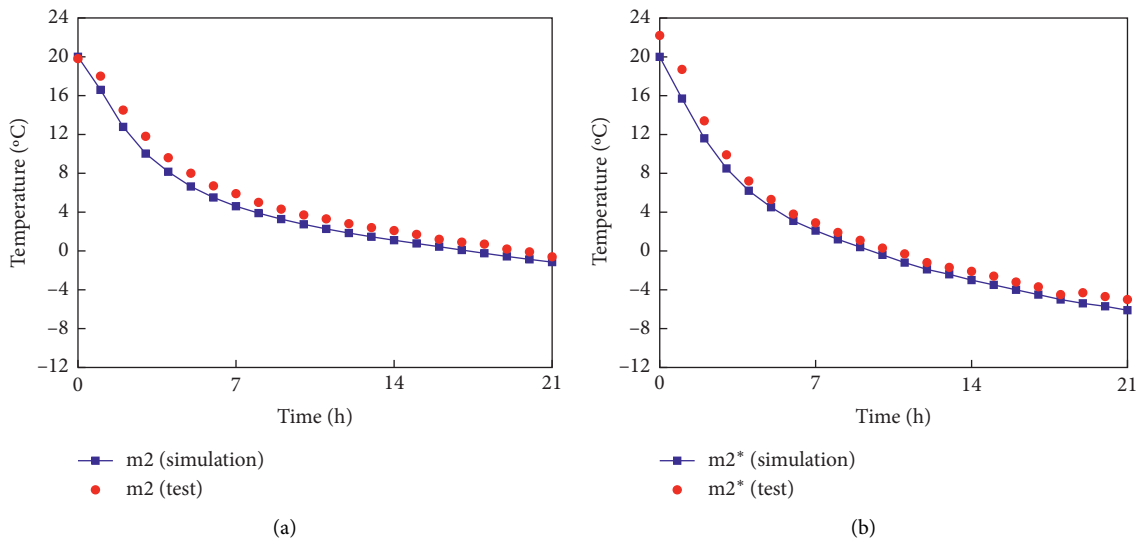
FIGURE 13: Comparison between simulation data and test data: (a) m2 (Configuration A). (b) m2* (Configuration B).

(a)

(b)
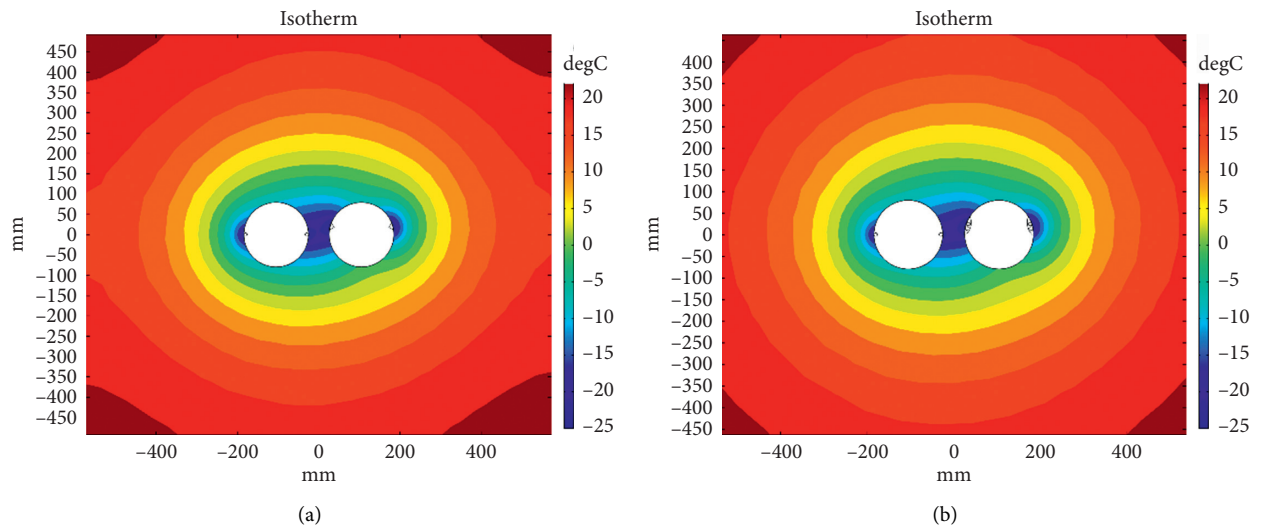
FIGURE 14: Distribution of freezing temperature field at 21 h. (a) Configuration A. (b) Configuration B.

(a)

(b)
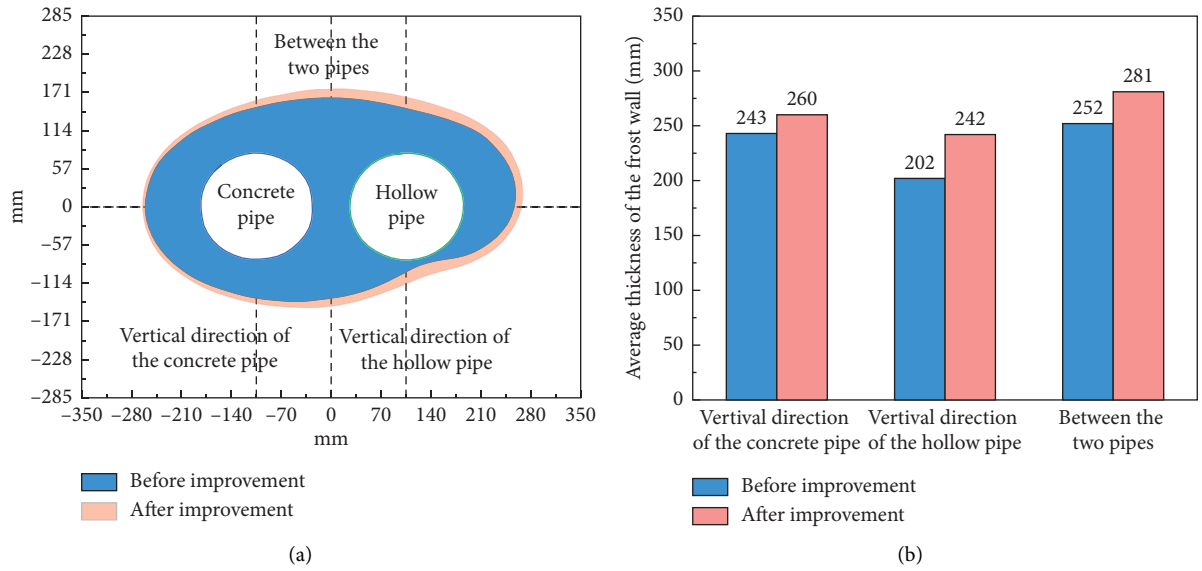
Figure 15: Comparison of the frozen soil wall at different positions at 21 h.

(a)

(b)

(c)

(d)
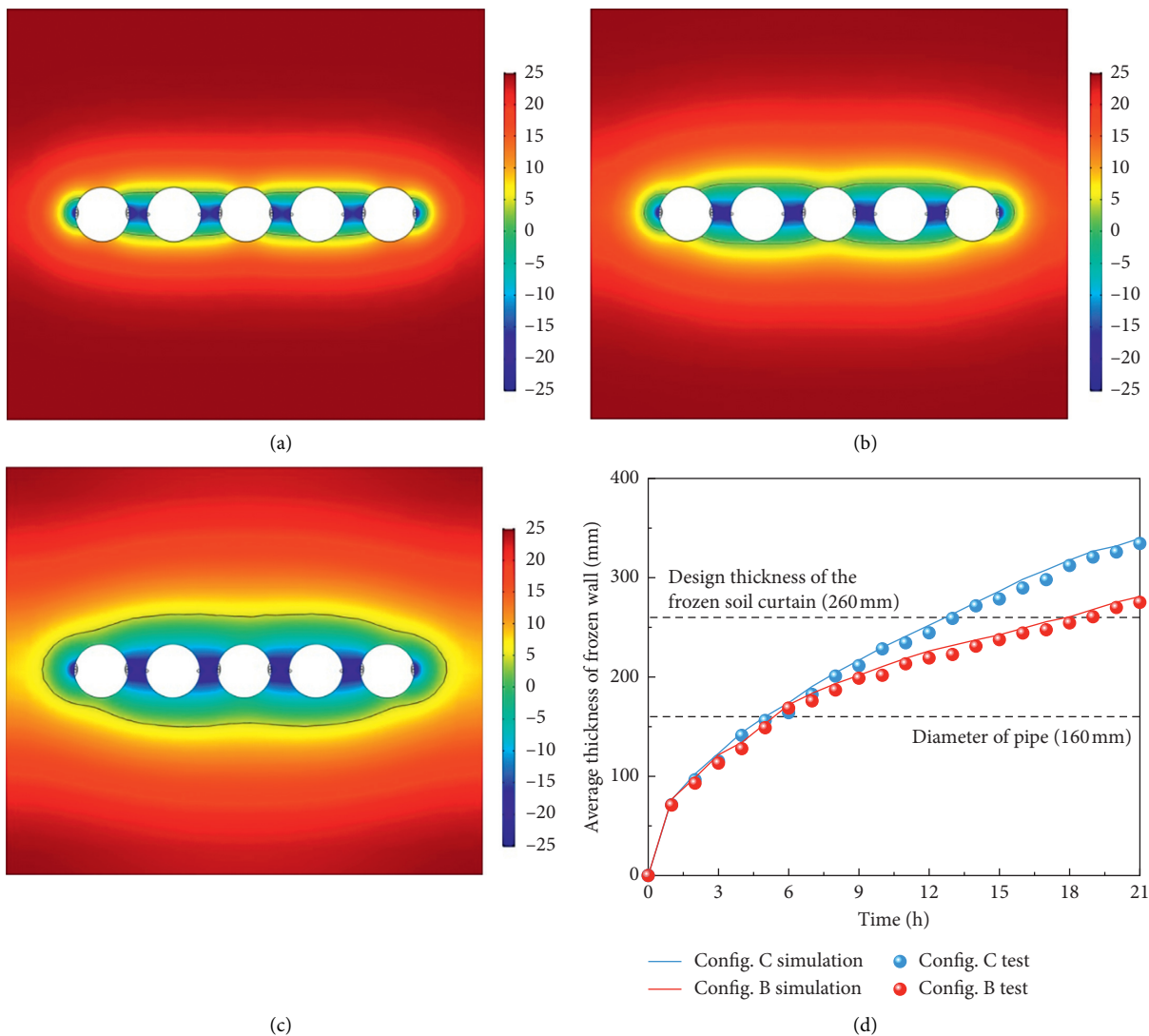
Figure 16: Distribution of the freezing temperature field of Configuration C and curves of the average frozen soil wall thickness: (a) Freezing temperature field at 3 h. (b) Freezing temperature field at 6 h. (c) Freezing temperature field at 21 h. (d) Comparison of the development curves of average frozen wall thickness in Configurations B and C.

due to the influences of external factors, such as ground stresses and construction thermal disturbances. The frozen soil wall completely wrapped the concrete pipe at 6 h (Figure 16(b)), and the temperatures at 15# and 16# had reached the freezing point. Some soil on the upper and lower sides of the hollow pipe remained unfrozen, and the average thickness of the frozen soil wall between the pipes was about 174 mm. However, it was still necessary to closely observe the development of the frozen soil wall at the upper and lower contour lines of the hollow pipe to avoid the effects of thermal disturbances. At 21 h (Figure 16(c)), the range of the frozen soil wall was further expanded, all pipes were wrapped by it, and the contour of it had an uneven shape. At this stage, a "steel pipe-frozen soil curtain" composite structure with better carrying capacity and water sealing performance had been formed. The average thickness of the frozen soil curtain around the concrete pipe (349.5 mm) was slightly larger than that around the hollow pipe (336.9 mm); thus, this pipe configuration effectively met the freezing design requirements.

It was evident from Figure 16(d) that the curves of average frozen soil wall thickness in Configurations B and C obtained from numerical simulation were consistent with the test results. At the beginning of the freezing process, the frozen soil walls of Configurations B and C developed rapidly, and the time taken to expand their range to the pipe diameter (160 mm) was about 5 hours. After 7 hours, the "group pipe effect" became evident in Configuration C, and the development speed was faster, reaching a design thickness of 260 mm at 13 h (5 hours earlier than Configuration B). Therefore, by adopting the improved double circular freezing tubes, the freezing effect was further strengthened in the pipe roof structure (Configuration C). Subsequently, the development entered a relatively slower stage. At this time, the thickness of the frozen soil curtain should be monitored precisely, and the formation of excessive frost heave should be reduced through technical means, such as cooling capacity control of the refrigeration system.

5. Conclusions

(1) To solve the existing problems of the Gongbei Tunnel Project, an improved design was proposed based on the FSPR. The temperature field distribution characteristics and freezing performances for three different pipe configurations were investigated by scaled model tests and numerical simulations. The improved double circular freezing tubes were easy to manufacture and install, and this approach could solve several practical problems in the actual project, such as profiled freezing tube welding difficulties, refrigerant leakage, and working environment hazards.

(2) The improved results (Configuration B) exhibited a better freezing effect in terms of lower temperature and higher cooling rate and significantly shortened the time required for soil freezing in the test. In comparison to the prototype (Configuration A), the

average thickness of the frozen wall on the vertical line of the hollow pipe, the vertical line of the concrete pipe, and between two pipes increased by 20%, 7%, and 12%, respectively.

(3) Compared with the first two configurations, the "group pipe effect" was more significant in Configuration C; thus, the freezing effect was further improved. Numerical simulation results revealed that a certain thickness of the frozen wall was quickly formed between the pipes at first. Subsequently, the concrete pipe was completely wrapped by frozen soil, and the freezing range then gradually expanded to the hollow pipe. Finally, a composite structure of "pipe roof and frozen soil curtain" with better carrying capacity and water sealing performance had been formed. It was suggested to strengthen the monitoring of frozen soil temperature at the pipe wall in the preliminary stage of the freezing construction process to avoid "thermal disturbances" causing cracks and water flow channels at the interface between the frozen soil and the pipe wall. In the later stage, the thickness of the frozen curtain should be monitored precisely, and the excessive frost heave should be reduced through technical means, such as cooling capacity control.

Data Availability

The data used to support the findings of this study are available from the corresponding author upon request.

Conflicts of Interest

The authors declare that there are no conflicts of interest regarding the publication of this paper.

Acknowledgments

References

[1] X. Chen, "Research on combined construction technology for cross-subway tunnels in underground spaces," *Engineering*, vol. 4, no. 1, pp. 103–111, 2018.

[2] X. Chen, Z. Xu, X. Bao, X. Wang, and Y. Fu, "Challenges and technological breakthroughs in tunnel construction in China," *China Journal of Highway and Transport*, vol. 33, no. 12, pp. 1–14, 2020.

[3] H. Zhu, W. Ding, Y. Qiao, and X. Wang, "Issues and challenges in urban underground space utilization in China," *Earth Science Frontiers*, vol. 26, no. 3, pp. 022–031, 2019.

[4] Z. Xiong, H. Lu, M. Wang, Q. Qian, and X. Rong, "Research progress on safety risk management for large scale geotechnical engineering construction in China," *Rock and Soil Mechanics*, vol. 39, no. 10, pp. 3703–3716, 2018.

[5] H. Zhu, Z. Yang, X. Li, X.-Z Liu, and G.-P. Shen, "Analysis of construction risk for pipe-roofing tunnel in saturated soft soil," *Chinese Journal of Rock Mechanics and Engineering*, vol. 24, no. S2, pp. 5549–5554, 2005.

[6] J. Sun, X. F. Yu, M. Sun, and X. Li, "Analysis and prediction on soft ground deformation of a super-large shallow buried "pipe-roofing and box-culvert" jacking project under construction," *Rock and Soil Mechanics*, vol. 27, no. 7, pp. 1021–1027, 2006.

[7] Y. Li, Y. Zhang, and W. Li, "Research and application of pipe roofing method in soft soil," *Chinese Journal of Underground Space and Engineering*, vol. 7, no. 5, pp. 962–967, 2011.

[8] X. Guo, H. Zhang, J. Meng, X. Zhang, M. Wang, and Y. Zhu, "Model test to earth pressure distribution on pipe roof of tunnels as pre-supporting system in weak surrounding rock," *Chinese Journal of Rock Mechanics and Engineering*, vol. 35, no. 6, pp. 1214–1224, 2016.

[9] W. Pan, "Monitoring and analysis of ground settlement during pipe roof construction of pipe-jacking groups in soft soil areas," *Chinese Journal of Geotechnical Engineering*, vol. 41, no. S1, pp. 201–204, 2019.

[10] X. Chen, "Several key points of artificial ground freezing method and its latest application in China," *Tunnel Construction*, vol. 35, no. 12, pp. 1243–1251, 2015.

[11] H. Cai, S. Li, Y. Liang, Z. Yao, and H. Cheng, "Model test and numerical simulation of frost heave during twin-tunnel construction using artificial ground-freezing technique," *Computers and Geotechnics*, vol. 115, pp. 103–155, 2019.

[12] H. Cai, L. Peng, and T. Zheng, "A method for predicting ground surface settlement in the artificial thawing period of tunnel horizontally frozen wall," *Rock and Soil Mechanics*, vol. 36, no. 12, pp. 3516–3522, 2015.

[13] H. Cai, Z. Liu, S. Liu, and T. Zheng, "Improved analytical prediction of ground frost heave during tunnel construction using artificial ground freezing technique," *Tunnelling and Underground Space Technology*, vol. 92, 2019.

[14] H. Song, H. Cai, Z. Yao, C. Rong, and X. Wang, "Finite element analysis on 3D freezing temperature field in metro cross passage construction," *Procedia Engineering*, vol. 165, pp. 528–539, 2016.

[15] Y. Mei, L. Zhao, D. Zhou, J. Liu, J. Zhu, and J. Zhu, "Application of AGF in underground excavation construction of water-rich sand layer," *China Railway Science*, vol. 41, no. 4, pp. 1–10, 2020.

[16] J. Yu, Y. Cheng, R. Jia et al., "Option demonstration for the Gongbei tunnel at the Zhuhai link of the Hong Kong-Zhuhai-Macau bridge," *Modern Tunnelling Technology*, vol. 49, no. 1, pp. 119–125, 2012.

[17] J. Liu, Y. Cheng, X. Guo et al., "Design for a super-shallow large-section double-level tunnel in complex conditions underneath sensitive buildings," *Modern Tunnelling Technology*, vol. 51, no. 5, pp. 174–179, 2014.

[18] X. Hu and S. She, "Study of freezing scheme in freeze-sealing pipe roof method based on numerical simulation of temperature field," in *Proceedings of the International Conference on Pipeline and Trenchless Technology*, pp. 19–22, Wuhan, China, October 2012.

[19] X. Hu and T. Fang, "numerical simulation of temperature field at the active freeze period in tunnel construction using freeze-sealing pipe roof method," in *Proceedings of the Geo-Shanghai 2014*, pp. 731–741, Shanghai, China, May 2014.

[20] Y. Wang, "Mechanical property analysis of steel pipe-frozen soil composite structure in freeze-sealing pipe roof method," Master's Thesis, Tongji University, Shanghai, China, 2013.

[21] X. Hu, H. Ren, J. Chen et al., "Model test study of the active freezing scheme for the combined pipe-roof and freezing method," *Modern Tunneling Technology*, vol. 51, no. 5, pp. 92–98, 2014.

[22] X. Hu, X. Guo, Q. Wang et al., "Field test study on freezing technology of freeze-sealing pipe roof," *Tunnel Construction*, vol. 35, no. S2, pp. 1–7, 2015.

[23] H. Ren, X. Hu, J. Chen et al., "Study on freezing effect and operation of profiled enhancing freezing-tube in freeze-sealing pipe roof," *Tunnel Construction*, vol. 35, no. 11, pp. 1169–1175, 2015.

[24] X. Ji, B. Long, and X. Yang, "3D simulation analysis of closely jacking pipe in pipe curtaining pre-reinforcement," *Chinese Journal of Underground Space and Engineering*, vol. 12, no. S1, pp. 267–274, 2016.

[25] Y. Kang, Q. Liu, Y. Cheng et al., "Combined freeze-sealing and New Tubular Roof construction methods for seaside urban tunnel in soft ground," *Tunnelling and Underground Space Technology*, vol. 58, pp. 1–10, 2016.

[26] Y. Lu, H. Zhang, L. Wei et al., "Numerical simulation of temperature field in freezing process with pipe roof freezing method," *Railway Engineering*, vol. 57, no. 12, pp. 52–54, 2017.

[27] J. Zhang, P. Shi, and J. Pan, "Study of ground frost heave control technology used in Gongbei tunnel constructed by pipe roof and ground freezing method," *Tunnel Construction*, vol. 38, no. 5, pp. 809–817, 2018.

[28] H. Ren, X. Hu, Z. Hong et al., "Experimental study on active freezing scheme of freeze-sealing pipe roof used in ultra-shallow buried tunnels," *Chinese Journal of Geotechnical Engineering*, vol. 41, no. 2, pp. 320–328, 2019.

[29] W. Long, C. Rong, Y. Duan et al., "Numerical calculation of temperature field of freeze-sealing pipe roof method in Gongbei tunnel," *Coal Geology & Exploration*, vol. 48, no. 3, pp. 160–168, 2020.

[30] K. Guo, Y. Duan, and Y. Ding, "Numerical simulation of temperature field of tube–curtain freezing method for shallow buried tunnel," *Journal of Anhui University of Science and Technology*, vol. 39, no. 2, pp. 63–68, 2019.

[31] G. X. Cui and Q. G. Lu, "Study on law of thickness and deformation of ice-wall by using models," *Journal of China Coal Society*, vol. 17, pp. 37–47, 1992.

[32] H. Cheng, Z. Yao, J. Zhang et al., "A model test study on the effect of freeze heaving and thaw subsidence for tunnel construction with artificial horizontal ground freezing," *China Civil Engineering Journal*, vol. 40, no. 10, pp. 80–85, 2007.

[33] R. N. Taylor, "Geotechnical centrifuge technology," *Blackie Academic & Professional*pp. 273–280, CRC Press, London, UK, 1st edition, 1994.

[34] H. Cai, H. Cheng, Z. Yao et al., "Numerical analysis of ground displacement due to orthotropic frost heave of frozen soil in freezing period of tunnel," *Chinese Journal of Rock Mechanics and Engineering*, vol. 34, pp. 1667–1676, 2015.

[35] Y. Lai, S. Liu, Z. Wu et al., "Approximate analytical solution for temperature fields in cold regions circular tunnels," *Cold Regions Science and Technology*, vol. 34, pp. 43–49, 2002.

[36] X.-D. Hu, T. Fang, and Y.-G. Han, "Mathematical solution of steady-state temperature field of circular frozen wall by single-circle-piped freezing," *Cold Regions Science and Technology*, vol. 148, pp. 96–103, 2018.

[37] COMSOL Multiphysics Reference Manual, COMSOL AB, Stockholm, Sweden, 2018, http://cn.comsol.com/.

Research Article

Effects of Different Construction Sequences on Ground Surface Settlement and Displacement of Single Long Pile due to Twin Paralleled Shield Tunneling

Kan Huang,[1,2] **Yiwei Sun** ⓘ**,**[1] **Xianqiang Huang** ⓘ**,**[1] **Yujian Li** ⓘ**,**[1] **Meng Jiang,**[1] **and Runing Liu** ⓘ[1]

[1]*School of Civil Engineering, Changsha University of Science and Technology, Changsha 410114, China*
[2]*School of Civil Engineering, Changsha University, Changsha 410022, China*

Correspondence should be addressed to Yiwei Sun; yiweisun@sina.cn and Xianqiang Huang; huangxianqiang99@163.com

Shield tunneling activities inevitably pass through pile foundations at close distance in densely urban areas. Various studies have investigated the interaction between newly constructed tunnels and existing pile foundations. However, the influence of different construction sequences of twin paralleled shield tunneling on single long pile is seldom considered. A case was found in the project of Changsha Metro Line 5, where the twin paralleled tunnels were constructed near the Wanjiali Viaduct piles. A three-dimensional finite element model was established to analyze the pier settlement, ground surface settlement trough, and the vertical and horizontal displacement of pile under different construction sequences in layered soil. The results show that the adjacent pile and surrounding environment are affected substantially with the change of construction sequence of twin paralleled tunnels. The construction sequence of condition (b), in which the tunnel closer to the pile foundation is first constructed and then the tunnel farther away from the pile foundation is second constructed, can reduce the settlement of pier by 13.1%, the maximum surface settlement by 7.0%, the maximum vertical displacement of pile foundation by 7.9%, and the maximum horizontal displacement by 6.9%. The present findings can provide reference for similar projects.

1. Introduction

With the increasing congestion of surface traffic, exploiting the potential and promoting the benefits of the subsurface in cities have become an indispensable approach. Shield tunneling has a lot of advantages such as its high degree automation, easy management, no climate influence, one-time hole formation, and fast construction speed, which makes a rapid development of a new layer of supplemental infrastructure possible, allowing us new combinations that serve the modern needs of the city [1–3]. Meanwhile, a growing demand on housing, viaduct, infrastructure, and open space is competing for the urban surface areas, but also the subsurface, which makes shield tunneling often needs to pass through lots of pile foundations. However, even the most advanced shield technology will inevitably redistribute the initial stress of surrounding soil, causing surface subsidence,

inclination, and discontinuous deformation, which may affect adjacent pile foundations [4–8].

In order to understand the pile-soil-tunnel interaction mechanism, many scholars have conducted centrifuge model tests and field measurement analysis [9–13]. Franza and Marshall [11] presented outcomes from 24 geotechnical centrifuge tests and investigated the global tunnel-piled frame interaction scenario by using a newly developed real-time hybrid testing technique. The results illustrated that pile settlement and failure mechanisms are highly dependent on the load redistribution that occurs between piles during tunnel volume loss, which are related to structure weight and stiffness. Wang et al. [14] studied the construction schemes and influence of shield tunneling on reinforcing and rebuilding bridges in the case of shield tunnel of Hangzhou Metro 2 crossing through Fengqi Bridge. Sirivachiraporn and Phienwej [15] analyzed the field measurement data of

the first Bangkok subway project to evaluate the ground movement characteristics and responses of adjacent buildings. The results indicate that buildings on long piles showed the least induced settlements. But for buildings on short piles, the settlements depend on the distance from tunnel center line and pile tip depth. In addition, the interaction between shield tunnel and adjacent pile foundation has also been studied by proposing theoretical analytical solutions and numerical simulation by some scholars [16–25]. Franza et al. [16] presented an elastic study of tunnel-pile-structure interaction through Winkler-Based Two-Stage Analysis Methods. The results illustrated how pile foundations increase the risk of structural damage compared to shallow foundations, whereas structural stiffness can reduce building deformations. Zhang et al. [17] proposed a simplified solution based on Pasternak's foundation model to predict the lateral displacements of a single pile and group piles induced by shield tunneling considering the effects of lateral soil displacements. Lee [19] studied the effects of tunneling in weak weathered rock on the behavior of a preexisting single pile by performing three-dimensional elastoplastic numerical analyses. The results showed that the reduction of the apparent allowable pile capacity due to tunneling-induced pile head settlement is significant. Huang et al. [24] analyzed the displacement process of pile vertical, horizontal and along the tunnel based on the theory of fluid-soil coupling. As a summary, the above scholars all conducted that shield tunneling adjacent to existing pile foundations will cause pile settlement, lateral displacement of pile, additional axial load on piles, and induced bending moments along piles, which is mainly dependent on the distance between piles and tunnels, the ratio of pile length to tunnel depth, and the stratum loss.

Although a lot of studies have been carried out to investigate the effects of tunneling on existing piles, the excavation of only one tunnel is often considered. The underground transportation system often involves twin paralleled tunnels, which are sometimes inevitably constructed adjacent to existing pile foundations. Different construction sequences of twin paralleled shield tunnels will certainly make some differences in ground surface settlement and displacement of pile foundation. However, it is difficult to accurately consider the influence of different construction sequences by using theoretical analysis method, especially the blocking effect of tunnel constructed first. At present, few scholars study the effects of different construction sequences by performing numerical calculation method to systematically analyze the influence on adjacent pile foundations.

In view of the aforementioned issues, it is of great significance to study the effects of different construction sequences on ground surface settlement and displacement of single pile due to twin paralleled shield tunneling.

The outline of this paper is as follows: Firstly, the disturbance zone of stratum perpendicular to the direction of shield tunneling is explained, and the mechanism of shield tunneling on adjacent single pile foundation is further discussed. Secondly, the project overview and site geology of Changsha Metro Line 5 (from South Gaoqiao Station to Guitang Station) are presented as engineering background.

Thirdly, a three-dimensional finite element numerical calculation model is established. The constitutive model, calculation parameters, and construction simulation procedure of the numerical model are described in detail. Fourthly, combined with field measured data, the changing trend of bridge pier settlement and the results of ground surface settlement and displacement of pile foundation caused by shield tunneling under different construction sequences are analyzed. Finally, through the comparative analysis of the data, the most appropriate construction sequence of the twin paralleled shield tunnels passing through the pile foundation is proposed, which provides reference for similar projects.

2. Mechanism of Shield Tunneling on the Adjacent Single Long Pile

Shield tunneling inevitably causes stratum loss, and the stratum in disturbed zone will produce uneven settlement in the process of stress redistribution, which causes the wedge-caulking of soil particles. If the overburden layer of the tunnel is thick enough, the arching effect will occur in the stratum in a certain range above the tunnel. As shown in Figure 1, the strata perpendicular to the direction of shield tunneling can be divided into three zones according to the different degree of stratum disturbance caused by shield tunneling passing through pile foundation. Zone I (strong disturbance zone): the zone between shield tunnel vault, rupture surface, and collapse arch, where the strata appear plastic flow and collapse will occur if there is no support; Zone II (medium disturbance zone): a certain range of zone outside the rupture surface, where the strata have elastic deformation or increased stress, which belongs to the elastic zone; Zone III (weak disturbance zone): the zone is less affected by shield tunneling. When the thickness of overburden layer of shield tunnel is small or the tunnel section is large, the scope of Zone I and Zone II disturbed by shield tunneling will expand, even extend to the ground surface. In addition, when the distance between the two lines of the shield tunnel is relatively close, the disturbance effect of the two lines will show superposition effect, and the disturbed zone will be connected.

Pile foundations are used to support the load of superstructure by transferring it to the surrounding soil resulting in the stress concentration near the pile. On the contrary, shield tunneling is a process of releasing stress which results in the ground movements. After shield tunneling, one side of the pile is unloaded, which affects the mechanical performance of the pile.

The influence of shield tunneling on displacement of adjacent pile foundation is mainly reflected in the effect of soil displacement caused by shield tunneling. The object of this study is single long pile, such as urban viaduct pile. As the pile toe of urban viaduct is deep, it is usually lower than the shield tunnel. Therefore, shield tunneling have less effect on the bearing capacity of pile toe. The main factors influencing the pile foundations are as follows:

(1) The stratum loss caused by shield tunneling
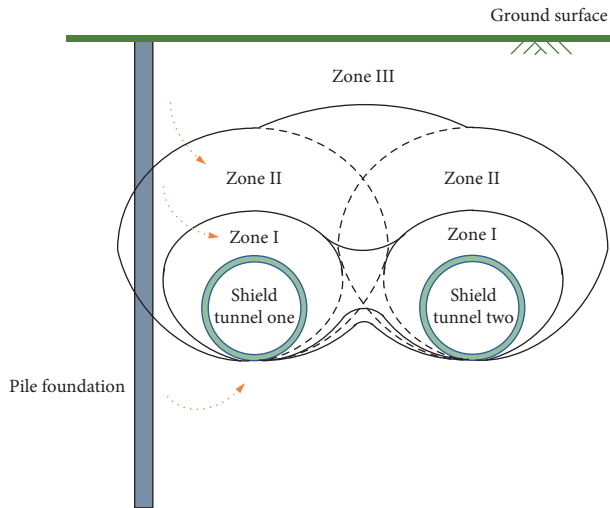
FIGURE 1: Stratum disturbance zone caused by shield tunneling (perpendicular to the direction of shield tunneling).

(2) The lateral displacement of pile caused by the lateral displacement of soil

(3) The negative friction caused by the settlement of soil around the pile will further lead to additional settlement of the pile

3. Engineering Background

3.1. Project Overview. Changsha Metro Line 5 is the north-south backbone line in Changsha, Hunan Province, China. The first phase of Changsha Metro Line 5 successively crosses the Guitang River, Changsha Metro Line 4, and passes through the Wanjiali Viaduct, gas stations, houses, and other major risk sources in close range. Among them, Changsha Metro Line 5 and Wanjiali Viaduct parallel up to 16.7 kilometers. As shown in Figure 2, the most representative tunnels between South Gaoqiao Station and Guitang Station were selected as the engineering background. The interval tunnels are located on the east side of Wanjiali Viaduct. Under the influence of the existing river and the Guitang River Bridge, the layout of the piles of Wanjiali Viaduct has changed when crossing the Guitang River. Comparison of site viaduct pile layout is shown in Figure 3. This makes the shortest distance between the left tunnel and two C35 bored concrete piles with a diameter of 1.2 m only 3.07 meters. The code for this pier is Pm334, and the pile length is 50 m. The twin paralleled tunnels made of C50 precast concrete segments, with an inner diameter of 5.4 m and buried depth of 19.2 m, having a lining thickness of 0.3 m, width of 1.5 m, are excavated using Earth pressure balance shield tunnel boring machine. The distance between the left line and the right line is 6.15 m.

According to the requirements of construction organization and arrangement, two shield machines are configured in this interval. The two shield tunneling machines started from the south end of South Gaoqiao Station in a staggered month and reached Guitang Station in the direction of small mileage of the line. In the actual construction of this project,

the construction sequence of this project is to excavate the right tunnel which is farther from the piles and then the left tunnel which is closer to the piles. The construction sequence has not been analyzed in detail before. The finite element modeling area is located near the design mileage between ZDK27 + 352.322 and ZDK27 + 397.322. The monitoring layout of viaduct pier settlement is shown in Figure 4. Precision level, theodolite, indium steel gauge, inclinometer, and other equipment are used to measure the settlement of bridge piers and the ground surface settlement trough. Two measuring points are arranged symmetrically on each pier. The monitoring period is once a day.

3.2. Site Condition. There are 5 layers of soil from the ground surface to the depth of 70 m, which are miscellaneous fill, silty clay, pebble, strongly weathered conglomerate, and moderately weathered conglomerate in sequence. The ground water table is located at 11.4 m above the top of the twin paralleled tunnels. In addition, the bedrock of the site can be divided into two zones of high weathering and moderate weathering within the scope of investigation depth. According to previous geological drilling report, the highly weathered conglomerate is grayish white with purplish red, partly with thin layers of argillaceous siltstone, clastic structure and massive structure. The natural compressive strength is from 1.19 to 1.96 MPa, and the average value is 1.59 MPa. The moderately weathered conglomerate is purplish red with clastic structure, thick laminated structure, mainly argillaceous cementation. The natural compressive strength ranges from 6.15 to 18.67 MPa, with an average of 10.57 MPa.

As shown in Figure 5, the pile bearing layer of Wanjiali Viaduct is moderately weathered conglomerate, and the twin paralleled tunnels are located in the strongly weathered conglomerate. Physical and mechanical parameters of surrounded layers are listed in Table 1.

4. Numerical Calculation

4.1. Three-Dimensional Finite Element Model. To understand ground surface settlement and displacement of single long pile due to twin paralleled shield tunneling with different construction sequences in layered soils, Midas GTS NX was employed to conduct a three-dimensional finite element model, including twin paralleled shield tunnels, viaduct piles, segments, grouting and surrounding soils. As shown in Figure 6, based on the actual project, two different tunnel construction sequences were considered in this study. Among them, condition (a) is consistent with the actual construction sequence, that is, the right line which is farther away from the pile foundation is excavated first, and then the left line which is closer to the pile foundation is excavated. Condition (b) is opposite to condition (a), that is, the left line which is closer to the pile foundation is excavated first, and then the right line which is farther away from the pile foundation is excavated.

Considering the influence of boundary effects on the accuracy of the numerical results, the size of the three-dimensional model was determined as 60 m in length, 50 m in width, and 70 m in height. The soil was treated as the

FIGURE 2: The location of the interval tunnel.

| (a) | (b) |

FIGURE 3: Comparison of site viaduct pile layout. (a) Normal. (b) Across the river.

horizontal layered foundation to simplify the calculation. A perspective view of the finite element model is shown in Figure 7. Segments were simulated as plate elements, while the soil mass, piles, and grouting were simulated using tetrahedral and hexahedral hybrid elements. The density of elements in critical areas, such as twin paralleled tunnels and pile foundations, was increased to improve the calculation accuracy. The mesh applied in this model consisted of 247322 elements and 155046 nodes.

4.2. Constitutive Model and Calculation Parameters. It is well recognized that in order to properly capture the ground surface settlement and displacement of adjacent piles

induced by unloading, it is of great significance to take into account the effect of soil unloading caused by shield tunneling in the constitutive model. The modified Mohr–Coulomb constitutive is an elastoplastic constitutive, which is closer to plasticity theory than Mohr–Coulomb constitutive, and is a constitutive model combining nonlinear elasticity and plasticity. It can consider the different elastic modulus values according to the loading and unloading conditions. The modified Mohr–Coulomb constitutive can also consider the relationship between the soil stiffness and the stress state. Meanwhile, the modified Mohr–Coulomb constitutive can simulate the behavior of different types of soil including soft and hard soil, taking the dilatancy of soil into account. The comparison of the
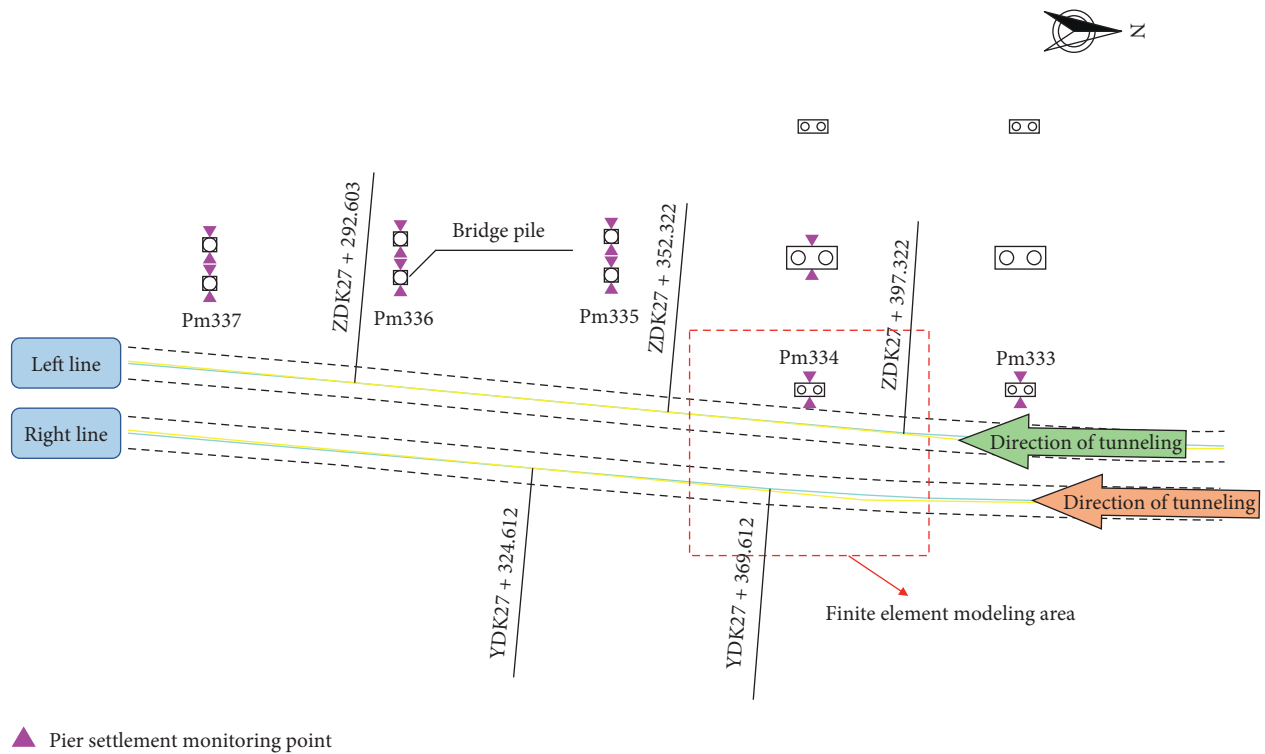
Figure 4: The monitoring layout of viaduct pier settlement.
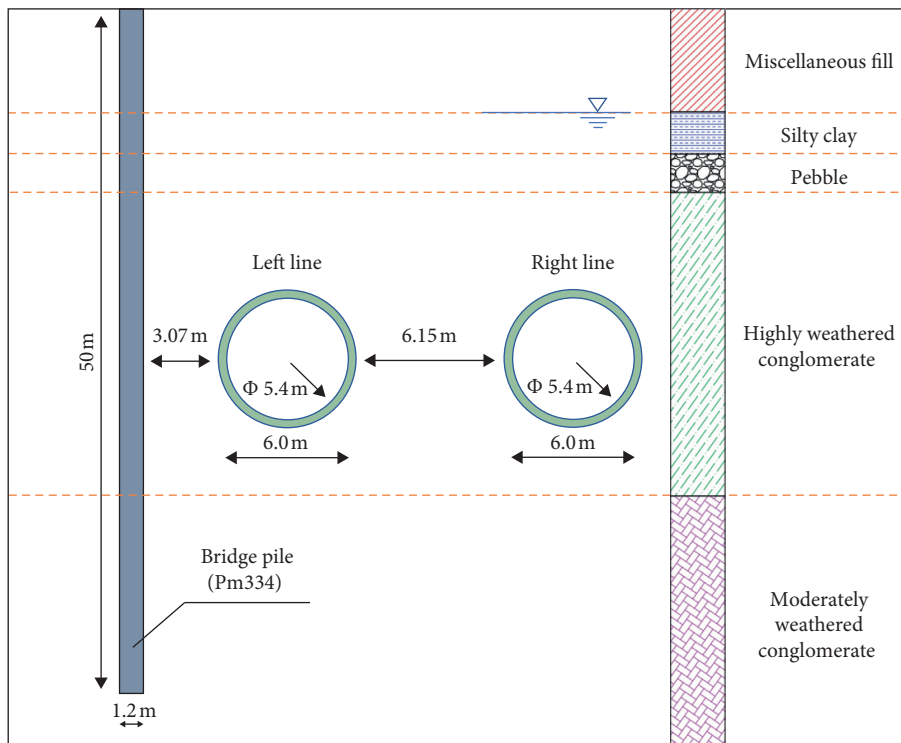
Figure 5: Engineering geology profile.

Mohr–Coulomb yield criterion and the modified Mohr–Coulomb yield criterion in the π plane is shown in Figure 8. The modified Mohr–Coulomb yield criterion adopts the rounded corner treatment in π plane, which can eliminate the unstable factors in the analysis process. Therefore, the modified Mohr–Coulomb constitutive model

TABLE 1: Physical mechanical parameters of surrounded layers.

Soil type at each layer	Thickness H (m)	Elasticity modulus E (MPa)	Poisson's ratio μ	Unit weight γ (kN·m^{-3})	Cohesion c (kPa)	Internal friction angle φ (°)	Permeability coefficient k (m·d^{-1})
① Miscellaneous fill	7.8	8.5	0.35	19.0	10	12	0.700
② Silty clay	3.2	15.5	0.30	20.0	30	16	0.008
③ Pebble	2.9	35.0	0.25	20.0	2	36	25.000
④ Highly weathered conglomerate	23.0	38.5	0.27	23.5	40	30	0.500
⑤ Moderately weathered conglomerate	33.1	47.0	0.24	25.0	120	35	0.100
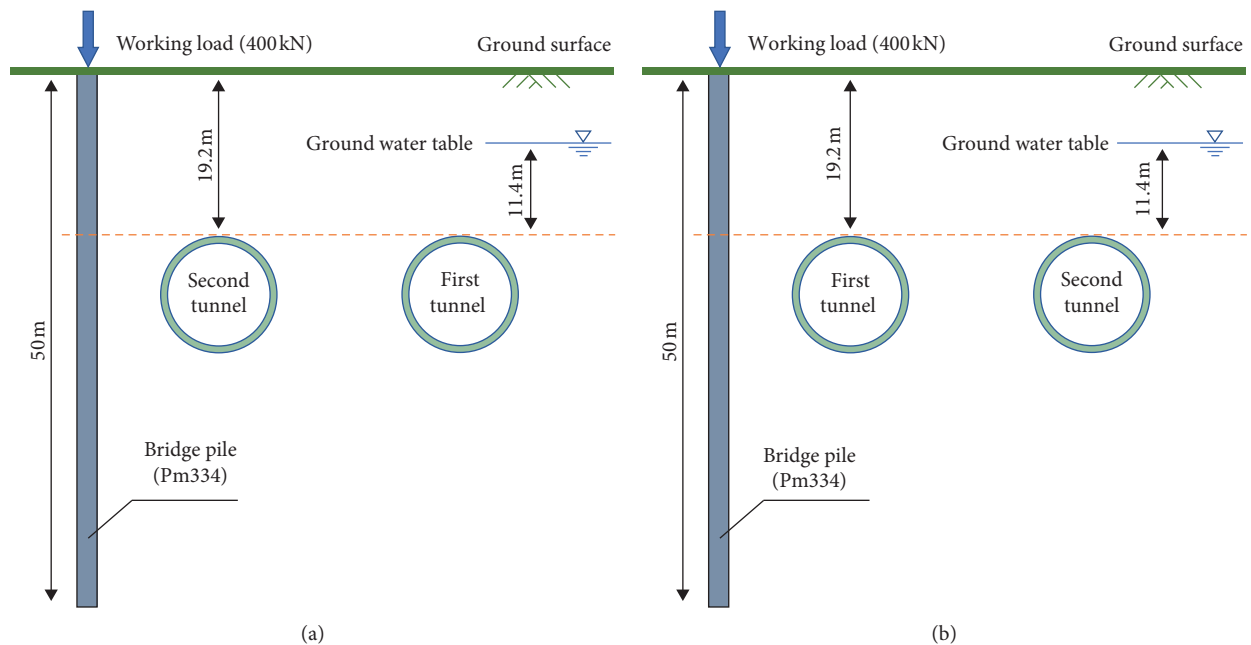
FIGURE 6: Different tunnel construction sequences. (a) Condition (a). (b) Condition (b).

of soil was selected from the constitutive model library of Midas GTS NX, which has better simulation results and computational convergence.

In addition, the calibration of soil parameters is an important factor to ensure the reliability of finite element calculation results. The calculation parameters of surrounded layers after calibration are shown in Table 2.

Shield segments, pile foundations, and grouting were simplified with elastic materials. The shield segments were treated as homogeneous rings, made of C50 concrete, and the pile foundations were made of C35 concrete. It is assumed that perfect bond between the pile and soil is maintained, and no detachment occurs. The material parameters of bridge pile, segment, and grouting are shown in Table 3.

4.3. Numerical Simulation Procedure. Excavation construction stages were simulated step by step; each excavation stage forwards 1.5 m. The excavation construction was realized by the method of "element birth and death." According to the section size of the viaduct pile and the arrangement of the upper lane, the uniform distribution load on the single pile is set as 400 kN. Generally, when the shield passes through an important structure in a close distance, the thrust force in front of the shield machine and the grouting pressure will be controlled. Therefore, the thrust force of the shield machine is set as 8000 kN and the grouting pressure is set as 0.6 MPa in this study. The concrete numerical analysis is executed according to the following steps:

(1) Activate all the soil mass, including the tunnel excavation area and the soil at the grouting layer. Set the displacement boundary, stable ground water table, and gravity acceleration. Then, balance the initial stress field by displacement clearance.

(2) Activate the pile attribute, apply the superstructure load of 400 kN on the pile head, and reset the displacements to 0.

(a)

(b)
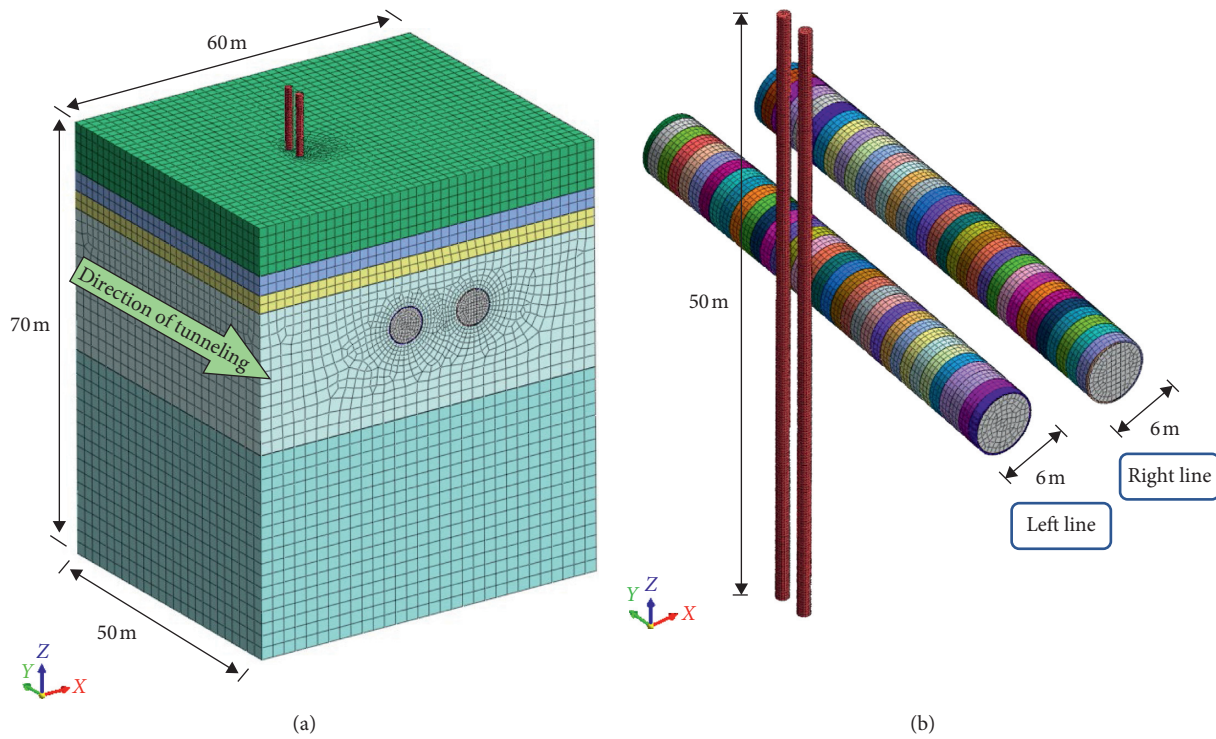
FIGURE 7: Three-dimensional finite element model. (a) Global model. (b) Relationship between the pile and tunnel.
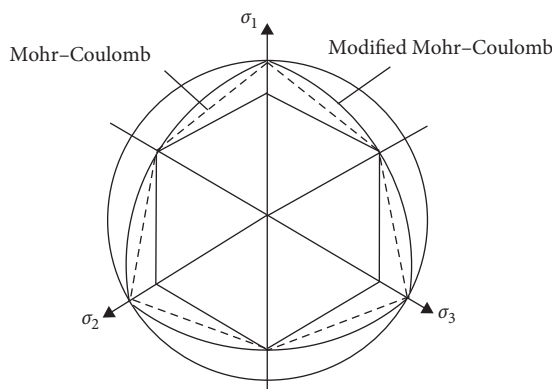
FIGURE 8: The modified Mohr–Coulomb yield criterion in the π plane.

TABLE 2: Parameters of soil surrounded layers after calibration.

Soil type	E_{50}^{ref} (MPa)	$E_{\mathrm{oed}}^{\mathrm{ref}}$ (MPa)	$E_{\mathrm{ur}}^{\mathrm{ref}}$ (MPa)
Miscellaneous fill	6.4	5.3	19.8
Silty clay	10.8	9.0	34.6
Pebble	23.8	19.0	78.5
Highly weathered conglomerate	28.5	24.9	115.5
Moderately weathered conglomerate	35.6	34.0	134.5

E_{50}^{ref} is the secant stiffness in standard drainage triaxial tests, $E_{\mathrm{oed}}^{\mathrm{ref}}$ is the tangent stiffness in loading of main consolidation instrument, and $E_{\mathrm{ur}}^{\mathrm{ref}}$ is the elastic modulus of reloading after elastic unloading. The above parameters are derived from the laboratory test of the preliminary geological survey.

(3) Taking the right line as an example, the thrust force of 8000 kN on the face of the first ring of the right tunnel is firstly applied to deactivate the soil and the grouting layer in the first ring.

(4) Continue to apply the thrust force on the face of the second ring of the right tunnel to deactivate the soil and the grouting layer in the second ring. After this step, the grouting layer, grouting attribute, and shield segment of the first ring are reactivated, and the grouting pressure is set at 0.6 MPa.

(5) Repeat the above steps (3) and (4) successively until the first shield tunnel is completely finished. Then, the second shield tunnel will be constructed.

5. Analysis of Numerical Calculation Results

5.1. Induced Pier Settlement during Twin Paralleled Shield Tunneling with Different Construction Sequences. During the construction simulation, there are 73 steps in total. Each tunnel has 35 construction steps. The settlement of viaduct pier Pm334 caused by twin paralleled shield tunnels in different construction sequences is compared with the field measured data, as shown in Figure 9. Taking the position where the shield machine enters the boundary of the model as the reference point, the changing process of the field measured settlement of pier Pm334 was recorded when the shield passed through the pile for the first time. The field measured settlement of the pier when the shield left the boundary of the model was also recorded. Compared with the field measured settlement of the bridge pier when the

TABLE 3: Parameters of pile, segment, and grouting material.

Materials	Elasticity modulus (MPa)	Poisson's ratio	Density (kN·m^{-3})
Pile foundation	3.15×10^4	0.3	23.0
Shield segment	2.415×10^4	0.2	25.0
Grouting	2×10^2	0.3	22.0
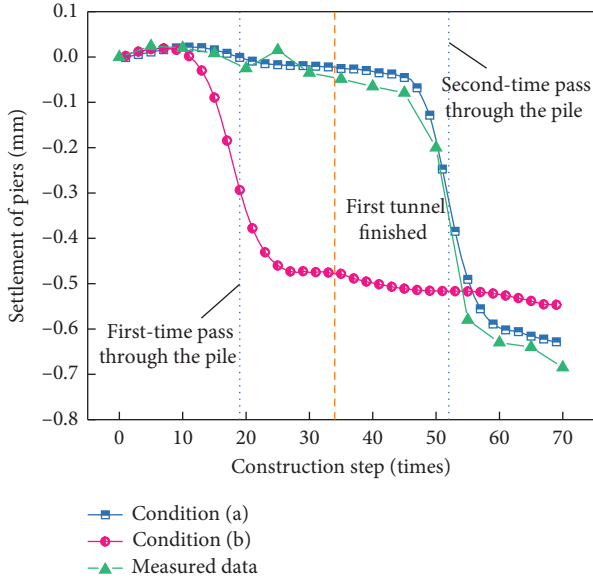
FIGURE 9: The settlement of viaduct pier Pm334.

shield machine reached the boundary of the model for the second time, the bridge pier settlement of non-shield construction factors was removed so as to ensure the monitoring data is comparable and reliable. Condition (a) is consistent with the sequence of site construction. To facilitate the comparison between the finite element calculation results and the field measured data, the horizontal axis adopts construction steps, and each construction step represents a drive forward by 1.5 m of the shield. The measured data take the average value of the monitoring points of the settlement of the piers at the corresponding positions of the shield tunneling. It can be seen from Figure 9 that the numerical calculation results are in good agreement with the field measured data. It can be concluded that no matter what construction sequence is adopted, the settlement of the pier begins to increase significantly when the shield reaches the 8th ring (12 m) before the pile foundation. After the shield passes through the pile foundation, the settlement of the pier gradually tends to be stable at the position of the 10th ring (15 m) after the pile foundation. It is mainly caused by the thrust force in front of the shield machine, the protective effect of the shield shell, and the displacement of the soil after shield tunneling. At the same time, different shield construction sequence will have a certain influence on the final settlement of adjacent piers. After the completion of twin paralleled tunnel construction, the final settlement of bridge pier is −0.628 mm in condition (a) and −0.546 mm in condition (b). In the comparison of pier final settlement, condition (b) is 13.1% less than condition (a). The reason for that is as follows: in condition (a), the construction of the

right line which is far from the pile foundation will squeeze the soil near the pile foundation and disturb the stratum in the first construction process. Although the influence of the right tunnel on the pile foundation is relatively limited at this time, in the next construction process of the left tunnel, the strata disturbance in the early stage will aggravate the soil displacement and then cause greater settlement of the adjacent piers. However, in condition (b), first, the construction of the left line which is closer to the pile foundation will make the settlement of viaduct pier stable after the increase. Meanwhile, in the horizontal direction to the right tunnel, due to the blocking effect of the existing left tunnel and segment grouting reinforcement during the construction of the left tunnel, part of the soil displacement will be controlled, thus reducing the settlement of adjacent pile foundation. Therefore, excavating the left tunnel near the pile foundation first and then the right tunnel far away from the pile foundation is the most beneficial construction sequence to control the settlement of adjacent piers without setting protective isolation.

5.2. Induced Ground Surface Settlement during Twin Paralleled Shield Tunneling with Different Construction Sequences. In 1969, at the 7th International Conference on Soil Mechanics and Foundation Engineering, Peck [25] proposed that the surface settlement trough caused by tunneling presented a normal distribution in the lateral area, in which the width of settlement trough i and the stratum loss V_s were two important parameters in the Peck formula. However, Peck's formula does not consider stratum characteristics and construction factors. Clough and Schmidt [26], Attewell and Woodman [27], O'Reilly and New [28], Loganathan and Poulos [29] proposed different calculation methods for the value of i. After analyzing a large number of surface settlement data and engineering data after tunnel excavation, Peck [25] believed that the volume of settlement trough should be equal to the volume of stratum loss, and the surface settlement trough presented normal distribution in the lateral direction. Gaussian distribution of surface settlement trough is defined as

$$S(x) = S_{\max} \cdot e^{-\left(x^2/2i^2\right)},$$

$$S_{\max} = \frac{V_s}{\sqrt{2\pi} \cdot i}, \tag{1}$$

$$i = \frac{Z_0}{\sqrt{2\pi} \tan\left(45° - (\varphi/2)\right)},$$

where $S(x)$ is the ground surface settlement caused by stratum loss, V_s is the stratum loss per unit length caused by shield tunneling, x is the distance from the tunnel centerline,

$S_{\max}$ is the maximum ground surface settlement caused by stratum loss, i is the distance from the tunnel centerline to the inflexion point of the settlement trough, Z_0 is the buried depth of tunnel, and φ is the internal friction angle of soil.

To predict the ground surface settlement above twin paralleled tunnels, Attewell and Farmer [30] suggested summing the Gaussian curves induced by two tunnels. In this study, the results of finite element numerical calculation in different construction sequences are compared with the results of Gaussian distribution curve at the position of pile foundation, as shown in Figure 10. As can be seen from Figure 10, influenced by the existing pile foundation, the ground surface settlement trough will stay a certain value near the pile foundation. It can be seen from the curve that the surface settlement trough will present a "hanging phenomenon" near the location of pile foundation. Under the same parameter condition, the maximum value of Gaussian distribution curve is obviously larger than that of finite element calculation. The main reason for the above phenomenon is that the stiffness of pile foundation affects the displacement of soil around the tunnel. The soil will naturally deform to the side without pile foundation after excavation and unloading. Meanwhile, due to the existence of pile foundation, it will control the displacement of soil around the pile. Therefore, the surface settlement trough caused by shield tunneling under the influence of adjacent bridge piles will present an asymmetric skewed normal distribution, and the maximum value of surface settlement will decrease. In condition (a), after the completion of construction of the first tunnel, the maximum value appears in the centerline of the first tunnel. The maximum value calculated by finite element method is −3.524 mm, which is 17.2% less than that of the Gaussian distribution curve, which is −4.255 mm. After the completion of the second tunnel construction, the maximum value appears in the middle position of the twin paralleled tunnel, and the maximum value calculated by finite element method is −5.563 mm, which is reduced by 14.2% compared with the maximum value of −6.485 mm after the cumulative Gaussian distribution curve. In condition (b), after the first tunnel construction is completed, the maximum value calculated by finite element method appeared in the right side of the centerline of left tunnel with a maximum of 3.029 mm, which is reduced by 28.8% compared with the maximum of Gaussian distribution curve. After the completion of construction of the second tunnel, the maximum value of finite element calculation results of is 5.173 mm, which is 20.2% less than that of the Gaussian distribution curve. In view of this, the maximum value of ground surface settlement will be reduced to a certain extent in the process of shield tunneling passing through the viaduct pile at close distance. At the same time, the ground surface settlement trough will have an asymmetric skewed distribution.

In order to further study the influence of different construction sequences of twin paralleled shield tunnels on the ground surface settlement trough, the finite element calculation results of the ground surface settlement trough under different construction sequences are compared with the field measured data, as illustrated in Figure 11. As can be seen from Figure 11, compared with the Gaussian distribution curve, the calculation results of finite element can better reflect the actual situation. In condition (b), the maximum ground surface settlement after the completion of the first tunnel is reduced by 14.1% compared with that in condition (a). Similarly, the maximum value of the cumulative ground surface settlement after the completion of the second tunnel in condition (b) is reduced by 7.0% compared with that in condition (a). The reason causing this difference is that the left tunnel is closer to the adjacent pile foundation than the right tunnel. Due to the influence of the stiffness of the existing viaduct pile, the ground surface settlement trough caused by excavating the left line will be limited by the pile foundation firstly, which will reduce the maximum value. On the one hand, the soil displacement caused by the excavation of the right tunnel which is farther away from the pile foundation is obstructed by the existing left tunnel. On the other hand, due to segment grouting reinforcement during the construction of the left tunnel, the strata around the left tunnel were reinforced. Therefore, from the results of ground surface settlement, the construction sequence of condition (b) is more conducive to controlling ground surface settlement.

5.3. Induced Vertical and Horizontal Displacement of the Pile during Twin Paralleled Shield Tunneling with Different Construction Sequences. The unloading effect and the squeezing action of shield tunneling will cause a certain vertical and horizontal displacement of adjacent pile foundation. When the superstructure load continues to be applied on the deformed pile foundation, the pile foundation will be in an unfavorable state of eccentric compression, which impedes normal load transfer and causes damage to the superstructure. Therefore, induced vertical and horizontal displacement of pile during twin paralleled shield tunneling with different construction sequences should be discussed and analyzed as a significant research direction. Figures 12 to 15 show the vertical and horizontal displacement of pile foundation and tunnel under different construction sequences of twin paralleled shield tunnels. In order to more visually reflect the displacement, the displacement of pile foundation and tunnel shown in Figures 12 to 15 is exaggerated on the basis of actual displacement. It can be seen from the figures that no matter which tunnel construction sequence is adopted, the adjacent pile foundation will produce displacement. When the construction of twin paralleled tunnels is completed, the overall displacement of pile presents an S-shaped distribution. In terms of the vertical displacement, the pile head settles downward, and the pile toe is jacked. In terms of the horizontal displacement, the maximum displacement appears near the buried depth of tunnel, which is manifested as that the pile body which overlaps with the buried depth of the tunnel moves away from the tunnel, while the upper part of pile body and the lower part of pile body deform towards the tunnel. The reason is that with the continuous construction of tunnel, the soil above the top of tunnel settles. And the upper part of pile foundation, driven by the surrounding

(a)

(b)
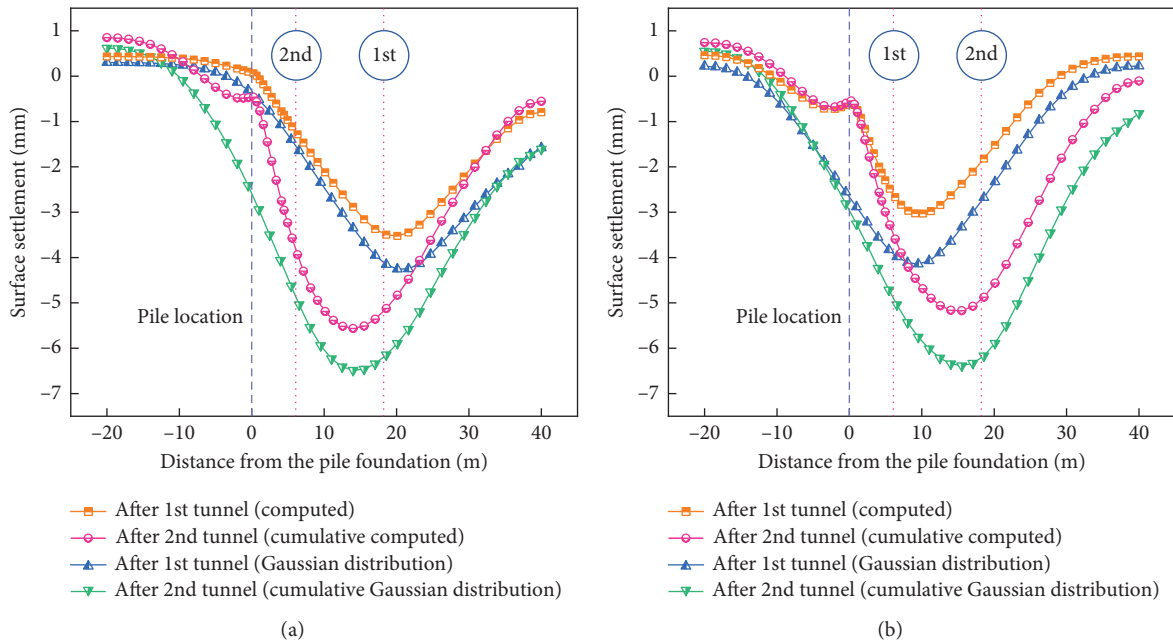
FIGURE 10: Ground surface settlement trough at pile location. (a) Condition (a). (b) Condition (b).
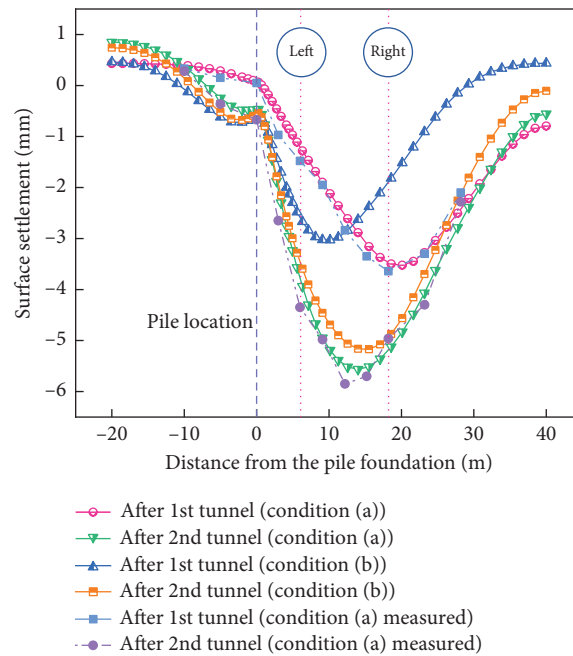
FIGURE 11: Comparison of calculation results and field measured data under different construction sequences.

soil, deforms downward and toward the direction near the tunnel. The soil below the tunnel bottom will rebound upward due to excavation and unloading, and the lower part of pile will deform upward and toward the direction near the tunnel driven by soil. Under the combination action of these forces, the pile will be bent.

Figure 16 illustrates the induced vertical and horizontal displacement of pile under different construction sequences. For each tunnel construction sequence, the vertical and horizontal displacement of pile due to the first tunnel and

the second tunnel and after twin paralleled tunneling which is cumulative are shown in Figures 16(a) and 16(b). In condition (a), after the completion of the first tunnel construction, the vertical displacement of the pile is small due to the long distance between the right tunnel and the pile foundation, and the maximum value appears at the pile toe, which is +0.166 mm. The maximum horizontal displacement of the pile appears at 3 m below the buried depth of the tunnel, which is −1.165 mm. It is different from the situation after the completion of the construction of the first tunnel in
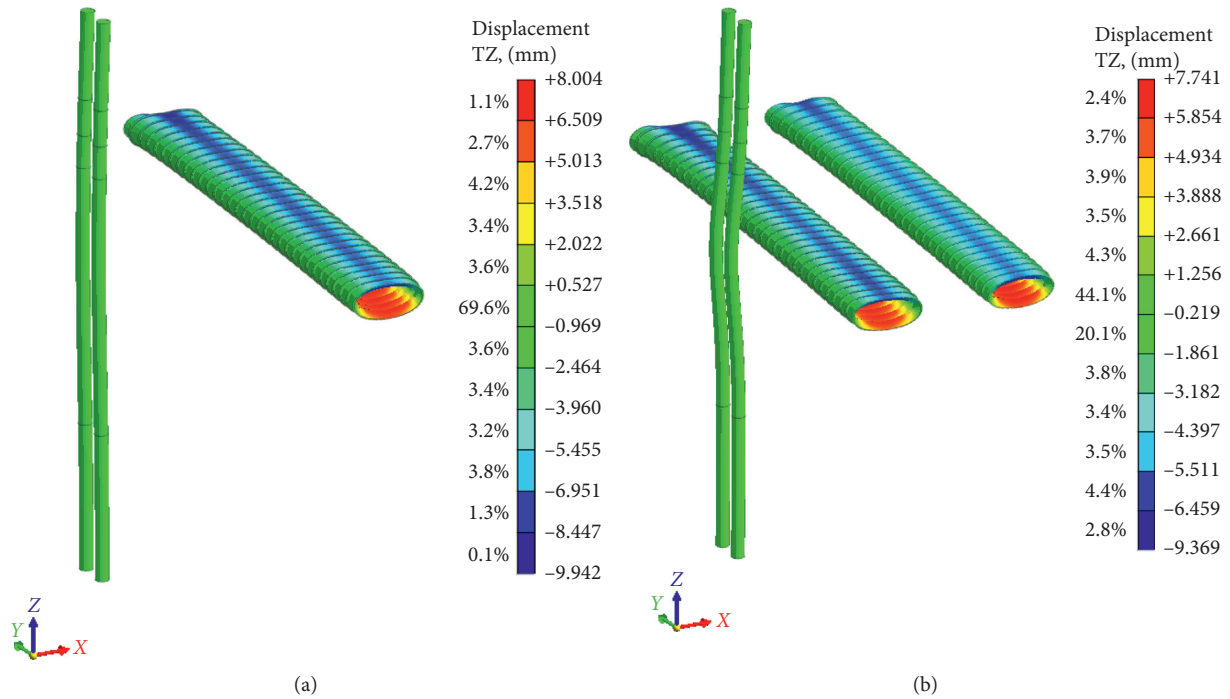
FIGURE 12: Vertical displacement of pile and tunnel in condition (a). (a) Right line finished. (b) Left line finished.
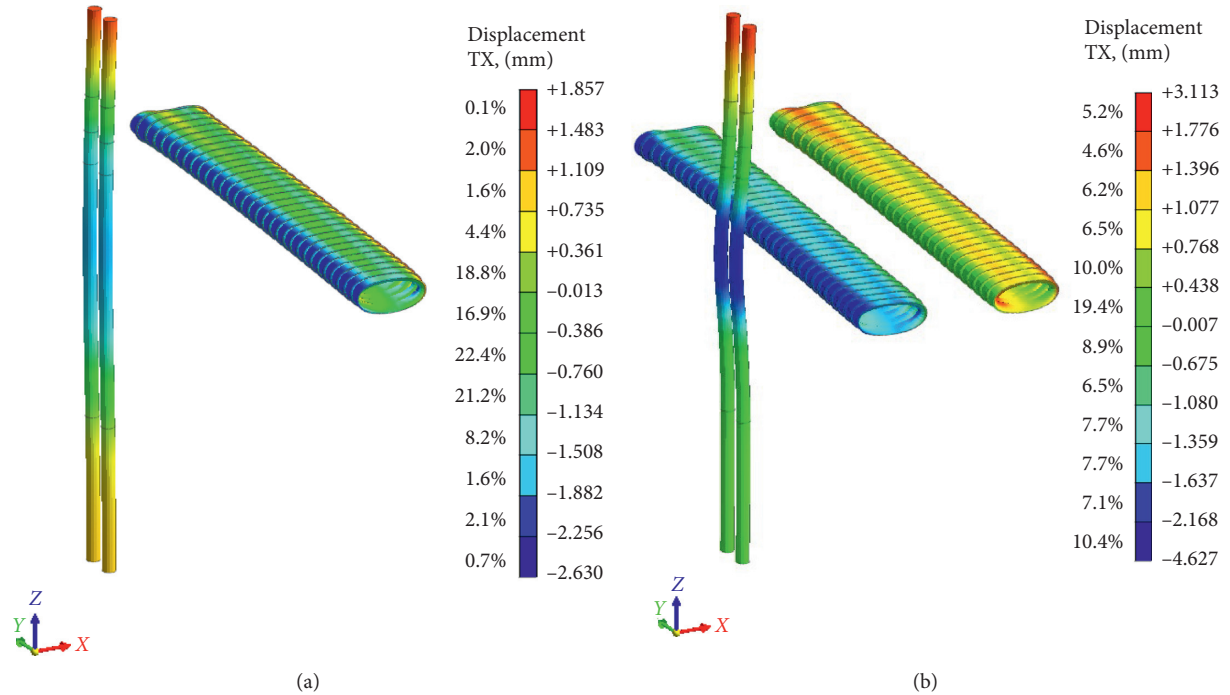
FIGURE 13: Horizontal displacement of pile and tunnel in condition (a). (a) Right line finished. (b) Left line finished.

condition (b). The maximum vertical displacement of the pile is +0.780 mm due to the close distance between the left tunnel and the pile foundation, and the maximum value still appears at the pile toe. The variation range of horizontal displacement curve of pile is more obvious than that in condition (a), and the maximum horizontal displacement of

the pile is −1.575 mm. When the construction of the twin paralleled tunnels is completed, the maximum vertical displacement of the pile in condition (a) is +1.037 mm, which is 7.9% larger than that in condition (b) of +0.955 mm. The maximum values all appear at the pile toe. Meanwhile, the maximum horizontal displacement of the
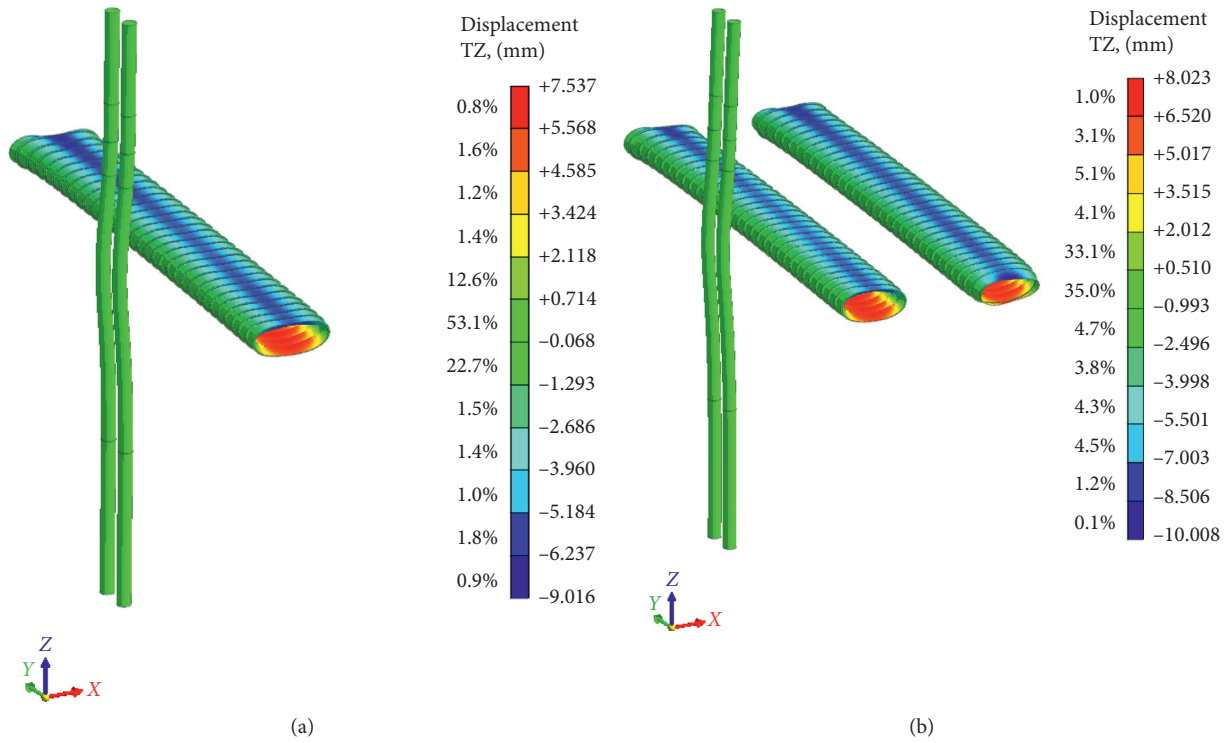
FIGURE 14: Vertical displacement of pile and tunnel in condition (b). (a) Left line finished. (b) Right line finished.
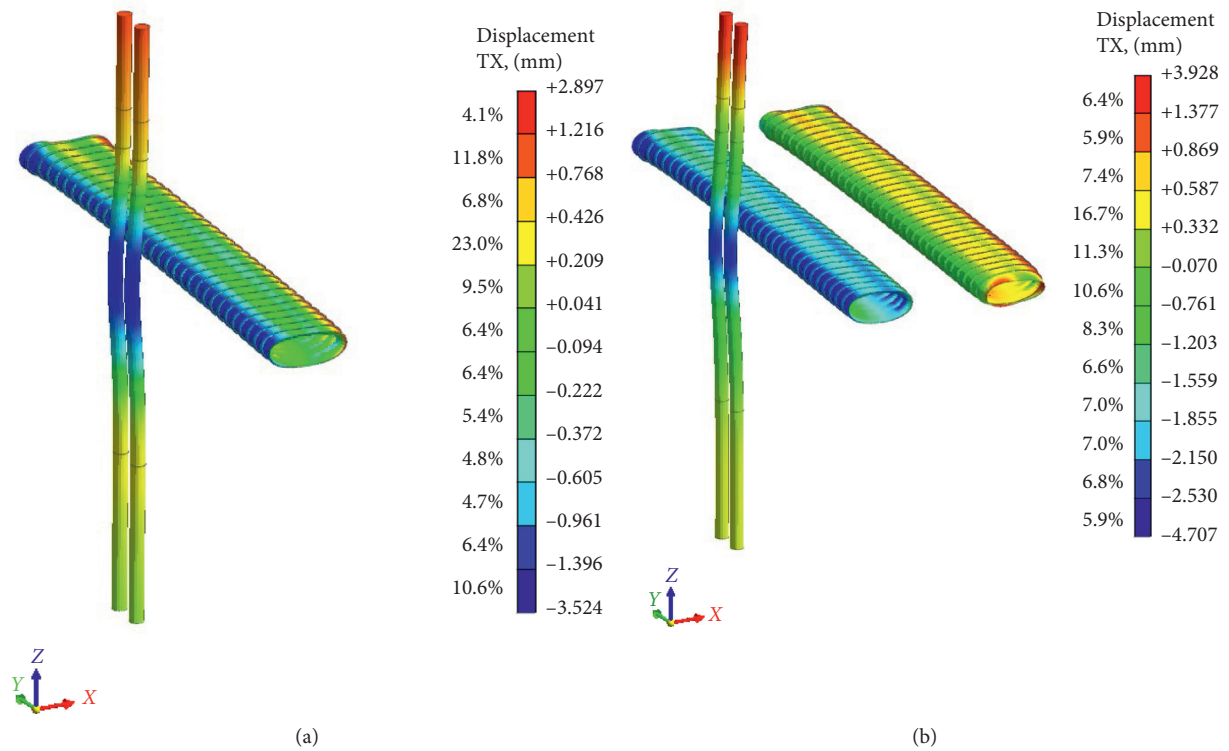
FIGURE 15: Horizontal displacement of pile and tunnel in condition (b). (a) Left line finished. (b) Right line finished.

pile in condition (a) is −2.526 mm, which is 6.9% larger than that in condition (b). The maximum values all appear at 3 m below the depth of the tunnel. Therefore, it can be concluded that the construction sequence of condition (b) can reduce the vertical and horizontal displacement of piles to a certain extent. In the future, we expect to carry
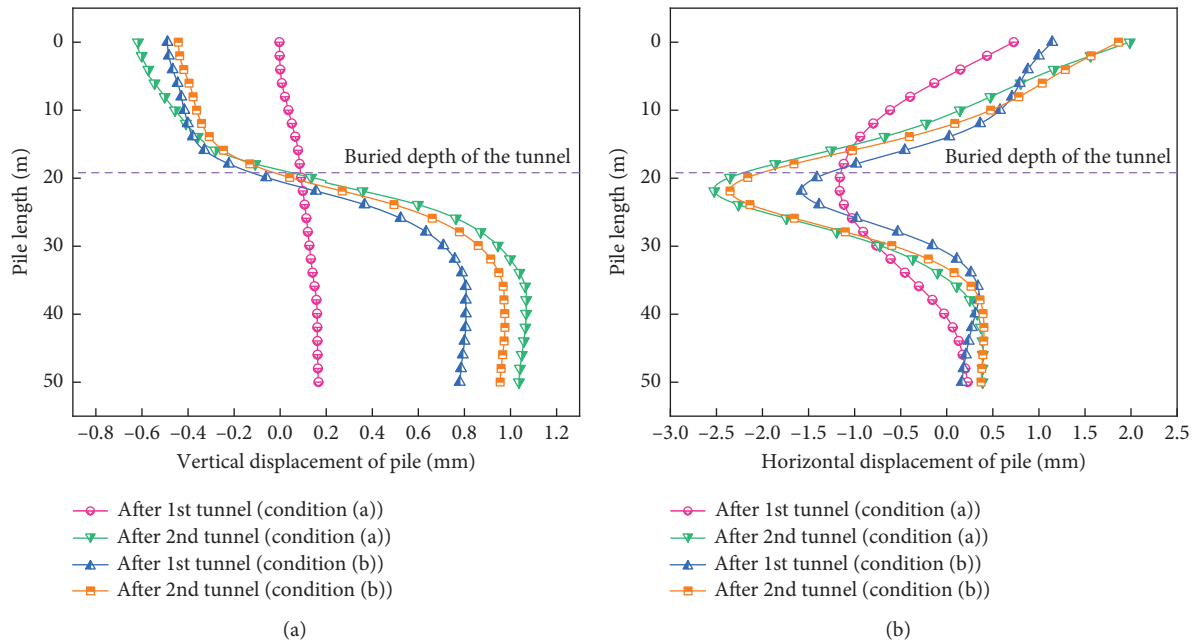
FIGURE 16: Displacement of pile foundation. (a) Vertical displacement. (b) Horizontal displacement.

out centrifuge model tests to further study this content. And we will actively strengthen the cooperation with the site construction company and the design department to jointly develop the most appropriate shield construction sequence to reduce the impact on the adjacent pile foundation.

6. Conclusions

This paper presents a three-dimensional finite element model to analyze ground surface settlement and displacement of single long pile due to twin paralleled shield tunneling with different construction sequences in layered soil. To accurately verify the calculation results, the monitoring data of piers settlement and measured ground surface settlement are compared with the numerical results. The main conclusions are as follows:

(1) The numerical results are in good agreement with the measured data. The computed results of induced pier settlement, ground surface settlement, and induced displacement of single pile due to twin paralleled shield tunnel reveal that the adjacent pile and surrounding environment are affected substantially with the change of construction sequence of twin paralleled tunnels. In comparison to the final pier settlement, condition (b) is 13.1% less than condition (a).

(2) Influenced by the existing viaduct pile, Gaussian distribution is no longer applicable to predict the displacement of ground surface settlement caused by shield tunneling. According to the comparison between the numerical results and the field measured data, the ground surface settlement trough will present a "hanging phenomenon" near the location

of pile. Meanwhile, when the tunnel is close to the pile foundation, the surface settlement trough will develop into an asymmetric skewed distribution. The construction sequence of condition (b) is more conducive to controlling ground surface settlement.

(3) After the construction of twin paralleled tunnels, the overall displacement of pile presents an S-shaped distribution. The pile body which overlaps with the buried depth of the tunnel moves away from the tunnel, while the upper part of pile body and the lower part of pile body deform towards the tunnel. By comparing the effects of different construction sequences on induced pile displacement, it is found that the construction sequence of condition (b) can reduce the vertical and horizontal displacement of pile.

Data Availability

The data used to support the findings of this study are available from the corresponding author upon request.

Conflicts of Interest

The authors declare that there are no conflicts of interest regarding the publication of this paper.

Acknowledgments

Development Project of Double-First-Class Scientific Research in Changsha University of Science & Technology (2018IC19).

References

[1] F. Li, J. Du, and B. Chen, "Unified analytical solution for deep circular tunnel with consideration of seepage pressure, grouting and lining," *Journal of Central South University*, vol. 24, no. 6, pp. 1483–1493, 2017.

[2] X. M. Zhang, X. F. Ou, J. S. Yang, and J. Y. Fu, "Deformation response of an existing tunnel to upper excavation of foundation pit and associated dewatering," *International Journal of Geomechanics*, vol. 17, no. 4, p. 14, Article ID 04016112, 2017.

[3] K. Huang, Y. W. Sun, L. Zhao et al., "Mechanical properties of segments when shield passes through upper-soft and lower-hard composite strata," *Journal of Central South University*, vol. 51, no. 5, pp. 1371–1383, 2020.

[4] P. Jongpradist, T. Kaewsri, A. Sawatparnich et al., "Development of tunneling influence zones for adjacent pile foundations by numerical analyses," *Tunnelling and Underground Space Technology*, vol. 34, pp. 96–109, 2013.

[5] D. S. Liyanapathirana and R. Nishanthan, "Influence of deep excavation induced ground movements on adjacent piles," *Tunnelling and Underground Space Technology*, vol. 52, pp. 168–181, 2016.

[6] Z. Ding, J. Wei, and G. Wei, "Prediction methods on tunnel-excavation induced surface settlement around adjacent building," *Geomechanics and Engineering*, vol. 12, no. 2, pp. 185–195, 2017.

[7] T. Liu, Y. Zhong, Z. Feng, W. Xu, and F. Song, "New construction technology of a shallow tunnel in boulder-cobble mixed grounds," *Advances in Civil Engineering*, vol. 2020, pp. 1–14, Article ID 5686042, 2020.

[8] L. An, J. Zhou, PB. Ouyang, and H. Li, "Analysis of tunnel face stability with advanced pipes support," *Journal of Central South University*, vol. 28, no. 2, pp. 604–617, 2021.

[9] C. W. W. Ng, H. Lu, and S. Y. Peng, "Three-dimensional centrifuge modelling of the effects of twin tunnelling on an existing pile," *Tunnelling and Underground Space Technology*, vol. 35, pp. 189–199, 2013.

[10] C. W. W. Ng, M. A. Soomro, and Y. Hong, "Three-dimensional centrifuge modelling of pile group responses to side-by-side twin tunnelling," *Tunnelling and Underground Space Technology*, vol. 43, pp. 350–361, 2014.

[11] A. Franza and A. M. Marshall, "Centrifuge and real-time hybrid testing of tunneling beneath piles and piled buildings," *Journal of Geotechnical and Geoenvironmental Engineering*, vol. 145, no. 3, Article ID 04018110, 2019.

[12] M. A. Soomro, M. Kumar, H. Xiong, D. A. Mangnejo, and N. Mangi, "Investigation of effects of different construction sequences on settlement and load transfer mechanism of single pile due to twin stacked tunnelling," *Tunnelling and Underground Space Technology*, vol. 96, Article ID 103171, 2020.

[13] Z. Ding, X. Wei, X. Zhang, and X. Yin, "Analysis of the field monitoring data on soil movements and adjacent building settlement due to shield tunnelling," *Engineering Computations*, vol. 36, no. 4, pp. 1219–1237, 2019.

[14] Z. Wang, W. Zhang, G. Wei, B. Li, Q. Li, and J. Yao, "Field measurement analysis of the influence of double shield tunnel construction on reinforced bridge," *Tunnelling and Underground Space Technology*, vol. 81, pp. 252–264, 2018.

[15] A. Sirivachiraporn and N. Phienwej, "Ground movements in EPB shield tunneling of Bangkok subway project and impacts on adjacent buildings," *Tunnelling and Underground Space Technology*, vol. 30, pp. 10–24, 2012.

[16] A. Franza, A. M. Marshall, T. Haji, A. O. Abdelatif, S. Carbonari, and M. Morici, "A simplified elastic analysis of tunnel-piled structure interaction," *Tunnelling and Underground Space Technology*, vol. 61, pp. 104–121, 2017.

[17] Z. Zhang, M. Huang, C. Xu, Y. Jiang, and W. Wang, "Simplified solution for tunnel-soil-pile interaction in Pasternak's foundation model," *Tunnelling and Underground Space Technology*, vol. 78, pp. 146–158, 2018.

[18] M. Yang, Q. Sun, C. Li, and K. Ma, "Three-dimensional finite element analysis on effects of tunnel construction on nearby pile foundation," *Journal of Central South University*, vol. 18, no. 3, pp. 909–916, 2011.

[19] C. J. Lee, "Three-dimensional numerical analyses of the response of a single pile and pile groups to tunnelling in weak weathered rock," *Tunnelling and Underground Space Technology*, vol. 32, pp. 132–142, 2012.

[20] A. M. Marshall and T. Haji, "An analytical study of tunnel-pile interaction," *Tunnelling and Underground Space Technology*, vol. 45, pp. 43–51, 2015.

[21] M. Nematollahi and D. Dias, "Three-dimensional numerical simulation of pile-twin tunnels interaction - case of the Shiraz subway line," *Tunnelling and Underground Space Technology*, vol. 86, pp. 75–88, 2019.

[22] J. Shi, Z. Fu, and W. Guo, "Investigation of geometric effects on three-dimensional tunnel deformation mechanisms due to basement excavation," *Computers and Geotechnics*, vol. 106, pp. 108–116, 2019.

[23] S. Li, L. Wei, X. Chen, and Q. He, "Numerical investigation on dynamic performance of a bridge-tunnel transition section with a deep buried pile-plank structure," *Advances in Civil Engineering*, vol. 2020, pp. 1–16, Article ID 8885535, 2020.

[24] K. Huang, Y. W. Sun, W. J. Yang et al., "Influence of shield tunneling on pile foundation of adjacent bridge using fluid-soil coupling theory," *Journal of Central South University*, vol. 52, no. 3, pp. 983–993, 2021.

[25] R. B. Peck, "Deep excavations and tunneling in soft ground," in *Proceedings of the 7th International Conference on Soil Mechanics and Foundation Engineering*, pp. 192–201, Mexico City : Sociedad Mexicana de Mecanica, Mexico City, Mexico, 1969.

[26] G. W. Clough and B. Schmidt, "Design and performance of excavations and tunnels in soft clay," *Developments in Geotechnical Engineering, Soft Clay Engineering*, vol. 20, pp. 569–634, 1981.

[27] P. B. Attewell and J. P. Woodman, "Predicting the dynamics of ground settlement and its derivatives caused by tunneling in soil," *Ground Engineering*, vol. 15, no. 8, pp. 13–36, 1982.

[28] M. P. O'Reilly and B. M. New, "Settlements above tunnels in the United Kingdom - their magnitude and prediction," in *Proceedings of Tunnelling'82 symposium*, pp. 173–181, Brighton, UK, June 1982.

[29] N. Loganathan and H. G. Poulos, "Analytical prediction for tunneling-induced ground movements in clays," *Journal of Geotechnical and Geoenvironmental Engineering*, vol. 124, no. 9, pp. 846–856, 1998.

[30] P. B. Attewell and I. W. Farmer, "Ground deformations resulting from shield tunnelling in london clay," *Canadian Geotechnical Journal*, vol. 11, no. 3, pp. 380–395, 1974.

Research Article

Analysis of Vertical Load Transfer Mechanism of Assembled Lattice Diaphragm Wall in Collapsible Loess Area

Mingtan Xia,[1] Xudong Zhang,[1] Gengshe Yang,[2] Liu Hui [ID],[2] and Wanjun Ye[2]

[1]*China Railway 11 Burea Group Co., Ltd., Wuhan, China*
[2]*College of Architecture and Civil Engineering, Xi'an University of Science and Technology, Xi'an, China*

Correspondence should be addressed to Liu Hui; 67646930@qq.com

Based on analysis of the formation mechanism and characteristics of the negative friction in collapsible loess areas, this study investigates the load transfer law of a wall-soil system under a vertical load, establishes the vertical bearing model of a lattice diaphragm wall, and analyzes the vertical bearing capacity of an assembled latticed diaphragm wall (ALDW) in a loess area. The factors influencing the vertical bearing characteristics of the ALDW in a loess area are analyzed. The vertical bearing mechanism of the lattice diaphragm wall in the loess area is investigated. The failure modes of the ALDW in the loess area are mainly shear failure of the soil around the wall and failure of the wall-soil interface. In the generation and development of negative friction, there is always a point where the relative displacement of the wall-soil interface is zero at a certain depth below the ground; at this point, the wall and soil are relative to each other. The collapsibility of loess, settlement of the wall and surrounding soil, and rate and method of immersion are the factors affecting the lattice diaphragm wall. The conclusions of this study provide a reference for the design and construction of ALDWs in loess areas.

1. Introduction

Through many years of urban construction practice, relatively mature enclosure structure designs have been developed for different foundation pit conditions. The commonly used retaining structures include diaphragm walls, bored piles, steel sheet piles, soil mix wall (SMW) methods, cement-soil mixing piles, and composite soil nail walls. With the development of modern construction technology, diaphragm walls can serve the functions of acting as a gravity retaining wall, bearing the vertical load of the structure, and providing waterproofing.

The assembled lattice diaphragm wall (ALDW) retaining structure is a new type of retaining structure that has been applied in foundation pit engineering in recent years [1, 2]. Because of its unique geometric structure, it has many advantages in deformation control and sustainable development and can meet the requirements of shortening the construction period and reducing land occupation. As a result, ALDWs have become a new structural form for public foundation pit support.

In the excavation stage of a foundation pit, the lattice diaphragm wall is used as an enclosure structure and seepage control structure. After excavation of the foundation pit, it can begin to function as the regular use stage. Because the lattice diaphragm wall has very high strength and individual vertical bearing capacity, it can directly bear the vertical load of the upper structure as part of the main structure or as the main structure itself. The lattice diaphragm wall can play a role in the enclosure structure during the construction period, while it can also play the role of vertical support in the use stage. Fully utilizing the lattice diaphragm wall structure can effectively reduce project costs. ALDWs have played an essential role in urban construction in Xi'an, particularly for subway construction.

Many scholars [3–7] have studied the bearing characteristics of diaphragm walls in different strata. Previous research on lattice wall retaining structures has mainly employed field monitoring, centrifugal model tests, and numerical simulations. In terms of field monitoring, Mei [8] determined that the horizontal deformation law of a lattice

wall retaining structure is similar to that of a gravity retaining structure based on deformation data measured for a dock foundation pit. The field monitoring data reported by Liang et al. [9] showed that the ratio of the horizontal displacement of the lattice wall to the excavation depth of the foundation pit was between 0.15% and 0.50%, and the horizontal displacement of the lattice wall was significantly lower than that of a tension anchor diaphragm wall. In terms of centrifugal model tests, Zuo et al. [10] noted that the variation in the Earth pressure between the front and back walls was not obvious based on centrifugal model tests of a lattice wall in sand. The centrifugal model test results for a lattice wall in soft soil reported by Zhou et al. [11] showed that the Earth pressure in the passive zone was greater than the Rankine passive Earth pressure, whereas the Earth pressure in the active zone was greater than the Rankine active Earth pressure but less than the static Earth pressure. Chen et al. [12] demonstrated that the bending moment, deformation, and Earth pressure of a lattice wall in clay were greater than those in sand. In terms of numerical simulations, Hou [13] studied the stress deformation characteristics and strata displacement law of a lattice wall during foundation pit excavation based on the finite element method and carried out extensive parameter analyses. The ideal elastic-plastic Coulomb friction model was used to describe the tangential contact characteristics between the wall and soil.

Masuda [14] collected data measured for 52 foundation pits in different areas of Japan having a diaphragm wall as the enclosure. The analysis results showed that the maximum lateral displacement of the diaphragm wall in sandy soil was approximately 0.05%–0.5% of the excavation depth, and the maximum lateral displacement in the clay layer was generally less than 0.5% of the excavation depth. Thus, these measures can effectively reduce displacement. Carder [15] collected data for the deformation of pits enclosed by cast-in-place piles and continuous walls in Britain under hard clay conditions. The results showed that the maximum lateral displacement limits of the enclosure structures were 0.125% H, 0.2% H, and 0.4% H at high, medium, and low stiffness, respectively. Yoo [16] analyzed the measured data for foundation pit projects in Seoul and other regions of Korea. It was found that the maximum lateral displacement of the diaphragm wall foundation pit was 0.05% H, while that of other supports was 0.13%–0.15% H, and the maximum lateral displacement of the anchor support was slightly smaller than that of the inner support. Moormann [17] collected a large amount of deformation data for foundation pits worldwide using methods similar to those of Long [18]. The deformation laws of small support structures under each soil condition were analyzed, and the influences of the type of enclosure structure and support on the deformation were discussed. Zuo et al. [10] used centrifuge tests to investigate the mechanical properties and deformation characteristics of the foundation of a grille diaphragm wall in sandy soil. To investigate the applicability of the lattice-shaped diaphragm wall (LSDW) as a bridge foundation in soft soil, Wu et al. [1] considered three models (a pile group, LSDW with a single chamber, and LSDW with two chambers) having similar

material quantities using small-scale model tests and numerical analyses based on FLAC3D. The soil arching effect of the LSDWs was investigated based on PFC2D, and special attention was given to the influencing factors [19]. Wu et al. [20] carried out comparative model tests on three types of foundations (group pile, single room diaphragm wall, and two-room grid diaphragm wall) with similar material quantities. The results showed that, in soft soil, using a diaphragm wall foundation instead of a group pile could improve the bearing capacity of the foundation and reduce settlement.

The current research mainly focuses on foundations with a single-chamber diaphragm wall [21, 22], while research on foundations comprising ALDWs is still in its infancy. Cheng [23] introduced the mechanism and application prospects of using a grid diaphragm wall to provide antiliquefaction capability under earthquakes. Hou [24, 25] studied the vertical bearing mechanism of a lattice diaphragm wall based on in situ static load tests and three-dimensional finite element analysis. Xie et al. [26] presented lattice-shaped diaphragm wall as a new method of foundation improvement for high embankment culverts on soft foundation; high strength exchanging-fill materials are adopted to partially replace the foundation soil. Wu et al. [27] conducted a numerical study to compare the static and seismic responses of LSDWs and pile groups having similar material quantities in soft soil.

As a new type of bridge foundation, the ALDW is highly applicable in practical engineering; however, theoretical research on its vertical bearing capacity is insufficient, especially in areas of collapsible loess. Xi'an is a typical collapsible loess area; it has high strength under natural humidity, and its structural damage and strength decrease significantly after being wetted. The soil skeleton structure is destabilized, and collapsible deformation occurs under the action of the soil self-weight or overlying load. The collapsible deformation of the soil causes relative displacement of the wall and soil, which leads to negative friction of the pile side, thus increasing the wall settlement and decreasing the bearing capacity. At present, research on the vertical bearing characteristics of lattice diaphragm walls in loess areas has not been carried out. There is thus an insufficient theoretical basis for this new type of bearing structure, especially regarding its bearing mechanism, design, and vertical bearing capacity calculation method, which limits the practical applications of the project. Therefore, it is of practical engineering significance to analyze the load-bearing mechanism of ALDWs in loess areas.

2. Structure of the Lattice Diaphragm Wall

The total length of the Xi'an Metro Phase III line is 280.8 km, with 156 stations, which encounters many problems of foundation pit support. The excavation depth of these foundation pits is large. Due to the complex building environment around the city, the traditional prefabricated diaphragm wall cannot play a role when the foundation pit support system cannot set internal support. In addition, in the subway deep foundation pit excavation, the width of the

foundation pit is large; if the internal support is used, it must be used with columns; otherwise, its stability cannot be guaranteed, which undoubtedly limits the internal operation space of the foundation pit, which is extremely inconvenient for mechanized construction, and the ALDW can make up for the above shortcomings.

The ALDW is a lattice structure connected by a series of grooves on the diaphragm wall, as shown in Figure 1. The lattice diaphragm wall is composed of inner and outer longitudinal walls and transverse diaphragm walls. The lattice structure composed of inner and outer longitudinal walls and the undisturbed soil inside the diaphragm wall jointly form a semigravity structure. As the retaining structure of a foundation pit, the water and soil pressure outside the pit can be borne by the lattice diaphragm wall during the construction of the foundation pit. The lattice diaphragm wall is a semigravity self-supporting retaining structure. It has the advantages of a diaphragm wall, that is, high stiffness and excellent impermeability, which can better limit the deformation of the foundation pit and bear the vertical load.

The upper structure is loaded as a permanent structure. A T-shaped groove section is usually used at the intersection of the diaphragm wall and inner and outer longitudinal walls to improve the integrity of the lattice diaphragm wall. At present, the thickness of the groove section of the diaphragm wall is typically 50–120 cm, although the thickness can reach 320 cm. The soil depth is generally in the range of 10–50 m, although the maximum depth can reach 170 m.

The wall can be considered as an infinite elastic body. The external force is parallel to the cross section of the wall and remains constant along the length direction; therefore, it can be regarded as a plane strain problem.

3. Formation Mechanism and Negative Friction Characteristics of the Lattice Diaphragm Wall in a Collapsible Loess Area

3.1. Formation of Negative Friction Resistance. The problem of wall frictional resistance is essentially a contact problem caused by the interaction between the wall and soil. Because of the difference in material properties between the soil and wall, the relative displacement between the wall and soil is nonzero under vertical loading, which leads to the generation of wall side friction. When the wall moves downward relative to the soil under a vertical load, the soil produces upward shear stress, i.e., positive friction resistance, owing to the relationship between the action force and the reaction force. However, in a collapsible loess area, the collapsibility of the loess often causes the soil around the wall to move downward relative to the wall. This produces downward shear stress on the wall, i.e., negative friction. The distribution and variation of the negative frictional resistance are highly complex. The settlement, velocity, and stability of the soil around the walls and piles, the collapsibility of the loess, the immersion method, and the duration of immersion all have different effects on the negative frictional resistance.

3.2. Collapse Displacement Load Transfer Principle. For a wall whose bearing capacity is mainly borne by the interaction at the wall-soil interface, if the interaction between the walls is not considered, the settlement displacement between the soil elements far from the center of the wall will be synchronized after the foundation is immersed and collapsible. There is no collapsible load transfer; therefore, it is a noncollapsible load transfer range. Within a specified thickness range from the wall, the settlement displacement of the adjacent soil elements differs, which is within the scope of the collapsible load transfer.

As shown in Figure 2, the soil in a range x from the center of the wall is within the range of collapsible load transfer. After collapsing, the farthest element in the influence range, $ABCD$, sinks to the location of $A'B'C'D'$ under gravity. This generates a downward shear force on the adjacent element, $CDEF$. $ABCD$ transfers a load to $CDEF$ through the difference in collapsible displacement, and $CDEF$ sinks and deforms accordingly to state $C'D'E'F'$. In the elemental analysis with a width dr and thickness in this range, the transfer of the collapsible load is an energy transfer process. The displacement, S_G, occurs under the action of gravity, G. The work of gravity, $S_G \cdot G$, is a dynamic source of collapsibility. Under the shear force and action, $\tau \prime$, of adjacent elements on both sides, shear deformation and volume deformation of the element occur. In the plastic deformation part of the lossy collapsible energy, the residual collapsible potential is transmitted to the adjacent elements on one side of the wall through shear force (which is related to the bonding and particle friction). Thus, the collapsible potential decreases gradually as it approaches the wall, and the subsidence displacement of the soil element decreases, finally reaching the surface element of the wall, HH. The load is a negative friction, q. The collapsible load transfer process can be described as follows:

$$f \cdot S_f \propto [(G \cdot S_G): \tau], \tag{1}$$

where S_f is the action range of the negative friction in the length direction of the wall. If the action distance of the negative friction along the wall is equal to the settlement displacement of the soil around the wall, the equation can be written as follows:

$$f \propto [G: \tau]. \tag{2}$$

Equation (2) shows that the collapse process is formally transformed from a physical force (gravity) to a surface force (negative friction).

The elastic modulus, E, and shear modulus, G, of the soil around the wall vary in the radial direction. The closer the collapse is to the wall, the more energy is dissipated by plastic deformation and the smaller the shear deformation will be under the same shear stress.

3.3. Calculation of the Negative Friction Resistance Based on the Load Transfer Method. In the wall with a depth of l, the upper soil will be displaced downward relative to the wall (the maximum, s, is at the surface), which produces negative

(a)

(b)
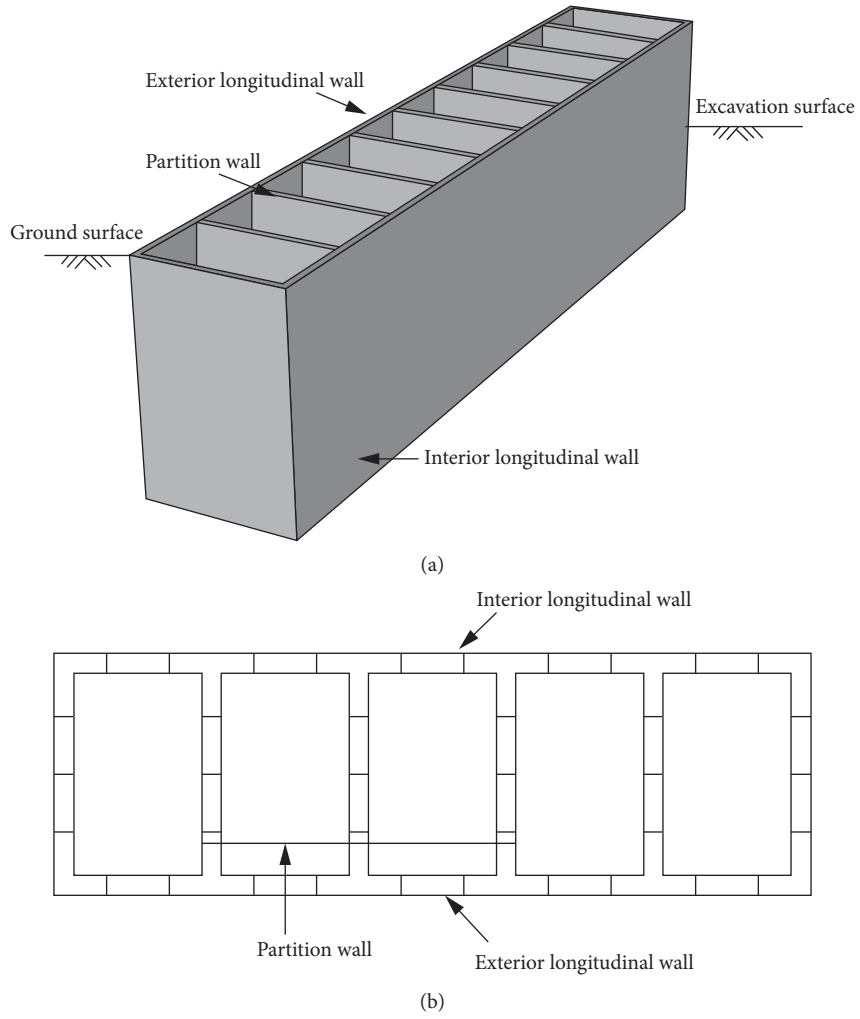
Figure 1: Structural sketch of the lattice diaphragm wall. (a) 3D view. (b) Top view.
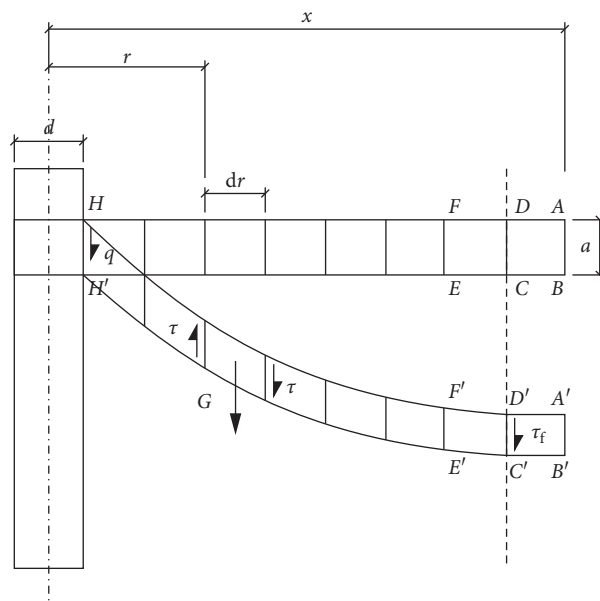
Figure 2: Principle of collapsible load transfer.

friction, q, and acts on the wall, causing the end of the wall to sink into the soil by δl; the end resistance, Qb, also plays a role. The soil near the end of the wall shows a positive friction, q', as shown in Figure 3(a). The contribution of the wall compressive deformation to the wall top displacement under negative friction is δ_f (including the total displacement, δ_0, of the wall top sinking through deformation). The movement of the soil relative to the wall is zero at vertical position ln; that is, the neutral point is located there. The displacement of the decomposed wall and the corresponding lateral resistance are shown in Figures 3(b) and 3(c).

It is assumed that the interface between the wall and soil is fully contacted, the diaphragm wall material is completely linearly elastic and is not destroyed before reaching the ultimate bearing capacity, and the mechanical action of the contact surface of the wall-soil element is a spring action model. The equilibrium equation can be obtained by considering the microelement dz at depth z as follows:

$$Uq\mathrm{d}z + N(z) + \mathrm{d}N(z) = N(z), \tag{3}$$

$$q = -\frac{1}{U}\frac{\mathrm{d}N(z)}{\mathrm{d}z}. \tag{4}$$

For elastic member element dz, $\mathrm{d}N(z) = EA(\mathrm{d}u(z)/\mathrm{d}z)$. Substituting this into equation (4) yields the following:

$$q = -\frac{1}{U}EA\frac{\mathrm{d}^2u(z)}{\mathrm{d}^2z}. \tag{5}$$

Equation (5) is the transfer differential equation for the negative frictional resistance, U is the circumference of the wall cross section, and $N(z)$ is the axial force of the wall at depth z.

The negative frictional resistance, q, is an irregular distribution along the wall and a function of the depth, z, defined as $q(z)$. The key to solving the equation is to determine the functional relationship between $q(z)$ and the relative displacement, $u(z)$. For this reason, many scholars have proposed $q(z)$–$z(u)$ distribution functions to improve the calculation of the negative frictional resistance, for example, Sato's double-folded line model and the linear elastic full-plastic model.

Negative frictional resistance has several unique characteristics, as described as follows.

3.3.1. Neutral Point. During the generation and development of negative frictional resistance, there always exists a point at a certain depth below the ground at which the relative displacement between the wall and soil is zero. The soil moves downward relative to the wall in the section above this point, and the wall is subjected to a negative frictional resistance. The wall moves downward relative to the soil in the section below this point, and the wall is subjected to positive friction. The inflection point of the wall frictional resistance is the neutral point under the action of resistance, as shown in Figure 4. The neutral point has three distinct characteristics: the relative displacement of the wall and soil at this point is zero, the friction resistance is zero, and the

axial force is the maximum. The main factors affecting the location of the neutral point are the degree of immersion, collapsibility of the soil around the wall, stress history, stiffness of the bearing layer at the end of the wall, and length-to-diameter ratio of the wall.

3.3.2. Time Effect of the Negative Friction Resistance. Because the negative friction on the wall side involves settlement of the soil around the wall, its development process is affected by the completion time of the settlement. Analyses can be performed according to the neutral point and pull-down load.

(i) Time effect of the neutral point: the position of the neutral point constantly changes as the wall and soil settle. Because the settlement of the soil around the wall and the wall itself is time-dependent, the position of the neutral point also has a time dependency. Generally, the position of the neutral point moves downward with time; however, if the settlement of the soil is completed before the wall sinks, the neutral point will move upward. Finally, when the relative displacement of the wall and soil is stable, the position of the neutral point also tends to be stable.

(ii) Time effect of the pull-down load: the pull-down load refers to the downward force exerted on the wall by the soil around the wall as it moves downward relative to the wall, that is, the area integral of negative friction in the extended area of the wall. The pull-down load also has a time dependency. The pull-down load development can be divided into two stages according to the development speed of the negative friction. As shown in Figure 5, the process can be described in two parts: first, the negative friction develops rapidly with time, and the pull-down load also increases rapidly; then, as the negative friction approaches the limit value, it increases more gradually, and ultimately the negative friction increases to be a stable limit value.

4. Vertical Load Transfer Mechanism of the ALDW in a Loess Area

4.1. Vertical Bearing Capacity of the Lattice Diaphragm Wall in a Loess Area. Because of its complex structure, the vertical bearing mechanism of the ALDW is more complex than that of an ordinary diaphragm wall. Under a vertical load, the core soil, inner and outer longitudinal walls, and wall end soil of the diaphragm wall in a loess area bear the upper load together. Therefore, the vertical bearing capacity, Q_u, of the lattice diaphragm wall in a loess area is mainly composed of five parts: the side friction, Q_s, provided by the lateral soil; negative friction, Q_f, of the collapsible loess; side friction, Q_{si}, provided by the core soil; negative friction, Q_{fi}, of the collapsible loess; and end resistance, Q_p, of the lattice diaphragm wall. The vertical bearing capacity can be expressed as follows:
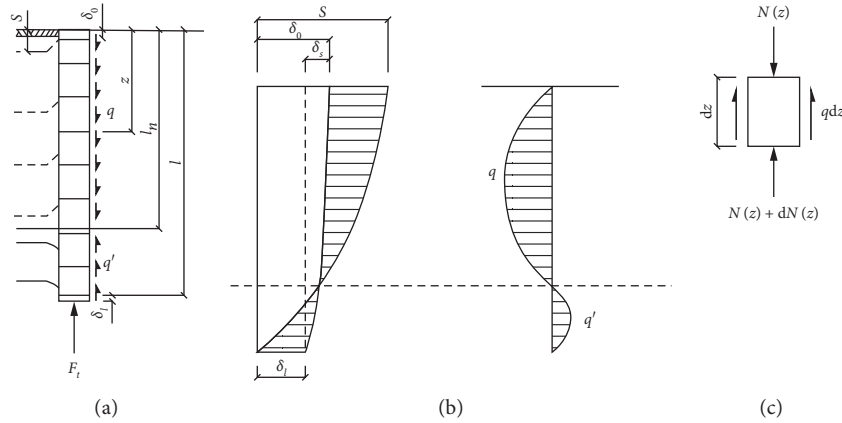
Figure 3: Schematic diagram of the calculation of negative friction in a lattice diaphragm wall located in a loess area.
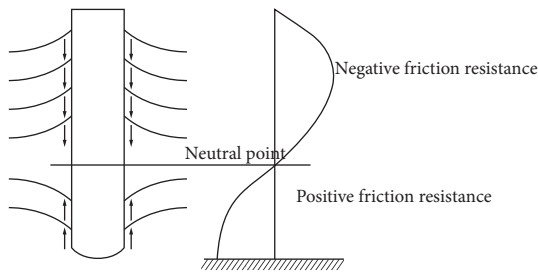
Figure 4: Neutral point diagram.
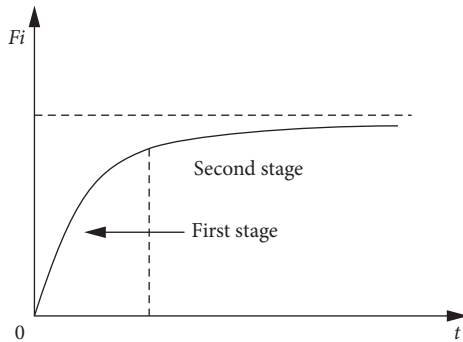
Figure 5: Two stages of pull-down load development.

$$Q_u = Q_s - Q_f + Q_{si} - Q_{fi} + Q_p. \tag{6}$$

Assuming that the distribution of the lateral friction, Q_s, provided by the soil outside the lattice diaphragm wall is similar to that of a pile foundation, the calculation equation for the lateral friction, Q_s, provided by the soil outside the lattice diaphragm wall refers to the equation for the lateral friction of a pile foundation.

$$Q_s = u_c \sum q_{sik} l_i, \tag{7}$$

where u_c is the outer circumference of the lattice diaphragm wall, q_{sik} is the standard value of the ultimate lateral friction of the ith soil layer on the wall side, and l_i is the thickness of the ith soil layer on the wall side.

The wall end resistance, Q_p, is composed of the internal and external wall end resistance, Q_{pl}, and the diaphragm wall end resistance, Q_{pt}.

$$\begin{aligned} Q_p &= Q_{pl} + Q_{pt} \\ &= q_{pl} A_{pl} + q_{pt} A_{pt}, \end{aligned} \tag{8}$$

where A_{pl} is the section area of the internal and external walls, q_{plk} is the section area of the partition wall, q_{plk} is the allowable value of the bearing capacity of the soil at the end of the internal and external walls, and q_{ptk} is the allowable value of the bearing capacity of the soil at the end of the partition wall.

The lateral friction resistance, Q_{si}, of the core soil is given as follows:

$$Q_{si} = q_{st} A_{st}, \tag{9}$$

where q_{stk} is the allowable bearing capacity of the soil at the end of the wall core and A_{st} is the sectional area of the wall core.

Therefore, the equation for calculating the vertical bearing capacity of the lattice diaphragm wall in a loess area is shown in Figure 6.

$$\begin{aligned} Q_{uk} &= Q_{sk} - Q_{fk} + Q_{sik} - Q_{fik} + Q_{pk} \\ &= u_c \sum q_{sik} l_i + q_{stk} A_{st} + q_{plk} A_{pl} + q_{ptk} A_{pt} - Q_{fk} - Q_{fik}. \end{aligned} \tag{10}$$

4.2. Analysis of the Load-Settlement Law of a Single Lattice Diaphragm Wall in a Loess Area. The load transfer analysis method was proposed by Seed and Rees in 1957. It was first used to analyze the load transfer law of piles and to predict the settlement. This method divides the pile into several elastic elements along the pile body. Each element simulates the connection between the pile body and soil at the pile side as a grounded inelastic spring. The connection between the pile end and the soil has also been simulated as a nonlinear spring, as shown in Figure 7. The load transfer method was applied for analysis of the vertical bearing capacity of the diaphragm wall, and the load-settlement law of a single diaphragm wall was
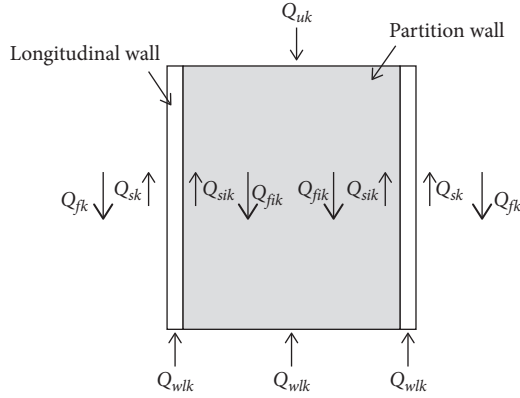
FIGURE 6: Diagram of the wall stress analysis.
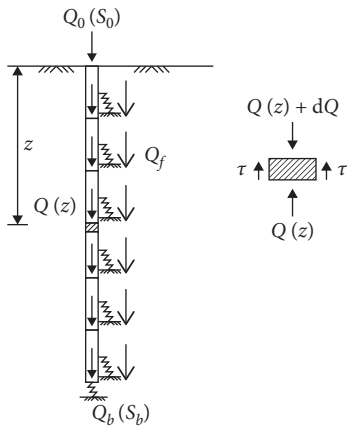
FIGURE 7: Diagram of the load transfer method.

analyzed. The vertical bearing capacity of the diaphragm wall could then be determined, and the vertical bearing characteristics of the diaphragm wall could be theoretically analyzed.

As shown in Figure 7, the analysis model of the diaphragm wall includes the load on the wall top and the settlement of the wall top. In this model, Q_p and S_p are the resistances at the end of the wall and the settlement at the end of the wall, respectively; $Q(z)$ and $\tau(z)$ are the load and side friction at the z section of the wall, respectively; and $\delta_s(z)$ and Q_f are the settlement and negative friction caused by the loess, respectively. Assuming that the diaphragm wall material is completely linearly elastic and will not be destroyed before reaching the ultimate bearing capacity, the load on the wall section at any depth z is as follows:

$$Q(z) = Q_0 - \int_0^\tau \tau_s(z)\mathrm{d}z + Q_f. \tag{11}$$

The vertical displacement of the wall section at any depth z is

$$S(z) = S_0 + \delta_s(z) - \frac{1}{EA}\int_0^\tau Q(z)\mathrm{d}z. \tag{12}$$

According to the equilibrium condition of the vertical force, the governing equation under a vertical load can be obtained from equation (5):

$$\tau(z) = \frac{\mathrm{d}Q(z)}{\mathrm{d}z} + q$$
$$= \frac{\mathrm{d}Q(z)}{\mathrm{d}z} - \frac{1}{U}EA\frac{\mathrm{d}^2u(z)}{\mathrm{d}^2z}. \tag{13}$$

The compression, $\mathrm{d}S(z)$, of microelement $\mathrm{d}z$ is given as follows:

$$\mathrm{d}S(z) = -\frac{Q(z)}{EA}\mathrm{d}z. \tag{14}$$

The basic differential governing equation of the load transfer in the wall-soil system can be obtained as follows:

$$EA\frac{\mathrm{d}^2S(z)}{\mathrm{d}z^2} - \tau(z) = 0, \tag{15}$$

where E is the elastic modulus of the wall and A is the cross-sectional area of the wall.

It can be seen from equation (15) that the key to solving the fundamental equation for the load transfer of the wall-soil system is establishing a transfer function ($\tau(z) - S(z)$ function) that genuinely reflects the relationship between the lateral friction and shear displacement of the wall-soil interface. In a collapsible loess area, with increasing depth, the collapsible deformation of the soil causes relative displacement of the wall-soil interface and, consequently, negative friction on the wall side. As a result, the wall settlement increases, and the bearing capacity decreases. The wall displacement, $S(z)$, and wall load, $Q(z)$, show decreasing trends.

5. Discussion

5.1. Transfer Mechanism for the Side Friction Resistance of a Single Assembly Diaphragm Wall. For the ALDW, because of its high stiffness, the vertical load can be approximated as a rigid body, exhibiting a trend of overall subsidence. The side friction and end resistance of the diaphragm wall develop synchronously. Because the main bearing capacity of the diaphragm wall is wall side friction, the primary focus of the diaphragm wall load transfer mechanism is the mechanism of the wall side friction transmission.

Under a vertical load, the diaphragm wall and surrounding soil share the upper load through the shear action on the wall-soil interface. Under shear stress on the contact surface, relative displacement between the diaphragm wall and the soil occurs. Owing to the low stiffness of the soil itself, the shear stress on the contact surface leads to certain shear deformation of the soil around the wall. In general, shear deformation occurs around the wall without relative displacement between the wall and soil, which leads to a particular settlement of the diaphragm wall. With an increase in the vertical load on the wall top, the shear deformation of the soil around the wall further increases. The settlement of the ground wall increases, and the relative displacement between the diaphragm wall and soil around the wall increases gradually. When the vertical load reaches the ultimate load, the diaphragm wall will lose its stability. At

this time, the possible reasons for failure of the diaphragm wall are as follows: concrete failure of the diaphragm wall, shear failure of the soil around the wall, and failure of the diaphragm wall-soil interface.

The section size of the diaphragm wall is large, and the compressive rigidity of the concrete is usually also large. Therefore, the possibility of concrete failure is not significant. The main reasons for the failure of the diaphragm wall are described in the following.

5.1.1. Shear Failure of the Soil around the ALDW. If the shear strength of the diaphragm wall-soil interface is high and the mechanical properties of the soil around the wall are low, the failure of the ground wall is often caused by shear failure of the soil around the wall under a vertical load, as shown in Figure 8. When the vertical load is small, there is no relative displacement between the soil and the diaphragm wall along their interface, and the soil around the wall bears the shear load on the wall-soil interface. Because of the soil shear modulus, the diaphragm wall and soil on the wall side jointly bear the load applied on the wall top. The shear deformation of the soil causes settlement of the diaphragm wall. With an increase in the vertical load, the shear load of the soil around the wall increases, and the shear deformation also increases. When shear failure occurs in the soil around the wall owing to excessive shear deformation, the vertical load on the top of the diaphragm wall cannot be increased, which indicates that the diaphragm wall has been destroyed. At this time, it can be considered that the failure of the diaphragm wall is caused by shear failure of the soil around the wall, and the lateral friction of the diaphragm wall is determined by the mechanical properties of the soil around the wall.

The shear stress required for shear failure varies owing to the different stress states of the soil around the wall at different depths. As shown in Figure 9, the small circle indicates the stress state of the soil around a shallow wall in the equilibrium limit state, whereas the large circle indicates the stress state of the soil around a deep wall in the equilibrium limit state. Obviously, the greater the depth is, the higher the shear stress required for shear failure of the soil around the wall will be. Because the compression of the diaphragm wall is minimal, the settlement of the top of the wall is the same as the settlement of the wall, and thus it can be considered that the shear strain of the soil around the wall at different depths is the same. In other words, in the process of increasing the vertical load, the frictional resistance of the shallow wall first gives way and gradually develops to deeper areas.

5.1.2. ALDW-Soil Interface Damage. Under vertical loads, shear deformation of the soil around the wall may occur, and slipping may also occur between the diaphragm wall and the soil around the wall. When the shear strength of the interface is not greater than the shear strength of the soil around the wall, sliding failure of the interface between the diaphragm wall and the soil usually precedes shear failure of the soil around the wall. At this time, the vertical bearing capacity of the diaphragm wall mainly depends on the mechanical

properties of the interface between the wall and the soil, and the limit value of the wall side friction resistance has a greater effect than that of the wall-soil interface.

During construction of the diaphragm wall, mud is typically used to protect the wall. If the mud is thick, the shear strength of the wall-soil interface can easily be reduced. In addition, during excavation of diaphragm wall trenching, the mechanical properties of the soil around the wall in a certain range decrease to a greater extent due to the construction disturbance, and the shear strength of the wall-soil interface may also be reduced. In these two cases, the inducement of the failure at the wall-soil interface is different, but the failure mechanisms are similar. When the load on the wall top reaches a certain level, relative slip occurs between the ground wall and the soil around the wall, and the sliding surface is in a vertical state, as shown in Figure 10. With an increase in the vertical load, the relative displacement between the diaphragm wall and soil around the wall increases, but the development of shear deformation around the wall is not apparent. When the wall-soil interface is destroyed due to excessive relative displacement, the load on the top of the wall cannot continue to increase, and the wall is destroyed by instability. At this time, it can be considered that failure of the wall-soil interface causes the failure of the diaphragm wall, and the lateral friction of the diaphragm wall is determined by the mechanical index of the wall-soil interface.

In the process of vertical loading on the wall top, soil shear deformation around the wall occurs, and the shear stress at the interface of the wall and the soil around the wall is balanced. Because the diaphragm wall sinks as a whole, the shear strain of the soil around the wall is the same, and thus the shear stress along the wall depth is the same at all parts of the wall-soil interface. With an increase in the load on the wall top, the shear stress on the contact surface between the wall and soil at the shallow part of the wall reaches the shear strength of the contact surface first, and relative slip along the contact surface occurs between the shallow part of the diaphragm wall and the soil around the wall. When the load on the top of the wall increases further, the shear strain of the soil around the shallow wall ceases to increase because the shear strength of the interface of the shallow wall and the shear strain of the deep soil continue to increase until the shear stress on the interface between the deep wall and soil reaches the shear strength of the interface. Therefore, it can be considered that if the top wall load is increasing, the cause of wall instability is sliding failure of the wall-soil interface, and the development process is from the top of the wall to the bottom of the wall.

If the foundation soil around the diaphragm wall is not improved or reinforced, the surface of the diaphragm wall is sufficiently rough, and the shear strength of the interface between the wall and the soil is sufficiently large, shear failure of the foundation soil around the wall is the leading cause of the instability failure of the diaphragm wall in the process of increasing the load on the top of the wall.

In this case, the limit value of the wall side friction is determined by the mechanical index of the foundation soil. In construction of the diaphragm wall, a certain thickness of mud interlayer is formed between the wall and soil because
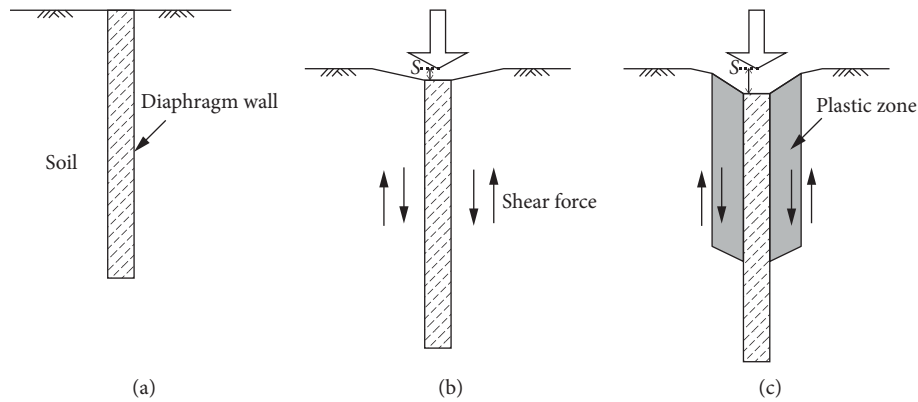
FIGURE 8: Shear failure of the soil around the wall.
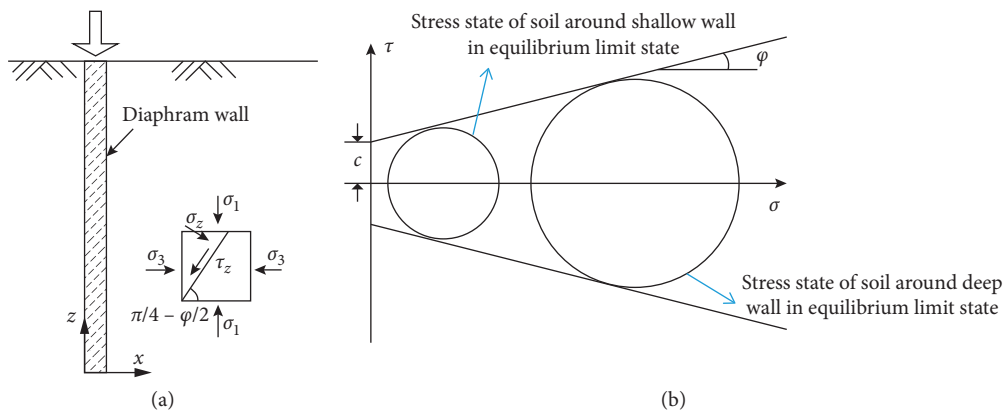
FIGURE 9: Stress state of the soil around the wall. (a) Stress strains of the soil around the wall. (b) Shear strain of the soil around the wall at different depths.

of the thick mud skin, or the strength of the soil around the wall is reduced; as a result, the shear strength of the interface between the diaphragm wall and soil becomes weak due to construction disturbance. Therefore, shear failure of the interface occurs before shear failure of the soil around the wall. In this case, as the load increases on the wall top, shear failure of the interface between the wall and soil causes instability failure of the ground wall. The ultimate value of the wall frictional resistance is determined by the mechanical index of the wall-soil interface. The ultimate value of the wall frictional resistance is smaller than that of the pile-side frictional resistance when the shear failure mode occurs in the soil around the pile.

5.2. Factor Analysis of the Vertical Bearing Behavior of a Lattice Diaphragm Wall in a Loess Area.

Many factors affect the vertical bearing behavior of a lattice diaphragm wall in a loess area, including (1) the elastic modulus, E_1, and Poisson's ratio, μ_1, at the side of the wall; (2) the elastic modulus, E_2, and Poisson's ratio, μ_2, at the end of the wall; (3) the cohesion, c_1, and internal friction angle, φ_1; (4) the cohesion, c_2, and internal friction angle, φ_2, at the end of the wall; (5) the static lateral pressure coefficient of the soil, K_0; (6) the friction coefficient of the wall-soil interface, μ, and the

allowable relative sliding, r; (6) the degree of immersion; (7) the collapsibility grade and stress history of the soil layer around the wall; and (8) the length-to-diameter ratio of the wall and other factors.

5.3. Analysis of Influence of Excavation Process on Stress of ALDW.

Based on ABAQUS, a three-dimensional finite element model of multigrid diaphragm wall is established to analyze the deformation and stress characteristics with different excavation depth. The simulated excavation depth of the foundation pit is 15 m, the depth of the lattice diaphragm wall is 30 m, the thickness of the wall is 0.8 m, the spacing between the horizontal partition wall axis is 6.0 m, and the spacing between the front and rear walls is 8.0 m. The size of the whole model is 103 m × 60 m × 30 m (Figure 11). Considering the influence of the construction steps on the foundation pit supporting structure, the excavation steps are divided into three steps when modeling; the excavation depth of each step is 5 m.

The Mohr-Coulomb ideal elastic-plastic model is adopted for soil constitutive model, in which the soil is divided into three layers for calculation, and the calculation parameters of each layer are shown in Table 1. The diaphragm wall is made of C35 concrete with elastic modulus of 35.1 GPa, Poisson's ratio of 0.2, and density of

(a) (b) (c)
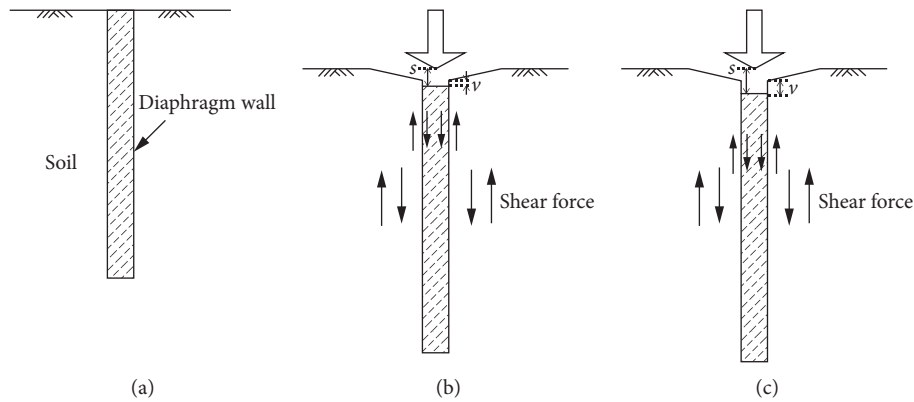
Figure 10: Shear failure of the wall-soil interface.
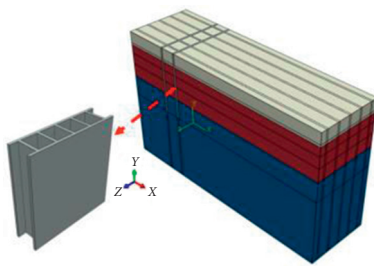
Figure 11: Numerical calculation model of ALDW.

2500 kg/m^3. The influence of groundwater is not considered in the analysis. The following assumptions are made in the simulation:

(1) The drainage consolidation of soil is not considered

(2) Soil excavation is completed instantaneously without considering time effect

If the position of the front and rear walls is shown in Figure 12, the internal force distribution nephogram of the step-by-step excavation lattice diaphragm wall (Figure 13) and the shear stress distribution curve of the front and rear walls and diaphragm wall (Figure 14) are obtained by numerical calculation. The positive value in the figure represents the tensile stress of the wall, and the negative value represents the compressive stress of the wall. It can be seen from Figure 13 that the internal force of diaphragm wall is larger at the bottom than at the top of the wall, the embedded section is larger than the excavation section, and the stress of the front wall > the stress of the cross wall > the stress of the back wall. The maximum stress appears at the bottom of the front wall, which is lower than the compressive limit of concrete. The stress at the top of the wall is far less than that at the bottom of the wall, and the stress concentration appears at the end of the front wall. After the excavation of foundation pit, the front and rear walls move to the pit under the action of unbalanced Earth pressure, and the soil in the pit prevents the wall from moving laterally, so the pressure on the embedded section of the front wall is greater.

It can be seen from Figure 14 that the shear stress of the front wall increases linearly along the depth direction of the wall,

and the wall is compressed. The shear stress of the back wall and the transverse wall changes nonlinearly along the depth direction of the wall. The cantilever section is compressed and the embedded section is tensioned along the depth direction of the wall. The cantilever section of the transverse partition wall is in tension along the depth direction of the wall, while the embedded section is in compression. With the increase of excavation depth, the shear stress of the front wall increases, and the maximum shear stress is 1.56 mpa. In the consolidation stage, the compressive stress of the back wall increases linearly along the depth of the wall. With the increase of excavation depth, the shear stress of back wall presents "s" type distribution, the compressive stress of cantilever section increases, and the compressive stress of embedded section decreases. When the excavation is 15 m, the tensile stress appears at the depth of 20 m. This is due to the excavation of the foundation pit; there is an unbalanced Earth pressure inside and outside the wall, which makes the wall move to the inside of the foundation pit. The pressure of the front wall is greater than that of the back wall, which prevents the wall from lateral displacement. At the same time, the tensile stress of the upper part of the transverse partition also prevents the wall from lateral displacement, so the tensile stress appears in the wall of the embedded section. It can be seen from Figure 14(c) that the stress of the transverse partition wall changes in an inverse "s" curve. Along the depth direction of the wall, the cantilever section is in tension and the embedded section is in compression. With the increase of excavation depth, the tensile stress of the wall increases and the compressive stress decreases. The stress of the wall changes from tension to compression, because the wall is cantilever structure, which dumps to the excavation side under the back pressure. The cross wall connects the front wall and the back wall and prevents the wall from moving to the foundation pit under the back wall gravity stress and the soil on both sides of the cross wall. When the back wall Earth pressure is greater than the wall side friction, the wall moves to the inside of the foundation pit, and the cross wall is compressed. The greater the excavation depth, the greater the tensile stress and the smaller the compressive stress. The results show that the function of transverse wall and back wall is the main reason why the fabricated lattice diaphragm wall can be used for foundation pit excavation without internal support structure.

TABLE 1: Soil layer calculation parameter.

Soil layer number	Thickness h (m)	Soil weight γ (kN/m³)	Cohesion c (kPa)	Internal friction angle φ (°)	Elastic modulus E (kPa)	Poisson's ratio ν
1	6	19.4	25	18	25000	0.31
2	15	20	35	19	33000	0.35
3	39	19.3	48	22	80000	0.35
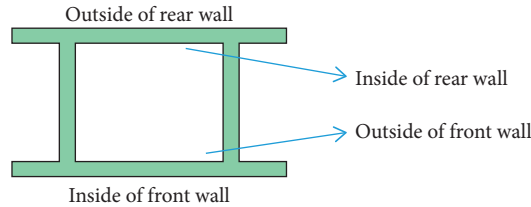
FIGURE 12: Location of front and back walls of lattice diaphragm wall.

(a)   (b)   (c)
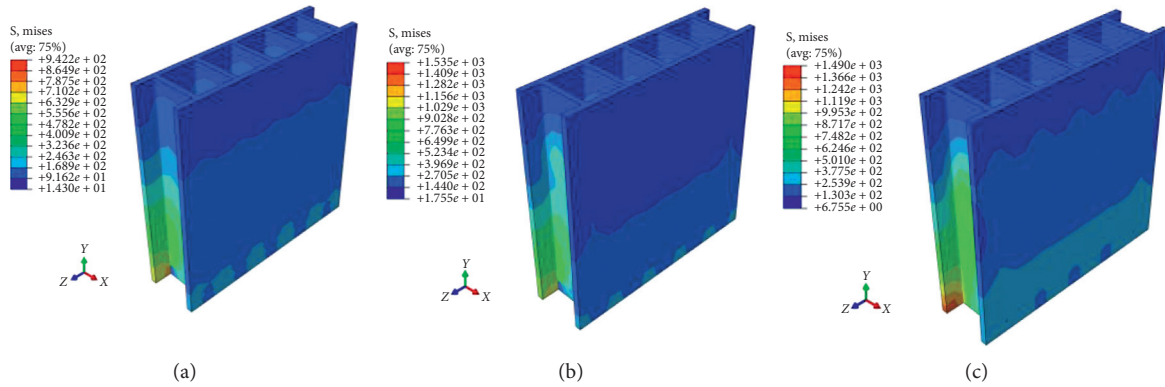
FIGURE 13: Internal force distribution of ALDW excavation. (a) Excavation of the first layer. (b) Excavation of the second layer. (c) Excavation of the third layer.

(a)   (b)   (c)
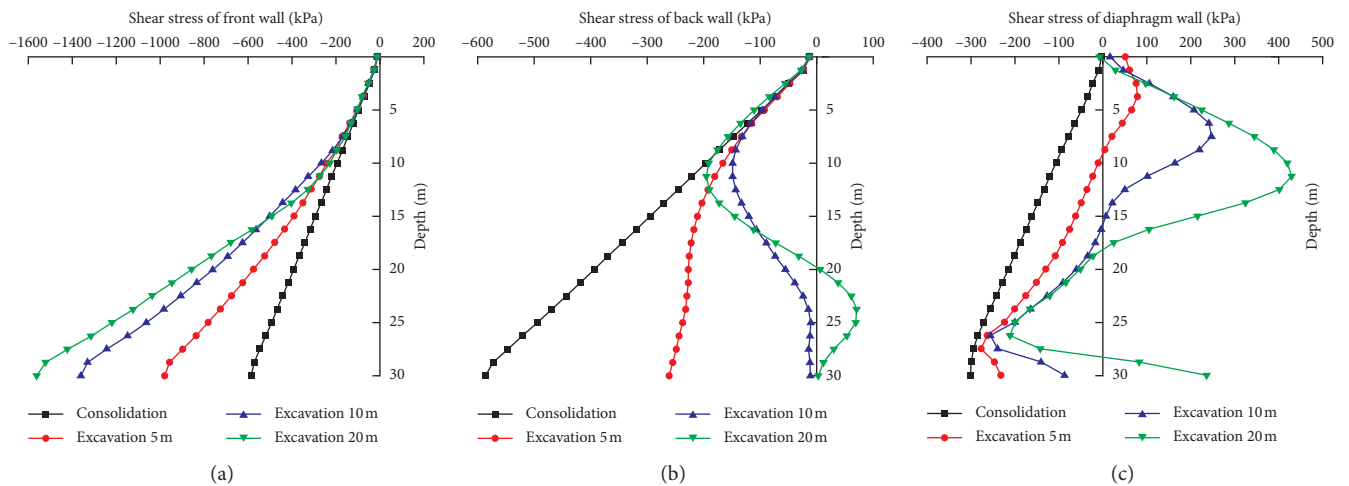
FIGURE 14: Shear stress distribution curve of ALDW. (a) Shear stress of front wall. (b) Shear stress of back wall. (c) Shear stress of diaphragm wall.

6. Conclusions

The load transfer method was used to analyze the process of negative friction and the transfer of collapsible displacement of an ALDW in a collapsible loess area. A preliminary theoretical analysis of the vertical bearing mechanism was carried out for the ALDW in a collapsible loess area. The main conclusions are as follows:

(1) The collapse process is formally expressed as the conversion of physical force (gravity) to surface force (negative friction). The closer the collapse is to the wall, the more energy is dissipated through plastic deformation and the smaller the shear deformation will be under the same shear stress. The negative friction, q, is distributed irregularly along the wall. The relative displacement between the wall and soil at the neutral point is zero; at this point, the friction resistance is zero, and the axial force is the maximum. The neutral position also varies with time.

(2) The equation for calculating the vertical bearing capacity of a lattice diaphragm wall in a loess area was deduced, and the load-settlement law for a single lattice diaphragm wall in a loess area was analyzed. In the collapsible loess area, with an increase in depth, the collapsible deformation of the soil causes relative displacement between the wall and soil, resulting in negative friction resistance on the wall side and leading to wall settlement. As the depth increases, the load-bearing capacity decreases.

(3) By analyzing the transfer mechanism of side friction of single assembled diaphragm wall, it is concluded that the main failure types are shear failure of soil around ALDW and failure of interface between continuous wall and soil.

(4) The factors affecting vertical bearing capacity of ALDW in loess area mainly include the mechanical properties of soil at side and end of wall, collapsibility grade of soil around wall, the degree of immersion and stress history, and the length-diameter ratio of the wall.

Data Availability

The data used to support the findings of this study are included within the article.

Conflicts of Interest

The authors declare that they have no conflicts of interest.

Acknowledgments

References

[1] J.-j. Wu, Q.-g. Cheng, H. Wen, and J.-l. Cao, "Comparison on the vertical behavior of lattice shaped diaphragm wall and pile group under similar material quantity in soft soil," *KSCE Journal of Civil Engineering*, vol. 19, no. 7, pp. 2051–2060, 2015.

[2] Q. Cheng, J. Wu, Z. Song, and H. Wen, "The behavior of a rectangular closed diaphragm wall when used as a bridge foundation," *Frontiers of Structural and Civil Engineering*, vol. 6, no. 4, pp. 398–420, 2012.

[3] Y. Arai, O. Kusakabe, O. Murata, and S. Konishi, "A numerical study on ground displacement and stress during and after the installation of deep circular diaphragm walls and soil excavation," *Computers and Geotechnics*, vol. 35, no. 5, pp. 791–807, 2008.

[4] C. De Lyra Nogueira, R. F. De Azevedo, and J. G. Zornberg, "Coupled analyses of excavations in saturated soil," *International Journal of Geomechanics*, vol. 9, no. 2, pp. 73–81, 2009.

[5] R. Schäfer and T. Triantafyllidis, "Modelling of earth and water pressure development during diaphragm wall construction in soft clay," *International Journal for Numerical and Analytical Methods in Geomechanics*, vol. 28, no. 13, pp. 1305–1326, 2004.

[6] C. Yoo and D. Lee, "Deep excavation-induced ground surface movement characteristics—a numerical investigation," *Computers and Geotechnics*, vol. 35, no. 2, pp. 231–252, 2008.

[7] Y. Chen, H. Lin, Y. Wang, R. Cao, C. Zhang, and Y. Zhao, "Modified double-reduction method considering strain softening and equivalent influence angle," *KSCE Journal of Civil Engineering*, vol. 24, pp. 1–10, 2020.

[8] Y. Mei, "Measured deformation of self-supporting lattice concrete diaphragm walls," *Chinese Journal of Geotechnical Engineering*, vol. 32, no. S1, pp. 463–467, 2010.

[9] S. Liang, W. Xu, and Y. Chen, "Lateral deformation of cellular diaphragm wall at excavation stage," *Journal of Southwest Jiaotong University*, vol. 50, no. 1, pp. 150–155, 2015.

[10] Y. Zuo, W. Xu, and Z. Xu, "Centrifugal model tests on mechanical property of gridding continuous diaphragm walls in sand," *Chinese Journal of Geotechnical Engineering*, vol. 32, no. S1, pp. 473–477, 2010.

[11] G. Zhou, W. Xu, and Y. Chen, "Centrifugal model test study of interaction of gridding concrete retaining wall and soft soil," *Rock and Soil Mechanics*, vol. 32, no. S1, pp. 134–140, 2011.

[12] X. Chen, W. Xu, and Y. Zuo, "Centrifugal model tests on mechanical property of cellular diaphragm wall," *Industrial Construction*, vol. 43, no. 2, p. 67, 2013.

[13] Y. Hou, *Behavior of cellular diaphragm wall in soft deposit*, Ph.D. thesis, Shanghai Jiao Tong University, Shanghai, China, 2010.

[14] T. Masuda, *Behavior of Deep Excavation with Diaphragm Wall*, Massachusetts Institute of Technology (MIT), Cambridge, MA, USA, 1993.

[15] D. R. Carder, *Ground Movements Caused by Different Embedded Retaining Wall Construction Techniques*, Vol. 172, Transport Research Laboratory Report, Berkshire, UK, 1995.

[16] C. Yoo, "Behavior of braced and anchored walls in soils overlying rock," *Journal of Geotechnical and Geoenvironmental Engineering*, vol. 127, no. 3, pp. 225–233, 2001.

[17] C. Moormann, "Analysis of wall and ground movements due to deep excavations in soft soil based on a new worldwide database," *Soils and Foundations*, vol. 44, no. 1, pp. 87–98, 2004.

[18] M. Long, "Database for retaining wall and ground movements due to deep excavations," *Journal of Geotechnical and Geoenvironmental Engineering*, vol. 127, no. 33, pp. 203–224, 2001.

[19] J.-j. Wu, L.-j. Wang, and Q.-g. Cheng, "Soil arching effect of lattice-shaped diaphragm wall as bridge foundation," *Frontiers of Structural and Civil Engineering*, vol. 11, no. 4, pp. 446–454, 2017.

[20] J. Wu, Q. Cheng, H. Wen, and J. L. Cao, "Vertical bearing behaviors of lattice shaped diaphragm walls and group piles as bridge foundations in soft soils," *Chinese Journal of Geotechnical Engineering*, vol. 36, no. 9, pp. 1733–1744, 2014.

[21] L. I. Tao, "Research on the calculation of diaphragm wall as bridge foundation in loess," *Chinese Journal of Geotechnical Engineering*, vol. 19, no. 3, pp. 47–54, 1997.

[22] G. Dai, W. Gong, X. Zhou, Y. Liu, and L. Liu, "Experiment and analysis on horizontal bearing capacity of single-chamber closed diaphragm wall," *Journal of Building Structures*, vol. 33, no. 9, pp. 67–73, 2012.

[23] Q. Cheng, "Mechanism of LSDW as bridge foundation against seismic liquefaction," *Academic News*, vol. 41, no. 1, pp. 35–44, 2014.

[24] Y.-m. Hou, *Behavior of Cellular Diaphragm wall in Soft Soil*, Shanghai Jiao Tong University, Shanghai, China, 2010.

[25] Y.-m. Hou, "Vertical bearing behaviors of cellular diaphragm wall," *Chinese Journal of Geotechnical Engineering*, vol. 34, no. 4, pp. 701–708, 2012.

[26] M. Xie, J. Zheng, J. Dong, and C. Miao, "Foundation improvement with lattice-shaped diaphragm wall treatment for high embankment culverts on soft foundation," *Tunnelling and Underground Space Technology*, vol. 10, no. 104, Article ID 103535, 2020.

[27] J. J. Wu, Q. G. Cheng, H. Wen, Y. Li, J. L. Zhang, and L. J. Wang, "Comparison on the horizontal behaviors of lattice-shaped diaphragm wall and pile group under static and seismic loads," *Shock and Vibration*, vol. 2016, Article ID 1289375, 17 pages, 2016.

Research Article

Ground Displacements due to the Deformations of Shallow Tunnels with Arbitrary Cross Sections in Soft Ground

Qiongfang Zhang [ID],[1,2] **Kang Cheng** [ID],[3,4] **Cungang Lin** [ID],[5] **Yadong Lou** [ID],[6] **Panpan Guo** [ID],[4] **and Xiaolu Gan** [ID][4]

[1]*Power China Huadong Engineering Corporation Limited, Hangzhou 311122, Zhejiang, China*
[2]*Engineering Research Center of Smart Rail Transportation of Zhejiang Province, Hangzhou 310014, Zhejiang, China*
[3]*China Railway 11th Bureau Group Co., Ltd., Wuhan 430061, China*
[4]*Research Center of Coastal and Urban Geotechnical Engineering, Zhejiang University, Hangzhou 310058, China*
[5]*School of Civil Engineering, Sun Yat-Sen University, Guangzhou 510275, China*
[6]*Hangzhou Metro Group Co., Ltd., Hangzhou 310003, Zhejiang, China*

Correspondence should be addressed to Cungang Lin; lincg@mail.sysu.edu.cn

Nowadays, a huge number of shield-driven tunnels with noncircular cross sections are constructed in urban areas all around the world. However, the ground displacements associated with tunneling still form a difficult issue, especially for noncircular tunnels. In this study, an analytical solution is derived to estimate the ground displacements induced by the deformations of shallow noncircular tunnels in soft ground. First, a solution for the stresses and displacements around a deep tunnel in a full plane is formulated by imposing a specified convergence pattern over the cavity boundary. Subsequently, this solution is validated using finite element simulations in a case study of an elliptical tunnel with four different convergence patterns. Afterward, the solution in the full plane is extended to a half plane using the virtual image technique to estimate the ground displacements around shallow tunnels. The solution is also validated using finite element simulations.

1. Introduction

In the last twenty years, a variety of special-shaped shields have been developed to build tunnels with many different shapes and cross sections [1–7]. Compared with the most widely used circular tunnels, noncircular tunnels are believed to have the advantage of making full use of excavated space [8]. Thus, they have been more and more frequently employed in urban areas for transportation development.

During the construction of shallow tunnels in soft ground, one critical concern is the ground movements associated with tunneling. At present, there have been several methods available for predicting tunneling-induced ground movements, including empirical methods, analytical solutions, model tests, and numerical simulations [9]. Although numerical simulations are generally powerful and elaborate,

analytical solutions are still necessary, as they are less time-consuming and easier for practical applications compared with other methods [6, 10]. In particular, when abundant experiences are obtained from field observations and model tests, analytical solutions with empirical modifications can provide as many accurate results as numerical simulations.

Among analytical solutions, those derived from elastic theories make up important categories. These elastic solutions can generally be formulated by a combination of complex variable methods [11] and some well-established theorems, such as the Cauchy's integral theorem [12], Laurent's theorem [13], and theorems on conformal mapping [12]. The elastic solutions for generated stresses and displacements around deep tunnels in rocks are mostly derived in infinite planes by imposing a specified loading distribution over boundaries at certain distances from

tunnels [14–17]. However, since the tectonic stresses acting on shallow openings are not as high as those acting on deep openings, such pressure-controlled derivation is generally not applicable to shallow tunnels [15]. Instead, a displacement-controlled method, in which, for example, a specified convergence pattern is imposed on the cavity of a shallow tunnel and is employed for estimating the soil stresses and displacements around shallow tunnels [18–24]. Sagaseta [22] regarded the excavation of a tunnel as the radial convergence of a small circle to the tunnel axis. The authors of [23] developed the study of [22] by considering the effect of Poisson's ratio of soil and an elliptical convergence pattern around a tunnel boundary. The authors of [19, 20] derived elastic solutions for soil displacements around both deep and shallow tunnels in clay by assuming four different convergence patterns. Pinto and Whittle [21] pointed out that tunneling-induced ground settlements depend on convergence patterns that are both uniformly radial and elliptical. Overall, it has been proven by previous studies that the ground displacements due to the excavations of shallow circular tunnels can be reliably calculated under appropriately assumed convergence patterns around cavities.

More and more tunnels with noncircular cross sections are constructed worldwide [25–29]. However, most of the abovementioned solutions for tunneling-induced soil stresses and displacements are related to circular tunnels, giving sparse attention to noncircular tunnels. Wang et al. [30] derived an elastic solution for shallow tunnels with arbitrary cross sections in rock and stiff soil using the Schwartz alternating method [31]. It is obtained by superimposing an infinite plane solution [32] and a half-plane solution [33]. However, this solution is only applicable to deep tunnels.

In this study, an elastic solution is derived to estimate the ground displacements around shallow tunnels in soft ground. First of all, an elastic solution in a full plane is formulated to calculate the ground displacements around deep tunnels with arbitrary cross sections. Afterward, it is employed in the deep tunnels of several commonly used shapes. Furthermore, the solution is extended to a half-plane for shallow tunnels using the virtual image technique [22].

2. Elastic Solutions in a Full Plane

2.1. Formulations.
In this section, the issue to be solved is the soil stresses and displacements around a deep tunnel with an arbitrary cross section in an infinite plane. It is assumed that the cavity occupied by the tunnel is vacuum and that the surrounding soil is homogeneous, isotropic, and linearly elastic. Elastic solutions for soil stresses and displacements can be obtained by following the steps as follows:

(1) Conformally mapping the glyphs in the original domain onto the regular graphs in the mapped plane

(2) Translating the conditions of the displacement boundary or stress boundary into a complex variable domain using the conformal mapping technique

(3) Getting the unknown parameters of the stress function while assuming that the stress of a point at infinity is zero

(4) Using the available theorems, such as Cauchy's integral theorem and Laurent's theorem, to simplify the stress function

2.1.1. Complex Variable Function.
In the absence of body forces, the stresses around a cavity can be solved using the Airy stress function F as

$$\frac{\partial^4 F}{\partial y^4} + 2\left(\frac{\partial^4 F}{\partial x^2 \partial y^2} + \frac{\partial^4 F}{\partial x^4}\right) = 0, \tag{1}$$

where x and y denote the horizontal and vertical axes, respectively, in a Cartesian coordinate system, as shown in Figure 1.

The equilibrium can be satisfied if F meets the following conditions [12]:

$$\sigma_x = \frac{\partial^2 F}{\partial y^2},$$

$$\sigma_y = \frac{\partial^2 F}{\partial x^2}, \tag{2}$$

$$\tau_{xy} = -\frac{\partial^2 F}{\partial x \partial y},$$

where σ_x and σ_y are the normal stresses in the x and y directions, respectively, and τ_{xy} is the shear stress in the x-y plane.

The displacements around the cavity can be expressed by the two harmonic functions, $\varphi(z)$ and $\psi(z)$, as follows [34]:

$$2G\left(u_x + iu_y\right) = \kappa\varphi(z) - z\overline{\varphi'(z)} - \overline{\psi(z)}, \tag{3}$$

where u_x and u_y are the displacements in the x and y directions, respectively; G is the shear modulus of the soil; z is a complex variable in the z-plane, $z = x + iy$; the constant κ is related to Poisson's ratio ν by $\kappa = 3 - 4\nu$ for the plane strain problems and $\kappa = 3 - \nu/1 + \nu$ for the plane stress problems, respectively; ν is Poisson's ratio of soil; and $\varphi(z)$ and $\psi(z)$ are functions with respect to the variable z, which can be determined by giving the displacement boundary conditions around the tunnel cavity. $\overline{\varphi'(z)}$ and $\overline{\psi(z)}$ are the conjugates of $\overline{\varphi'(z)}$ and $\overline{\psi(z)}$, respectively.

Afterward, the stresses around the cavity can be expressed in the form of complex functions as follows:

$$\begin{cases} \sigma_x + \sigma_y = 4\text{Re}\left[\varphi'(z)\right], \\ \left(\sigma_y - \sigma_x\right) + 2i\tau_{xy} = 2\left[\overline{z}\varphi''(z) + \psi'(z)\right], \end{cases} \tag{4}$$

where $\overline{z}$ is the conjugate of z and Re[.] denotes the real part of a generic complex variable [·].
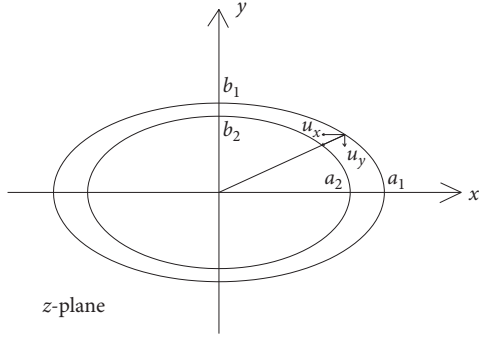
Figure 1: The z-plane.

2.1.2. Conformal Mapping.

A tunnel with an arbitrary cross section (ellipse, circle, oval, and rectangle) in the z-plane is transformed into a unit circular hole in the ζ-plane, as depicted in Figure 2. The employment of the mapping technique $z = w(\zeta)$ yield

$$\begin{cases} \varphi(z) = \varphi(w(\zeta)) = \varphi(\zeta), \\ \psi(z) = \psi(w(\zeta)) = \psi(\zeta). \end{cases} \tag{5}$$

For a 2-dimensional (2D) elastic problem, the displacements and stresses are expressed in terms of two complex variable functions, $\varphi(z)$ and $\psi(z)$, with $z = x + iy$ and $i = \sqrt{-1}$. By introducing conformal mapping and equation (5), the generated stresses and displacements around the tunnel cavity can be expressed as follows:

$$2G\left(u_x + iu_y\right) = \kappa\varphi(\zeta) - \frac{w(\zeta)}{\overline{w'(\zeta)}}\overline{\varphi'(\zeta)} - \overline{\psi(\zeta)}, \tag{6}$$

$$\begin{cases} \sigma_x + \sigma_y = 4\mathrm{Re}\left[\dfrac{\varphi'(\zeta)}{w'(\zeta)}\right], \\[3mm] \left(\sigma_y - \sigma_x\right) + 2i\tau_{xy} = \dfrac{2}{w'(\zeta)}\left[\overline{w(\zeta)}\left(\dfrac{\varphi'(\zeta)}{w'(\zeta)}\right)' + \psi'(\zeta)\right], \end{cases} \tag{7}$$

where $\overline{w(\zeta)}$ is the conjugate of the complex function $w(\zeta)$, ζ is a complex variable in the ζ-plane, $\zeta = \xi + i\eta = \rho e^{i\vartheta}$, ξ and η are variables of the Cartesian coordinates system in the mapped plane, and ρ and ϑ are variables of the polar coordinates system in the mapped plane.

From (7), the stress components can be obtained as follows:

$$\begin{cases} \tau_{xy} = \mathrm{Im}\left[\dfrac{1}{w'(\zeta)}\left(\overline{w(\zeta)}\left(\dfrac{\varphi'(\zeta)}{w'(\zeta)}\right)' + \psi'(\zeta)\right)\right], \\[3mm] \sigma_x = 2\mathrm{Re}\left[\dfrac{\varphi'(\zeta)}{w'(\zeta)}\right] - \mathrm{Re}\left[\dfrac{1}{w'(\zeta)}\left(\overline{w(\zeta)}\left(\dfrac{\varphi'(\zeta)}{w'(\zeta)}\right)' + \psi'(\zeta)\right)\right], \\[3mm] \sigma_x = 2\mathrm{Re}\left[\dfrac{\varphi'(\zeta)}{w'(\zeta)}\right] - \mathrm{Re}\left[\dfrac{1}{w'(\zeta)}\left(\overline{w(\zeta)}\left(\dfrac{\varphi'(\zeta)}{w'(\zeta)}\right)' + \psi'(\zeta)\right)\right], \end{cases} \tag{8}$$

where $\mathrm{Im}[\cdot]$ denotes the imaginary component of the generic complex variable $[\cdot]$.

Since (6) is analytic in the mapped ζ-plane, it can be expanded in the Laurent series of σ using $\zeta = \rho e^{i\vartheta} = \rho\sigma$ as follows:

$$2G\left(u_x + iu_y\right) = \sum_{-\infty}^{\infty} A_k e^{in\theta} = \sum_{-\infty}^{\infty} A_n \sigma^n = g(\sigma), \tag{9}$$

where σ denotes a point on the unit circle in the ζ-plane. Therefore, the coefficients A_k are determined by means of
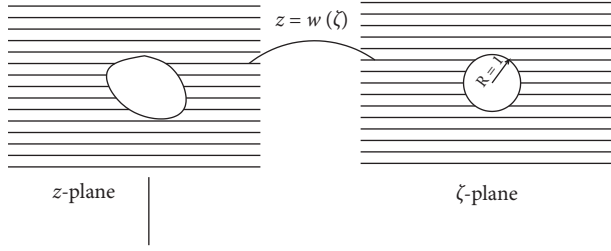
FIGURE 2: Conformal mapping of the exterior of an unlined tunnel of any shape onto the exterior of a unit circle.

the recursive relations derived from the given boundary conditions.

The displacement components can be obtained as follows:

$$
\begin{cases}
u_x = \text{Re}\left[g(\sigma)\right] = \dfrac{1}{2G}\text{Re}\left[\displaystyle\sum_{-\infty}^{\infty} A_n \sigma^n\right], \\[2mm]
u_y = \text{Im}\left[g(\sigma)\right] = \dfrac{1}{2G}\text{Im}\left[\displaystyle\sum_{-\infty}^{\infty} A_n \sigma^n\right].
\end{cases}
\tag{10}
$$

As shown by Muskhelishvili, the stress boundary condition in the phase plane can be expressed as follows:

$$
\varphi(\zeta) + \frac{w(\zeta)}{\overline{w(\zeta)}}\overline{\varphi'(\zeta)} + \overline{\psi(\zeta)} = i\int\left(f_x + f_y\right)ds,
\tag{11}
$$

where fx and fy are the surface stresses in the x and y directions, respectively, where they act on the elliptical cavity wall.

It can be verified [34] that the potentials can be written in the form as follows:

$$
\varphi(\zeta) = \frac{1}{8\pi(1-v)}\left(\overline{F_x + iF_y}\right)\ln\zeta + Bw(\zeta) + \varphi_0(\zeta),
\tag{12}
$$

$$
\psi(\zeta) = -\left(\frac{3-4v}{8\pi(1-v)}\right)\left(\overline{F_x - iF_y}\right)\ln\zeta + (B\prime + iC\prime)w(\zeta) + \varphi_0(\zeta),
\tag{13}
$$

where $\overline{F_x} + i\overline{F_y}$ is the resultant force applied to the boundary (which in this case is equal to zero). The variables B, $B' + iC'$, and $B' - iC'$ can be written as

$$
B = \frac{(\sigma_1 + \sigma_2)}{4},
\tag{14}
$$

$$
B' + iC' = -\left(\frac{1}{2}\right)(\sigma_1 - \sigma_2)e^{-2i\alpha},
\tag{15}
$$

where σ_1 and σ_2 are the principal stresses at infinity and α is the angle between the maximum principal direction and x-direction.

It is assumed that the stresses vanished at infinity and on the tunnel boundary. Thus,

$$
\begin{aligned}
\overline{F_x} + i\overline{F_y} &= 0, \\
B' + iC' &= 0.
\end{aligned}
\tag{16}
$$

By substituting (16) into (12) and (13),

$$
\begin{cases}
\varphi(\zeta) = \varphi_0(\zeta), \\
\psi(\zeta) = \psi_0(\zeta),
\end{cases}
\tag{17}
$$

where the functions $\varphi_0(\zeta)$ and $\psi_0(\zeta)$ are single-valued and analytic in the ζ-plane, including the point at infinity.

According to equations (6), (9), and (17),

$$
g(\sigma) = \sum_{-\infty}^{\infty} A_n \sigma^n = (3-4v)\varphi_0(\sigma) - \left(\frac{w(\sigma)}{w'(\sigma)}\right)\overline{\varphi_0'(\sigma)} - \overline{\psi_0(\sigma)}.
\tag{18}
$$

By taking the conjugate, then

$$
\overline{g(\sigma)} = \sum_{-\infty}^{\infty} \overline{A_n}\sigma^{-n} = (3-4v)\overline{\varphi_0(\sigma)} - \frac{\overline{w(\sigma)}}{w'(\sigma)}\varphi_0'(\sigma) - \psi_0(\sigma).
\tag{19}
$$

Equations 19 and 20 are multiplied by $d\sigma/2\pi i\,(\sigma - \zeta)$ and integrated along the unit circle in the ζ-plane:

$$
\frac{1}{2\pi i}(3-4v)\oint\frac{\varphi_0(\sigma)}{\sigma - \zeta}d\sigma - \frac{1}{2\pi i}\oint\frac{w(\sigma)}{w'(\sigma)}\frac{\overline{\varphi_0'(\sigma)}}{\sigma - \zeta}d\sigma - \frac{1}{2\pi i}\oint\frac{\overline{\psi_0(\sigma)}}{\sigma - \zeta}d\sigma = \frac{1}{2\pi i}\oint\frac{g(\sigma)}{\sigma - \zeta}d\sigma,
\tag{20}
$$

$$
\frac{1}{2\pi i}(3-4v)\oint\frac{\overline{\varphi_0(\sigma)}}{\sigma - \zeta}d\sigma - \left(\frac{1}{2\pi i}\oint\frac{\overline{w(\sigma)}}{w'(\sigma)}\frac{\varphi_0'(\sigma)}{\sigma - \zeta}d\sigma - \frac{1}{2\pi i}\oint\frac{\psi_0(\sigma)}{\sigma - \zeta}d\sigma\right) = \frac{1}{2\pi i}\oint\frac{\overline{g(\sigma)}}{\sigma - \zeta}d\sigma.
\tag{21}
$$

According to the properties of the Cauchy integral, $\overline{w(\sigma)}$, $w'(\sigma)$, and $\varphi_0'(\sigma)$ are analytic functions in the unit circle. Then, $\overline{w(\sigma)}/w'(\sigma)\varphi_0'(\sigma)$ is analytic in the unit circle. It can be concluded that the second and third terms on the left-hand side of (17) are zero and that the first term on the left-hand side of (18) is zero. Thus, it can be concluded that

$$
\varphi_0(\zeta) = -\left(\frac{1}{3-4v}\right)\frac{1}{2\pi i}\oint\frac{g(\sigma)}{\sigma - \zeta}d\sigma.
\tag{22}
$$

By combining (9) and (23),

$$
\varphi_0(\zeta) = \left(\frac{1}{3-4v}\right)\sum_{-\infty}^{0} A_n\zeta^n.
\tag{23}
$$

A similar process could be performed to find $\psi_0(\zeta)$, where A_n are the only unknown constants in the two complex variable functions.

2.1.3. Tunnels with Different Cross Sections.

To find a solution for the present problem, we first consider the transformation of the tunnels with arbitrary cross sections, such as ellipses, circles, oval shapes, and squares, in the z-plane into a unit circular hole in the ζ-plane. The transformation function [35] is assumed as

$$z = w(\varsigma) = R\left(\varsigma + \sum_{n=1}^{N} a_n \varsigma^{-n}\right),$$

$$\varsigma = \rho e_{i\theta}, \tag{24}$$

where R is a real number that refers to the cross-section size and a_n is a general complex coefficient satisfying $|a_n < 1/n|$ [36]. Inverse mapping is analytical, single-valued, and nonzero in the exterior part of the curve.

In many instances, it is assumed that the physical domain possesses p symmetry axes and then yields

$$z = w(\varsigma) = R\left(\varsigma + \sum_{n=1}^{N} a_{1pn}\varsigma^{1-pn}\right). \tag{25}$$

The tunnel cavity assigns the prescribed radial displacement along its boundary, and the central position of the curve remains unchanged after deformation. It remains axisymmetric along the x-axis and y-axis. After deformation, the curve can be expressed as

$$Z = w_c(\zeta) = R_c\left(\zeta + \sum_{n=1}^{N} b_n \zeta^{-n}\right). \tag{26}$$

The total displacement u_k at the tunnel boundary can be expressed as

$$u = Z - z,$$

$$= (u_x + iu_y),$$

$$= (R_c - R)\zeta + \sum_{n=1}^{N}(R_c b_n - R a_n)\zeta^{-n}. \tag{27}$$

Compared with (10), the coefficient A_k is obtained as follows:

$$\begin{cases} A_1 = 2G(R_c - R) \\ A_n = 0 \quad n \geq 2 \\ A_n = 2G(R_c b_k - R a_k) \quad n \leq -1. \end{cases} \tag{28}$$

For a cylindrical cavity of radius r in isotropic soil, the boundary condition is solved by mapping onto a circle of a unit radius:

$$z = r\zeta. \tag{29}$$

When undergoing uniform convergence u_ε, the deformed tunnel boundary is expressed as follows:

$$Z = (r - u_\varepsilon)\zeta. \tag{30}$$

Considering an infinite plane containing an elliptical tunnel cavity with a major axis $2a_1$ and a minor axis $2b_1$, the transformation function became

$$z = w(\zeta),$$

$$= R_0(\zeta + m\zeta^{-1}), \tag{31}$$

where $R_0 = (a_1 + b_1)/2$ and $m = (a_1 - b_1)/(a_1 + b_1)$.

Heller et al. [37] provide a mapping function for a rectangular opening of unit width and height, K, using the Schwarz–Christoffel integral:

$$z = R\left[\zeta + \left(\frac{1 - K^2}{4}\frac{1}{\zeta}\right) - \left(\frac{K^2}{24}\frac{1}{\zeta^3}\right) - \left(\frac{K^2(1 - K^2)}{160}\frac{1}{\zeta^5}\right) - \left(\frac{K^2(1 - 3K^2 + K^4)}{896}\frac{1}{\zeta^7}\right) + \cdots\right]. \tag{32}$$

Manh et al. [16] propose that, to get a smaller error for the elastic fields at the corner of a rectangular opening, at least 10 terms must be used in the conformal mapping functions. Once an approximate polynomial mapping for the origin and deformed shape of a cavity boundary is known, the elastic solution can be determined using the analytical method proposed in the paper. Generally, tunnel contours comprise complex curves. To generalize these studies, it is reasonable to simplify complicated tunnels as unlined tunnels with elliptical outlines [38].

2.1.4. Different Deformation Patterns.

It is of practical significance to determine the coefficients of the approximate polynomial mapping function after deformation. Taking the elliptical tunnel as an example, four convergence patterns in Figure 3 are assumed to describe the displacement on the boundary of the elliptical tunnel:

$$B.C. - 1: u_c = -u_0(\sin\theta + t\cos^2\theta), \tag{33}$$

$$B.C. - 2: u_c = -u_0(1 + \sin\theta - (1 - t)\cos^2\theta), \tag{34}$$
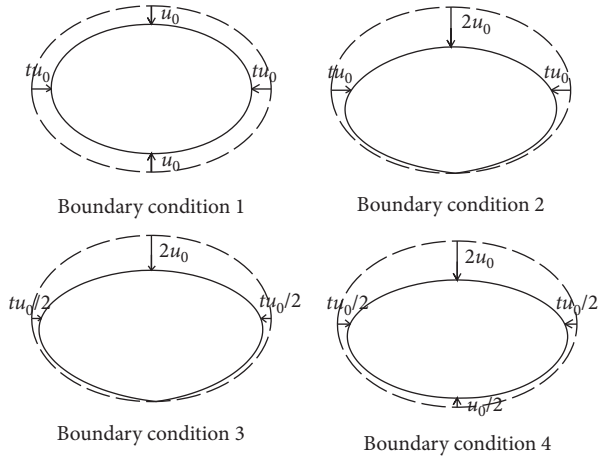
FIGURE 3: Boundary conditions of the given displacement.

$$\text{B.C.} - 3: u_c = -u_0 \left(1 + \sin \theta - \left(1 - \frac{t}{2} \right) \cos^2 \theta \right), \tag{35}$$

$$\text{B.C.} - 4: u_c = -\frac{u_0}{4} \left(5 + 3 \sin \theta - (5 - 2t) \cos^2 \theta \right),$$
$$1 \le t \le \frac{a_1}{b_1}. \tag{36}$$

It should be noted that the given convergence patterns are reduced to the boundary conditions given by [19] when $t = 1$ and $a_1 = b_1$.

On the boundary of the elliptical cavity in the z-plane,

$$z_c = x_c + iy_c = (a \cos \theta + ib \sin \theta) \atop \overline{z}_c = x_c - iy_c = (a \cos \theta - ib \sin \theta) \Rightarrow \begin{cases} \cos \theta = \left(\dfrac{z_c + \overline{z}_c}{2a} \right), \\ \\ \sin \theta = \left(\dfrac{z_c - \overline{z}_c}{2bi} \right). \end{cases} \tag{37}$$

On the boundary of the unit circle in the ζ-plane,

$$\zeta = e^{i\vartheta} = \sigma,$$
$$\overline{\zeta} = e^{-i\vartheta} = \sigma^{-1}, \tag{38}$$

$$z_c = R \left(\zeta_c + \frac{m}{\zeta_c} \right) = R \left(\sigma + m\sigma^{-1} \right),$$
$$\overline{z}_c = R \left(\overline{\zeta}_c + \frac{m}{\overline{\zeta}_c} \right) = R \left(\sigma^{-1} + m\sigma \right). \tag{39}$$

By substituting (35) into (3),

$$\begin{cases} \cos \theta = \dfrac{R(1 + m)\left(\sigma + \sigma^{-1} \right)}{2a}, \\ \\ \sin \theta = \dfrac{R(1 - m)\left(\sigma - \sigma^{-1} \right)}{2bi}, \end{cases} \tag{40}$$

$$F(x, y) = 2G \left(u^0_{x_2} + iu^0_{y_2} \right) = 2Gu_c (\cos \theta + i \cos \theta). \tag{41}$$

By substituting (31)–(34) and (38) into (39), the displacement can be expressed as a polynomial of σ^k. The constant A_k is obtained through a comparison with (9). By substituting A_k in (8), the stress components are found.

2.2. Application to an Elliptical Tunnel in a Full Plane. Considering that an infinite plane contains an elliptical tunnel cavity with a major axis $2a_1$ and a minor axis $2b_1$, as illustrated in Figure 1, a uniform radial displacement (B.C.1, $t = 1$) is assumed as the boundary condition for the elliptical tunnel cavity. The initial elliptical tunnel cavity is converged without altering the ratio of the semimajor axis to the semiminor axis of the elliptical tunnel cavity.

$$\frac{a_1}{a_2} = \frac{b_1}{b_2},$$
$$= \frac{\rho_1}{\rho_2}, \tag{42}$$
$$= \frac{1}{k},$$

where a_2 and b_2 correspond to the current semimajor and semiminor axes of the elliptical tunnel cavity, respectively; ρ_1, ρ_2 denote the angular length of the elliptical tunnel at any point before and after the deformation in the polar coordinate system, respectively; and k is the convergence ratio.

At the boundary of the elliptical tunnel cavity,

$$u^0_x = -(1 - k),$$
$$x = -\frac{(1 - k)(z + \overline{z})}{2} = -(1 - k)R \frac{\left[(m + 1)\sigma + (m + 1)\sigma^{-1} \right]}{2},$$
$$u^0_y = -(1 - k),$$
$$y = -\frac{(1 - k)(z - \overline{z})}{2} = -(1 - k)R \frac{\left[(1 - m)\sigma - (1 - m)\sigma^{-1} \right]}{2}. \tag{43}$$

By comparing (23) and (25), there are only two Fourier coefficients for the complex variable function:

$$A_1 = 2G(1-k)R,$$
$$A_{-1} = 2G(1-k)Rm, \quad\quad (44)$$
$$A_k = 0 \, (k > 1, k < -1).$$

2.2.1. Comparison of the Solutions for the Elliptical and Circular Tunnels.

The ratio of the semimajor and semiminor axes of the initial elliptical cavity (a/b) is 5/4, and the soil Poisson's ratio equals 0.5. The elastic solution of the elliptical tunnel cavity and the circumscribed circular tunnel cavity expansion shown in Figure 4 are obtained using the analytical method. The orthoradial displacement and shearing stress caused by the radial displacement of the circumscribed circular tunnel cavity and elliptical tunnel cavity along the semimajor and semiminor axis directions of the elliptical tunnel cavity are zero.

Figure 5 shows the radial displacement variation of the soil in relation to the distance from the center of the cavities, normalized by the radius of the circumscribed circular tunnel cavity. The analytical results of the radial displacement along the major and minor axes of the elliptical tunnel cavity are compared with the results of the circumscribed circular tunnel cavity.

It can be seen that the radial displacement of the soil around the elliptical tunnel cavity along the major and minor axes and circumscribed circular tunnel cavity decreases with the increase in the distance from the cavity's center and that it eventually tends to zero. The radial displacement of the soil along the major axis of the elliptical tunnel cavity is equal to that of the circumscribed circular tunnel cavity.

Figure 6 shows the radial and orthoradial stresses of the soil, which are caused by the radial displacement of the elliptical tunnel cavity and circumscribed circular tunnel cavity in relation to the distance from the center of the cavities. The magnitude of the radial stress of the soil along the semimajor axis of the elliptical tunnel cavity is larger than the radial stress of the soil along the radial direction of the circumscribed circular. The radial stresses along the semiminor axis of the elliptical tunnel cavity are minimum. The magnitude of the soil orthoradial stress induced by the radial displacement of the circumscribed circular tunnel cavity is larger than the soil orthoradial stress caused by the elliptical tunnel cavity. As the distance from the cavity center increased, the soil radial and orthoradial stresses around the elliptical tunnel cavity and circumscribed circular tunnel cavity tend to zero.

When $a = 4$ m, $G = 2000$ kPa, and $k = 0.92$ are considered, the magnitudes of the soil stress and displacement around the cavities are very small ($|\sigma_\rho| < 1$ kPa, $|\sigma_\theta| < 1$ kPa, $|\tau_{\rho\theta}| < 1$ kPa, $|u_\rho| < 0.010$ mm), at ~50 m from the cavity center. That is, the influence radius of the convergence of the elliptical cavity is ~20 times that of the semimajor axis.

2.2.2. Elastic Solutions of the Soil around an Elliptical Tunnel Cavity Using the Analytical and Finite Element Method Methods.

To validate the accuracy of the results, the solution is compared with a finite element method (FEM) calculation using the ABAQUS 2D software. The FEM model size is 1000×1000 m, and the boundary elements were infinite elements. Since the whole model is symmetric about the origin point and the x, y axes, one-quarter of the whole model is selected for comparison. The soil's stress and displacement around the elliptical ellipse are compared and analyzed. Figures 7 and 8 show the contour of the normalized stresses and displacements of the soil from the analytical solution with the FEM solution. The selected parameters of the elliptical tunnel cavity and soil are as follows:

$$\frac{a_1}{H} = \frac{5}{47},$$
$$k = 0.92,$$
$$G = 2000 \text{ kPa}, \quad\quad (45)$$
$$v = 0.4.$$

where a is the semimajor axis, k is the convergence ratio, G is the shear modulus, and v is the soil Poisson's ratio.

It can be seen from Figures 7(a)–7(e) that the soil shearing stress in the directions of the x-axis and the y-axis is zero. There are some differences between the values of the vertical stresses and displacements because the boundary condition of the ABAQUS model is finite and fixed at the bottom. The soil stress and displacement calculated using the complex function method and FEM are approximately equal, which verifies the correctness of the theoretical method in this paper.

2.2.3. Elastic Solutions of the Soil around the Elliptical Tunnel Cavity with Different Ellipticity Values.

Figures 8(a)–8(e) show the soil stress and displacement caused by the convergence of the elliptical cavities with different ellipticity values. From the figures, it can be seen that the ellipticity of the cavity decreased, the soil stress in the x-axis direction of the soil increased, and that the soil stress and displacement in the y-axis direction decreases. Also, the soil displacement in the x-axis direction can be seen.

3. Elastic Solutions in a Half-Plane

3.1. Virtual Image Technique.

So far, the displacement fields are considered in an infinite plane. The ground displacement induced by the deformation of the tunnel cavity with the arbitrary cross section in the half-plane can be obtained using the virtual image technique.

Figure 9 shows the diagram of the virtual image technique used in this paper. Supposing that $y = 0$ is the surface, there are two convergence elliptical cavities at the points O_1 $(0, -h)$ and O_2 $(0, h)$. Then, at the surface,
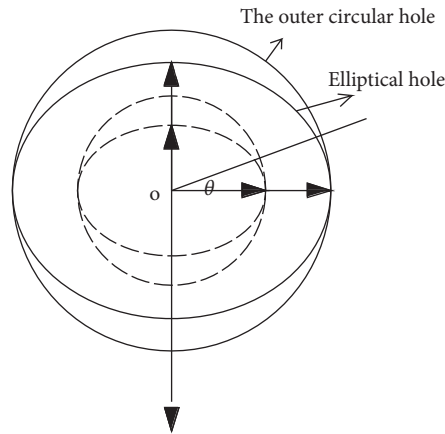
FIGURE 4: Current elliptical tunnel cavity and circumscribed circular tunnel cavity before and after the radial displacement at the boundary of the original tunnel cavity.
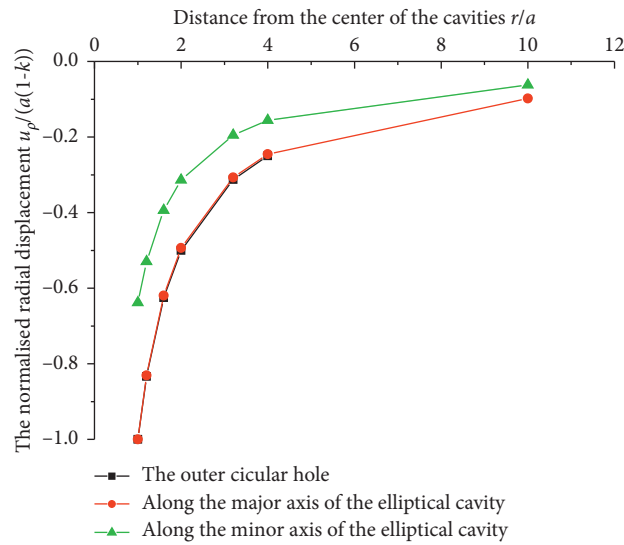
FIGURE 5: Distribution of the radial displacement of the soil due to the radial displacement at the boundaries of the cavities.
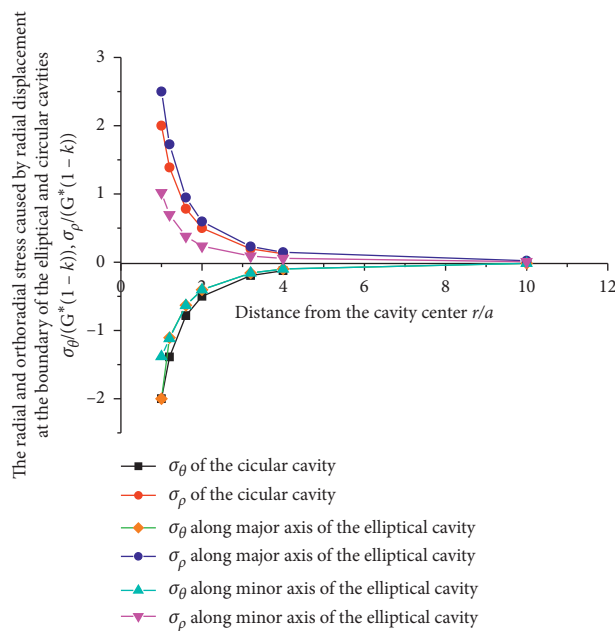
FIGURE 6: Distribution of the stress of the soil elements due to the radial displacement at the boundaries of the cavities.
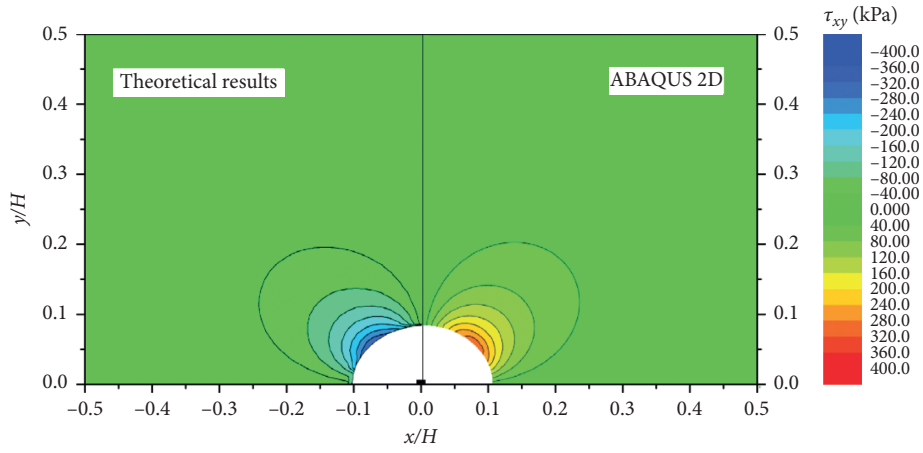
(a)
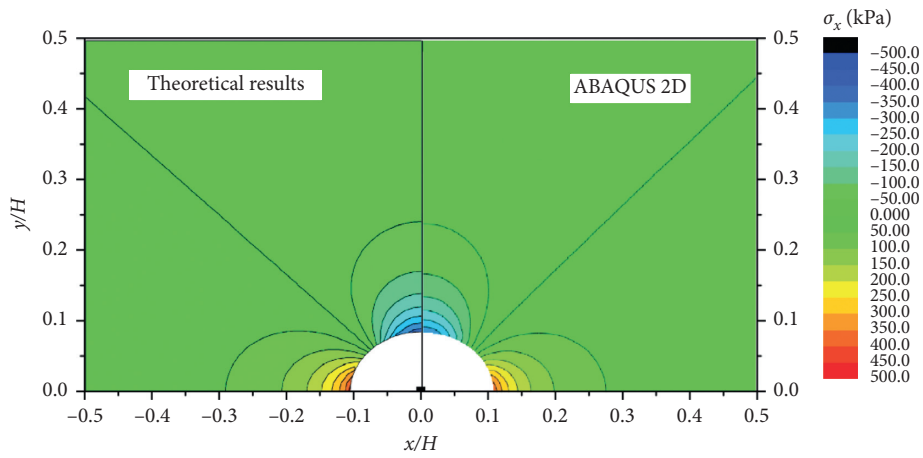
(b)
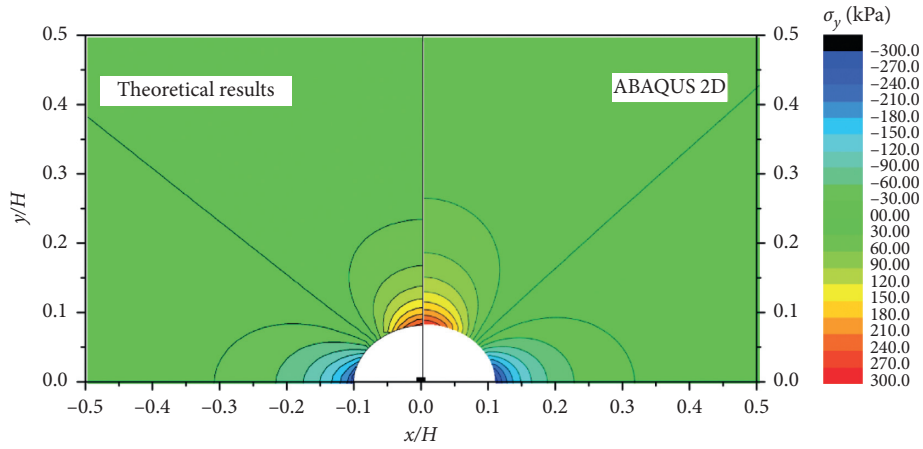
(c)

Figure 7: Continued.

(d)

(e)
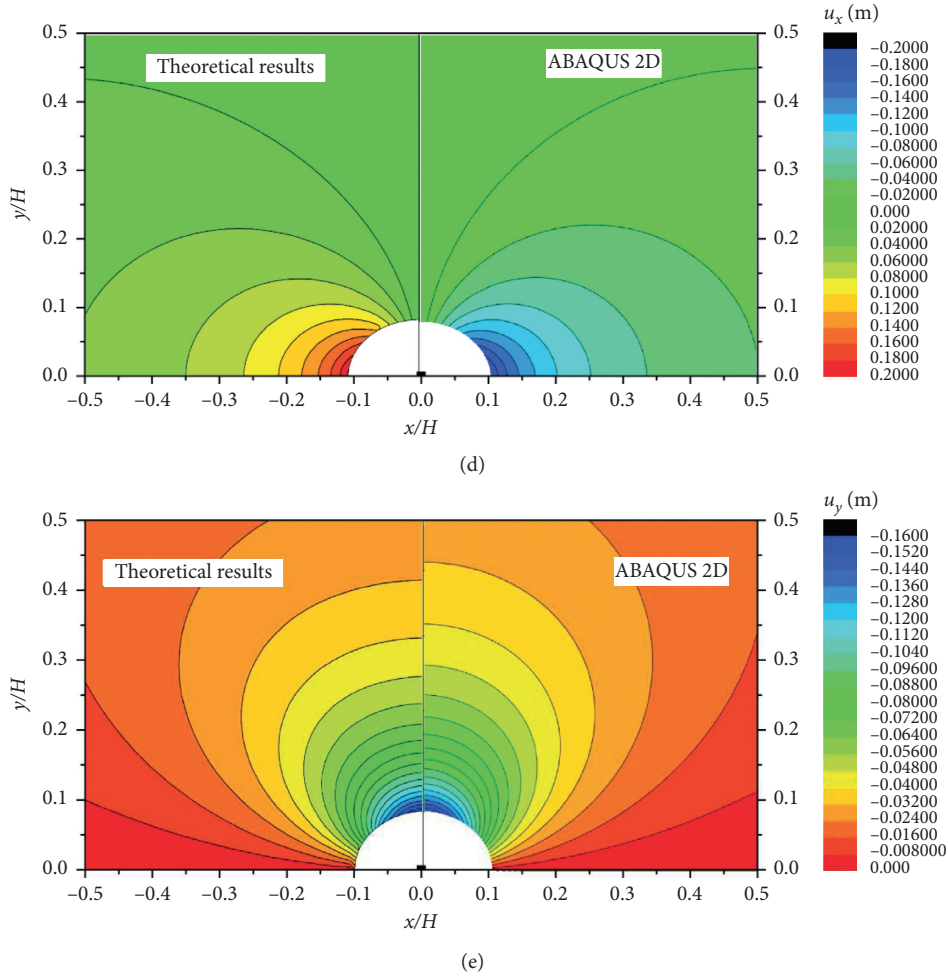
FIGURE 7: Contours of the normalized stresses and displacements in the case of (a)/(b) = 2 as derived by the theoretical method and ABAQUS 2D. (a) Shear stress of the soil. (b) Soil stress in the x-direction. (c) Soil stress in the y-direction. (d) Soil displacement in the x-direction. (e) Soil displacement in the y-direction.

$$u_y|_{y=0} = 0;$$
$$u_x|_{y=0} = 2u_x(x, h),$$
$$\sigma_y|_{y=0} = 2\sigma_y(x, h);$$
$$\tau_{xy}|_{y=0} = 0.$$

(46)

The boundary of the half-plane is considered to be stress-free. The normal stresses at the surface $y = 0$ are made to be equal to zero, meaning that it is necessary to apply a reverse force to balance the normal stress at the surface induced by the two convergence elliptical tunnel cavities. This problem turns into a Boussinesq problem for the half plane $y \leq 0$ with the following boundary conditions:

$$y = 0: \sigma_{y1} = -2\sigma_y(x, 0),$$
$$\tau_{xy}(x, 0) = 0.$$

(47)

In the case of a circular tunnel, the ground displacement induced by the reverse vertical stress applied to the ground surface can be solved using the Fourier formula [23]. When the section shape of the tunnel is elliptical, the vertical stress expression is complex, and the Fourier transform is no longer applicable. In this paper, the numerical solution of the surface displacement can be derived using the formula proposed by [39].

Reference [39] uses the complex variable function and virtual image technique to obtain the displacement caused

(a)

(b)

(c)

(d)
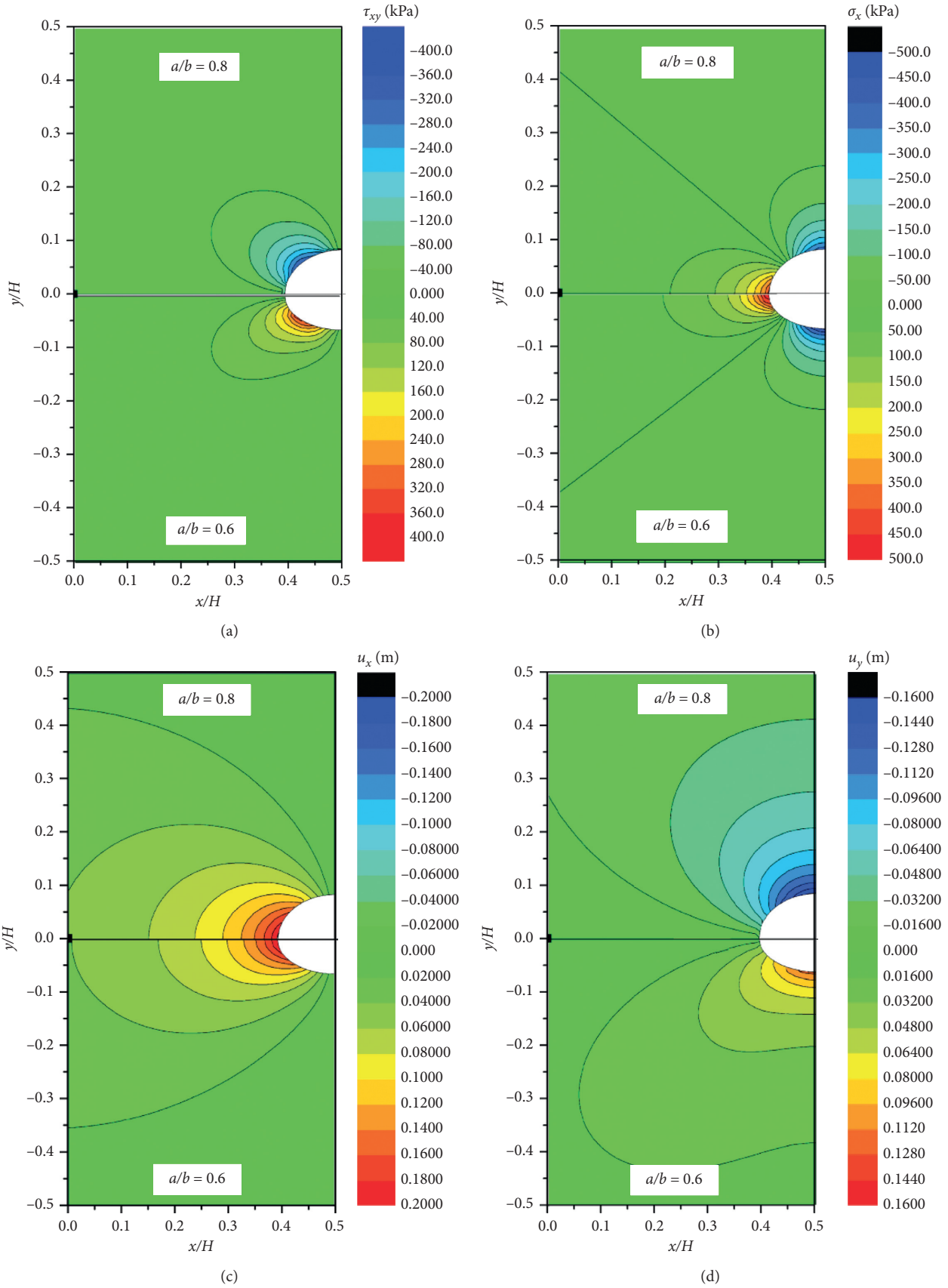
Figure 8: Continued.

(e)
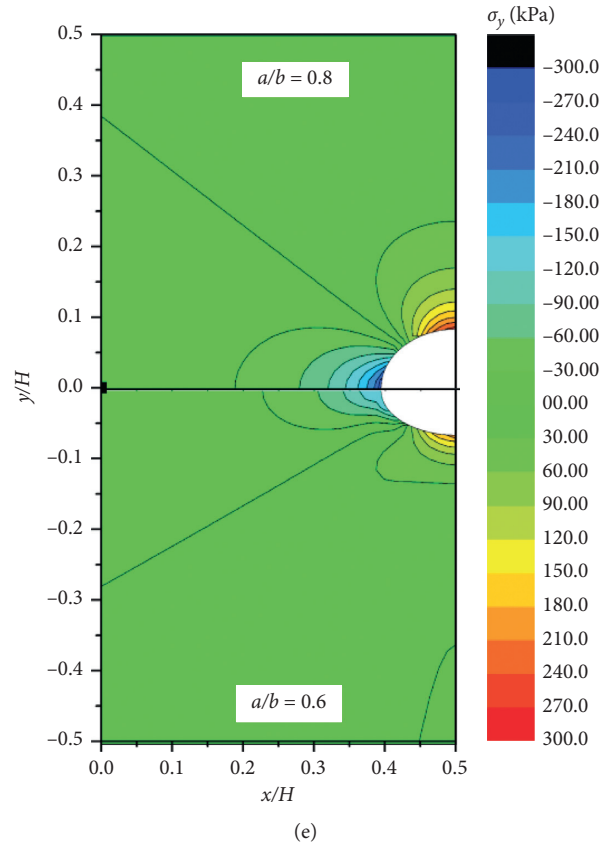
FIGURE 8: Contours of the normalized stresses and displacements in the case of the elliptical tunnel with different ellipticity values. (a) Shearing stress of soil. (b) Soil stress in the x-direction. (c) Soil displacement in the x-direction. (d) Soil displacement in the y-direction. (e) Soil stress in the y-direction.

by the vertical and horizontal concentrated forces at any point in the half plane. When a unit vertical concentrated force applies to a point m in the half plane, as illustrated in Figure 10, the stress function becomes

$$\varphi_1(z) = \frac{iP}{8\pi(1-v)}\log\left(\frac{z-ih}{z+ih}\right) - \frac{iP}{2\pi}\log(z-ih) + \frac{P}{4\pi(1-v)}\frac{h}{z-ih},$$

$$\psi_1(z) = \frac{iP}{8\pi(1-v)}\left[(3-4v)\log\left(\frac{z-ih}{z+ih} + \frac{ih}{z-ih} + \frac{ih}{z+ih}\right)\right],$$

$$-\frac{iP}{2\pi}\log(z-ih) - \left(\frac{P(1-2v)}{4\pi(1-v)}\frac{ih}{z-ih}\right) + \frac{P}{4\pi((1-v))}\frac{hz}{(z-ih)^2},$$

(48)

$$2G\left(u_x + iu_y\right) = \kappa\varphi_1(z) - z\overline{\varphi_1'(z)} - \overline{\psi_1(z)}.$$

(49)

Similarly, the stress function is obtained when a unit horizontal concentrated force is applied to a point m in the half plane, as seen in Figure 10(b). Supposing that $h = 0$ in (44) and (43), the surface displacement caused by the unit force applied to the surface can be obtained.

Figure 11 shows a schematic diagram of solving the vertical displacement method. Due to the concentrated force P applied to the boundary, the subsidence of the point K to the boundary (the distance from the origin is r) relative to the subsidence of the reference point B (the distance from the origin is s) is

$$\eta = \frac{2P(1-v^2)}{\pi E}\ln\frac{s}{r}.$$

(50)

The relative horizontal displacement is
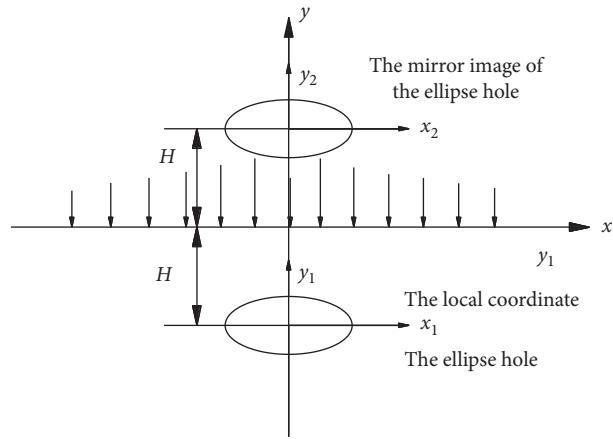
FIGURE 9: Diagram of the virtual image technique.

(a)

(b)
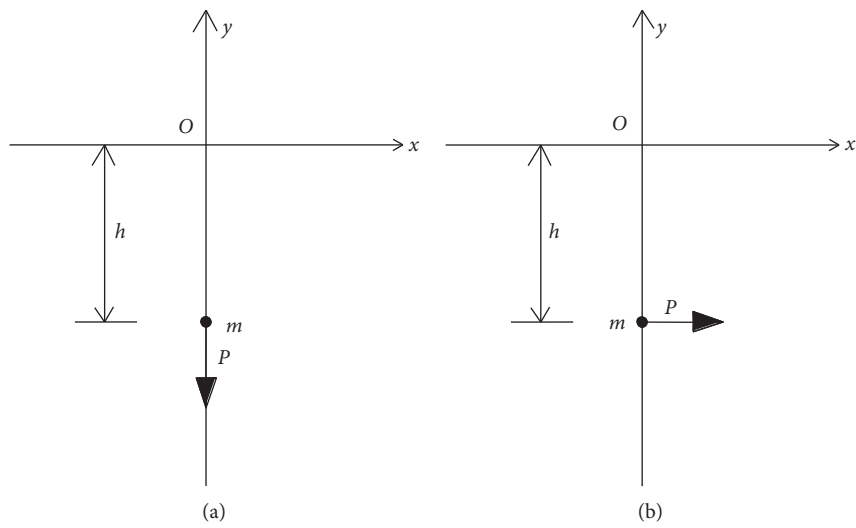
FIGURE 10: Schematic diagram of the vertical and horizontal concentrated forces applied to the half-plane.
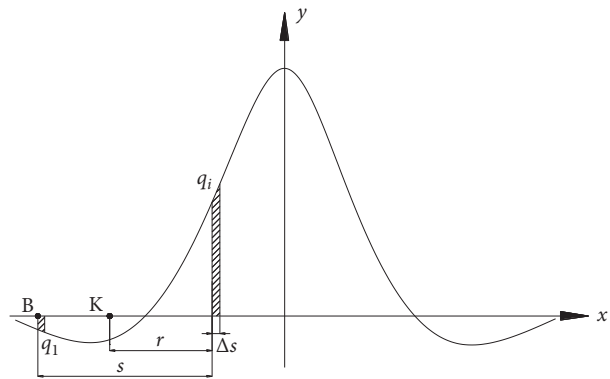
FIGURE 11: Schematic diagram of solving the vertical displacement method.
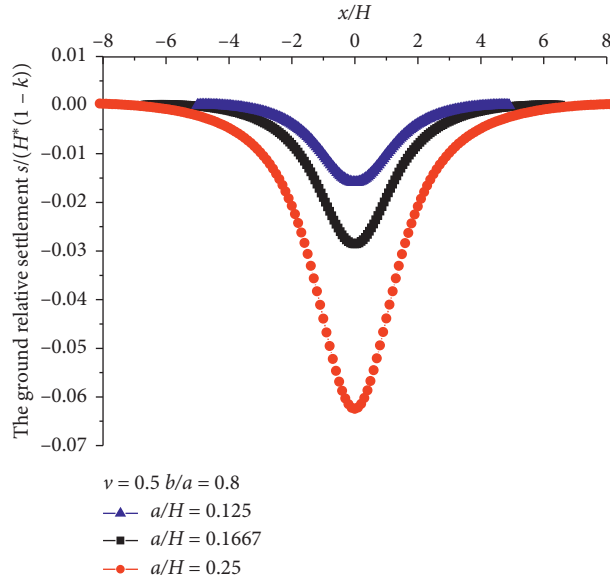
FIGURE 12: Vertical displacement of ground when a/H changes.
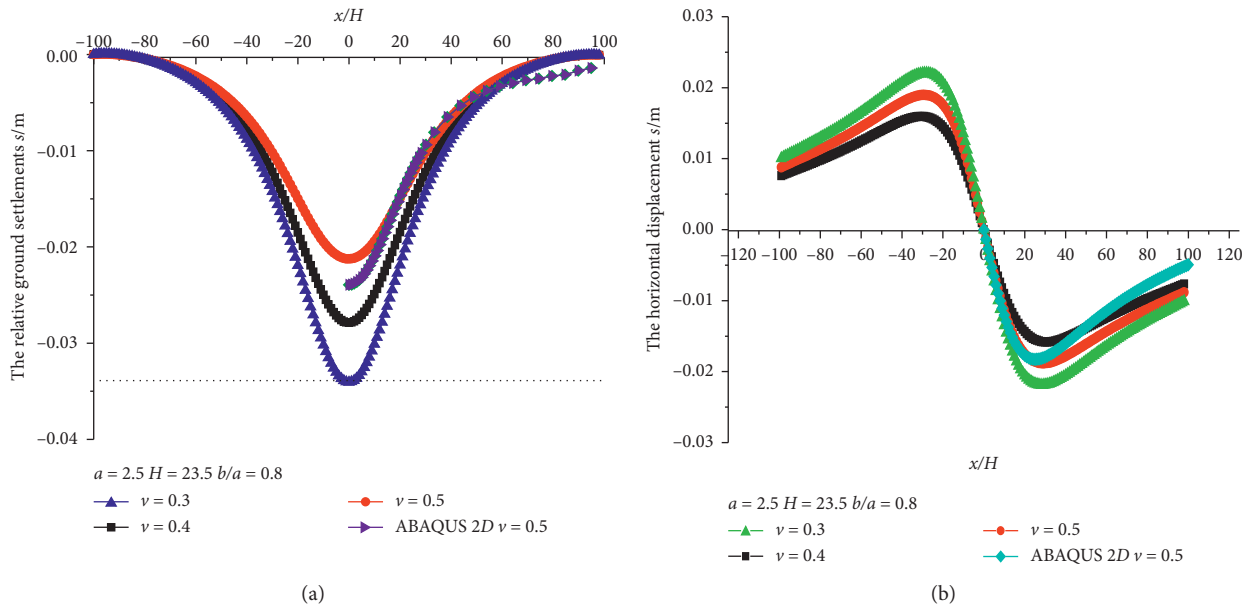
FIGURE 13: Influence of Poisson's ratio on the horizontal and vertical displacements of ground induced by the elliptical tunnel cavity's deformation. (a) Vertical displacement of ground. (b) Horizontal displacement of ground.

$$u_x = -\frac{1+\nu}{\pi E}\left[\frac{(3-4\nu)}{4(1-\nu)}\ln\frac{r^2}{s^2} + \left(\frac{(1-2\nu)^2}{2(1-\nu)}\right)\ln\frac{r}{s}\right], \quad (51)$$

where r is the distance from the position of the concentrated force P to the point K and s is the distance between the position of the concentrated force P and the reference point B. The method adopted in this paper is mainly to divide the applied uneven vertical load into n parts. As shown in Figure 10, the vertical load applied to the boundary was symmetrical about the y-axis, and the magnitude of the vertical load at infinity was zero. The reference point B is the

start point of the 1st load, and point K is the start point of the j-th load. The settlement of point K could be expressed as follows:

$$\eta_K = \sum_{i=1}^{n}\frac{2q_i\Delta s}{\pi E}\ln\frac{(i-1)\Delta s}{|(i-1)\Delta s - r_{BK}|} \quad r_{BK} \neq (i-1)\Delta s,$$

$$r_{BK} = (j-1)\Delta s.$$

$$(52)$$

The relative settlement of point K to the point B could be expressed as follows:

$$\eta_K = \sum_{i=1}^{n} \frac{2q_i \Delta s}{\pi E} \text{In} \frac{(i-1)}{|(i-j)|} \quad i \neq j. \tag{53}$$

The farther the distance from the reference point B to the origin point and the finer the load element division, the more accurate the results.

3.2. Vertical and Horizontal Displacements Induced by the Elliptical Tunnel. Figure 12 shows that when the buried depth of the tunnel decreased, the ground displacement caused by the elliptical tunnel decreased. The vertical displacement of any point on the ground in Figure 13(a) is relative to the vertical displacement of point $x = -100$. Since the horizontal stress applied to the ground is symmetrical about the y-axis, the horizontal displacement of the ground should be symmetrical with respect to the origin point, and the horizontal displacement of the origin point is zero, so the relative horizontal displacement of any point subtracts the horizontal displacement of the origin point can obtain the absolute value of the horizontal displacement of the point, as shown in Figure 13(b). It can be seen from the above two figures that when the depth of the elliptical tunnel decreased, the surface displacement caused by the contraction of the elliptical tunnel gradually decreases. When Poisson's ratio decreases, the relative vertical displacement and horizontal displacement of the ground caused by the elliptical tunnel increases.

4. Conclusions

The paper proposes an analytical method for modeling ground displacements for the tunnels with arbitrary cross sections in clay. The following main conclusions are drawn:

(1) Once an approximate polynomial mapping for the original and deformed shapes of a cavity boundary is obtained, the elastic solution in the full plane can be determined using the proposed analytical method in this paper.

(2) The magnitude of the radial stress of the soil along the semimajor axis of the elliptical tunnel cavity is larger than the radial stress of the soil along the radial direction of the circumscribed circular. The magnitude of the orthoradial stress of the soil induced by the radial displacement of the circumscribed circular tunnel cavity is larger than the orthoradial stresses of the soil caused by the elliptical tunnel cavity. Also, the influence radius of the convergence of the elliptical cavity is 20 times that of the semimajor axis in the full plane.

(3) A good agreement of elastic solutions is found between the analytical solutions and FEM results in the full plane for the elliptical tunnel. As the distance from the cavity center increases, the soil radial and orthoradial stresses around the elliptical tunnel cavity decrease.

(4) The ellipticity of the tunnel cavity decreases, and the soil stress in the x-axis direction of the soil increases.

Also, the soil displacement in the x-axis direction and the soil stress and displacement in the y-axis direction decrease.

(5) The surface displacement in the half-plane can be obtained using the virtual image technique. When the depth of the elliptical tunnel decreases, the surface displacement caused by the contraction of the elliptical tunnel gradually decreases. When Poisson's ratio of the soil decreases, the relative vertical and horizontal displacements of the ground caused by the elliptical tunnel increase.

The solution is under the assumption of elasticity and the certain deformation at the tunnel boundary, and the surcharge loadings and internal forces are not considered in the derivation. The solution is only valid for the shallow tunnels excavated in clay.

Data Availability

The data used to support the findings of this study are available from the corresponding author upon request.

Conflicts of Interest

The authors declare that there are no conflicts of interest regarding the publication of this paper.

Acknowledgments

References

[1] A. J. Abbo, D. W. Wilson, S. W. Sloan, and A. V. Lyamin, "Undrained stability of wide rectangular tunnels," *Computers and Geotechnics*, vol. 53, no. 3, pp. 46–59, 2013.

[2] B. Chow, "Double-O-Tube shield tunneling technology in the shanghai rail transit project," *Tunnelling and Underground Space Technology*, vol. 21, no. 6, pp. 594–601, 2006.

[3] R. Liang, C. Kang, L. Xiang et al., "Responses of in-service shield tunnel to overcrossing tunneling in soft ground," *Environmental Earth Sciences*, vol. 80, p. 183, 2021.

[4] H. Nakamura, T. Kubota, M. Furukawa, and T. Nakao, "Unified construction of running track tunnel and crossover tunnel for subway by rectangular shape double track cross-section shield machine," *Tunnelling and Underground Space Technology*, vol. 18, no. 2, pp. 253–262, 2003.

[5] J. B. Si, Y. H. Zhu, C. Ji, and S. H. Zhou, "Measurement and analysis of vertical deformation of stratum induced by quasi-rectangular shield tunneling in soft ground," *Chinese Journal of Rock Mechanics And Engineering*, vol. 36, no. 6, pp. 1551–1558, 2017, in Chinese.

[6] P. Guo., X. Gong, and Y. Wang, "Displacement and force analyses of braced structure of deep excavation considering unsymmetrical surcharge effect," *Computers and Geotechnics*, vol. 113, Article ID 103102, 2019.

[7] D. Wu, K. Xu, P. Guo, G. Lei, K. Cheng, and X. Gong, "Ground deformation characteristics induced by mechanized shield twin tunnelling along curved alignments," *Advances in Civil Engineering*, vol. 2021, Article ID 6640072, 17 pages, 2021.

[8] Y. Koyama, "Present status and technology of shield tunnelling method in Japan," *Tunnelling and Underground Space Technology*, vol. 18, pp. 145–159, 2013.

[9] R. J. Mair, "Tunnelling and geotechnics: new horizons," *Géotechnique*, vol. 58, no. 9, pp. 695–736, 2008.

[10] C. G. Lin, T. D. Xia, R. Z. Liang, and S. M. Wu, "Estimation of shield tunnelling-induced ground surface settlements by virtual image technique," *Chinese Journal of Geotechnical Engineering*, vol. 36, no. 8, pp. 1438–1446, 2014, in Chinese.

[11] A. Verruijt, "He complex variable method," *Theory of Groundwater Flow*, Macmillan Education, London, UK, 1982.

[12] S. G. Lekhnitskii, P. Fern, and J. J. Brandstatter, *Theory of Elasticity of an Anisotropic Elastic Body*, Holden Day, San Fransisco, NW, USA, 1963.

[13] A. K. Kapoor, "Cauchy's integral formula," *Principles and Problem Sessions*, Cambridge University Press India Private Limited, Delhi, India, 2015.

[14] A. Bobet, "Lined circular tunnels in elastic transversely anisotropic rock at depth," *Rock Mechanics and Rock Engineering*, vol. 44, no. 2, pp. 149–167, 2011.

[15] G. E. Exadaktylos and M. C. Stavropoulou, "A closed-form elastic solution for stresses and displacements around tunnels," *International Journal of Rock Mechanics and Mining Sciences*, vol. 39, no. 7, pp. 905–916, 2002.

[16] H. T. Manh, J. Sulem, and D. Subrin, "A closed-form solution for tunnels with arbitrary cross section excavated in elastic anisotropic ground," *Rock Mechanics and Rock Engineering*, vol. 16, no. 3, pp. 277–288, 2015.

[17] Z. Zhang and Y. Sun, "Analytical solution for a deep tunnel with arbitrary cross section in a transversely isotropic rock mass," *International Journal of Rock Mechanics and Mining Sciences*, vol. 48, no. 8, pp. 1359–1363, 2011.

[18] A. Verruijt, "A complex variable solution for a deforming circular tunnel in an elastic half-plane," *International Journal for Numerical and Analytical Methods in Geomechanics*, vol. 21, no. 2, pp. 77–89, 1997.

[19] K. H. Park, "Elastic solution for tunneling-induced ground movements in clays," *International Journal of Geomechanics*, vol. 4, no. 4, pp. 310–318, 2004.

[20] K. H. Park, "Analytical solution for tunnelling-induced ground movement in clays," *Tunnelling and Underground Space Technology*, vol. 20, no. 3, pp. 249–261, 2005.

[21] F. Pinto and A. J. Whittle, "Ground movements due to shallow tunnels in soft ground. I: analytical solutions," *Journal of Geotechnical and Geoenvironmental Engineering*, vol. 140, no. 4, Article ID 04013040, 2013.

[22] C. Sagaseta, "Analysis of undrained soil deformation due to ground loss," *Géotechnique*, vol. 37, no. 3, pp. 301–320, 1987.

[23] A. Verruijt and J. R. Booker, "Surface settlements due to deformation of a tunnel in an elastic half-plane," *Géotechnique*, vol. 46, no. 4, pp. 753–756, 1996.

[24] D. M. Zymnis, A. J. Whittle, and I. Chatzigiannelis, "Effect of anisotropy in ground movements caused by tunnelling," *Géotechnique*, vol. 63, no. 13, pp. 1083–1102, 2013.

[25] A. Inokuma, T. Ishimura, H. Asakura et al., "The design of the primary lining for an elliptical shield tunnel," in *Proceeding of the International Congress towards New Worlds in Tunnelling*, Helsinki, Finland, May 1992.

[26] C. He, K. Feng, and Y. Fang, "Review and prospects on constmcting technologies of metro tunnels using shield tunnelling method," *Joumal of Southwest Jiaotong University*, vol. 50, no. 1, pp. 97–109, 2015, in Chinese.

[27] Y. Kashima, N. Kondo, and M. Inoue, "Development and application of the DPLEX shield method: results of experiments using shield and segment models and application of the method in tunnel construction," *Tunnelling and Underground Space Technology*, vol. 11, no. 1, pp. 45–50, 1996.

[28] T. Sonoda, H. Hagiwara, H. Osaki, T. Noguchi, and M. Nakamura, "Construction of underground space by a new shield tunnelling method: spiral tunnelling and ramification of multi-circular face shield," *Tunnelling and Underground Space Technology*, vol. 7, no. 4, pp. 355–361, 1992.

[29] T. L. Sun, "The research status and engineering application of non-circular shield method," *Journal of Railway Science and Engineering*, vol. 9, pp. 1959–1966, 2017, in Chinese.

[30] H. N. Wang, G. S. Zeng, and M. J. Jiang, "Analytical stress and displacement around non-circular tunnels in semi-infinite ground," *Applied Mathematical Modelling*, vol. 63, pp. 303–328, 2018.

[31] I. S. Sokolnikoff, *Mathematical Theory of Elasticity*, McGraw-Hill, Pennnsylvania, NW, USA, 1956.

[32] A. Z. Lu, N. Zhang, and L. Kuang, "Analytic solutions of stress and displacement for a non-circular tunnel at great depth including support delay," *International Journal of Rock Mechanics and Mining Sciences*, vol. 70, no. 9, pp. 69–81, 2014.

[33] A. Flamant, "Sur la répartition des pressions dans un solide rectangulaire chargé transversalement," *ComptesRendus Academiedes Scincies Paris*, vol. 114, pp. 1465–1468, 1892.

[34] N. I. Muskhelishvili, *Some Basic Problems of the Mathematical Theory of Elasticity*, Popko Noordhoff, Groningen, Netherlands, 1963.

[35] C. Q. Ru, "Eshelby inclusion of arbitrary shape in an anisotropic plane or half-plActa," *Acta Mechanica*, vol. 160, no. 3, pp. 219–234, 2003.

[36] W. Zou, Q. He, M. Huang, and Q. Zheng, "Eshelby's problem of non-elliptical inclusions," *Journal of the Mechanics and Physics of Solids*, vol. 58, no. 3, pp. 346–372, 2010.

[37] S. R. J. Heller, J. S. Brock, and R. Bart, "The stresses around a rectangular opening with rounded corners in a uniformly loaded plate," in *Proceedings of the Third U.S. National Congress of Applied Mechanics*, pp. 357–368, Brown University, Rhode Island, NW, USA, June 1959.

[38] F. Yang, J. Zhang, J. Yang et al., "Stability analysis of unlined elliptical tunnel using finite element upper-bound method with rigid translatory moving elements," *Tunnelling and Underground Space Technology*, vol. 50, pp. 13–22, 2015.

[39] E. Melan, "Der Spannungszustand der durch eine Einzelkraft im Innern beanspruchten Halbscheibe," *ZAMM—Journal of Applied Mathematics and Mechanics/Zeitschrift für Angewandte Mathematik und Mechanik*, vol. 12, no. 6, pp. 343–346, 1932.

Research Article

Performance of a Large-Scale Excavation by Bottom-Up Technique in Hangzhou Soft Clay

Ri-qing Xu ⓘ,[1,2] **Yi-hong Zhu** ⓘ,[1,2] **and Pan Ding** ⓘ[1,2]

[1]*Research Center of Coastal and Urban Geotechnical Engineering of Zhejiang University, Hangzhou 310058, China*
[2]*Engineering Research Center of Urban Underground Space Development of Zhejiang Province, Hangzhou 310058, China*

Correspondence should be addressed to Yi-hong Zhu; zjuzhuyihong@zju.edu.cn

This paper studied the excavation of a foundation pit above a running subway tunnel in Hangzhou soft soil. The zoned excavation and top-down construction techniques were adopted to control the deformation caused by foundation pit excavation. The excavation was divided into four parts, named Zone A, B, C, and D. Zone A adopted temporary diagonal bracing, and the control effect of deformation was poor; it was cancelled and changed to rapid excavation and thicker cushion in Zones B, C, and D. During the whole construction process, the lateral displacement and settlement of the diaphragm wall, surrounding ground surface, and building settlement were monitored and analysed. The data showed that the lateral displacement of the diaphragm wall was effectively reduced by the zoned excavation technique, and the maximum lateral displacement value of the diaphragm wall in Zone A was the least; rapid excavation and reduced soil exposure time also could effectively control the deformation, and the lateral displacement of the diaphragm wall in Zone C is less than Zone B and Zone D. The ground settlement is strongly related to the lateral displacement of the diaphragm wall. In order to reduce the surrounding ground and building settlements, efforts should be made to reduce the wall lateral displacement.

1. Introduction

In recent years, the scale of Hangzhou has expanded rapidly. The development of underground space will cause the redistribution of soil stress and affect the surrounding environment. Development in the central area of the city will have a greater impact on nearby buildings. In order to make full use of the land resources in the central area of the city, the excavation depth of the foundation pit is large and the scope of influence is wide. With the continuous maturity of engineering technology in our country, the core contradiction of deep foundation pit excavation has gradually changed from the problem of foundation pit safety to the problem of foundation pit deformation control.

Scholars had collected a large number of excavation cases, compared the deformation characteristics of foundation pits under various geological conditions with indicators such as the maximum lateral displacement of the excavation and the maximum ground surface settlement, and then established empirical parameters in different regions for future design practices [1–4]. Some scholars also conducted statistical analysis on regional foundation pits and formed regional indicators; the maximum lateral displacement of the foundation pit in the hard clay soil area collected by Clough [5], Yoo [6], Long [7], etc., was between 0.05 and 0.20% H_e (H_e was the excavation depth of the foundation pit, omitted later). The maximum lateral displacement of foundation pits in soft soil areas collected by Ou [8] and Long [7] was between 0.40 and 0.48% H_e.

Chinese scholars had also performed the analysis of deformation characteristics of foundation pits. Wang [9, 10] conducted a statistical analysis of the deformation of the foundation pit under the condition of deep and soft soil in the Shanghai area. It was found that the average horizontal displacement of foundation pits in the Shanghai area was 0.26–0.50% H_e. Tan [11, 12] reported a large-scale deep foundation pit in Shanghai, and the maximum lateral

displacement ranged between 0.35% H_e and 0.55% H_e. And, many other cases had also been reported and used in foundation pit deformation analysis [13, 14].

This project was located in a prosperous land in the center of Hangzhou city. Using the top-down construction method, the excavation depth of the foundation pit reached 23.0 m. The method to control the deformation of the project could be available for reference for similar projects of the same type.

2. Project and Environmental Conditions

2.1. Project Description. This project was located in the Wulin Square of Hangzhou. It was a three-storey underground building with no ground buildings. The main structure of the underground mall was about 190 m long in the north-south direction and 220 m long in the east-west direction, with the area of 36794.5 m². The excavation depth reached 23.0 m, and the excavation depth of the section of Line 3 reached 27.0 m. There was a deep and weak soil layer within the excavation area, and it ranged between 5.3 m and 22.7 m below the ground.

The north side of the project was only 17.0 m away from Zhejiang Exhibition Hall, and the east side was only 30.1 m away from Zhejiang Telecom Company; the south side was Stadium Road; the northeast corner was the subway station Wulin Square Station. The Metro Line 1 was built, and the tunnel section of Metro Line 3 was constructed with the project.

The project was divided into two small foundation pits by Metro Line 1. The monitoring value of horizontal deformation could be used to explore the control effect of dividing a large foundation pit. During the implementation of the project, there were a large excavation and four vertical excavations in the western zone of Metro Line 1. So the excavation speed was relatively fast, and the support can be formed quickly. The influence of the excavation exposure time on the deformation of the foundation pit could be studied by comparing the deformation of the monitoring points on the east, west, and north sides of the foundation pit.

2.2. Engineering Geological Conditions. As shown in Figure 1, the embedment depth and representative soil properties of typical soil profiles in different soil layers were plotted, including the maximum, minimum, and average values of geotechnical parameters. Note that $Es_{0.1-0.2}$ was defined as the ratio of stress change to strain change when the stress increases from 0.1 MPa to 0.2 MPa in a one-dimensional compression test. The soil at the excavation depth was mainly composed of clay and silty clay, which was weak.

2.3. Design and Construction. The diaphragm wall of the foundation pit of this project was 1200 mm thick. The horizontal support system was dominated by structural floor slabs, and the three underground floors were designed with temporary diagonal bracing due to the

storey height. The thickness of the roof slab was 500 mm. The thickness was 300 mm for the B1 and B2 floor slabs, and it was 1200 mm thick for the bottom slabs. The cushion layer was 250 mm. The diagonal brace was supported by φ609-16 steel, supported on the corbel or pile cap, and the diagonal brace was supported on the bottom plate at a distance of 5.5 m from the diaphragm wall. The temporary diagonal brace layout is shown in Figure 2(a).

In order to control the deformation of the diaphragm wall of the foundation pit, a large-scale foundation reinforcement was carried out at the bottom of the pit which is shown by Figure 2(b). As shown in Figure 3, the foundation pit was divided into 4 zones.

At the beginning of the project, there were no significant problems in the construction according to the above construction plan, but when the construction reached the three-storey underground floor in Zone A, it was found that the diagonal brace needed about 40 days to reach the design strength level. On the contrary, due to the dense arrangement of diagonal braces, the construction work surface was difficult to expand after the diagonal braces were supported; the excavation efficiency was low. After the test construction in Zone A, the support plan was reviewed and discussed by experts. After the discussion, experts suggested to cancel the diagonal brace and thicken the cushion layer to 300 mm.

Table 1 shows the schedule of the main construction procedures of the project.

2.4. Built Environment. As shown in Figure 3, the surrounding environment of the project was complex and many buildings were affected by excavation. The Zhejiang Exhibition Hall was located to the north of the project, Hangzhou Tower and Hangzhou Theatre were located to the west, Stadium Road was located to the south, and the Zhejiang Association for Science and Technology Building and Zhejiang Telecom Company were located to the east. The southwest and southeast corners were crossing passages, and the northeast corner was the Wulin Square Station of Metro Line 1; the distance of these buildings away from the excavation ranges from 17.0 m to 33.2 m. The Zhejiang Exhibition Hall and the crossing passage were shallow foundations, and the rest of the buildings were pile foundations.

2.5. Engineering Monitoring. In order to comprehensively and systematically monitor the deformation and stress changes of the project during the construction period, the project has established a number of monitoring contents. The layout of monitoring points is shown in Figure 3. And, there were 21 inclinometer pipes for ground wall inclinometer monitoring, 15 inclinometer pipes for soil inclinometer monitoring outside the wall, 63 measuring points for ground settlement monitoring, 114 settlement observations for surrounding buildings, and 10 holes for groundwater level observation. Third-party monitoring would be monitored at a frequency of once every three
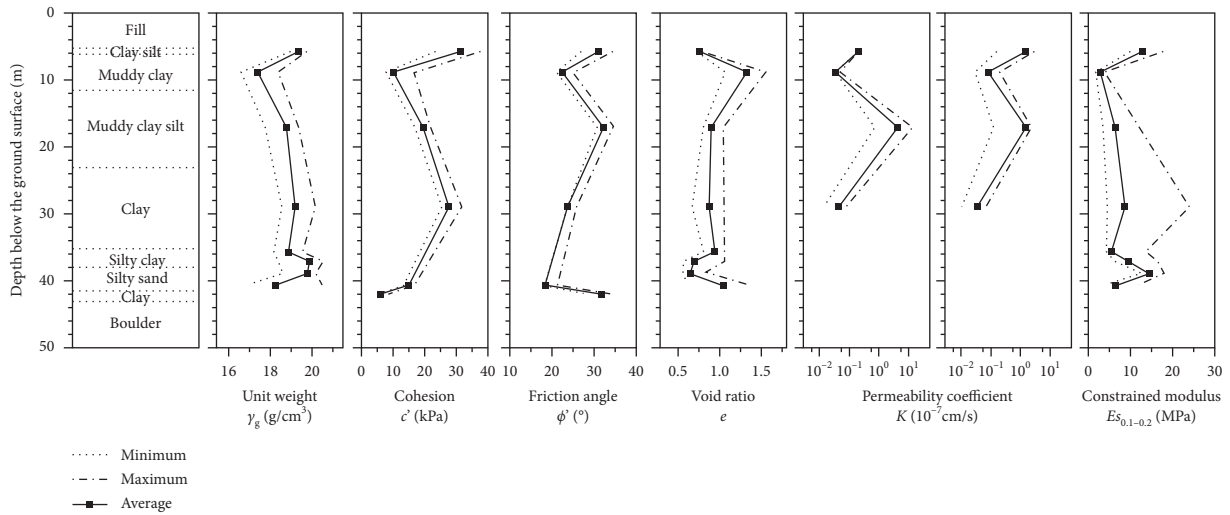
FIGURE 1: Soil profile and typical soil properties of the construction site.

(a)

(b)
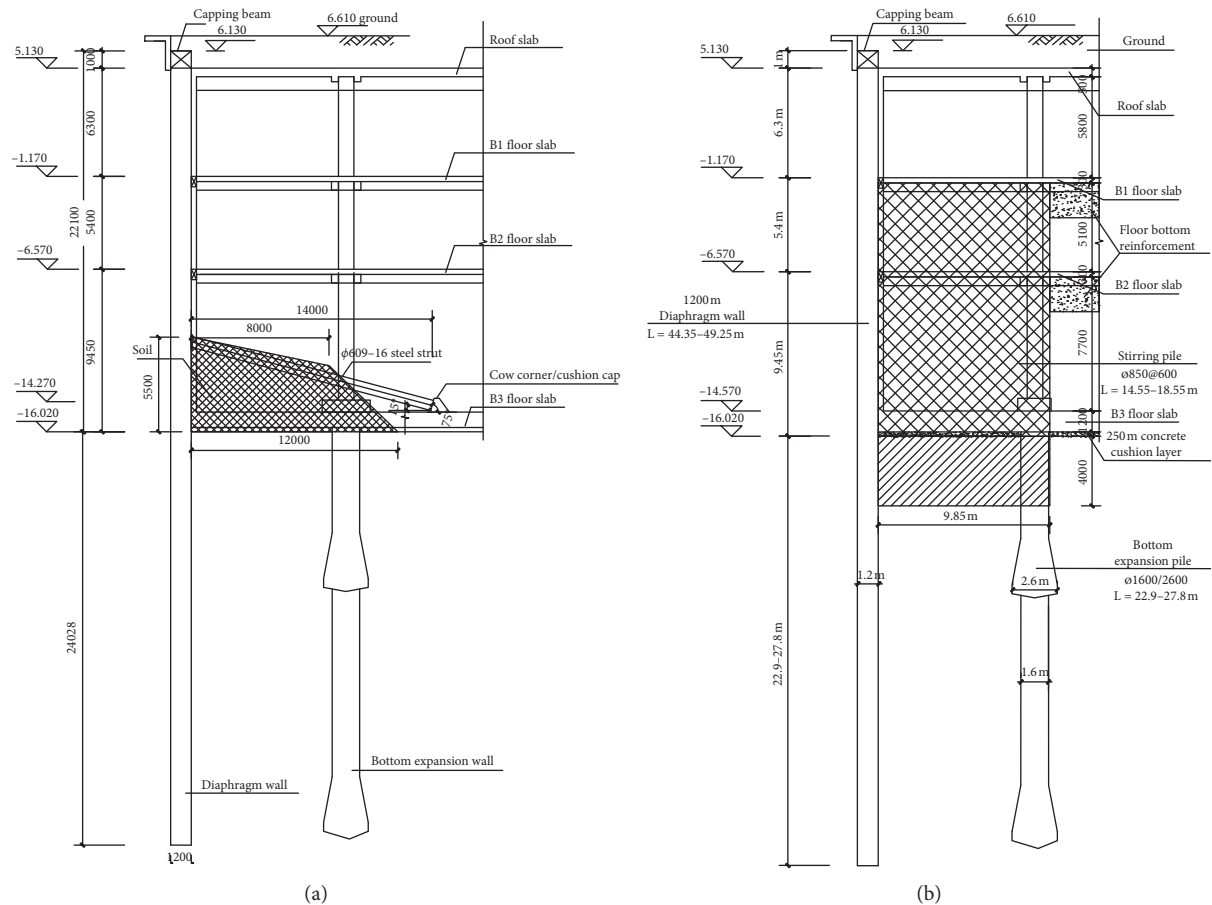
FIGURE 2: Typical cross of the excavation. (a) The south side of the excavation. (b) The north side of the excavation.

days and would be intensively monitored during peak construction periods and when monitoring was abnormal. The data in this paper was mainly based on third-party monitoring, and construction monitoring data was referred to during peak construction.

3. Field Measurements

3.1. Lateral Displacement of Diaphragm Wall.
As shown in Figure 4(a), the measurement point with the largest deformation among the measurement points on each side of
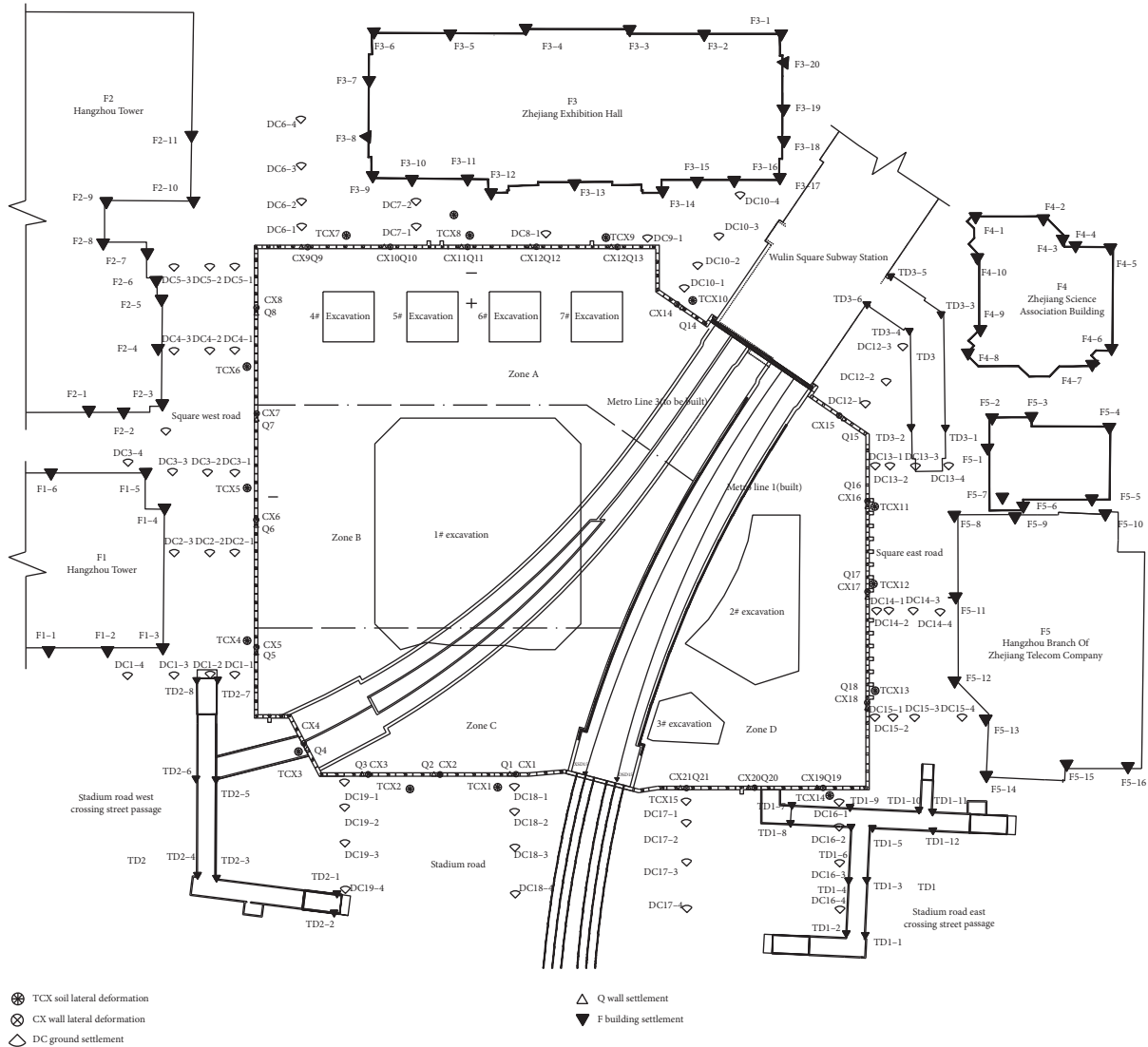
Figure 3: Layout of excavation and monitoring points.

Table 1: Construction schedule of the project.

Stage	Construction activity	Period (day/month/year)			
		Zone A	Zone B	Zone C	Zone D
1	Construction of diaphragm wall	1/8/2013–10/2/2014			
2	Construction of pile foundation	31/1/2014–15/7/2014			
3	Excavation to 2.3 m below the ground and construction of roof slabs	5/6/2014–20/1/2015			
4	Excavation to 7.7 m below the ground	20/1/2015–5/4/2015	20/1/2015–26/4/2015	20/1/2015–20/4/2015	20/1/2015–25/4/2015
5	Construction of B1 floor slabs	13/3/2015–24/4/2015	1/4/2015–15/5/2015	11/4/2015–17/5/2015	3/4/2015–14/5/2015
6	Excavation to 13.2 m below the ground	2/4/2015–15/5/2015	17/5/2015–15/6/2015	2/5/2015–20/6/2015	25/4/2015–9/6/2015
7	Construction of B2 floor slabs	3/5/2015–3/6/2015	9/6/2015–3/7/2015	28/5/2015–6/7/2015	31/5/2015–27/6/2015
8	Excavation to 22.6 m below the ground	22/5/2015–16/7/2015	3/7/2015–4/8/2015	10/6/2015–28/8/2015	13/6/2015–18/8/2015
9	Construction of B3 floor slabs	3/7/2015–8/9/2015	23/7/2015–15/8/2015	12/8/2015–10/9/2015	9/7/2015–23/8/2015
10	Construction of the slabs of excavation	28/8/2015–15/11/2015			

(a)

(b)
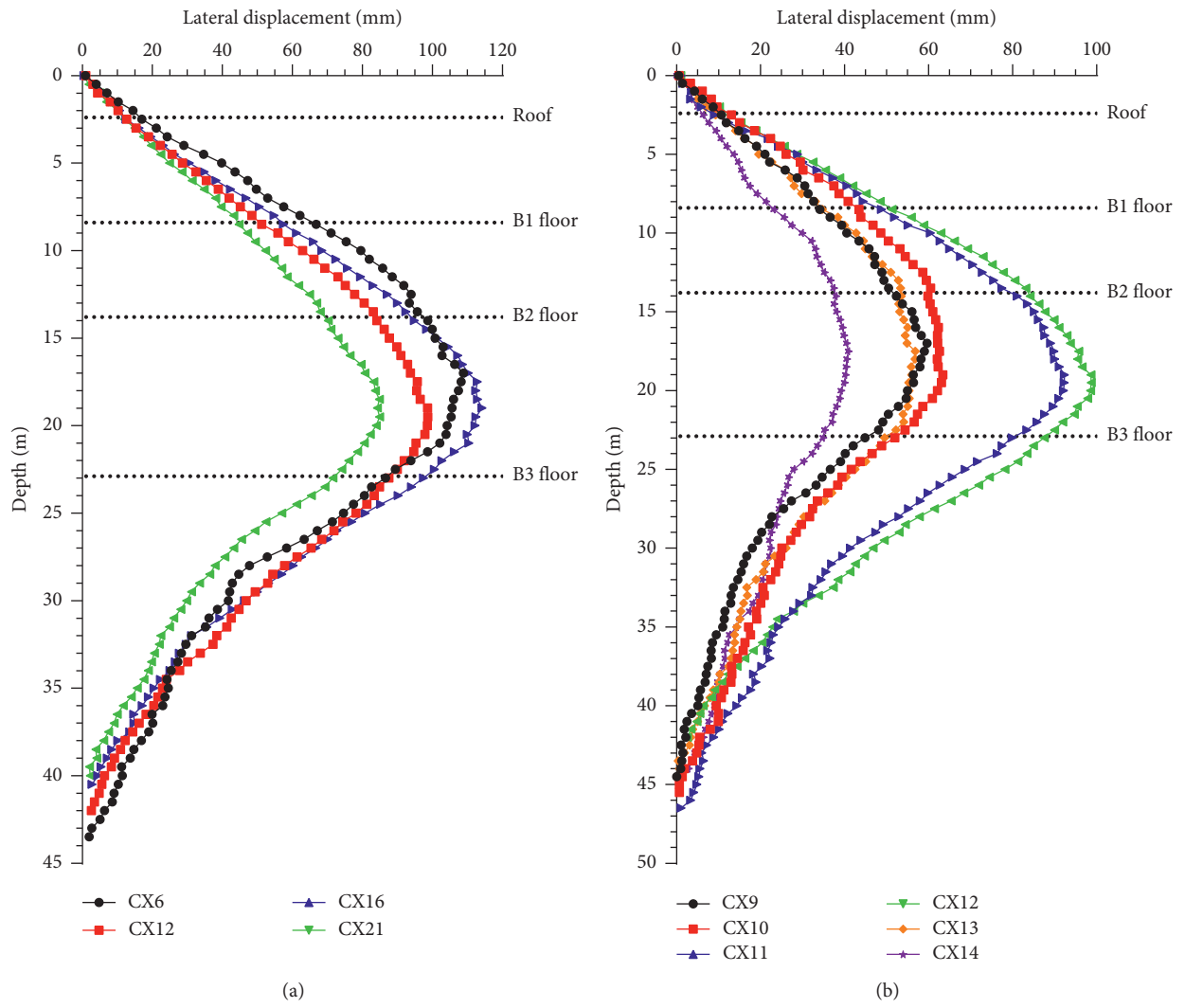
FIGURE 4: Continued.
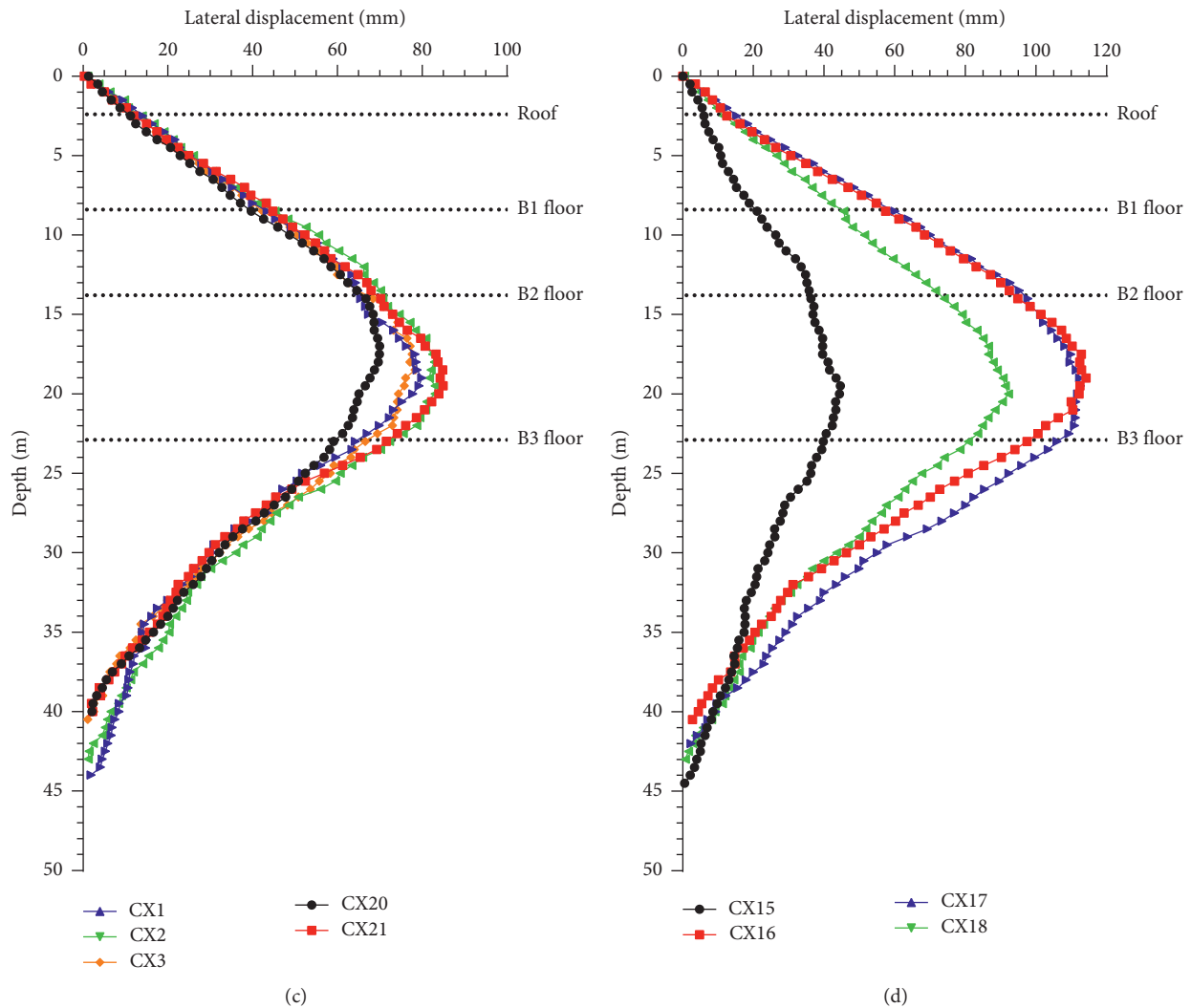
Figure 4: Lateral displacement of the excavation. (a) The maximum deformation monitoring points of each side. (b) The north side of the excavation. (c) The south side of the excavation. (d) The east side of the excavation.

the diaphragm wall was selected as a typical representative. The selected monitoring point was basically near the midpoint of each side of the foundation pit. CX6 was the measurement point on the west side of the foundation pit, CX12 was the northern measurement point, CX16 was the eastern measurement point, and CX21 was the southeast measurement point. The final horizontal displacement state of each measurement point is shown in Figures 5 and 6. The lateral displacement of CX16 was the largest, reaching 114.19 mm.

It could be seen from Figure 4(a) that the lateral displacement deformation of the diaphragm wall was similar to the "saddle shape." The maximum lateral displacement position was 18.5–19 m.

For the convenience of comparison, the maximum lateral displacement value of CX16 was used as the reference value. The maximum lateral displacement of CX6 was 95.33% of CX16. The lateral displacement of CX12 was 98.69 mm, which was 86.43% of CX16. The maximum lateral displacement of CX21 in the southeast of the

foundation pit was 84.93 mm, which was 74.38% of CX16 horizontal displacement.

As shown in Figure 4(b), CX11 and CX12 measuring points had the largest lateral displacement. The measuring points CX9, CX10, and CX13 were relatively close to the diaphragm wall on the west or east side of the project. The lateral stiffness provided by the diaphragm wall at the corner assisted to control the deformation.

Figure 4(c) is the lateral displacement of the north side diaphragm wall. The lateral displacement of the diaphragm wall on the south side was relatively balanced, and there was no significant maximum deformation measuring point.

The deformation characteristic on the east and west sides was similar, so just selected the east side as Figure 4(d). CX19 measuring point on the east side was damaged during the project implementation, so there were only 4 measuring points on the east side. Although the maximum lateral displacements on the east and west sides were close, the difference was only 4.67%, but there is a significant difference in the horizontal displacement distribution along the
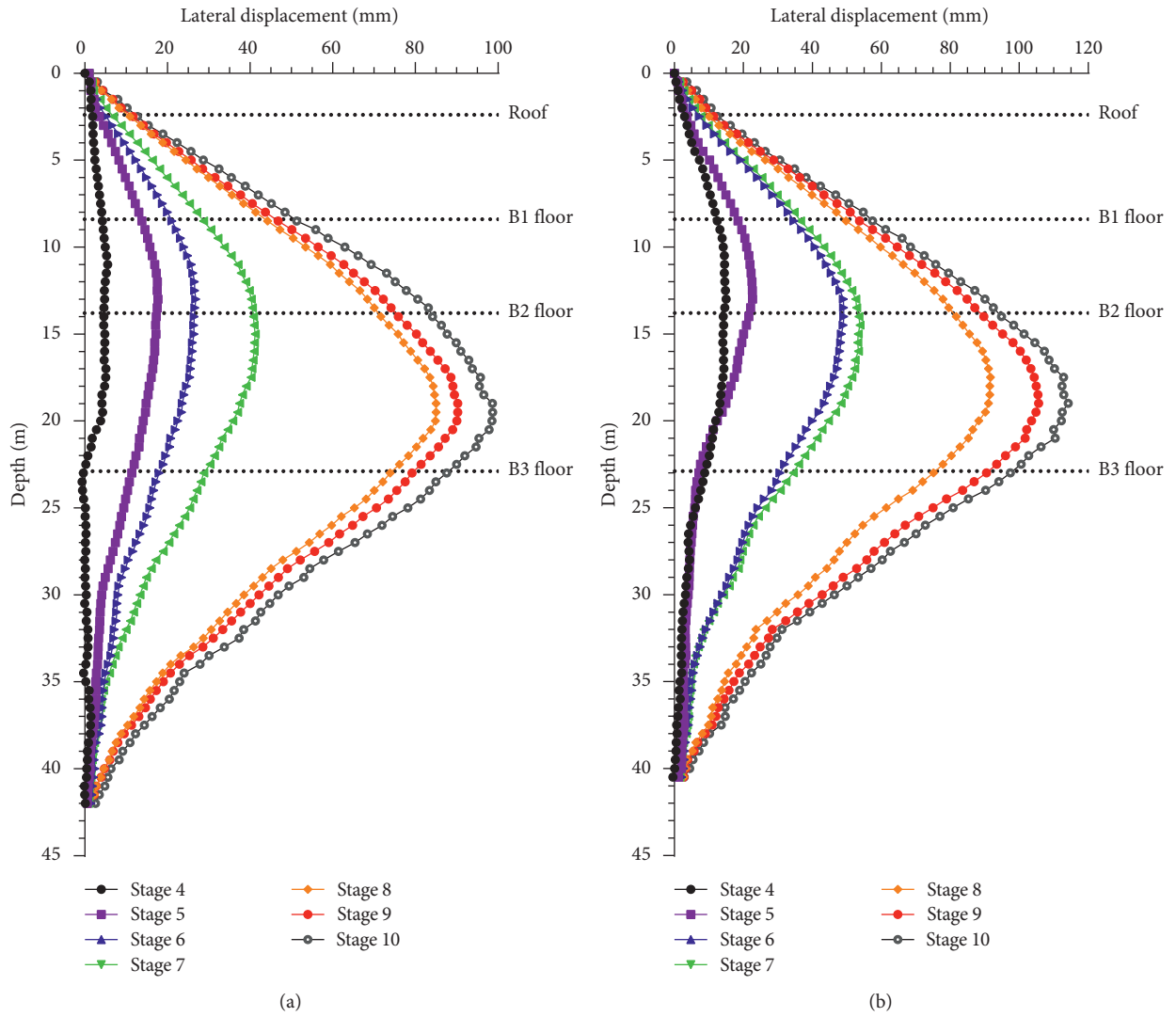
Figure 5: Lateral displacement of each stage. (a) CX12. (b) CX16.
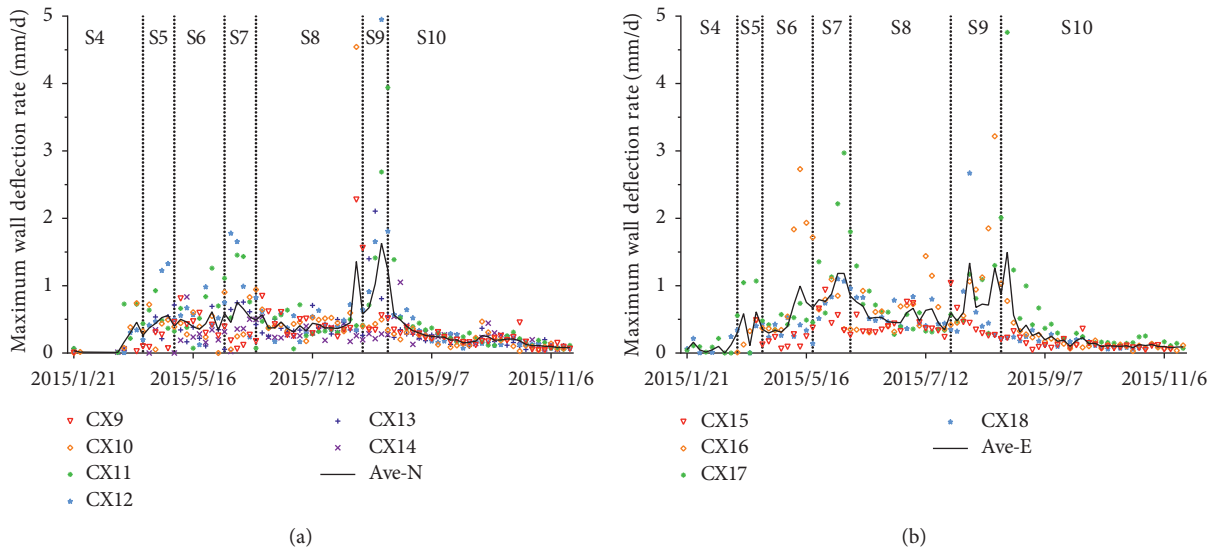
Figure 6: Maximum wall deformation rate over time. (a) CX12. (b) CX16.

side of the foundation pit. The maximum lateral displacement on the east side was larger. The maximum lateral displacements of CX16 and CX17 were very close, indicating that at least 30 m of the diaphragm wall in the east side had reached a large lateral displacement.

Figure 7 is the stage incremental diagram of the lateral displacement of the typical measurement points of the diaphragm wall. It could be seen that the lateral displacement of stage 8 was significantly greater than the other stage and ranged from 27.71% to 46.13% of the total displacement.

Since the exposure duration of CX16 in stage 6 was much longer than the other monitoring points, the incremental deformation of CX16 reached 23.12% of the total deformation, which was significantly higher than other monitoring points. The CX6 monitoring point in stage 7 had a large deformation due to the long exposure time of the excavation. Various construction methods should be used to shorten the exposure duration especially excavating deep soil layers, and it could contribute to controlling the deformation of the diaphragm wall.

Figure 5 is a diagram of the lateral displacement of the diaphragm wall under various working conditions. It was easy to know that the stage 8, which was the three-storey underground excavation stage, was the stage with the largest lateral displacement increment, which was significantly larger than the other stage.

Since the excavation depth of the three underground floors of this project was 9.1 m, the excavation depth was large and deep, so the diaphragm wall had a large deformation in the stage 8. As the excavation depth gradually increased, the location of the maximum deformation of the diaphragm wall also gradually moved downward.

Comparing Figures 5(a) and 5(b), the exposure duration of CX16 in stage 6 was much longer than the other monitoring points, resulting in large deformation. And, the deformation of the stage 6 reached 29.2% of the total deformation and was significantly greater than any other points. The deformation distribution of other monitoring points was similar to that of CX12.

Figure 6 shows the distribution of diaphragm wall lateral displacement rates during the project period. Figure 6(a) shows the north side, and Figure 6(b) shows the east side. There was a significant deformation rate peak on the north side, which was the stage 9 that was the B3 slab construction stage. The maximum deformation rate was 4.95 mm/d, the maximum average deformation rate was 1.63 mm/d, and the deformation rate remained below 0.5 mm/d at other times. There were multiple peaks in the east side; each excavation would cause large wall deformation; the maximum deformation rate was 4.76 mm/d; the maximum average rate was 1.49 mm/d, but there were multiple peak deformation rates over 0.8 mm/d.

Figure 8(a) shows the relationship of the maximum lateral displacement of the diaphragm wall and excavation depth. Figure 8(b) shows the relationship of the location of maximum lateral displacement and excavation depth. The zone division is shown in Figure 3. H_e represents the excavation depth of the foundation pit, H_m represents the depth of the maximum lateral displacement, and δ_{hm}

represents the maximum lateral displacement of the diaphragm wall. The lines Ave-S5, Ave-S7, and Ave-S10 in the figure represent the average value of the lateral displacement of all the diaphragm walls in the corresponding stage, and the Min and Max lines were the envelope lines of the lateral displacement of the diaphragm walls.

It could be seen that, as the excavation depth gradually increased, the lateral displacement of the diaphragm wall gradually increased. When the excavation reached the bottom of the pit, the average value of the maximum lateral displacement of the diaphragm wall reached 0.30% H_e. The maximum deformation point of the foundation pit was CX16 in the middle of the east side. And, its maximum lateral displacement was 0.50% H_e; the minimum deformation point was CX4 which was the southwest of the excavation, and the maximum lateral displacement was 0.14% H_e. Zone D was the east side of the foundation pit, and the lateral displacement of Zone D was larger than the other sides.

With the increasing of the excavation depth, the maximum lateral displacement depth of the diaphragm wall was gradually increasing. The average depth of maximum lateral displacement of the wall under the stage 5, stage 7, and stage10 separately was 12.04 m, 13.35 m, and 18.33 m. The maximum lateral deformation depths separately were 13.50 m, 14.38 m, and 19.50 m compared with Zone D. The maximum lateral displacement depths of other zones were close to the average value, indicating that the slower excavation and support in Zone D made the maximum lateral displacement point of the diaphragm wall move down.

3.2. Settlement of Diaphragm Wall. Figure 9 shows the settlement of the top of the diaphragm wall. Most of monitoring points bulged upward in stage 4, indicating that the rebound of the deep stratum caused by the excavation and unloading of the shallow layers puts the upward stress on the diaphragm wall and causes it to move upward. With the continuous increasing of the excavation depth, the top of the diaphragm wall gradually transformed into settlement. The settlement in the midspan area was the largest, which also indicated that the settlement of the diaphragm wall was mainly due to excessive lateral displacement.

3.3. Ground Surface Settlement. The surface settlement on the north and east sides of the foundation pit is shown in Figures 10(a) and 10(b). The maximum settlement point in the northern side of the foundation pit was DC7-1, with a maximum settlement of 71.93 mm. There were several monitoring points on the east side of the foundation pit that had reached 80 mm, and the maximum settlement was 86.75 mm. Compared with the ratio of the lateral displacement of each other, the ratio of surface settlement had increased.

The rapid settlement period of the surface lagged behind the rapid development period of lateral displacement of the diaphragm wall. The lateral displacement rate of the diaphragm wall dropped quickly after stage 9, while the surface settlement generally entered the rapid settlement period in
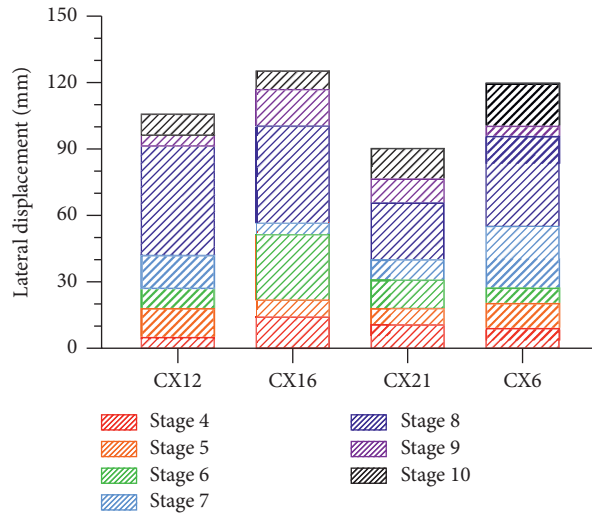
FIGURE 7: Lateral displacement increment of the maximum deformation monitoring points of each side.

(a)

(b)
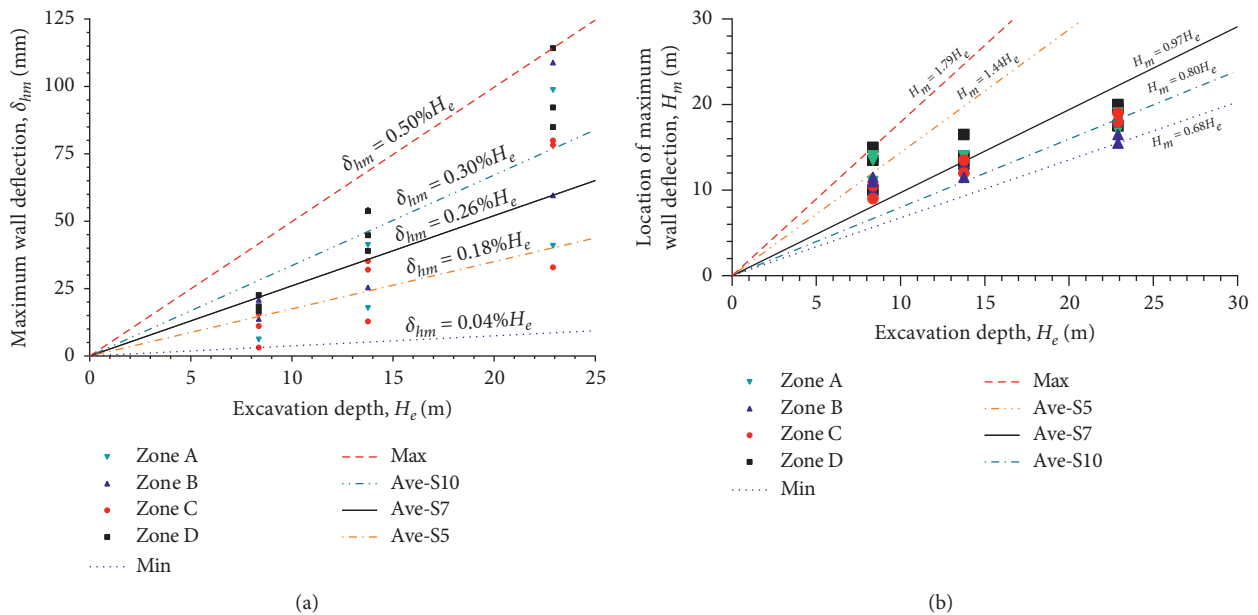
FIGURE 8: Relationship between (a) maximum wall deformation and excavation depth and (b) location of maximum wall deformation and excavation depth.

the late stage 9 and kept the rate about one month, and there was no significant settlement rate convergence in stage 10.

Figure 11 shows the relationship between the maximum lateral displacement of the diaphragm wall and the corresponding maximum settlement of the ground surface. The average value of the ratio of surface settlement to lateral displacement of the foundation pit was 0.82. The surface settlement in Zone C was all arranged on the Stadium Road on the south side, and the traffic flow was much larger than other roads around the project. Therefore, the ratio of surface settlement to lateral displacement in Zone C was larger than others, reaching 0.90. Therefore, in addition to the positive correlation between the surface settlement and

the lateral displacement of the adjacent diaphragm wall, it was also related to the traffic load nearby.

3.4. Settlement of Buildings. Figures 12(a) and 12(b) are the time history curves of the settlement monitoring points of the buildings on the north and south sides of the Zhejiang Exhibition Hall. F3-12, F3-13, and F3-14 were arranged on the south steps of the exhibition hall, and the remaining monitoring points were arranged on the wall of the exhibition hall. The monitoring data could not be updated after the remaining monitoring points were scrapped during the later wall decoration of the exhibition hall. The monitoring
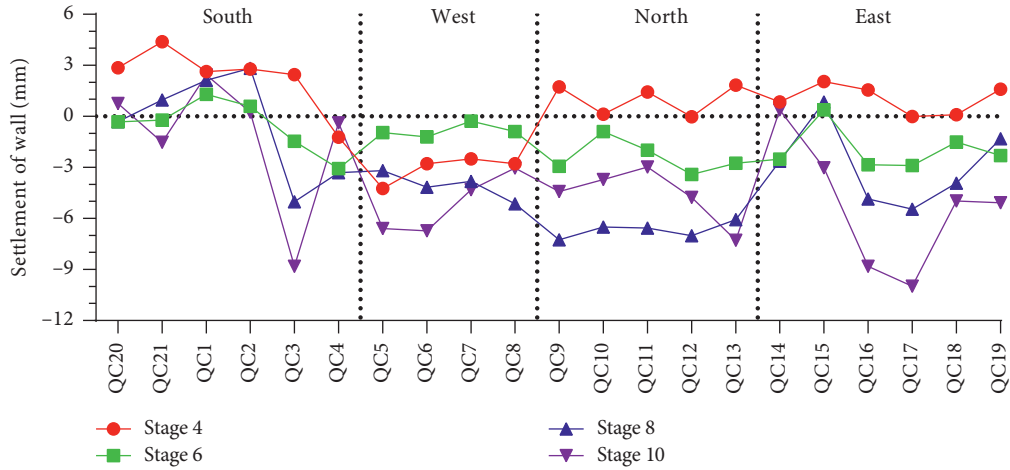
FIGURE 9: Settlement of walls.

(a)

(b)
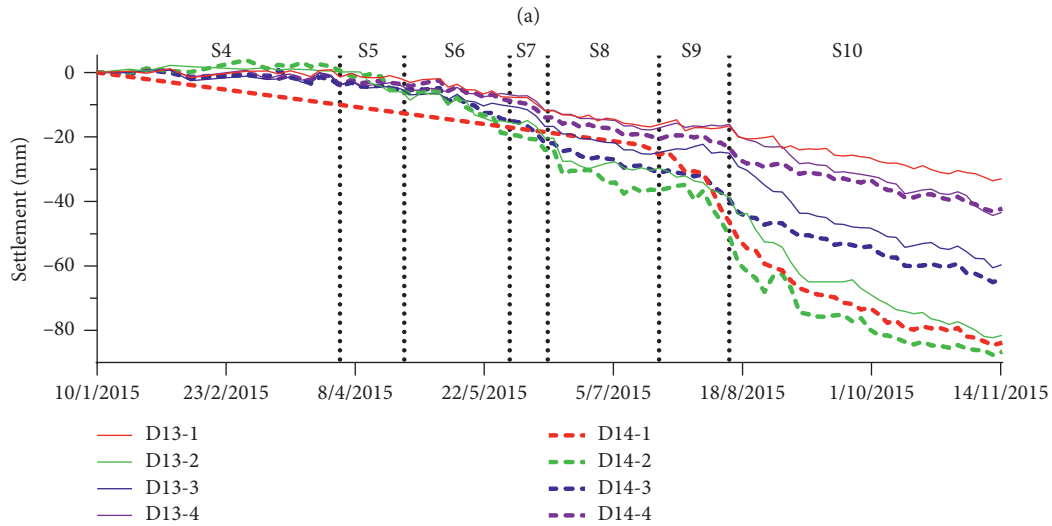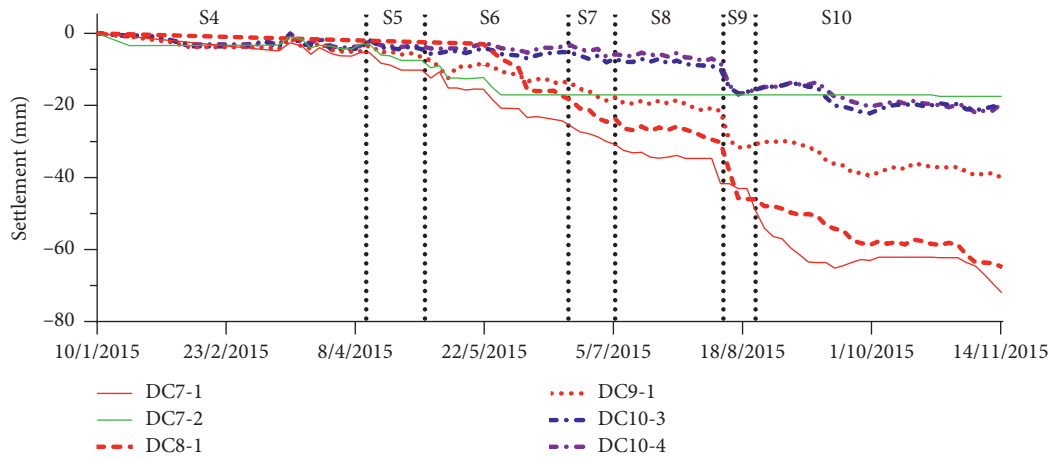
FIGURE 10: Settlement of ground surface over time. (a) North side. (b) East side.
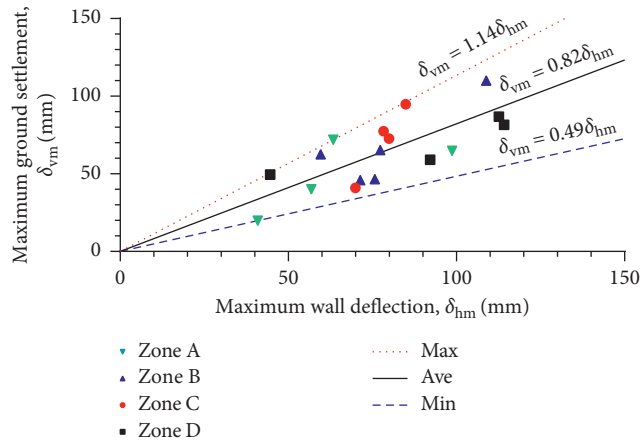
FIGURE 11: Relationship between maximum wall deflection and maximum ground settlement.

(a)

(b)
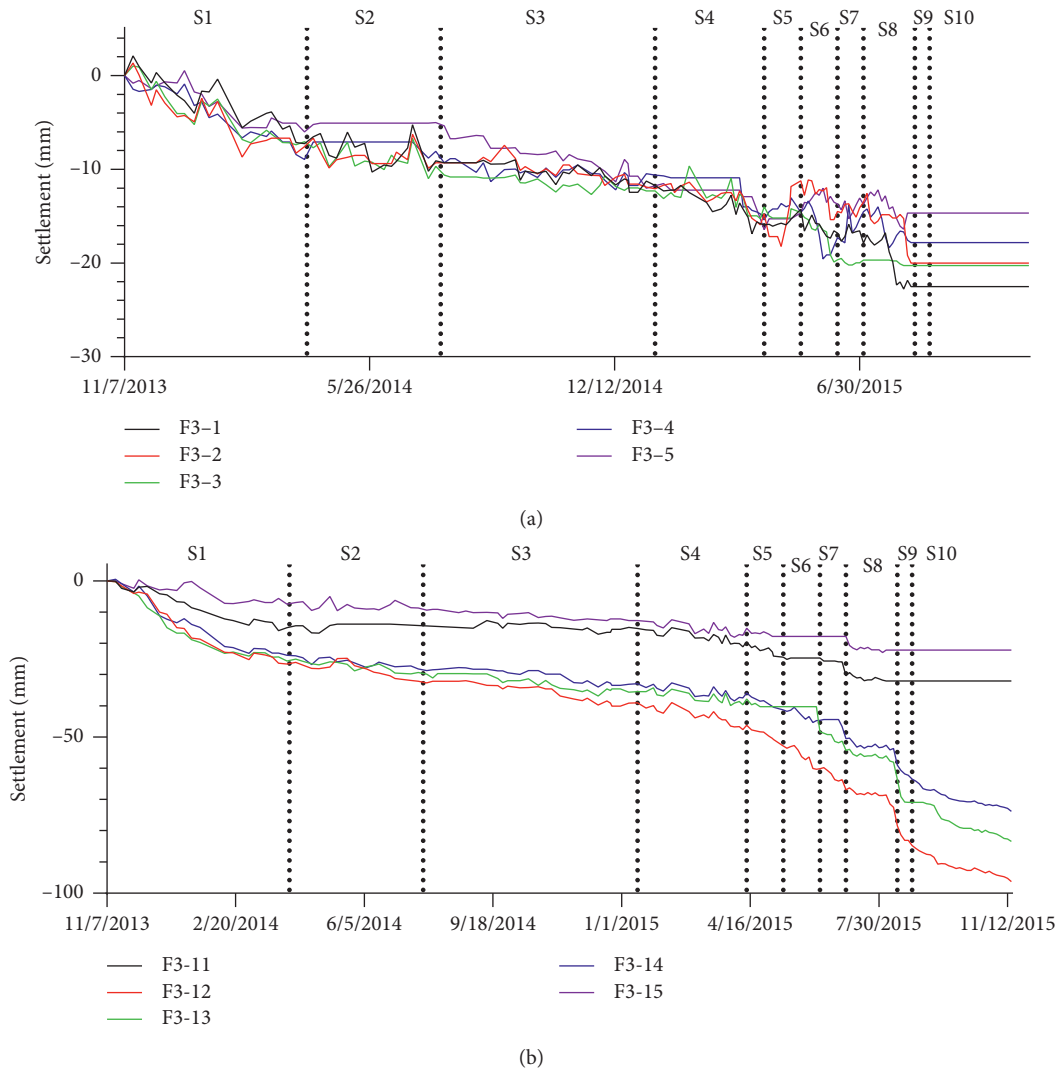
FIGURE 12: Continued.

(c)
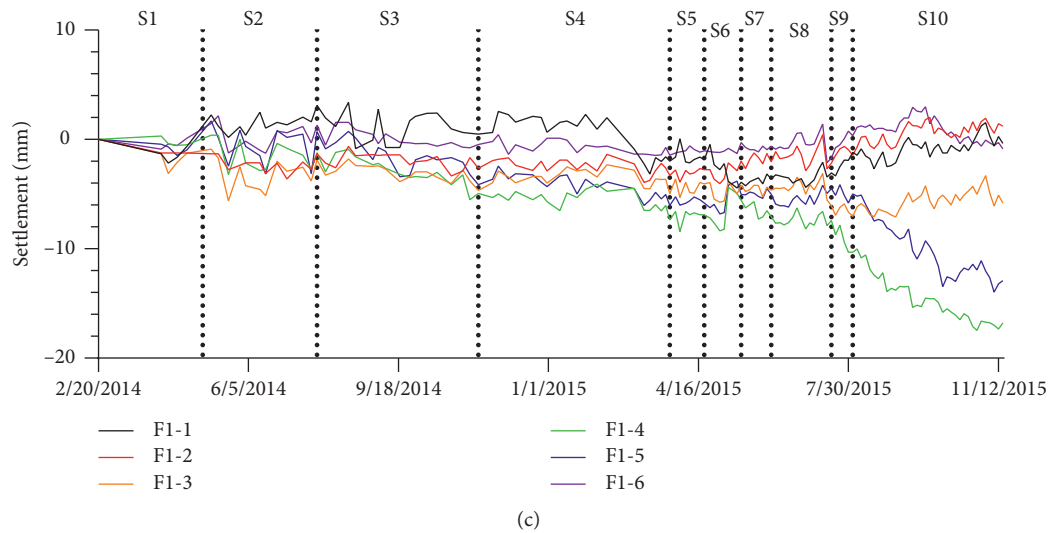
FIGURE 12: Settlement of nearby buildings. (a) North side of Zhejiang Exhibition Hall. (b) South side of Zhejiang Exhibition Hall. (c) Hangzhou Theatre.

points F3-12 to F3-14 were closest to the middle of the north side of the foundation pit and were set on the steps of the exhibition hall. And, other monitoring points were set on the wall of the exhibition hall.

It could be seen that the maximum settlement point on the north side of the exhibition hall was F3-1, the maximum settlement was 22.51 mm, and the settlement of this monitoring point had reached 15.92 mm before stage 4, and the stage of excavation did not cause the significant settlement of this monitoring point; the total settlement during stage 4 to stage 10 was 8.25 mm. The conditions of the other observation points on the north side were similar.

The settlement of the monitoring point on the south side of Zhejiang Exhibition Hall had a greater correlation with the excavation of the foundation pit, especially F3-12, which was the closest to the largest lateral displacement area. The maximum settlement of F3-12 was 97.42 mm. The settlement of F3-11 was significantly smaller than that of F3-12, only 32.09 mm. As the foundation pit construction was completed, the exhibition hall was still undergoing reinforcement construction, and subsequent settlement values could not be collected.

The settlement of the steps was close to that of the ground surface, and the settlement of the outer wall was smaller, which represented the settlement of the main structure of the exhibition hall after reinforcement.

Figure 12(c) shows the settlement of Hangzhou Theatre. The F1-4 and F1-5 monitoring points of the Hangzhou Theatre were also arranged on the outdoor steps of the building. The settlement was larger than the other points, reaching 16.78 mm. The settlements of F1-4 and F1-5 in the stage 10 were 38.49% and 61.34% of the total settlement, respectively, which were similar to the ground settlement characteristics around the foundation pit.

The Hangzhou Theatre was basically not affected by the excavation of the foundation pit, which showed that the

frame structure of the pile foundation within about 30 m from the foundation pit will basically not caused harmful structural damage due to the excavation of the foundation pit. So the other buildings are not discussed in this paper.

3.5. Corresponding Deformation Analysis. The exhibition hall on the north side of the excavation was greatly affected by the excavation of the foundation pit, resulting in larger settlement. In order to study the deformation relationship between the exhibition hall, the monitoring point CX12, which was the largest deformation in the middle of the north side foundation pit, and other monitoring points that were closest to CX12 were selected, which includes the inclination of deep soil monitoring point TCX8, the surface settlement monitoring point DC8-1, and the building settlement monitoring points F3-3, F3-12, and F3-13.

Figure 13(a) is the deformation rate time history curve. It is shown that when the CX12 measuring point produced a larger deformation, other monitoring points would also have a corresponding larger deformation rate, and the deformation peaks were successively reached according to the distance from the CX12 monitoring point. The CX12 monitoring point was the cause of the deformation of other monitoring points, and its maximum deformation rate was 4.89 mm/d, and the maximum deformation rate of other measuring points was between 2.5 and 3.0 mm/d.

Figure 13(b) is the violin-shaped deformation rate distribution curve. The deformation rate of CX12, except for the extreme point, was 4.89 mm/d, and the rate did not exceed 2 mm at other times, and the corresponding three-time rapid deformation distribution corresponded to three excavations. Other monitoring points also had significant rapid deformation periods, but the three excavation conditions could not be distinguished.
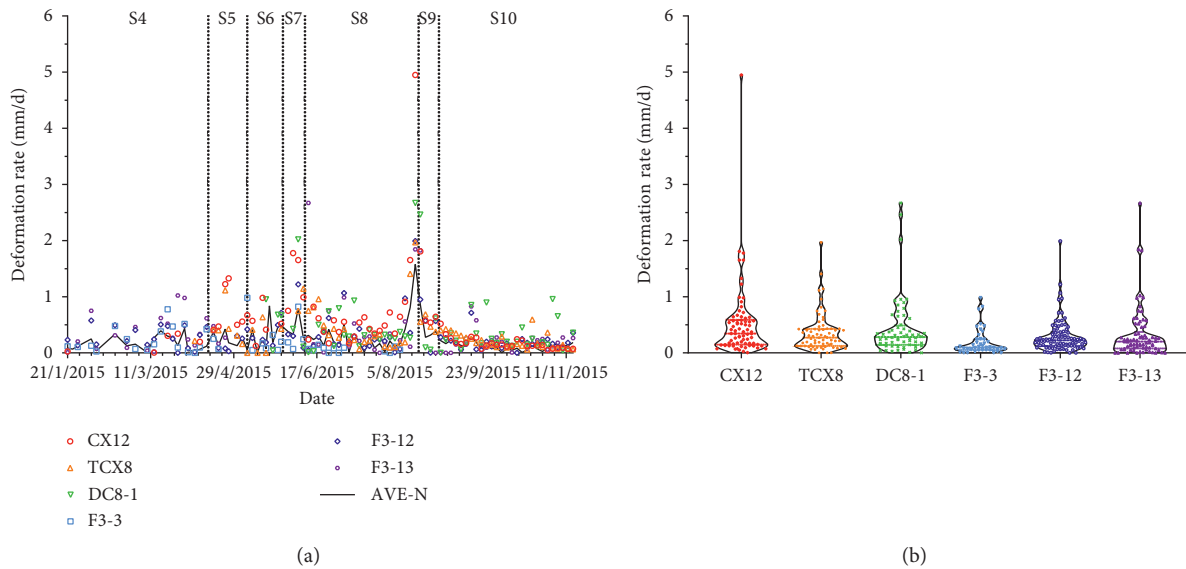
FIGURE 13: Deformation rate of the north side of the excavation. (a) Time history curve. (b) Violin distribution.

4. Conclusions

This paper introduces the deformation characteristics of the diaphragm wall and surrounding environment of the deep excavation using the top-down construction method in the soft clay area of Hangzhou. The following conclusions are drawn:

(1) The top-down construction method can effectively control the deformation of the deep excavation in the Hangzhou area. The maximum wall lateral displacement of this project was 114.19 mm, and the maximum ground settlement was 110.02 mm.

(2) The maximum lateral displacement of this project was 0.49% H_e, and the maximum surface settlement of the excavation was 0.48% H_e. There was a strong correlation between ground settlement and lateral displacement of the diaphragm wall.

(3) Factors such as zoned excavation, pit bottom support method, and excavation exposure time had a greater impact on the deformation characteristics of the diaphragm wall. The zoned excavation had the greatest impact, and the exposure time of the foundation pit had less impact

(4) The constructions around the foundation pit of this project had caused a certain amount of settlement due to the excavation of the foundation pit. The maximum settlement is 96.31 mm at the measuring point of the south-facing steps of the exhibition hall which was 17.0 m away from the excavation, but its main structure would not be affected after reinforcement; the maximum settlement during the excavation was only 17.12 mm.

Data Availability

The data used to support the findings of this study are available from the corresponding author upon request.

Conflicts of Interest

The authors declare that they have no conflicts of interest regarding the publication of this paper.

Acknowledgments

References

[1] R. J. Finno, D. K. Atmatzidis, and S. B. Perkins, "Observed performance of a deep excavation in clay," *Journal of Geotechnical Engineering*, vol. 115, no. 8, pp. 1045–1064, 1989.

[2] P.-G. Hsieh and C.-Y. Ou, "Shape of ground surface settlement profiles caused by excavation," *Canadian Geotechnical Journal*, vol. 35, no. 6, pp. 1004–1017, 1998.

[3] G. T.-C. Kung, "Comparison of excavation-induced wall deflection using top-down and bottom-up construction methods in taipei silty clay," *Computers and Geotechnics*, vol. 36, no. 3, pp. 373–385, 2009.

[4] C.-Y. Ou, J.-T. Liao, and H.-D. Lin, "Performance of diaphragm wall constructed using top-down method," *Journal of Geotechnical and Geoenvironmental Engineering*, vol. 124, no. 9, pp. 798–808, 1998.

[5] G. W. Clough and T. D. O 'Rourke, "Construction induced movements of in situ walls,"vol. 25, pp. 439–470, in *Proceedings of ASCE conference on design and performance of earth retaining structures*, vol. 25, pp. 439–470, Geotechnical Special Publication, Ithaca, NY, USA, June 1990.

[6] C. Yoo, "Behavior of braced and anchored walls in soils overlying rock," *Journal of Geotechnical and Geoenvironmental Engineering*, vol. 127, no. 3, pp. 225–233, 2001.

[7] M. Long, "Database for retaining wall and ground movements due to deep excavations," *Journal of Geotechnical and Geoenvironmental Engineering*, vol. 127, no. 3, pp. 203–224, 2001.

[8] C. Y. Ou, P. G. Hsieh, and D. C. Chiou, "Characteristics of ground surface settlement during excavation," *Canadian Geotechnical Journal*, vol. 30, no. 5, pp. 758–767, 1993.

 [9] J. H. Wang, Z. H. Xu, and G. E. Di, "Performance of a deep excavation constructed using the united method: bottom-up method in the main building part and top-down method in the annex building part," in *Proceedings of the GeoShanghai International Conference*, pp. 385–392, Shanghai, China, June 2006.

[10] J. H. Wang, Z. H. Xu, and W. D. Wang, "Wall and ground movements due to deep excavations in Shanghai soft soils," *Journal of Geotechnical and Geoenvironmental Engineering*, vol. 136, no. 7, pp. 985–994, 2010.

[11] Y. Tan and D. Wang, "Characteristics of a large-scale deep foundation pit excavated by the central-island technique in Shanghai soft clay. I: bottom-up construction of the central cylindrical shaft," *Journal of Geotechnical and Geoenvironmental Engineering*, vol. 139, no. 11, pp. 1875–1893, 2013.

[12] Y. Tan and D. Wang, "Characteristics of a large-scale deep foundation pit excavated by the central-island technique in Shanghai soft clay. II: top-down construction of the peripheral rectangular pit," *Journal of Geotechnical and Geoenvironmental Engineering*, vol. 139, no. 11, pp. 1894–1910, 2013.

[13] H. Wu, Y. J. Zhong, W. Xu, W. Shi, X. Shi, and T. Liu, "Experimental investigation of ground and air temperature fields of a cold-region road tunnel in NW China," *Advances in Civil Engineering*, vol. 2020, Article ID 4732490, 13 pages, 2020.

[14] H. Li, E. L. Ma, J. X. Lai et al., "Tunnelling-induced settlement and treatment techniques for a loess metro in Xi'an," *Advances in Civil Engineering*, vol. 2020, Article ID 1854813, 20 pages, 2020.

Research Article

Analytical Method to Interpret Displacement in Elastic Anisotropic Soil due to a Tunnel Cavity with an Arbitrary Cross Section

Qiongfang Zhang [1,2] **Kang Cheng,** [3,4] **Yadong Lou,** [5] **Tangdai Xia,** [4] **Panpan Guo,** [4] **and Xiaolu Gan** [4]

[1] *Power China Huadong Engineering Corporation, Zhejiang, Hangzhou 310014, China*
[2] *Engineering Research Center of Smart Rail Transportation of Zhejiang Province, Zhejiang, Hangzhou 310014, China*
[3] *China Railway 11th Bureau Group Co., Ltd., Wuhan 430061, China*
[4] *Research Center of Coastal and Urban Geotechnical Engineering, Zhejiang University, Hangzhou 310058, China*
[5] *Hangzhou Metro Group Co., Ltd., Zhejiang, Hangzhou 310003, China*

Correspondence should be addressed to Yadong Lou; 21212107@zju.edu.cn

Based on complex variable theory and conformal mapping method, the paper presents full plane elastic solutions around an unlined tunnel with arbitrary cross section in anisotropic soil. The solutions describe soil elastic solutions for assuming that the displacement vectors along the tunnel boundary are directed towards the center of the tunnel. Tunnels with different cross sections are used to illustrate the method and its correctness. An elliptical unlined tunnel case is discussed in detail in the paper. Using the image method, an approximate solution for predicting surface displacement and subsurface horizontal displacement around an unlined tunnel in anisotropic soil can be obtained. The results show anisotropic stiffness properties n ($n = E_h/E_v$) and m ($m = G_{vh}/E_v$) have a great effect on the displacement distribution patterns around an elliptical tunnel with certain shape.

1. Introduction

Due to the complexity of metro projects, many metro shields use varying cross-sectional shapes for the shield, such as rectangular [1], quasi-rectangular [2, 3], elliptical, horseshoe-shaped, and double-O-tube [4]. Research on tunnels with arbitrary cross sections can guide engineers in predicting ground displacement and underground deformation.

Currently, numerous research efforts have focused on ground displacement caused by circular shield tunnels. In this context, four primary methods are employed—empirical formula, analytical, model test, and numerical methods. Although numerical methods can easily identify the elastic solution for an underground excavation, analytical methods provide important information.

Carranzatorres and Fairhurst [5] stated that closed-form results can help engineers assess the general accuracy of numerical analysis and provide valuable means for obtaining insights into the general nature of a solution. Elasticity problems can be solved by combining the complex variable method with numerous theorems arising from analytical functions, such as Cauchy's integral theorem, Laurent's theorem, and theorems on conformal mapping [6, 7]. These theories are widely used for the first fundamental problem of deep tunnels. Bobet [8] developed analytical solutions for a lined deep tunnel with a circular cross section in transversely isotropic rock using the Lkehnitskii formalism [9]. Zhang and Sun [10] derived an analytical solution for the radial displacement of an unlined deep tunnel with an arbitrary cross section in transversely isotropic rock using Kolosov–Muskhelishvili complex potentials [11]. Exadaktylos

[12] and Manh [13] proposed closed-form solutions for the stress and displacement around an unlined deep tunnel with an arbitrary cross section in elastic isotropic and anisotropic ground, respectively. Exadaktylos [12] applied the method of Kolosov–Muskhelishvili complex potentials, whereas Manh [13] used Green's theory [14–16].

Analytical solutions have been reported for displacement-prescribed problems (also known as the second fundamental problem) in the context of unlined shallow tunnels in elastic soil. Moreover, analytical solutions have been developed for ground movements induced by tunnels with a circular cross section in clay by using the complex variable method. Sagaseta [17] considered tunnel excavation as the radial convergence of a point to the tunnel axis in an elastic half plane. Verruijt [18] extended the work of Sagaseta for arbitrary Poisson ratios and proposed an elliptical deformation mode for the tunnel boundary. Sagaseta found that the deformation modes of the tunnel boundary significantly influence the distribution of stress and displacement at the surface and in the internal soil. Park [19, 20] proposed four deformation patterns for tunnel boundaries and established the analytical displacement of the soil due to deep and shallow buried tunnels in clay. Pinto [21] discussed vertical displacement of a circular tunnel undergoing uniform radial deformation or exhibiting an elliptical deformation mode. The elliptical deformation mode was verified by comparing the analytical results with the measured results. Zymnis [22, 23] extended the analytical solutions proposed by Pinto to account for the cross-anisotropic stiffness properties of the soil. These studies show that the ground displacement caused by excavation of a circular tunnel in clay can be accurately predicted if appropriate soil parameters and tunnel deformation patterns are considered.

Using finite element analysis, Simpson et al. [24] confirmed that anisotropy has significant effects on both the magnitude of the surface settlement and shape of the surface settlement trough, whereas nonlinear behavior has only subtle effects. Lee and Rowe [25] showed that the elastic cross-anisotropy of soil has a significant effect on the computed settlements above the tunnel.

Relatively few studies have focused on the displacement-prescribed problem for a tunnel with an arbitrary cross section in anisotropic soil. In this paper, it is assumed that the tunnel is so long and the plane-strain condition is employed. Full-plane elastic solutions are proposed for an unlined tunnel with an arbitrary cross section subjected to certain deformation modes. Several typical tunnel shapes are used to illustrate the proposed method. To verify the accuracy of this method, results for an elliptical unlined tunnel in transversely isotropic soil with stiffness parameters that correspond to isotropic conditions are compared with that for isotropic soil. The elastic solutions derived for isotropic soil and London clay are also compared to analyze the effect of anisotropic stiffness. Moreover, analytical solutions of displacements in half plane are obtained by using a virtual image technique. The effect of stiffness parameters, n and m, on the distribution of the predicted displacement for an unlined elliptical tunnel is also analyzed.

2. General Equations

2.1. General Equations for Anisotropic Soil.

For plane-strain problems, the constitutive relation can be given as

$$\begin{Bmatrix} \varepsilon_x \\ \varepsilon_y \\ \gamma_{xy} \end{Bmatrix} = \begin{bmatrix} \beta_{11} & \beta_{12} & \beta_{16} \\ \beta_{12} & \beta_{22} & \beta_{26} \\ \beta_{16} & \beta_{26} & \beta_{66} \end{bmatrix} \begin{Bmatrix} \sigma_x \\ \sigma_y \\ \tau_{xy} \end{Bmatrix}, \tag{1}$$

where the β_{ij} coefficients can be expressed as material stiffness parameters E_1, E_2, v_1, v_2, G_2, and α_0 by Zymnis [22], for example,

$$\begin{aligned} \beta_{11} =\ & \cos^2\alpha_0 \left(\frac{\cos^2\alpha_0}{E_1} - \frac{v_2\sin^2\alpha_0}{E_2} \right) + \sin^2\alpha_0 \left(\frac{\sin^2\alpha_0}{E_2} - \frac{v_2\cos^2\alpha_0}{E_2} \right) \\ & - E_1 \left(\frac{v_1\cos^2\alpha_0}{E_1} + \frac{v_2\sin^2\alpha_0}{E_2} \right) + \frac{\sin^2 2\alpha_0}{4G_2}, \end{aligned} \tag{2}$$

where α_0 is dip angle of plane with isotropic properties; E_1, E_2 are Young's moduli of the soil in a direction parallel and normal to the isotropic plane, respectively; v_1 is Poisson's ratio in the plane of isotropy; v_2 is Poisson's ratio in the y' direction due to strain in the x' direction; and G_{vh} is the shear modulus for strain in the $y\prime$ direction.

For $\alpha_0 = 0$,

$$\begin{aligned} E_1 &= E_h, \\ v_1 &= v_{hh}, \\ E_2 &= E_v, \\ v_2 &= v_{vh}, \\ G_2 &= G_{vh}. \end{aligned} \tag{3}$$

The following stiffness parameters are commonly used to measure the anisotropy of soil:

$$\begin{aligned} n &= \frac{E_h}{E_v}, \\ m &= \frac{G_{vh}}{E_v}. \end{aligned} \tag{4}$$

Chatzigiannelis and Whittle [21] conducted laboratory tests on elastic anisotropic parameters for various types of soil. Their results are summarized in Table 1.

The elastic parameters are further constrained by thermodynamic considerations [22], such as

$$\begin{aligned} G_{vh}, E_v, E_h &> 0, \\ 0 < n &< 4, \\ -1 < n_{hh} &< 1, \\ n_{hh} + 2n_{hv}n_{vh} &\leq 1. \end{aligned} \tag{5}$$

2.2. Compatibility Equation for Transverse Isotropy.

The equation for equilibrium under plane-strain conditions is given as follows:

TABLE 1: Transverse isotropic parameters of different types of soil as reported in the literature [21].

Soil	E_v (MPa)	$n = E_h/E_v$	$m = G_{vh}/E_v$	v_{vh}	v_{hh}
London clay	112	2.11	0.64	0.25	−0.19
Gravel	305	0.51	0.3	0.25	0.18
Sand	330	0.94	0.4	0.15	0.17
Silts	300	0.79	0.78	0.06	0.29
Soft clays	80	0.86	0.33	0.34	0.3
Clays	100	1.46	0.44	0.34	0.27
Stiff clays	110	1.23	0.46	0.28	0.13

$$\frac{\partial^2 \varepsilon_x}{\partial y^2} + \frac{\partial^2 \varepsilon_y}{\partial x^2} - \frac{\partial^2 \gamma_{xy}}{\partial y \partial x} = 0. \tag{6}$$

In the absence of body forces, the stresses can be derived from the Airy stress function F as follows:

$$\sigma_x = \frac{\partial^2 F}{\partial y^2},$$

$$\sigma_y = \frac{\partial^2 F}{\partial x^2}, \tag{7}$$

$$\tau_{xy} = -\frac{\partial^2 F}{\partial x \partial y}.$$

Substituting equations (1) and (6) into equation (5), we obtain

$$\beta_{22}\frac{\partial^4 F}{\partial x^4} + (2\beta_{12} + \beta_{66})\frac{\partial^4 F}{\partial x^2 \partial y^2} + \beta_{11}\frac{\partial^4 F}{\partial y^4} = 0. \tag{8}$$

The general solution can be expressed in terms of two analytic functions F_1, F_2 and their conjugates:

$$F(x, y) = 2\mathrm{Re}[F_1(z_1) + F_2(z_2)] \\ = F_1(z_1) + \overline{F_1(z_1)} + F_2(z_2) + \overline{F_2(z_2)}, \tag{9}$$

where the overscript "−" denotes the complex conjugate and $z_k = x + \lambda_k y$, $k = 1, 2$ are arguments in the z_k plane. This plane is obtained from the affine transformation as follows:

$$z_k = x_k + iy_k \\ = x + \lambda_k y, \tag{10}$$

where λ_k are the material eigenvalues.

By introducing equation (9) into equation (8), we can obtain the characteristic equation of λ_k:

$$\beta_{11}\lambda^4 - 2\beta_{16}\lambda^3 + (2\beta_{12} + \beta_{66})\lambda^2 - 2\beta_{26}\lambda + \beta_{22} = 0, \tag{11}$$

where the roots of the equation are conjugate complex numbers, $\lambda_k, \overline{\lambda_k}, k = 1, 2$.

New generalized complex variable functions are introduced as follows:

$$\Phi_k(z_k) = \frac{dF_k}{dz_k}, \Phi_k'(z_k) \\ = \frac{d\Phi_k}{dz_k}, \tag{12}$$

where $\Phi_k(z_k)$ can be assumed in the form of an infinite power series.

From equations (7) and (12), the stress components are related to the variable functions as follows:

$$\sigma_x(x, y) = 2\mathrm{Re}[\lambda_1^2\Phi_1'(z_1) + \lambda_2^2\Phi_2'(z_2)],$$

$$\sigma_y(x, y) = 2\mathrm{Re}[\Phi_1'(z_1) + \Phi_2'(z_2)], \tag{13}$$

$$\tau_{xy}(x, y) = -2\mathrm{Re}[\lambda_1\Phi_1'(z_1) + \lambda_2\Phi_2'(z_2)].$$

Additionally, the cavity is assumed to be free of forces along its surface. The displacement components are determined by integrating the strain components ($\varepsilon_x = \partial u/\partial x, \varepsilon_y = \partial v/\partial y, \gamma_{xy} = \partial u/\partial y + \partial v/\partial x$) to obtain

$$U(x, y) = 2\mathrm{Re}[p_1\Phi_1(z_1) + p_2\Phi_2(z_2)], \\ V(x, y) = 2\mathrm{Re}[q_1\Phi_1(z_1) + q_2\Phi_2(z_2)], \tag{14}$$

with

$$p_1 = \beta_{11}\lambda_1^2 + \beta_{12},$$

$$p_2 = \beta_{11}\lambda_2^2 + \beta_{12},$$

$$q_1 = \beta_{12}\lambda_1 + \frac{\beta_{22}}{\lambda_1}, \tag{15}$$

$$q_1 = \beta_{12}\lambda_2 + \frac{\beta_{22}}{\lambda_2}.$$

3. Closed-Form Solution Obtained by Conformal Mapping

To find solutions for this problem, we first consider the transformation of tunnels with an arbitrary cross section, such as an ellipse, circle, or square, in the z plane to a unit circular hole in the ζ plane, as shown in Figure 1. The transformation function can be assumed as

$$z = w(\zeta) \\ = R\left(\zeta + \sum_{n=1}^{N} a_n\zeta^{-n}\right), \quad \zeta = \rho e^{i\theta}, \tag{16}$$

where R is a real number related to the size of the tunnel and a_n are generally complex coefficients that satisfy $|a_n| < 1/n$ [26]. The inverse mapping function $w^{-1}(z)$ is analytic, single valued, and nonzero outside the tunnel boundary.

In many cases, it can be assumed that the physical domain possesses p symmetry axes, which yields
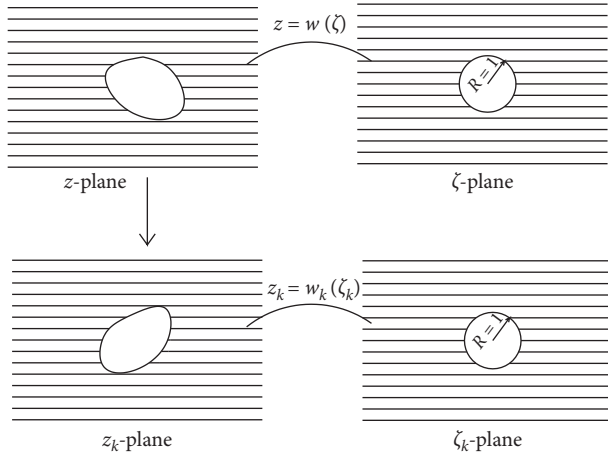
FIGURE 1: Conformal mapping of a region outside an unlined tunnel to the exterior region of a unit circle.

$$z = w(\zeta)$$
$$= R\left(\zeta + \sum_{n=1}^{N} a_{1-pn}\zeta^{1-pn}\right). \tag{17}$$

Assuming that the central position of the tunnel boundary remains unchanged after deformation, the boundary remains axisymmetric along the x and y axes. After deformation, the curve can be expressed by

$$Z = w_c(\zeta),$$
$$= R_c\left(\zeta + \sum_{n=1}^{N} b_n\zeta^{-n}\right), \tag{18}$$
$$= R\left(\frac{R_c}{R}\zeta + \frac{R_c}{R}\sum_{n=1}^{N} b_n\zeta^{-n}\right).$$

Because the soil is transversely isotropic, the boundary of the tunnel in the original plane (z plane) is affine transformed to cutouts in the z_k planes:

$$z_k = x_k + iy_k = x + \lambda_k y, \quad k = 1, 2. \tag{19}$$

The exterior region of an unlined tunnel in the z_k plane can be mapped to the exterior region of a unit circle in the ζ_k plane. The conformal mapping functions corresponding to the original and deformed tunnel boundaries are as follows:

$$z_k = w_k(\zeta_k) = R\sum_{n=1}^{N}\left(c_{kn}\zeta_k^n + d_{kn}\zeta_k^{-n}\right),$$
$$Z_k = w_k(\zeta_k) = R\sum_{n=1}^{N}\left(g_{kn}\zeta_k^n + r_{kn}\zeta_k^{-n}\right), \quad |\zeta_k| \geq 1, \text{ for } k = 1, 2, \tag{20}$$

where the circles $\zeta_k = 1$ correspond to the circle $\zeta = 1$ and $\zeta_k \longrightarrow \infty$ when $\zeta \longrightarrow \infty$.

To ensure that the transformed equations (19) and (20) are single valued, all roots of $dz_k/d\zeta_k = 0$ must be located inside the unit circle $|\zeta_k| = 1$, thereby giving

$$\begin{cases} |\zeta_k^{2n}| = \left|\dfrac{d_{kn}}{c_{kn}}\right| < 1, \\[3mm] |\zeta_k^{2n}| = \left|\dfrac{r_{kn}}{g_{kn}}\right| < 1, \end{cases} \tag{21}$$

which should be located inside the unit circle. Thus, one-to-one mapping is obtained.

Using equations (17) and (20), z_k can also be expressed as

$$z_k = \frac{z + \overline{z}}{2} + \lambda_k \frac{z - \overline{z}}{2i}$$
$$= \frac{R\left\{(i + \lambda_k)\left(\zeta + \sum_{n=1}^{N} a_n\zeta^{-n}\right) + (i - \lambda_k)\left(\zeta^{-1} + \sum_{n=1}^{N} \overline{a_n}\zeta^n\right)\right\}}{2i}. \tag{22}$$

By comparing the coefficients of equations (20) and (22) for the tunnel boundary ($\rho = 1$), one can obtain c_{kn} and d_{kn}. Hence,

$$\begin{cases} c_{k1} = \dfrac{(1 - \lambda_k i) + (1 - \lambda_k i)\overline{a_1}}{2}, \\[3mm] d_{k1} = \dfrac{(1 - \lambda_k i)a_1 + (1 - \lambda_k i)}{2}. \end{cases} \tag{23}$$

For $n \geq 2$,

$$\begin{cases} c_{kn} = \dfrac{(1 - i\lambda_k)a_n}{2}, \\[3mm] d_{kn} = \dfrac{(1 + i\lambda_k)\overline{a_n}}{2}. \end{cases} \tag{24}$$

Similarly,

$$\begin{cases} g_{k1} = \dfrac{R_c}{R}\dfrac{(1 - \lambda_k i) + (1 + \lambda_k i)\overline{b_1}}{2}, \\[3mm] r_{k1} = \dfrac{R_c}{R}\dfrac{(1 - \lambda_k i)b_1 + (1 + \lambda_k i)}{2}. \end{cases} \tag{25}$$

For $n \geq 2$,

$$\begin{cases} g_{kn} = \dfrac{R_c}{R}\dfrac{(1 - i\lambda_k)b_n}{2}, \\[3mm] r_{kn} = \dfrac{R_c}{R}\dfrac{(1 + i\lambda_k)\overline{b_n}}{2}. \end{cases} \tag{26}$$

$\Phi_k(z_k)$ is assumed to have the following form:

$$\Phi_k(z_k) = \sum_{n=1}^{N} A_{kn}(\zeta_k)^{-n}. \tag{27}$$

The displacement components on the tunnel boundary can be obtained using equation (16):

$$U(x, y) = 2 \sum_{k=1}^{2} \left(p_k \sum_{n=1}^{N} A_{kn} e^{-in\theta} + \overline{p_k} \sum_{n=1}^{N} \overline{A_{kn}} e^{in\theta} \right),$$

$$V(x, y) = 2 \sum_{k=1}^{2} \left(q_k \sum_{n=1}^{N} A_{kn} e^{-in\theta} + \overline{q_k} \sum_{n=1}^{N} \overline{A_{kn}} e^{in\theta} \right). \tag{28}$$

It is assumed that the displacement vectors along the tunnel boundary are directed toward the center of the tunnel. The displacement u_k at the tunnel boundary can be expressed as

$$u_k = U(x, y) + \lambda_k V(x, y)$$

$$= 2(p_1 + \lambda_k q_1) \sum_{n=1}^{N} A_{1n} e^{-in\theta} + 2(p_2 + \lambda_k q_2) \sum_{n=1}^{N} A_{2n} e^{-in\theta}$$

$$+ 2(\overline{p_1} + \lambda_k \overline{q_1}) \sum_{n=1}^{N} \overline{A_{1n}} e^{-in\theta} + 2(\overline{p_2} + \lambda_k \overline{q_2}) \sum_{n=1}^{N} \overline{A_{2n}} e^{-in\theta}. \tag{29}$$

The total displacement u_k at the tunnel boundary $\rho = 1$ can also be expressed as

$$u_k = Z_k - z_k$$

$$= R \sum_{n=1}^{N} \left((g_{kn} - c_{kn}) e^{in\theta} + (r_{kn} - d_{kn}) e^{-in\theta} \right). \tag{30}$$

Equating the coefficients for similar terms of $e^{in\theta}$ and $e^{-in\theta}$ in equations (29) and (30) yields

$$\begin{cases} 2(p_1 + \lambda_k q_1) A_{1n} + 2(p_2 + \lambda_k q_2) A_{2n} = R(r_{kn} - d_{kn}), \\ 2(\overline{p_1} + \lambda_k \overline{q_1}) \overline{A_{1n}} + 2(\overline{p_2} + \lambda_k \overline{q_2}) \overline{A_{2n}} = R(g_{kn} - c_{kn}). \end{cases} \tag{31}$$

The above equations are satisfied by

$$\begin{cases} A_{1n} = \dfrac{R((r_{1n} - d_{1n})(p_2 + \lambda_2 q_2) - (r_{2n} - d_{2n})(p_2 + \lambda_1 q_2))}{2(\lambda_1 - \lambda_2)(p_2 q_1 - p_1 q_2)}, \\[2ex] A_{2n} = \dfrac{R((r_{1n} - d_{1n})(p_1 + \lambda_2 q_1) - (r_{2n} - d_{2n})(p_1 + \lambda_1 q_1))}{2(\lambda_1 - \lambda_2)(p_1 q_2 - p_2 q_1)}, \\[2ex] \overline{A_{1n}} = \dfrac{R((g_{1n} - c_{1n})(\overline{p_2} + \lambda_2 \overline{q_2}) - (g_{2n} - c_{2n})(\overline{p_2} + \lambda_1 \overline{q_2}))}{2(\lambda_1 - \lambda_2)(\overline{p_2 q_1} - \overline{p_1 q_2})}, \\[2ex] \overline{A_{2n}} = \dfrac{R((g_{1n} - c_{1n})(\overline{p_1} + \lambda_2 \overline{q_1}) - (g_{2n} - c_{2n})(\overline{p_1} + \lambda_1 \overline{q_1}))}{2(\lambda_1 - \lambda_2)(\overline{p_1 q_2} - \overline{p_2 q_1})}. \end{cases} \tag{32}$$

It can be seen that once the mapping function for the original and deformed tunnel boundaries and the parameters of elastic anisotropic soil are determined, the coefficients of equation (27) can be ascertained. The elastic solutions around the tunnel can be obtained using equations (12) and (13).

4. Validation of the Proposed Solution with Known Solutions

4.1. Circular Tunnel. For a cylindrical cavity of radius R in infinite anisotropic soil, the boundary condition can be solved by mapping onto a circle of unit radius:

$$z = R\zeta. \tag{33}$$

The conformal mapping function of z_k can be written as

$$z_k = R\left(\zeta_k + \zeta_k^{-1} \right). \tag{34}$$

When undergoing uniform convergence u_ε, the deformed tunnel boundary can be expressed as

$$Z = (R - u_\varepsilon)\zeta. \tag{35}$$

The conformal mapping function of z_k can be written as

$$Z_k = (R - u_\varepsilon)\left(\zeta_k + \zeta_k^{-1} \right). \tag{36}$$

When subjected to the ovalization mode u_δ, the deformed tunnel boundary can be expressed as

$$Z = R\left(\zeta + \frac{u_\delta}{R} \zeta^{-1} \right). \tag{37}$$

The conformal mapping function of z_k can be written as

$$Z_k = R\left(\frac{(1 - \lambda_k i) + (1 + \lambda_k i)(u_\delta/R)}{2} \zeta_k + \frac{(1 - \lambda_k i)(u_\delta/R) + (1 + \lambda_k i)}{2} \zeta_k^{-1} \right). \tag{38}$$

The expression for the displacement can be obtained using equations (13) and (32), which is identical to the solution obtained by Zymnis [22].

4.2. Nonelliptical Tunnels. It is useful to determine the coefficients of approximate polynomial mapping functions.

$$z = R\left[\zeta + \frac{1 - K^2}{4} \frac{1}{\zeta} - \frac{K^2}{24} \frac{1}{\zeta^3} - \frac{K^2(1 - K^2)}{160} \frac{1}{\zeta^5} - \frac{K^2(1 - 3K^2 + K^4)}{896} \frac{1}{\zeta^7} + \ldots \right]. \tag{39}$$

For nonelliptical holes with rounded corners, we have the following approximate polynomial mapping functions [28]:

$$z = R\left[\zeta + \frac{1}{3} \frac{1}{\zeta^2} + \frac{1}{45} \frac{1}{\zeta^5} \right] \text{(triangle)},$$

$$z = R\left[\zeta - \frac{1}{6} \frac{1}{\zeta^3} + \frac{1}{56} \frac{1}{\zeta^7} \right] \text{(square)},$$

$$z = R\left[\zeta + \frac{1}{2} \frac{1}{\zeta} - \frac{1}{8} \frac{1}{\zeta^3} - \frac{3}{80} \frac{1}{\zeta^5} \right] \left(\frac{\text{rectangle with length}}{\text{width ratio of 3.24: 1}} \right),$$

$$z = R\left[\zeta + 0.643 \frac{1}{\zeta} - 0.098 \frac{1}{\zeta^3} - 0.038 \frac{1}{\zeta^5} \right] \left(\frac{\text{rectangle with length}}{\text{width ratio of 5: 1}} \right). \tag{40}$$

Manh [13] proposed that, to reduce the error for elastic fields at the corner of a rectangular opening, at least 10 terms must be used in the conformal mapping functions. Once an approximate polynomial mapping for the original and deformed shapes of the hole boundary is obtained, the elastic solution can be determined using the analytical method proposed herein.

4.3. Elliptical Tunnel

4.3.1. Solutions for an Unlined Elliptical Tunnel. Assuming that the ratio of the semi-major and semi-minor axes remains unchanged during uniform radial convergence of an elliptical tunnel boundary, as shown in Figure 2, we observe that

This problem has been previously addressed in literature. Heller [27] provided the mapping function for a rectangular opening of unit width and height K, using the Schwarz–Christoffel integral:

$$\frac{a_1}{a_2} = \frac{b_1}{b_2}$$

$$= \frac{\rho_1}{\rho_2} \tag{41}$$

$$= \frac{1}{k},$$

where a_1, a_2 are the semi-major axes of the elliptical tunnel before and after deformation, respectively; b_1, b_2 are the semi-minor axes of the elliptical tunnel before and after deformation, respectively; ρ_1, ρ_2 are the extreme diameter of any point on the elliptical tunnel before and after deformation, respectively; and k is a length ratio.

For an elliptical cavity illustrated in Figure 2 in an infinite medium undergoing uniform convergence, u_x and u_y, the displacement components at the tunnel wall, can be expressed by

$$\begin{cases} u_x = -(1 - k)x \\ u_y = -(1 - k)y \end{cases}, \quad (0 < k \le 1), z = w(\zeta) = R\left(\zeta + m\zeta^{-1}\right), \tag{42}$$

where $R = (a_1 + b_1)/2, m = (a_1 - b_1)/(a_1 + b_1)$. The mapping function transforms the elliptical cavity to a unit circle as follows:

$$Z = w(\zeta)$$
$$= kR\left(\zeta + m\zeta^{-1}\right). \tag{43}$$

Thereafter, we introduce the following mapping functions, $z_k(\zeta_k)$ and $Z_k(\zeta_k)$:

$$z_k = R\left(\frac{(1 - \lambda_k i) + (1 + \lambda_k i)m}{2} \zeta_k + \frac{(1 - \lambda_k i)m + (1 + \lambda_k i)}{2} \zeta_k^{-1} \right),$$

$$Z_k = R\left(k \frac{(1 - \lambda_k i) + (1 + \lambda_k i)m}{2} \zeta_k + k \frac{(1 - \lambda_k i)m + (1 + \lambda_k i)}{2} \zeta_k^{-1} \right). \tag{44}$$
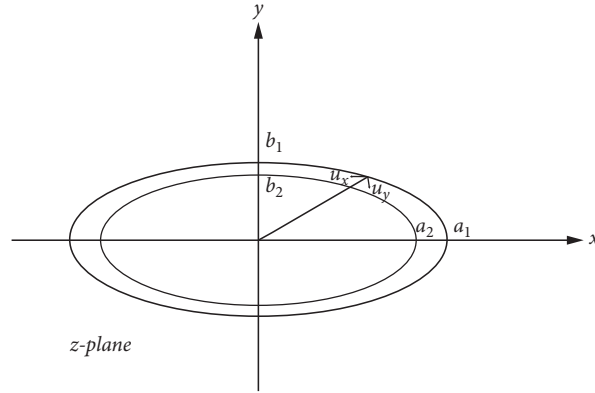
FIGURE 2: Original and transformed (z) plane.

The coefficients A_{1n} and A_{2n} can be obtained from equation (32):

$$\begin{cases} A_{1n} = \dfrac{(1-k)(q_2 a_1 - p_2 i b_1)}{2(p_2 q_1 - p_1 q_2)}, \\[3mm] A_{2n} = \dfrac{(1-k)(-q_1 a_1 + p_1 i b_1)}{2(p_2 q_1 - p_1 q_2)}, \\[3mm] \overline{A_{1n}} = \dfrac{(1-k)(\overline{q_2} a_1 + \overline{p_2} i b_1)}{2(\overline{p_2 q_1} - \overline{p_1 q_2})}, \\[3mm] \overline{A_{2n}} = \dfrac{(1-k)(-\overline{q_1} a_1 + \overline{p_1} b_1 i)}{2(\overline{p_1 q_2} - \overline{p_2 q_1})}. \end{cases} \tag{45}$$

When $a_1 = b_1$, the results can be reduced to the results obtained by Zymnis [22].

4.3.2. Comparison with Isotropic Soil. In general, tunnel contours comprise complex curves; thus, to generalize these contours, it is reasonable to simplify complicated tunnels as unlined tunnels with an elliptical outline [29]. To verify the proposed method, we utilized approximately equal stiffness parameters in anisotropic soil; i.e., $n = E_h/E_v = 1.0$, $v_{vh} = v_{hh} = 0.5$, $m = G_{vh}/E_v = 0.335$. In addition, we compared the stress and displacement obtained with the proposed theoretical method with the results obtained by the method used in isotropic soil. Figures 3(a)–3(e) compare the distribution of elastic solutions around an elliptical tunnel with $a/H = 0.1064$; $b/a = 0.8$. The analyses can be applied under the assumption of incompressible behavior, when the soil is soft clay. The conditions for incompressibility have been given by Gibson [27] as $v_{vh} = 0.5$, $v_{hh} = 1 - 2nv_{vh}^2 = 1 - (n/2)$. Because the distribution of displacement does not depend on the magnitude of the elliptical tunnel and the distribution of stress does not depend on the magnitude of the modulus, the displacement and stress fields are given by the dimensionless coordinates, x/H and y/H. The results for isotropic soil are shown for $x/H < 0$, and the results for transversely isotropic soil are shown for $x/H > 0$ in the following figures.

Figures 3(a)–3(e) indicate that when the boundary of an elliptical tunnel uniformly converges to the center of the tunnel, the absolute values of the results increase as we approach the boundary of the elliptical tunnel. Similarly, as we move farther away from the boundary of the elliptical tunnel, the absolute values of the results decrease more rapidly. In all the cases, the normal stress and horizontal displacement are symmetric with respect to the x axis, whereas the shear stress and vertical displacement are antisymmetric with respect to the y axis. Excellent agreement is observed between the results for isotropic and transversely isotropic soils, verifying that the anisotropic solutions obtained by the analytical method proposed herein can converge to the isotropic solution with appropriate stiffness parameters.

4.3.3. Comparison of Results for Isotropic Soil and London Clay. Gasparre [28] noted that London clay exhibits significant anisotropy at low strain levels, i.e., <0.001%. Figures 4(a)–4(e) compare the distribution of elastic solutions around an unlined elliptical tunnel with $b/a = 0.8$, obtained for the isotropic model (with $v = 0.5$) and London clay with stiffness parameters of $n = E_h/E_v = 2.125$; $m = G_{vh}/E_v = 1.125$; $v_{vh} = 0.25$; $v_{hh} = -0.19$. The results for isotropic soil are shown for $x/H < 0$, whereas the results for London clay are shown for $x/H > 0$ in Figure 4.

Figures 4(a)–4(e) present a comparison of the analytical solutions for isotropic soil and London clay under uniform radial convergence deformation of an elliptical tunnel. The anisotropic parameters of London clay have little influence on the horizontal stress, horizontal displacement, and shear stress. However, a slightly faster attenuation of vertical stress and vertical displacement with distance is observed.

5. Solutions of Ground Displacement in Half Plane

5.1. Virtual Image Technique. The tunnel is embedded at a depth H from the ground surface. In accordance with the study by Sagaseta, the ground movements associated with an unlined tunnel located at a depth H below the traction-free ground surface can be approximately represented by a
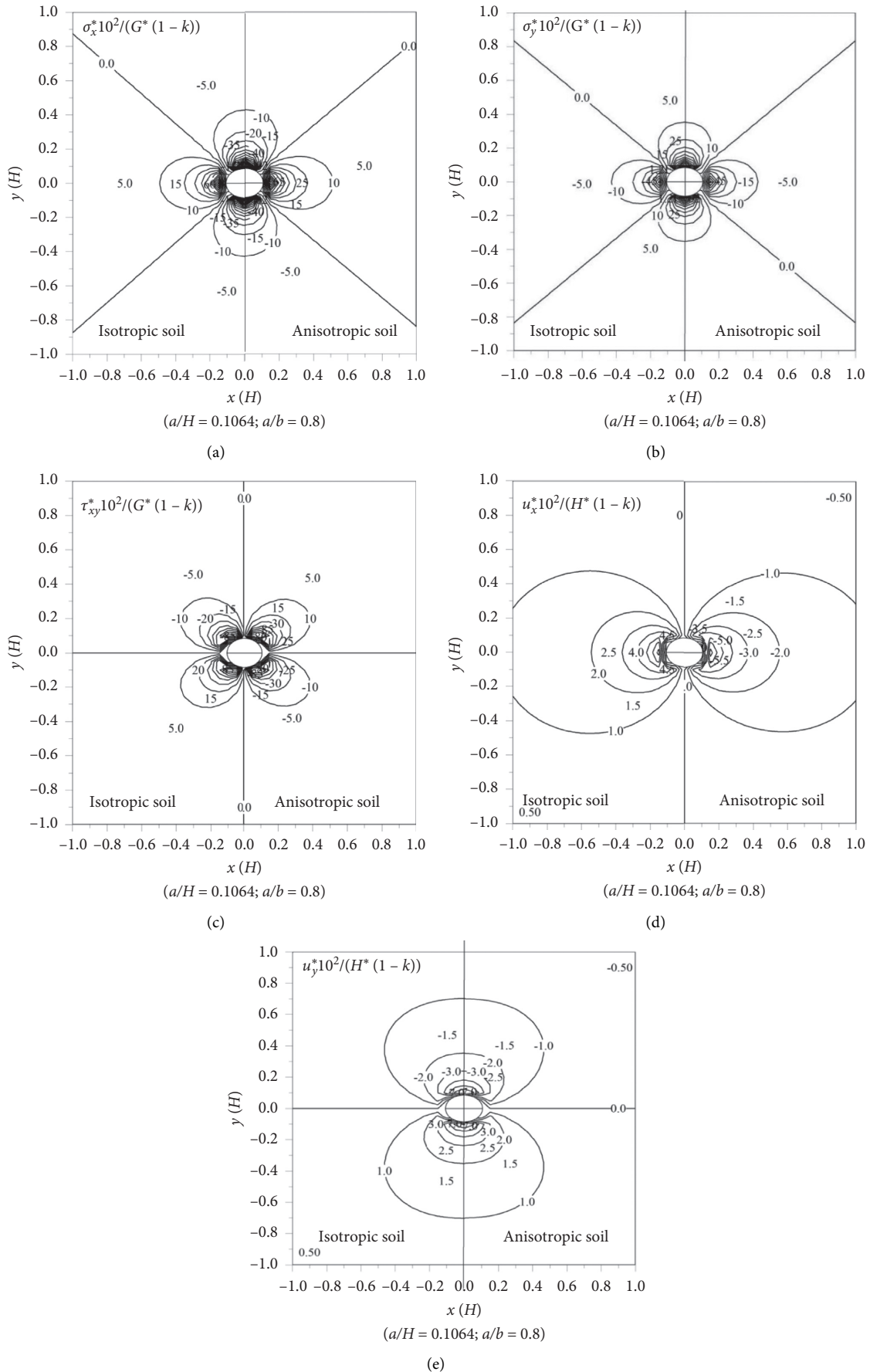
FIGURE 3: Analytical predictions of elastic solutions with isotropic and cross-anisotropic stiffness parameters for London clay. (a) Horizontal normal stress. (b) Vertical normal stress. (c) Shear stress. (d) Horizontal displacement. (e) Vertical displacement.
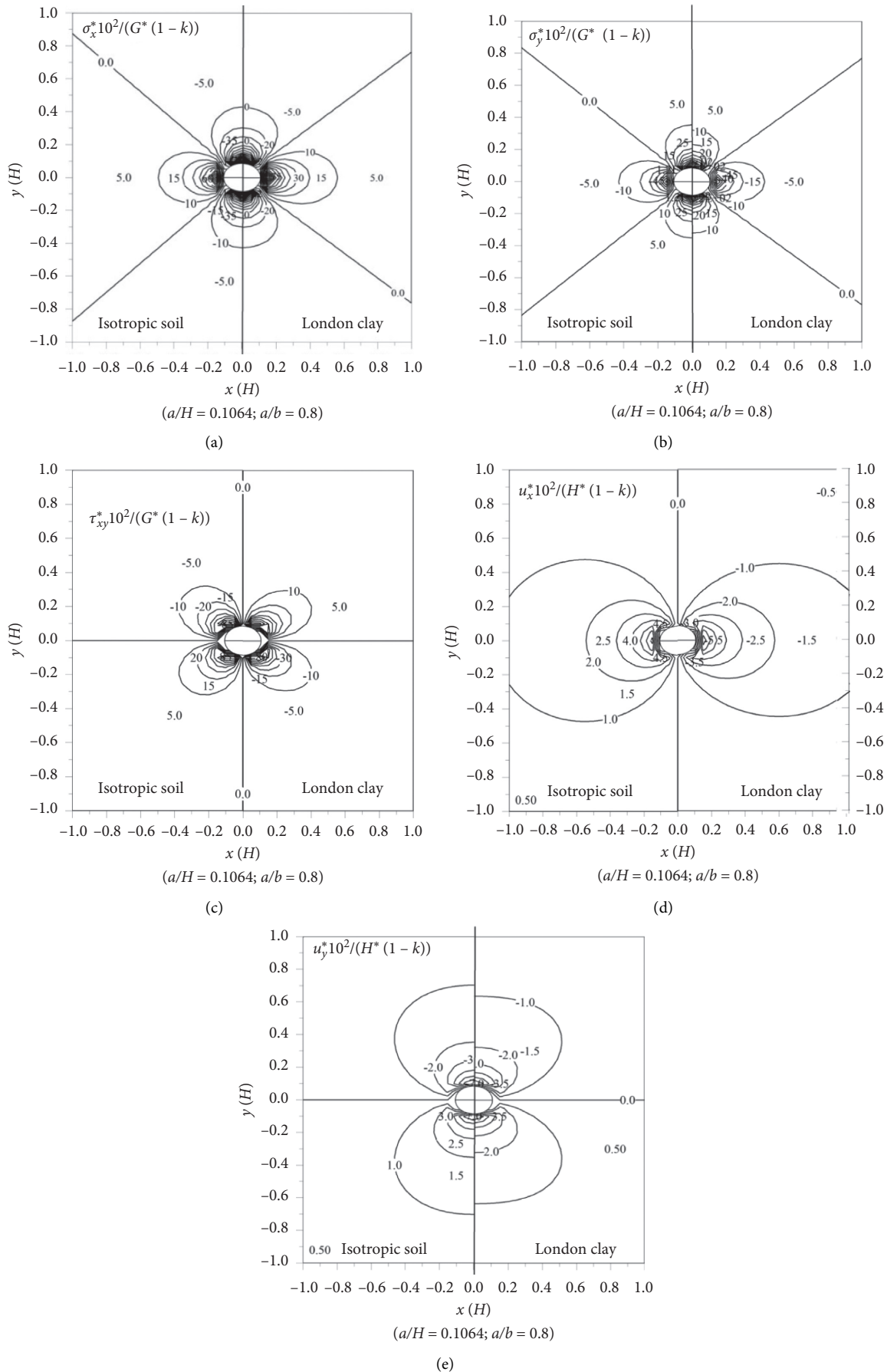
Figure 4: Analytical predictions of elastic solutions with isotropic and cross-anisotropic stiffness properties for London clay. (a) Horizontal normal stress. (b) Vertical normal stress. (c) Shear stress. (d) Horizontal displacement. (e) Vertical displacement.
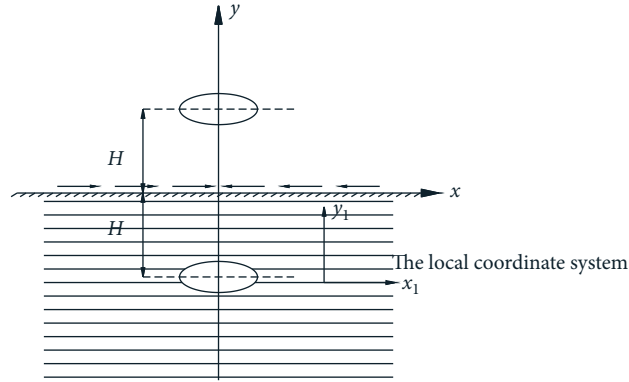
FIGURE 5: Schematic of the image method.
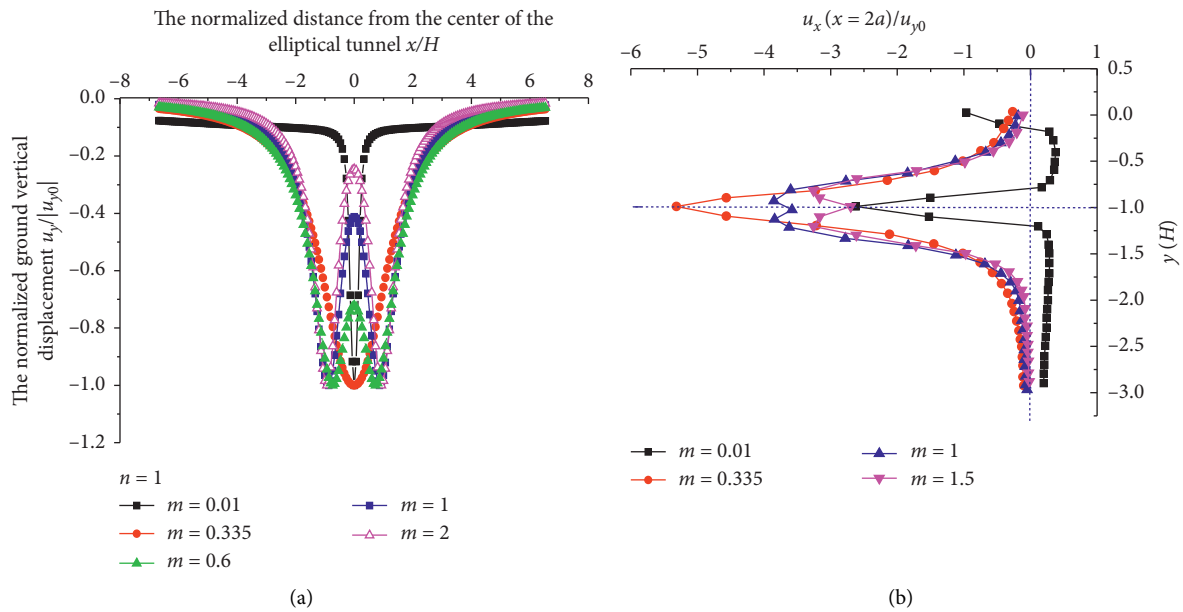
FIGURE 6: Influence of anisotropic stiffness ratio (m) on ground settlement and distribution of underground horizontal displacement. (a) Normalized ground settlement trough. (b) Normalized lateral displacement at offset, $x/2R = 1$.

singularity superposition technique (Figure 5). The displacement fields caused by a point source/sink $(0, -H)$ in a full plane and an image source $(0, +H)$ of equal and opposite deformation located equidistant above the ground surface are as follows:

$$u^+(x, y) + u^-(x, y) = U(x, y + H) - U(x, y - H),$$
$$v^+(x, y) + v^-(x, y) = V(x, y + H) - V(x, y - H). \quad (46)$$

The resulting normal and shear tractions along the bisecting line $y = 0$ (simulating a traction-free ground surface) produced by two mirror images are as follows:

$$N^c(x, 0) = 0$$
$$T^c(x, 0) = -2\tau_{xy}(x, -H). \quad (47)$$

A distribution of corrective shear tractions along the bisecting line is obtained:

$$T_0^c(x, 0) = -T^c(x, 0). \quad (48)$$

The displacement results can be obtained from the following formula:

$$u_x^c = 2\text{Re}\left[p_1\Phi_1^c(z_1) + p_2\Phi_2^c(z_2)\right],$$
$$u_y^0 = 2\text{Re}\left[q_1\Phi_1^c(z_1) + q_2\Phi_2^c(z_2)\right], \quad (49)$$

where $\Phi_1^c(z_1)$ and $\Phi_2^c(z_2)$ are stress potential functions produced by corrective shear tractions.

The final expression for displacement field is determined by combining equations (46) and (49):

$$u(x, y) = u^+(x, y) + u^-(x, y) + u^c(x, y),$$
$$v(x, y) = v^+(x, y) + v^-(x, y) + v^c(x, y). \quad (50)$$

This expression is still an approximate solution as two types of tunnels have not been considered.
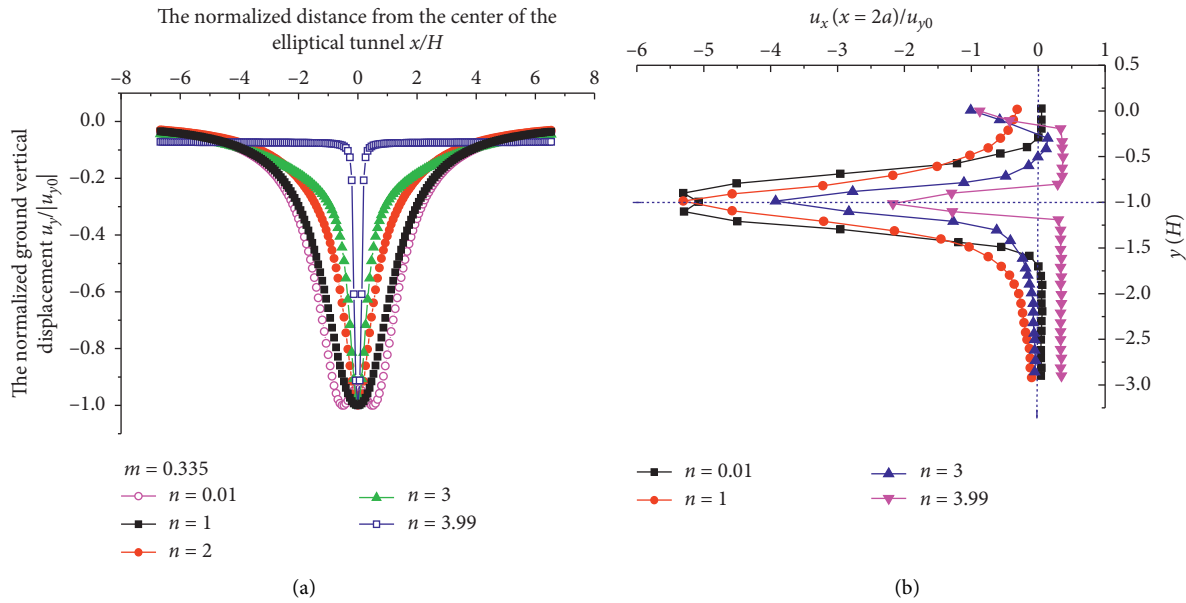
Figure 7: Influence of anisotropic stiffness ratio (n) on ground settlement and distribution of underground horizontal displacement. (a) Normalized ground settlement trough. (b) Normalized lateral displacement at offset, $x/2R = 1$.
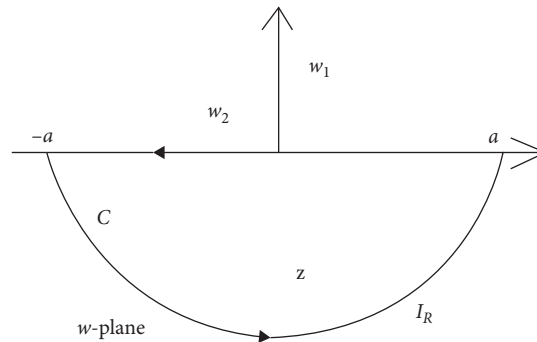
Figure 8: Integral path of the complex variable function.

5.2. Effect of Anisotropic Stiffness Ratios on the Predicted Displacement. We examined the effect of the anisotropic stiffness parameters, n ($n = E_h/E_v$) and m ($m = G_{vh}/E_v$), on the predictions of the ground settlement trough and subsurface horizontal displacement curves for a point offset at a distance $x = 2a$ from the center of the elliptical tunnel. These results correspond to the solutions for an elliptical tunnel with $a/H = 0.1064$, $b/a = 0.8$, and $v_{vh} = v_{hh} = 0.5$.

Figures 6 and 7 show the effect of the anisotropic stiffness ratios, m and n, on the normalized ground displacement and underground horizontal displacement at a reference vertical offset, $x = 2a$. The results indicate that the stiffness parameters, m and n, have a significant influence on the shape of the displacement distribution. In Figure 7(b), u_{y0} is the maximum vertical ground displacement calculated for varying values of the anisotropic stiffness parameter m, with $n = 1$. The point corresponding to $y = H$ is the peak value when $m \leq 0.355$, and the solutions generate narrower troughs when $m = 0.01$. The shape of the displacement trough also changes for $m > 0.355$, exhibiting double peaks.

In Figure 7, u_{y0} is the maximum vertical displacement calculated for varying values of the anisotropic stiffness parameter n, with $m = 0.335$. It can be seen that increasing the stiffness parameter n has the opposite effect compared with that for m. The results indicate narrow troughs when $n \geq 1$ (such as London clay), particularly for $n > 3$. In contrast, for soils with $n < 1$, double peaks are observed in the curves.

6. Conclusions

This paper has proposed an analytical method for modeling the displacement due to an unlined tunnel with an arbitrary cross section in an anisotropic plane. For this method, the following features are critical: (1) the original and deformed tunnel boundaries can be written in the form of exact or approximate polynomial mapping functions in the full plane, and the inverse mapping function must be single valued; (2) the solutions describe elastic solutions for soil under the assumption that the displacement vectors along the tunnel boundary are directed toward the center of the

tunnel. By introducing parameters of elastic anisotropic soil, this method can easily provide elastic solutions for a tunnel with an arbitrary cross section. Several examples are used to illustrate the proposed method, and the case of an elliptical tunnel is discussed in detail to verify the accuracy of the proposed method in full plane. The anisotropic parameters of London clay have negligible influence on the horizontal stress, horizontal displacement, and shear stress; however, these parameters lead to a slightly faster attenuation of the vertical stress and vertical displacement with distance. Surface and ground displacement in half plane can be obtained using a virtual image technique. Consequently, the method developed by Zymnis [22] can be extended from a circular tunnel to a tunnel with an arbitrary cross section. Our results clearly show that the anisotropic stiffness parameters, m and n, significantly influence the predicted displacement patterns for an unlined tunnel with a certain shape (b/a) and relative embedded depth (a/H).

Appendix

A. Solution of the Stress Potential Function Caused by Shear Stress

The analytical solution of $\Phi_1^c(z_1)$, $\Phi_2^c(z_2)$ can be obtained by the following integrals [7]:

$$
\begin{aligned}
\Phi_1^c(z_1) &= \frac{1}{\lambda_1 - \lambda_2} \frac{1}{2\pi i} \int_{-\infty}^{\infty} \frac{\lambda_2 f_1(\xi) + f_2(\xi)}{\xi - z_1} d\xi, \\
\Phi_2^c(z_2) &= -\frac{1}{\lambda_1 - \lambda_2} \frac{1}{2\pi i} \int_{-\infty}^{\infty} \frac{\lambda_2 f_1(\xi) + f_2(\xi)}{\xi - z_1} d\xi.
\end{aligned}
\tag{A.1}
$$

The normal and shear tractions are integrated along the surface of the curve and expressed as follows:

$$
\begin{aligned}
f_1(s) &= -\int_{\infty}^{s} N(x) dx = 0, \\
f_2(s) &= \int_{\infty}^{s} T_0^c(x) dx \\
&= \int_{s}^{\infty} T^c(x) dx.
\end{aligned}
\tag{A.2}
$$

Using equation (47), we find

$$
\begin{aligned}
f_2(s) &= \int_{s}^{\infty} T^c(x) dx, \\
&= -4\mathrm{Re}\left(\int_{s}^{\infty} \{\lambda_1 \Phi_1'(z_1) + \lambda_2 \Phi_2'(z_2)\} dx \right) \\
&= -4\mathrm{Re}\left(\int_{s}^{\infty} \{\lambda_1 \Phi_1'(x, -\lambda_1 H) + \lambda_2 \Phi_2'(x, -\lambda_2 H)\} dx \right) \\
&= -4\mathrm{Re}\left(\lambda_1 \Phi_1(s, -\lambda_1 H) + \lambda_2 \Phi_2(s, -\lambda_2 H) \right).
\end{aligned}
\tag{A.3}
$$

Substituting the above formula into equation (A.1), we obtain

$$
\begin{aligned}
\Phi_1^c(z) &= \frac{1}{\lambda_1 - \lambda_2} \frac{1}{2\pi i} \int_{-\infty}^{\infty} \frac{f_2(\xi)}{\xi - z} d\xi \\
&= -\frac{1}{\pi i (\lambda_1 - \lambda_2)} \int_{-\infty}^{\infty} \frac{\lambda_1 \Phi_1(\xi - \lambda_1 H) + \overline{\lambda_1 \Phi_1(\xi - \lambda_1 H)} + \lambda_2 \Phi_2(\xi - \lambda_2 H) + \overline{\lambda_2 \Phi_2(\xi - \lambda_2 H)}}{\xi - z} d\xi.
\end{aligned}
\tag{A.4}
$$

Let us assume that the integral path of the complex variable function is C, as shown in Figure 8. We also assume $\phi(w) = \Phi_k(w - \lambda_k H)$; $\overline{\phi(w)} = \overline{\Phi_k(w - \lambda_k H)}$; hence, there are two branch points $w_k (k = 1, 2)$. To obtain the branch points for the function $\phi(w)$, we differentiate $\Phi_k'(\zeta_k)$ with respect to $w_k'(\zeta_k)$, which yields

$$
\begin{aligned}
\Phi'(w - \lambda_k H) &= \frac{\Phi_k'(\zeta_k)(\zeta_k)}{w_k'(\zeta_k)} \\
&= \frac{\sum_{n=1}^{\infty} -nA_{kn}(\zeta_k) - (n+1)}{R \sum_{n=1}^{\infty} n(c_{kn}\zeta_k^{n-1} - d_{kn}\zeta_k - (n+1))} \\
&= \frac{\sum_{n=1}^{\infty} -A_{kn}}{R \sum_{n=1}^{\infty} (c_{kn}\zeta_k^{2n} - d_{kn})}.
\end{aligned}
\tag{A.5}
$$

The branch points w_k $(k = 1, 2)$ can be determined as

$$
\begin{aligned}
w_k &= \pm 2\sqrt{c_{kn}d_{kn}} + \lambda_k H \\
&= \begin{cases} \pm 2\sqrt{c_{k1}d_{k1}} + \lambda_k H & n = 1 \\ \pm \sqrt{\left(1 + \lambda_k^2\right)a_n\overline{a_n}} + \lambda_k H & n \geq 2 \end{cases}, \quad k = 1, 2.
\end{aligned}
$$
(A.6)

When the two branch points are located in the upper half plane and outside the integral path, $\phi(w)$ is analytic in the w plane, according to the properties of the Cauchy integral:

$$
\oint_C \frac{\phi(w)\mathrm{d}w}{w - z} = 2\pi\mathrm{i}\phi(z),
$$

$$
\oint_C \frac{\overline{\phi(w)}\mathrm{d}w}{w - z} = 0,
$$
(A.7)

$$
\begin{aligned}
\oint_C \frac{\phi(w)\mathrm{d}w}{w - z} &= \lim_{R \longrightarrow \infty}\left[\int_R^{-R} \frac{\phi(\xi)\mathrm{d}\xi}{\xi - z} + \int_{I_R} \frac{\phi(w)\mathrm{d}w}{w - z} \right] \\
&= -\int_{-\infty}^{\infty} \frac{\phi(\xi)\mathrm{d}\xi}{\xi - z}\oint_C \frac{\phi(w)\mathrm{d}w}{w - z}, \\
&= -\int_{-\infty}^{\infty} \frac{\phi(\xi)\mathrm{d}\xi}{\xi - z}.
\end{aligned}
$$
(A.8)

The final result of $\Phi_1^c(z_1), \Phi_2^c(z_2)$ can be obtained by simplifying equation (A.4) using equations (A.7) and (A.8).

Data Availability

The data used to support the findings of this study are available from the corresponding author upon request.

Conflicts of Interest

The authors declare that they have no conflicts of interest.

Acknowledgments

References

[1] A. J. Abbo, D. W. Wilson, S. W. Sloan, and A. V. Lyamin, "Undrained stability of wide rectangular tunnels," *Computers and Geotechnics*, vol. 53, no. 3, pp. 46–59, 2013.

[2] H. Nakamura, T. Kubota, M. Furukawa, and T. Nakao, "Unified construction of running track tunnel and crossover tunnel for subway by rectangular shape double track cross-section shield machine," *Tunnelling and Underground Space Technology*, vol. 18, no. 2, pp. 253–262, 2003, https://www.sciencedirect.com/science/article/abs/pii/S0886779803000348.

[3] J. B. Si, Y. H. Zhu, C. Ji, and S. H. Zhou, "Measurement and analysis of vertical deformation of stratum induced by quasi-rectangular shield tunneling in soft ground," *Chinese Journal of Rock Mechanics and Engineering*, vol. 36, no. 6, pp. 1551–1559, 2017.

[4] B. Chow, "Double-O-tube shield tunneling technology in the shanghai rail transit project," *Tunnelling and Underground Space Technology*, vol. 21, no. 6, pp. 594–601, 2006.

[5] C. Carranza-Torres and C. Fairhurst, "The elasto-plastic response of underground excavations in rock masses that satisfy the hoek-brown failure criterion," *International Journal of Rock Mechanics and Mining Sciences*, vol. 36, no. 6, pp. 777–809, 1999.

[6] B.-L. Li, X.-Q. Fang, T.-F. Zhang, and S.-P. Yang, "Elastic-slip interface effect on dynamic response of underwater convey tunnel in saturated poroelastic soil subjected to plane waves," *Tunnelling and Underground Space Technology*, vol. 103, Article ID 103468, 2020.

[7] X. Q. Fang, T. F. Zhang, B. L. Li, and R. J. Yuan, "Elastic-slip interface effect on dynamic stress around twin tunnels in soil medium subjected to blast waves," *Computers and Geotechnics*, vol. 119, Article ID 103301, 2020.

[8] A. Bobet, "Lined circular tunnels in elastic transversely anisotropic rock at depth," *Rock Mechanics and Rock Engineering*, vol. 44, no. 2, pp. 149–167, 2011.

[9] S. G. Lekhnitskii, *Theory of Elasticity of an Anisotropic Body*, Wiley, Hoboken, NJ, USA, 1963.

[10] Z. Zhang and Y. Sun, "Analytical solution for a deep tunnel with arbitrary cross section in a transversely isotropic rock mass," *International Journal of Rock Mechanics and Mining Sciences*, vol. 48, no. 8, pp. 1359–1363, 2011.

[11] N. I. Muskhelishvili, "Some basic problems of the mathematical theory of elasticity," *Mathematical Gazette*, vol. 48, no. 365, p. 351, 1953.

[12] G. E. Exadaktylos and M. C. Stavropoulou, "A closed-form elastic solution for stresses and displacements around tunnels," *International Journal of Rock Mechanics and Mining Sciences*, vol. 39, no. 7, pp. 905–916, 2002.

[13] H. T. Manh, J. Sulem, and D. Subrin, "A closed-form solution for tunnels with arbitrary cross-section excavated in elastic anisotropic ground," *Rock Mechanics & Rock Engineering*, vol. 16, no. 3, pp. 277–288, 2015.

[14] A. E. Green and G. I. Taylor, "Stress systems in aeolotropic plates. I," *Proceedings of the Royal Society of London. Series A. Mathematical and Physical Sciences*, vol. 173, no. 953, pp. 162–172, 1939.

[15] A. E. Green and G. I. Taylor, "Stress systems in aeolotropic plates, III," *Proceedings of the Royal Society of London. Series A. Mathematical and Physical Sciences*, vol. 184, no. 997, pp. 181–195, 1945.

[16] A. E. Green and G. I. Taylor, "Stress systems in aeolotropie plates. VI," *Proceedings of the Royal Society of London. Series A. Mathematical and Physical Sciences*, vol. 184, no. 998, pp. 289–300, 1945.

[17] C. Sagaseta, "Analysis of undraind soil deformation due to ground loss," *Géotechnique*, vol. 37, no. 3, pp. 301–320, 1987.

[18] A. Verruijt, "A complex variable solution for a deforming circular tunnel in an elastic half-plane," *International Journal for Numerical and Analytical Methods in Geomechanics*, vol. 21, no. 2, pp. 77–89, 1997.

[19] K. H. Park, "Elastic solution for tunneling-induced ground movements in clays," *International Journal of Geomechanics*, vol. 4, no. 4, pp. 310–318, 2004.

[20] K.-H. Park, "Analytical solution for tunnelling-induced ground movement in clays," *Tunnelling and Underground Space Technology*, vol. 20, no. 3, pp. 249–261, 2005.

[21] F. Pinto and A. J. Whittle, "Ground movements due to shallow tunnels in soft ground. I: analytical solutions," *Journal of Geotechnical & Geoenvironmental Engineering*, vol. 140, no. 4, Article ID 04013040, 2013.

[22] D. M. Zymnis, I. Chatzigiannelis, and A. J. Whittle, "Effect of anisotropy in ground movements caused by tunnelling," *Géotechnique*, vol. 63, no. 13, pp. 1083–1102, 2013.

[23] D. M. Zymnis, *Evaluation of Analytical Methods to Interpret Ground Deformations Due to Soft Ground Tunneling*, Cambridge University, England, UK, 2009.

[24] B. Simpson, J. H. Atkinson, and V. Jovicic, "The influence of anisotropy on calculations of ground settlements above tunnels," in *Proceeding International Symposium on Geotechnical Aspects of Underground Construction in Soft Ground*, R. J. Mair and R. N. Taylor, Eds., pp. 591–595, Balkema, London, UK, 1996.

[25] K. M. Lee and R. K. Rowe, "Deformations caused by surface loading and tunneling: the role of elastic anisotropy," *Géotechnique*, vol. 39, no. 1, pp. 125–140, 1989.

[26] D. J. Pickering, "Anisotropic elastic parameters for soil," *Géotechnique*, vol. 20, no. 3, pp. 271–276, 1970.

[27] R. E. Gibson, "The analytical method in soil mechanics," *Geotechnique*, vol. 24, no. 1, pp. 115–140, 1974.

[28] A. Gasparre, S. Nishimura, N. A. Minh, M. R. Coop, and R. J. Jardine, "The stiffness of natural London clay," *Géotechnique*, vol. 57, no. 1, pp. 33–47, 2007.

[29] W. Zou, Q. He, M. Huang, and Q. Zheng, "Eshelby's problem of non-elliptical inclusions," *Journal of the Mechanics and Physics of Solids*, vol. 58, no. 3, pp. 346–372, 2010.

Research Article

Simplified Analytical Method for Predicting the Lateral Ground Displacements due to Shield Tunnelling

Lianwei Sun (ID),[1] **Zhong-chao Li**,[2] **and Rong-zhu Liang** (ID)[3]

[1]*Shanghai Construction Group Co., Ltd., Shanghai 200080, China*
[2]*Wuhan Municipal Construction Group Co., Ltd., Wuhan 340023, Hubei, China*
[3]*China University of Geosciences (Wuhan), Faculty of Engineering, Wuhan 430074, China*

Correspondence should be addressed to Rong-zhu Liang; liangcug@163.com

Earth pressure balance or slurry shield tunnelling will squeeze the subsoils and lead to lateral outward ground displacement. However, current methods to estimate the shield tunnelling-induced ground displacements generally use the methods based on the face unsupported tunnelling (e.g., New Austrian tunnelling and open shield excavation), which cannot predict the lateral ground movement due to shield tunnelling. In this paper, a novel simplified analytical method is proposed to predict the ground lateral displacement during the shield advancing process. The key shield tunnelling operation factors, including the additional pressure of cutter head, the friction forces around shield body, the back-fill grouting pressure, and the soil volume loss are all considered. The lateral ground displacements induced by the four former factors are calculated by using Mindlin's solutions. The soil volume loss-induced lateral ground displacement is calculated by employing the expression introduced by Pinto and Whittle. Combining with the displacement obtained from all the factors, the analytical method for lateral ground displacement induced by shield tunnelling is obtained. The applicability of the proposed analytical approach is verified with three well-documented case histories involving slurry shield and EPB shield machines.

1. Introduction

Earth pressure balance (EPB) or slurry shield tunnelling technology has advantage of rapid construction efficiency and minor environment disturbance, which is widely used in metro tunnel construction in densely urban area. However, the shield tunnelling method is kind of a face pressured tunnelling method, which will squeeze the ground and lead to large horizontal ground displacement. The ground movement mechanisms associated with shield tunnelling are totally different from the face unsupported tunnelling, such as New Austrian tunnelling and open shield excavation, in which the inward ground movements are usually observed because of none face pressure or grouting pressure imposing on the excavation face. Therefore, accurate evaluation of the shield tunnelling-induced ground deformation is vital before assessment of the adverse effects on adjacent buildings and the nearby

underground utilities (e.g., shallow foundations, exiting tunnels, piles, and gas pipelines).

During the last decades, various approaches have been established for predicting the ground deformation associated with space unsupported tunnelling methods, namely, empirical method, analytical method, and finite-element method [1–11]. Peck [1] and Attewell and Woodman [2] indicated that the ground surface movement profile-induced tunnel excavation can be empirically described using Gaussian distribution curve. Mair et al. [3] and Fang et al. [4] further modified and improved the Peck formula and applied to predict the subsurface settlement caused by tunnel excavation. In recent years, lots of analytical methods have been established to predict the tunnelling-induced displacements. Sagaseta [5] and Verruijt and Booker [6] presented closed-form solutions for three-dimensional soil movements induced by tunnelling-caused soil loss in isotropic incompressible ground and compressible ground,

respectively. Loganathan and Polous [7] redefined equivalent ground loss and proposed a new analytical method to calculate the vertical and lateral soil movements in nonuniform convergence pattern. Bobet [8] and Osman et al. [9] deduced a series of solutions for two-dimensional soil movements based on the elasticity theory. The abovementioned analytical solutions are more suitable for estimating the ground movement associated with face unsupported tunnelling. Franza and Marshall [10] proposed empirical and semianalytical methods for evaluating the ground settlements induced by tunnelling in sands. Zhang et al. [11] proposed a closed-form elastic analytical solution for prediction of the tunnelling-ground displacement. However, the detailed observations from San Francisco [12], London [13], Shanghai [14], France [15], and Taipei [16] indicated that heaves and outward ground movements were always observed during tunnel excavation by using the advanced shield tunnelling methods (EPB and slurry shield machines). The main reason for the difference is due to the mechanization of shield tunnelling procedures. During the shield tunnelling, the subsoil is excavated by rotating cutter head. Then, the shield moves forwards by hydraulic jacks. Finally, back-fill grouting is carried out to fill the construction gap. All the procedures may lead to ground displacement which makes the ground movement pattern quite different from that of conventional tunnelling. Therefore, a suitable analytical method is urgently needed to reliably predict ground displacements due to shield tunnelling.

With the development of computer technology, the nonlinear finite-element analysis (FEA) has been carried out to simulate the entire tunnelling excavation process. Lee and Rowe [17] performed a 3D elastoplastic FE analysis to investigate the effects of shield tunnelling on the surface and subsurface ground movements. Dias and Kastner [15] established 3D finite-element models to simulate the slurry shield excavation processes in tunnel projects in France and China, respectively. Undoubtedly, the FEA is a direct method to model the 3D soil deformations, as well as tunnelling stages. Yiu et al. [18] explored the masonry building responses to shallow tunnelling using 3D finite-element modelling. Zhang et al. [19] established a 3D fluid-solid coupling finite-element model to investigate the unexpected ground settlement when the shield machine advanced from the low-permeability ground to the high-permeability ground.

In this paper, a novel simplified analytical method is proposed to predict the lateral ground displacements caused by shield tunnelling in soft ground. The key shield tunnelling operation parameters such as additional pressure of cutter head, the frictions around shield shell, the grout injection pressure, and the soil volume loss are taken into account in the proposed method to consider the shield tunnel construction performance. The proposed analytical method is verified against three well-documented case histories in San Francisco tunnel, Shanghai Metro Line-2 tunnel, and France Vaise subway tunnel.

2. Simplified Analytical Method for Predicting Lateral Ground Movement Induced by Shield Tunnelling

The mechanism of the interaction between shield tunnelling excavation and soil surrounding is highly complex. The ground deformation is mainly influenced additional pressures of cutter-head q, frictions around shied shell skin f, the tail grouting pressure p, and the soil volume loss v_l during shield machine advancing. Therefore, the four main influencing factors are considered in the proposed method. Figure 1 shows the mechanical model of shield tunnelling in ground. The lateral ground displacements induced by the variants of q, f, and p are estimated by using Mindlin's solutions [20]. The analytical solutions suggested by Pinto and Whittle [21] are applied to compute the lateral ground displacements caused by the soil volume loss v_l. Finally, the total lateral displacements can be estimated by superposing the results calculated by these separated variants. In the proposed method, the lateral displacement induced by shield tunnelling at transversal and longitudinal directions is considered.

Shield machine usually advances at a shallow depth, and the ground displacements caused by the variants q, f, and p are typical semi-infinite problems. Correspondingly, semi-infinite Mindlin's solutions [20] are selected to calculate the ground displacements caused by the variants q, f, and p in this analysis. A concentrated force p_h parallel to the surface boundary acting at a point in the interior of a half-space is shown in Figure 2.

The response of lateral displacements at both longitudinal and transversal directions to the horizontal concentrated force P_h is expressed as follows:

$$v_h = \frac{P_h x' y'}{16\pi G (1-\mu)} \left[\frac{1}{R_1^3} + \frac{3-4\mu}{R_2^3} - \frac{6cz'}{R_2^5} - \frac{4(1-\mu)(1-2\mu)}{R_2(R_2+z'+c)^2} \right], \tag{1}$$

$$u_h = \frac{P_h}{16\pi G (1-\mu)} \left\{ \frac{3-4\mu}{R_1} + \frac{1}{R_2} + \frac{x'^2}{R_1^3} + \frac{(3-4\mu)x'^2}{R_2^3} + \frac{2cz'}{R_2^3} \left(1 - \frac{3x'^2}{R_2^2} \right) + \frac{4(1-\mu)(1-2\mu)}{R_2+z'+c} \left[1 - \frac{x'^2}{R_2(R_2+z'+c)} \right] \right\}, \tag{2}$$
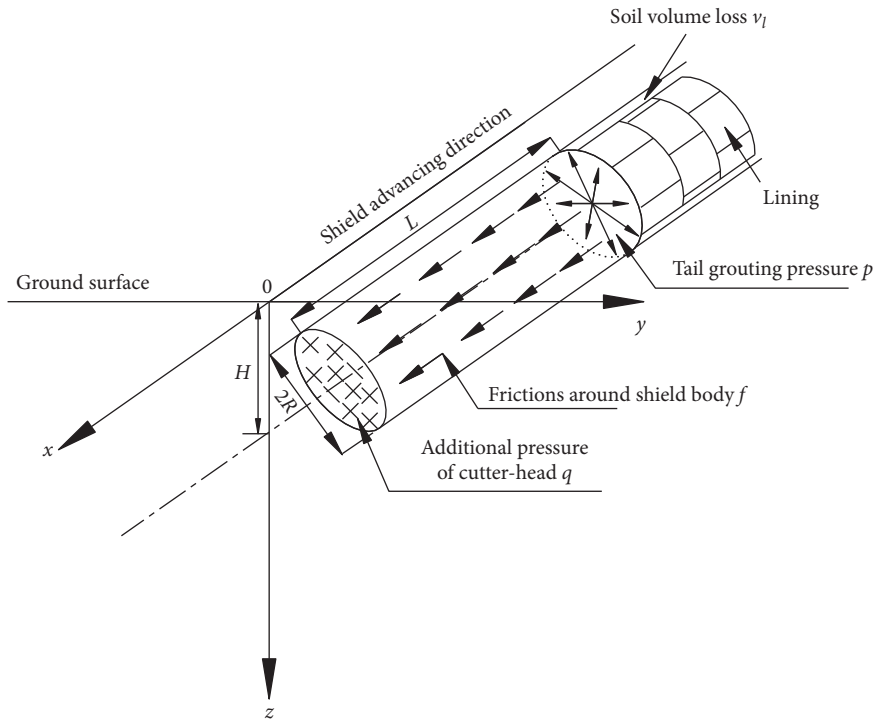
FIGURE 1: Mechanical model of shield tunnelling in soft ground.
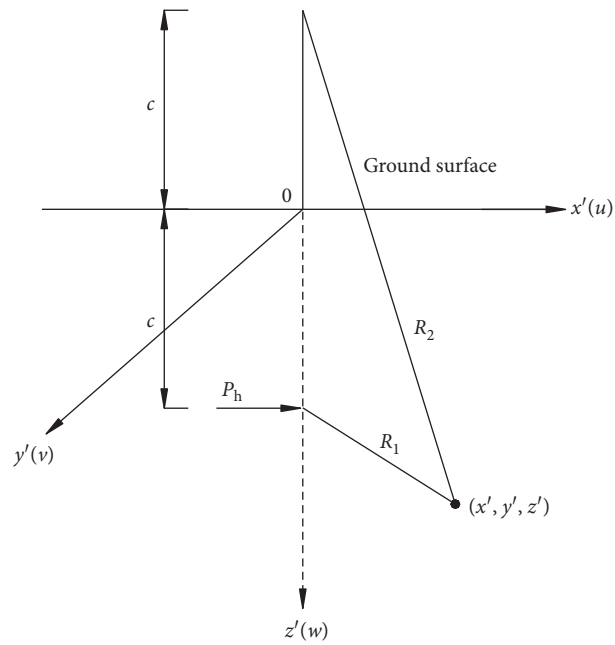
FIGURE 2: Mindlin's solutions of a concentrated force acting at a point in the interior of half-space solid parallel to the ground surface.

where v_h and u_h are the lateral displacements in longitudinal and transversal directions, respectively. μ is Poisson's ratio; G is the shear modulus. $R_1 = \sqrt{x'^2 + y'^2 + (z' - c)^2}$, $R_2 = \sqrt{x'^2 + y'^2 + (z' + c)^2}$.

$$u_{1q} = \int_0^R \int_0^{2\pi} qr \, dr \, d\theta \frac{1}{16\pi G(1 - \mu)} \left\{ \frac{3 - 4\mu}{R_1} + \frac{1}{R_2} + \frac{x^2}{R_1^3} + \frac{(3 - 4\mu)x^2}{R_2^3} + \frac{2(H - r \sin\theta)z}{R_2^3} \left(1 - \frac{3x^2}{R_2^2} \right) \right.$$
$$\left. + \frac{4(1 - \mu)(1 - 2\mu)}{R_2 + z + (H - r \sin\theta)} \left[1 - \frac{x^2}{R_2(R_2 + z + H - r \sin\theta)} \right] \right\},$$

$$v_{1q} = \int_0^R \int_0^{2\pi} qr \, dr \, d\theta \frac{x(y - r \sin\theta)}{16\pi G(1 - \mu)} \left[\frac{1}{R_1^3} + \frac{3 - 4\mu}{R_2^3} - \frac{6(H - r \sin\theta)z}{R_2^5} - \frac{4(1 - \mu)(1 - 2\mu)}{R_2(R_2 + z + H - r \sin\theta)^2} \right],$$

(3)

where u_{1q} and v_{1q} are the lateral displacements at both longitudinal and transversal directions, respectively; R is the radius of cutter head; R_1 and R_2 can be expressed as $R_1 = \sqrt{x^2 + (y - r \cos\theta)^2 + (z - H + r \sin\theta)^2}$ and $R_2 = \sqrt{x^2 + (y - r \cos\theta)^2 + (z + H - r \sin\theta)^2}$, respectively.

The additional face pressure q is assumed to be distributed uniformly at the cutter head. For a tunnel constructed by a slurry shield tunnel machine, the additional pressure of cutter-head q can be regarded as the difference between the measured slurry pressure p_{sl} and the in situ earth pressure at rest $K_0 \gamma H$ at the depth of tunnel axis:

$$q = p_{sl} - K_0 \gamma H, \tag{4}$$

where K_0 is the coefficient of lateral earth pressure at rest; γ and H are the representative unit weight and the depth from the ground surface to the spring-line of the tunnel, respectively.

However, for tunnel constructed by an EPB machine, Standing et al. [22] found the ground moved outward was measured and the pore-water pressures continuously increased in spite of the fact that the measured earth pressures at the soil chamber were significantly lower than the earth pressure at rest. Standing et al. [22] indicated that the actual normal stresses at cutter head were much larger than the measured earth pressure at the soil chamber. This phenomenon can be interpreted as ground squeezing effect caused by the rotating cutter head of EPB machine [23]. Taking the key cutting parameters and ground conditions into consideration, Wang [23] presented a theoretical

2.1. Lateral Ground Displacements Induced by the Additional Pressure of Cutter-Head q. Figure 3 shows the sketch of integration of additional pressure of cutter head. The lateral displacements at both longitudinal and transversal directions induced by additional pressure of cutter-head q are obtained by integrating (1) and (2), respectively:

solution to calculate the squeezing normal stress ahead of the cutter head. In this study, the squeezing normal stress is taken as the additional pressure of the cutter-head q:

$$q = \frac{10.13(1 - \mu)E_u \pi v(1 - \xi)^2}{(1 + \mu)(3 - 4\mu)Dkw} + \Delta p', \tag{5}$$

where E_u is undrained Young's modulus of soil; v is the driving rate of the shield; ξ is the open ratio of the cutter head; D is the diameter of the cutter head; k is number of the blind slots; w is the angular speed; and $\Delta p'$ is the squeezing pressure at the opening of cutter head, ranging from $10\,kPa$ to $20\,kPa$.

The operation parameters, such as the driving rate v and the rotating rate w, are continuously recorded during the advancing. Undrained Young's modulus of soil E_u in clayey ground can be obtained by the approximately relation between E_u and the undrained shear strength c_u as $E_u = 350\,c_u$ [24].

2.2. Lateral Ground Displacements Induced by the Frictions around Shield Body f. The frictions around shield body f are generated by the interaction between the moving shield body and the contacted soils. As shown in Figure 4, it is assumed that the frictions around shield body f are distributed uniformly in the longitudinal direction along the shield body, but nonuniformly around the shield periphery. The lateral ground displacements at longitudinal and transversal directions induced by the frictions around shield body f are obtained by integrating (1) and (2), respectively, as follows:
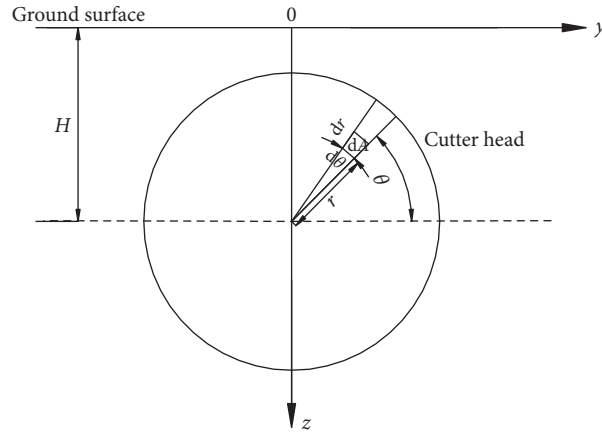
FIGURE 3: The sketch of integration of additional pressure of cutter head.
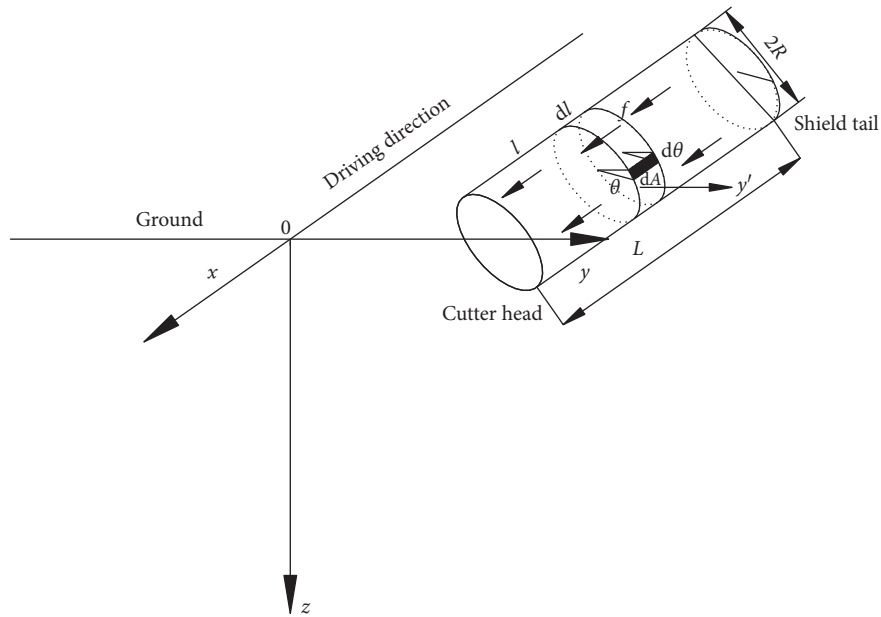
FIGURE 4: The relation of the global and local coordinate system and the sketch of frictions around the shield body.

$$u_{2f} = \int_0^{2\pi} \int_0^L \frac{fR\mathrm{d}l\,\mathrm{d}\theta}{16\pi G(1-\mu)} \left\{ \frac{3-4\mu}{R_1} + \frac{1}{R_2} + \frac{(x+l)^2}{R_1^3} + \frac{(3-4\mu)(x+l)^2}{R_2^3} + \frac{2(H-R\sin\theta)z}{R_2^3}\left(1 - \frac{3(x+l)^2}{R_2^2}\right) \right.$$

$$\left. + \frac{4(1-\mu)(1-2\mu)}{R_2 + z + (H - R\sin\theta)}\left[1 - \frac{(x+l)^2}{R_2(R_2 + z + H - R\sin\theta)}\right]\right\},$$ (6)

$$v_{2f} = \int_0^{2\pi} \int_0^L \frac{fR\mathrm{d}l\,\mathrm{d}\theta(x+l)(y-R\sin\theta)}{16\pi G(1-\mu)}\left[\frac{1}{R_1^3} + \frac{3-4\mu}{R_2^3} - \frac{6(H-R\sin\theta)z}{R_2^5} - \frac{4(1-\mu)(1-2\mu)}{R_2(R_2 + z + H - R\sin\theta)^2}\right],$$

where L is the length of shield shell; u_{2f} and v_{2f} are the lateral ground displacements in the longitudinal and transversal directions, respectively; R_1 is equal to $\sqrt{(x+l)^2 + (y - R\cos\theta)^2 + (z - H + R\sin\theta)^2}$; R_2 is equal to $\sqrt{(x+l)^2 + (y - R\cos\theta)^2 + (z + H - R\sin\theta)^2}$.

The friction around shield body f is estimated by

$$f = \tau_{sr}$$
$$= \beta_s \sigma_\theta \tan\delta,$$ (7)

where τ_{sr} is the residual shear force at the pile-soil interface; β_s is the softening coefficient, which is defined as the ratio of the residual shear force τ_{sr} to the ultimate shear force τ_u at the steel-soil interface. Its value varies from 0.83 to 0.97 for

soft soils [25]. δ is the interior angel between the shield shell and the contacted soils, which is presented in Table 1 based on Alonso et al.'s [26] interface shearing experiments.

σ_θ is the normal stress acting on the shield body:

$$\sigma_\theta = \sigma_v \sin^2\theta + \sigma_h \cos^2\theta, \tag{8}$$

where σ_v and σ_h are the vertical and horizontal effective stresses acting on the shield body, respectively:

$$\sigma_v = \sigma_t - \gamma R \sin\theta,$$
$$\sigma_h = K_0 \sigma_v, \tag{9}$$

where σ_t is the vertical earth stress at the shield axis.

2.3. Lateral Ground Displacements Induced by the Tail Grouting Pressure p.

As the shield moves forward, the grouting materials are injected synchronously to fulfill the annual void between the segmental lining and the excavation face. The back-fill grouting can effectively prevent the ground moving into the annual void. However, when the tail grouting pressure p is larger than the in situ earth pressure (both vertical and horizontal), the surrounding ground will be pushed away laterally and ground upheaval and outward

TABLE 1: The value of interface friction angle δ between different soils and smooth steel material.

Type of soils	Interface angel
Clays	$6.5°{\sim}9°$ or $0.55{\sim}0.56\ {\phi'}^*$
Sands	$23.5°{\sim}24°$ or $0.55{\sim}0.64\ {\phi'}^*$
Clayey gravel	$7.5°{\sim}9.5°$ or $0.44{\sim}0.58\ {\phi'}^*$

$^*\phi'$ is the effective interior angle of soil.

displacements occur. Therefore, the effects of tail grouting on the ground movements should be considered.

Figure 5 illustrates the calculation model of the lateral ground displacements induced by the tail grouting pressure p. It is assumed that the grouting pressure distributes uniformly around the shield tail periphery and the grouting length is equal to the width of the segmental lining. In reality, the tail grouting pressure p is continuously monitored during the shield advancing.

It is noted that the grouting pressure has little influence on the lateral ground displacement at longitudinal direction. Therefore, lateral ground displacement at longitudinal direction is not considered in this analysis. Based on Mindlin's solutions, the lateral displacements at transversal direction are obtained as follows:

$$v_{3p} = \int_0^S \int_0^{2\pi} \frac{(p - \sigma_\theta)\cos\theta R\,ds\,d\theta}{16\pi G(1-\mu)} \left\{ \frac{3-4\mu}{R_1} + \frac{1}{R_2} + \frac{(y - R\cos\theta)^2}{R_1^3} + \frac{(3-4\mu)(y - R\cos\theta)^2}{R_2^3} \right.$$
$$\left. + \frac{2(H - R\sin\theta)z}{R_2^3}\left[1 - \frac{3(y - R\cos\theta)^2}{R_2^2}\right] + \frac{4(1-\mu)(1-2\mu)}{R_2 + z + H - R\sin\theta}\left[1 - \frac{(y - R\cos\theta)^2}{R_2(R_2 + z + H - R\sin\theta)}\right] \right\}, \tag{10}$$

where S is the influencing length of grouting. As mentioned above, S is taken as the width of segmental lining. R_1 is equal to $\sqrt{(y - R\cos\theta)^2 + (x + L + s)^2 + (z - H + R\sin\theta)^2}$, and R_2 is equal to $\sqrt{(y - R\cos\theta)^2 + (x + L + s)^2 + (z + H - R\sin\theta)^2}$.

2.4. Lateral Ground Displacements Induced by the Soil Volume Loss vl.

Many studies have been proposed to estimate the lateral soil displacements associated with tunnelling-induced soil losses [7–11]. However, all of these methods offer

two-dimensional solutions, which are unable to capture the three-dimensional behavior of soil deformations associated with shield tunnelling. In this study, three-dimensional analytical solutions introduced by Pinto and Whittle [21] are applied to predict the lateral ground displacements.

Assuming the soil volume loss distributed uniformly along the tunnel axis, Pinto and Whittle [21] deduced three-dimensional closed-form solutions for ground displacements induced by the soil volume losses. The lateral ground displacement solutions in both longitudinal and transversal directions of shield advancing are given as follows:

$$u_{4v_l} = \frac{v_l}{4\pi}\left\{\frac{1}{R_{11}} + \frac{(3-4\mu)}{R_{22}} - \frac{2z(z-H)}{R_{22}^3}\right\}, \tag{11}$$

$$v_{4v_l} = \frac{v_l}{4\pi}\left\{\frac{y[R_{11} - (x+L)]}{r_1^2 R_{11}} + \frac{(3-4\mu)y[R_{22} - (x+L)]}{r_2^2 R_{22}} + \frac{yz(z+H)\left\{2(x+L)\left[3R_{22}^2 - (x+L)^2\right] - 4R_{22}^3\right\}}{r_2^4 R_{22}^3}\right\}, \tag{12}$$

where u_{4v_l} and v_{4v_l} are the lateral ground displacements in both longitudinal and transversal directions of shield advancing, respectively; v_l is the soil volume loss, $v_l = 2\pi R u_\varepsilon$,

where u_ε is the distance between the segmental lining and the excavated soils in uniform convergence pattern. The correlation between the soil volume loss v_l and the ratio of soil
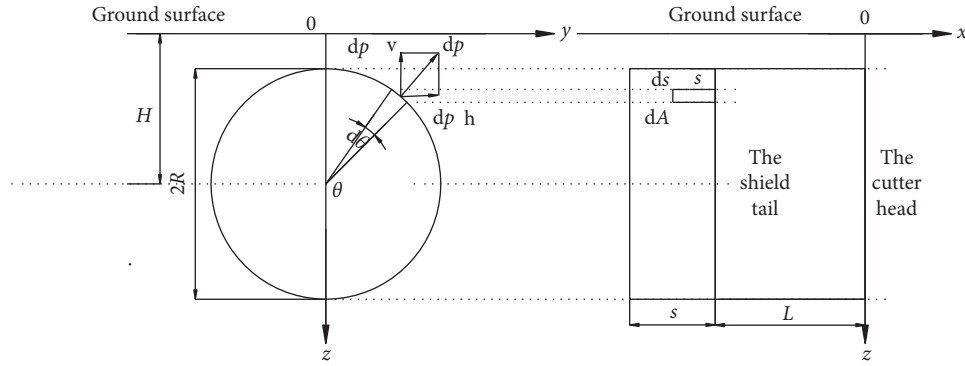
FIGURE 5: The sketch of integration of the grouting pressure.

loss v_{loss} is $v_l = v_{loss} \cdot \pi R_t^2$, where R_t is the radius of tunnel lining; r_1 is $\sqrt{y^2 + (z + H)^2}$; r_2 is $\sqrt{y^2 + (z - H)^2}$; R_{11} is $\sqrt{y^2 + (x + L)^2 + (z + H)^2}$; R_{22} is $\sqrt{y^2 + (x + L)^2 + (z - H)^2}$.

However, for the real situation, the presence of the shield body will significantly prevent the deformations transforming from the overexcavated soil volume loss around the tail. Thus, the longitudinal lateral displacements induced by the soil volume loss (12) around the shield tail are assumed as zero.

2.5. Total Lateral Ground Displacements Induced by Shield Tunnelling. Combining the lateral ground displacements induced by the additional pressure of cutter-head q, the frictions around shield body f, the tail grouting pressure p, and the soil volume loss v_l during shield advancing, the analytical solutions for predicting the lateral ground displacements in both longitudinal and transversal directions are obtained, respectively. They can be expressed as

$$
\begin{aligned}
u &= u_{1q} + u_{2f} + u_{4v_l}, \\
v &= v_{1q} + v_{2f} + v_{3p},
\end{aligned}
\tag{13}
$$

where u and v are the lateral ground displacements in longitudinal and transversal directions, respectively.

3. Cases Studies

Three previously published well-documented case histories are selected to assess the applicability of the proposed analytical solutions in this section. The measured field data, as well as FEA results, are compared with the predicted results.

3.1. Case 1: San Francisco Tunnel N-2 Contract. A 3.7 m outer diameter earth pressure balanced shield with 5 m long was employed to the San Francisco Clean Water tunnel project N-2 contract. A 917 m long, 3.55 m outer diameter tunnel was constructed in soft, saturated, and low-strength and permeability Bay Mud clay. Field instrumentation program was carefully conducted to observe the response of the ground during and after shield advancement. This well-

documented project provides a unique opportunity to study the lateral ground responses to shield construction. The predictions of the longitudinal lateral ground displacements are compared with the measured results, as well as the FEA simulation results.

A subsoil profile is shown in Figure 6. As shown in Figure 6, the tunnel axis was located at the depth of 10.9 m below the ground surface, which was entirely in the soft saturated stratum, known as recent Bay mud. The overlying and underlying strata were rubble fill with intermediate density and sandy colluvial soil, respectively. Detailed description of the site conditions and the shield tunnelling operation can be referred to Finno and Clough [27] and Clough et al. [12].

Some related parameters obtained from the Finno and Clough [27] are given as follows: based on the site investigation and laboratory tests, the average unit weight of the ground, including the fill ground and the Bay mud, can be taken as 17.6 kN/m³. The undrained shear strength s_u of recent Bay mud is 24.3 kPa at the top of layer and increases linearly with depth at 0.63 kPa/m. The shear modulus G is taken 3.24 MPa for recent Bay mud, which is approximately about 120 times of undrain shear strength s_u according to Hashimoto et al.'s [24] study. Undrained Young' modulus E_u is about 9.72 MPa according to $E_u = 2(1 + u)G$. Poisson's ratio u is assumed to be 0.5 for the undrained conditions of the soft recent Bay mud clay. The opening ratio of the applied EPB shield ξ and the number of blind slots k are assumed to be 30% and 3, respectively [27]. The average driving rate v is 9.1 m/day. The coefficient of earth pressure at rest K_0 is assumed to be 1. The angular speed w is assumed to be 3.6π rad/min. The softening coefficient β and the interface interior angle δ are taken as 0.9 and 9°, respectively. Thus, the calculated additional pressure of cutter head is about 24.5 kPa. Respecting that the grouting is inefficient in this project, the effects of the tail grouting on the ground are ignored in calculation.

The predicted and observed longitudinal horizontal displacements at 1.22 m and 2.44 m front of the shield face are plotted in Figures 6(a) and 6(b), respectively. It is found that the predictions at different distances at the front of the tunnel face are generally in good agreement with the field observations as well as the FEA results, although the predicted results are slightly larger than the observations below

(a)

(b)
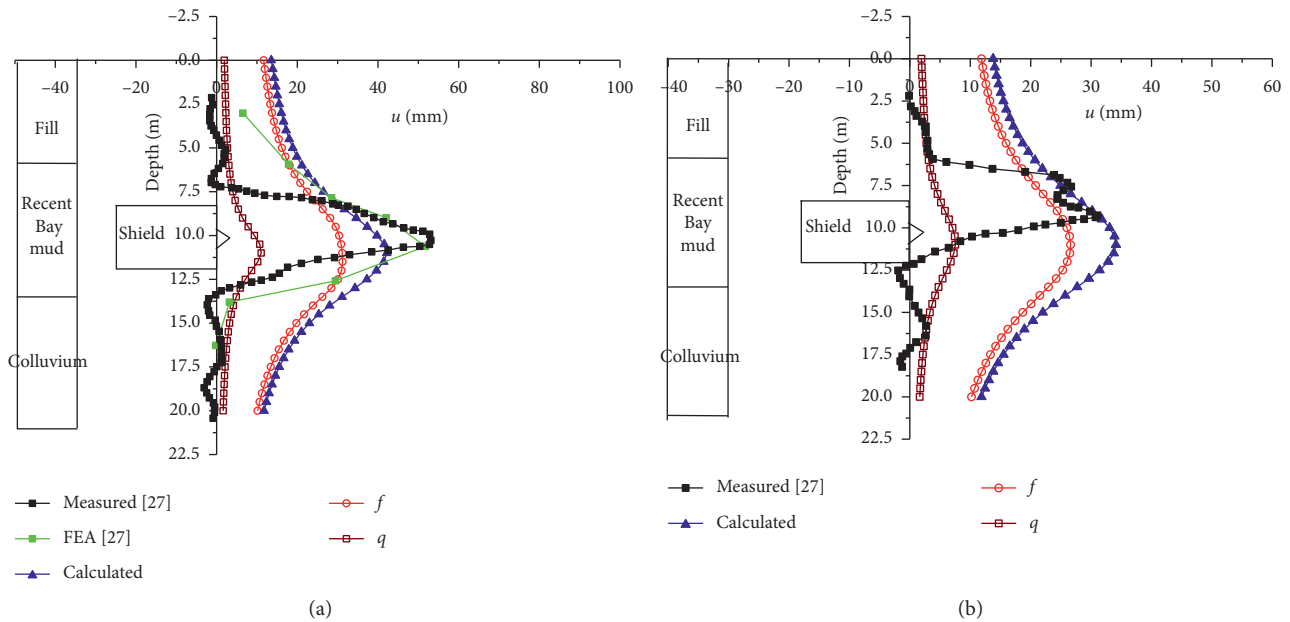
Figure 6: Comparison between the measured and predicted results of lateral ground displacements at the longitudinal direction of shield advancing, San Francisco tunnel N-2 project: (a) 1.22 m ahead of shield face (b) 2.44 m ahead of the shield face.

and above the tunnel lining level. It may be attributed to the site conditions where the overlaid rubble fill ground and underlaid colluvial soils would significantly confine the movements of inclinometers. Generally, the prediction accuracy is in an acceptable manner.

From Figures 6(a) and 6(b), it is noted that the lateral displacements contributed by frictions around the shield body f are obviously larger than the contribution of the additional pressure of cutter-head q. However, this differs from the common understanding that the additional pressure of cutter-head q contributes a large portion of the displacements. In general, the proposed analytical method can be reasonably used to predict the lateral ground displacements at the longitudinal direction of the advancing shield.

3.2. Case 2: Shanghai Metro Line-2 Tunnel.

Shanghai Metro Line-2 tunnel was constructed through soft, sensitive, saturated, and low-permeable soft clay by means of an advanced EPB shield machine. A typical soil profile of this project is presented in Figure 7. The responses of the soft ground during and after the advancement of tunnelling machine were carefully monitored. The inclinometer was located at 6.2 m beside the shield axis and the lateral displacement at transversal direction was monitored. The axis of 6.2 m-diameter tunnel was located at a depth of 15 m blow the ground surface. The detailed monitoring program and the measurements were well interpreted and discussed by Lee et al. [14].

The main parameters related to the analysis are listed as follows: the outer diameter of the shield D is 6.34 m; the length of the shield L is 6.24 m, the width of the segmental ling s is 1 m; the grouting pressure p is 250 kPa; the advancing rate v is 12 m/d; the equivalent Poisson ratio u is
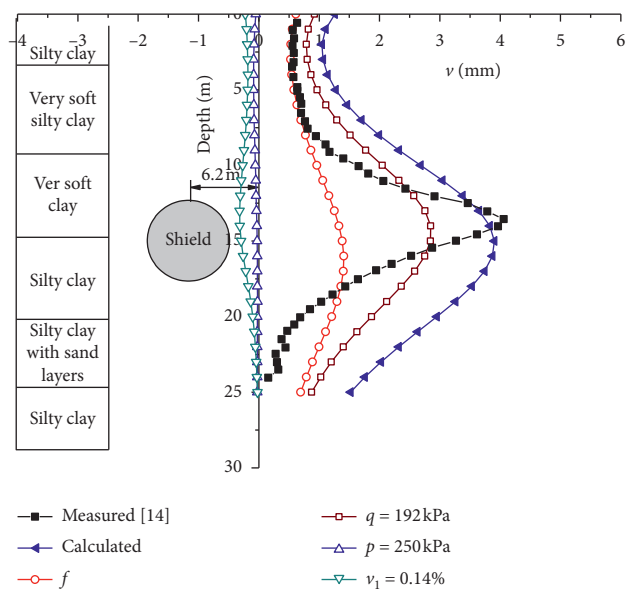
Figure 7: Comparison between the measured and the predicted lateral ground displacements at the transversal direction at the distance of one tunnel diameter ahead of the shield face, Shanghai Metro Line-2 tunnel.

0.35; the coefficient of lateral earth pressure K_0 is 0.57; based on the soil investigation, the equivalent undrained Young's modulus of the ground E_u is 9.3 MPa, so the equivalent soil shear modulus G is 3.5 MPa; the interface internal angel δ and the softening coefficient β is 9° and 0.9, respectively; the short-term soil volume loss ratio v_1 is 0.14%. Based on the related construction experience in Shanghai, the blind bolts of cutter-head k, the open ratio ξ, and the angel speed w are assumed to be 4, 40%, and 0.6 rad/min, respectively.
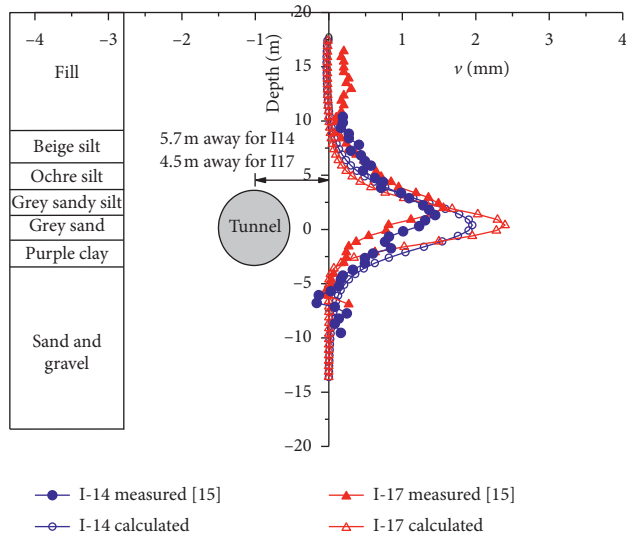
FIGURE 8: Comparison between the measured and predicted lateral ground displacements at the transversal direction at different distance away from the tunnel, France Vaise subway tunnel.

Therefore, the additional pressure of cutter-head q is 192 kPa.

The lateral displacements at transversal direction are presented and compared with predictions from the proposed method, as shown in Figure 7. It is observed that the prominent lateral outward deflections are concentrated at the level of shield centerline. As illustrated in Figure 7, the contribution to the calculated displacements is mainly from the additional pressure of cutter-head q and the frictions around the shield body f. The calculated lateral displacements at transversal direction below the tunnel invert are slightly larger than the observations. The reason may be due to the assumption of homogenous ground of the proposed method, which indicates the ground movement range is slightly greater that the observation. In general, the predicted lateral ground displacements are in good agreement with the measurements.

3.3. Case 3: France Vaise Subway Tunnel. Extension project of Line D subway network in Lyon, France, was constructed by slurry shield boring machine. The extension tunnel was approximately 1000-m long and had an outer diameter of 6.27 m. The tunnel axis is located at 17.4 m blow the ground surface, and the shield was mainly excavated through grey sandy slit, grey sand, and purple clay. Geotechnical investigation revealed that the subsurface stratification was relatively nonuniform, as shown in Figure 8. The lateral displacements were measured by two inclinometers, I14 and I17, located at 5.7 m and 4.5 m away from the tunnel axis. Detailed field measuring of lateral soil displacements and site properties are well described and interpreted by Dias and Kastner [15] and Emeriault et al. [28].

The monitored slurry pressure at the shield face was about 120 kPa. The grouting pressures varied from 200 kPa to 300 kPa. Based on the soil tests results [15], the equivalent

Poisson ratio u, shear modulus G, and the coefficient of lateral earth pressure K_0 are assumed to be 0.4, 2.5 MPa, and 0.57, respectively. The grouting pressure is assumed to be 280 kPa in this analysis. The interface internal angel δ and the softening coefficient β are 9° and 0.9, respectively.

The calculated transversal lateral ground displacements at the inclinometer I14 and I17 are also plotted in Figure 8. The comparison between the measured and predicted results indicates that, although the maximum lateral displacements calculated by proposed method are slightly larger than the observations, the trends of distribution of the calculated results are generally in good agreement with that of the monitored data.

Finally, the feasibility of the proposed analytical method is verified with three case histories. The proposed method takes the additional pressure of cutter head, frictions around the shield body, back-fill grouting pressure, and soil volume loss into account, which will generally reflect the interaction between the shield advancing and ground. The proposed method provides a novel method to predict the lateral ground responses to shield tunnelling.

4. Conclusions

(1) In this paper, a simplified analytical method is proposed to predict lateral ground displacements associated with shield tunnelling advancing. Key operation variants, such as the additional pressure of cutter-head q, frictions around shield body f, the grouting pressure p, and the soil volume loss v_1, are incorporated into the analytical method.

(2) The applicability of the proposed method is verified through with three well-documented case histories involving earth pressure balanced shield and slurry shield. Good agreements have been achieved between the filed measurements and the predictions.

(3) The proposed methods are able to estimate the lateral displacements associated with shield tunnelling.

Data Availability

Some or all data, models, or codes generated or used during the study are available from the corresponding author upon request (list items).

Conflicts of Interest

The authors declare no conflicts of interest.

Acknowledgments

References

[1] R. B. Peck, "Deep excavations and tunnelling in soft ground," in *Proceedings of the 7th International. Conference on Soil Mechanics. and Foundation Engineering (Mexico)*, pp. 225–290, Mexico, MX, USA, August 1969.

[2] P. B. Attewell and J. P. Woodman, "Predicting the dynamics of ground settlement and its derivitives caused by tunnelling in soil," *Ground Engineering*, vol. 15, no. 8, pp. 13–22, 1982.

[3] R. J. Mair, R. N. Taylor, and A. Bracegirdle, "Subsurface settlement profiles above tunnels in clays," *Géotechnique*, vol. 43, no. 2, pp. 315–320, 1993.

[4] Y.-S. Fang, C.-T. Wu, S.-F. Chen, and C. Liu, "An estimation of subsurface settlement due to shield tunneling," *Tunnelling and Underground Space Technology*, vol. 44, pp. 121–129, 2014.

[5] C. Sagaseta, "Analysis of undraind soil deformation due to ground loss," *Géotechnique*, vol. 37, no. 3, pp. 301–320, 1987.

[6] A. Verruijt and J. R. Booker, "Surface settlements due to deformation of a tunnel in an elastic half plane," *Géotechnique*, vol. 46, no. 4, pp. 753–756, 1996.

[7] N. Loganathan and H. G. Poulos, "Analytical prediction for tunneling-induced ground movements in clays," *Journal of Geotechnical and Geoenvironmental Engineering*, vol. 124, no. 9, pp. 846–856, 1998.

[8] A. Bobet, "Analytical solutions for shallow tunnels in saturated ground," *Journal of Engineering Mechanics*, vol. 127, no. 12, pp. 1258–1266, 2001.

[9] A. S. Osman, M. D. Bolton, and R. J. Mair, "Predicting 2D ground movements around tunnels in undrained clay," *Géotechnique*, vol. 56, no. 9, pp. 597–604, 2006.

[10] A. Franza and A. M. Marshall, "Empirical and semi-analytical methods for evaluating tunnelling-induced ground movements in sands," *Tunnelling and Underground Space Technology*, vol. 88, pp. 47–62, 2019.

[11] P. Zhang, Z.-Y. Yin, and R.-P. Chen, "Analytical and semi-analytical solutions for describing tunneling-induced transverse and longitudinal settlement troughs," *International Journal of Geomechanics*, vol. 20, no. 8, Article ID 04020126, 2020.

[12] G. W. Clough, B. P. Sweeney, and R. J. Finno, "Measured soil response to EPB shield tunneling," *Journal of Geotechnical Engineering*, vol. 109, no. 2, pp. 131–149, 1983.

[13] J. R. Standing and D. Selemetas, "Greenfield ground response to EPBM tunnelling in London clay," *Géotechnique*, vol. 63, no. 12, pp. 989–1007, 2013.

[14] K. M. Lee, H. W. Ji, C. K. Shen, J. H. Liu, and T. H. Bai, "Ground response to the construction of Shanghai metro tunnel-line 2," *Soils and Foundations*, vol. 39, no. 3, pp. 113–134, 1999.

[15] D. Dias and R. Kastner, "Movements caused by the excavation of tunnels using face pressurized shields—analysis of monitoring and numerical modeling results," *Engineering Geology*, vol. 152, no. 1, pp. 17–25, 2013.

[16] C. C. Kao, C. H. Chen, and R. N. Hwang, "Mechanism of ground settlements and heaves due to shield tunnelling," *Journal of GeoEngineering*, vol. 4, no. 2, pp. 63–72, 2009.

[17] K. M. Lee and R. K. Rowe, "An analysis of three-dimensional ground movements: the Thunder Bay tunnel," *Canadian Geotechnical Journal*, vol. 28, no. 1, pp. 25–41, 1991.

[18] W. N. Yiu, H. J. Burd, and C. M. Martin, "Finite-element modelling for the assessment of tunnel-induced damage to a masonry building," *Géotechnique*, vol. 67, no. 9, pp. 780–794, 2017.

[19] P. Zhang, R.-P. Chen, H.-N. Wu, and Y. Liu, "Ground settlement induced by tunneling crossing interface of water-bearing mixed ground: a lesson from Changsha, China," *Tunnelling and Underground Space Technology*, vol. 96, Article ID 103224, 2020.

[20] R. D. Mindlin, "Force at a point in the interior of a semi-infinite solid," *Physics*, vol. 7, no. 5, pp. 195–202, 1936.

[21] F. Pinto and A. J. Whittle, "Ground movements due to shallow tunnels in soft ground. I: analytical solutions," *Journal of Geotechnical and Geoenvironmental Engineering*, vol. 140, no. 4, Article ID 04013040, 2014.

[22] J. R. Standing, D. Selemetas, and J. N. Shirlaw, "Greenfield ground response to EPBM tunnelling in London clay," *Géotechnique*, vol. 64, no. 7, pp. 581–583, 2014.

[23] H. Wang, "Effect of cutterhead compressing the front soil and influence of head aperture ratio on contact pressure of EPB shield to the front soil," *China Civil Engineering Journal*, vol. 42, no. 7, pp. 113–118, 2009.

[24] T. Hashimoto, J. Nagaya, and T. Konda, "Prediction of ground deformation due to shield excavation in clayey soils," *Soils and Foundations*, vol. 39, no. 3, pp. 53–61, 1999.

[25] Q. Zhang, S. Li, and L. Li, "Simplified method for settlement prediction of pile groups considering skin friction softening and end resistance hardening," *Chinese Journal of Rock Mechanics and Engineering*, vol. 32, no. 3, pp. 615–624, 2013.

[26] E. E. Alonso, A. Josa, and A. Ledesma, "Negative skin friction on piles: a simplified analysis and prediction procedure," *Géotechnique*, vol. 34, no. 3, pp. 341–357, 1984.

[27] R. J. Finno and G. W. Clough, "Evaluation of soil response to EPB shield tunneling," *Journal of Geotechnical Engineering*, vol. 111, no. 2, pp. 155–173, 1985.

[28] F. Emeriault, D. Breysse, R. Kastner, and A. Denis, "Geotechnical survey and mechanical parameters in urban soils: modelling soil variability and inferring representative values using the extension of Lyon subway line D as a case study," *Canadian Geotechnical Journal*, vol. 41, no. 5, pp. 773–786, 2004.

Research Article

Analysis of the Three-Dimensional Dynamic Problems by Using a New Numerical Method

Yao Rong ⬤,[1] **Yang Sun,**[1] **LiQing Zhu,**[1] **and Xiao Xiao** ⬤[2]

[1]*Jiangxi Transportation Research Institute, Nanchang 330200, China*
[2]*Jiangxi Provincial Engineering Research Center of the Special Reinforcement and Safety Monitoring*
 Technology in Hydraulic & Civil Engineering, Nanchang 330099, China

Correspondence should be addressed to Xiao Xiao; xiaoxiao8808@163.com

The problems of the consolidation of saturated soil under dynamic loading are very complex. At present, numerical methods are widely used in the research. However, some traditional methods, such as the finite element method, involve more degrees of freedom, resulting in low computational efficiency. In this paper, the scaled boundary element method (SBFEM) is used to analyze the displacement and pore pressure response of saturated soil due to consolidation under dynamic load. The partial differential equations of linear problems are transformed into ordinary differential equations and solved along the radial direction. The coefficients in the equations are determined by approximate finite elements on the circumference. As a semianalytical method, the application of scaled boundary element method in soil-structure interaction is extended. Dealing with complex structures and structural nonlinearity, it can simulate two-phase saturated soil-structure dynamic interaction in infinite and finite domain, which has an important engineering practical value. Through the research, some conclusions are obtained. The dimension of the analytical problem can be reduced by one dimension if only the boundary surface is discretized. The SBFEM can automatically satisfy the radiation conditions at infinite distances. The 3D scaled boundary finite element equation for dynamic consolidation of saturated soils is not only accurate in finite element sense but also convenient in mathematical processing.

1. Introduction

Dynamic consolidation analysis of foundation is one of the most concerned problems, such as seismic design of large underground caverns, high arch dams, super high-rise buildings, and other large-scale industrial and their response characteristics under mechanical vibration (Chen and He [1], Lu et al. [2], and Jiang and Liang [3]). The free field formed by dynamic loads not only affects the dynamic response of long-span structures but also has feedback effect on the propagation of vibration waves by different components. Therefore, it is not reasonable to study the structure-constrained system as an isolator. It is necessary to consider the dynamic interaction between structure and foundation soil. For foundation soils in semi-infinite space, many literatures regard foundation soils as single-phase materials. When the foundation soil with high water content

is liquefied by earthquake load, the pore pressure will increase with time, which will have a greater impact on the safety of the structure (Du and Wang [4] and Xia et al. [5]). Therefore, considering that the foundation soil is saturated soil with two-phase coupling of water and soil, the analysis of dynamic consolidation can better reflect the engineering practice.

For infinite and semi-infinite foundation soils, the main numerical analysis methods are finite element method (FEM), boundary element method, and finite element-boundary element coupling method. The simulation of semi-infinite foundation soil is much more complicated compared to the finite element method mainly because of the large discrete range of foundation soil. In order to obtain enough calculation accuracy, the free degrees of the system increased inevitably. Although the computing power has been greatly improved, the computational units needed for some special

cases, such as the accurate analysis of 3D stress wave propagation in anisotropic soils, are still difficult to achieve. Generally, the finite element discrete analysis is used to study foundations around the structure. Free or fixed boundary conditions are used to simulate infinite foundation soil. At the same time, in order to eliminate false reflection on artificial boundary, a transmission boundary model is established, for example, viscous and viscoelastic boundary (Zhang [6]), superposition boundary (Smith [7]), paraxial boundary (Engquist and Majda [8]), transient transmission boundary (Liao et al. [9] and Liao et al. [10]), and multi-directional and bi-asymptotic multidirectional transmission boundary (Keys [11] and Wolf and Song [12]). The main problems of finite element method based on the infinite boundary model, when it is used to analyze the dynamic consolidation of infinite foundation soil, are the inadequate accuracy of low-order boundary and the poor stability of high-order boundary. It does not have the accuracy in the sense of finite element. In other words, the numerical solution can converge to the solution when the discrete mesh is infinitely small.

The wave attenuation factor is introduced into the shape function to describe the propagation of vibration waves along infinite distances for the infinite element method (Zhao and Valliappan [13] and Khaliliet al [14]), which is also a numerical method for infinite domain problems. However, the accuracy depends largely on the selection of radial shape function. When the order of the radial shape function is low, the infinite element must be placed far away for higher accuracy, which will lead to the expansion of the solution scale of the system. The higher order radial shape functions usually leads to ill-conditioned equations. In addition, similar to the local transmission boundary, the infinite element method is not accurate enough in the finite element sense. In dealing with these problems of infinite and semi-infinite domains, the boundary element method could satisfy the radiation conditions very well at infinity, and there is no reflection problem of artificial boundary (Bonnet [15] and Xu et al. [16]). However, the basic solutions needed to form the integral equation of boundary element method are generally complex, especially for anisotropic materials, and there is not even a basic analytical solution. On the contrary, the treatment of singular integral or even hyper-singular integral of boundary integral equation is very difficult, which limits the further application of boundary element method. The FEM-BEM coupling method has been widely used in the analysis of structure-foundation interaction (Yazdchiet al. [17] and Du [18]). However, it is difficult to coordinate the coupled deformation between FEM and BEM for the interface between structure and foundation.

Scaled boundary finite element method (SBFEM) is a boundary element method based on finite element method. Compared with the boundary element method, it does not need to solve the fundamental solution, so it can effectively deal with the problem of anisotropic media which is particularly complex and satisfies certain conditions. The scaled boundary finite element method (SBFEM) successfully satisfies Sommer field radiation condition by choosing

appropriate similar centers. Therefore, the waves emitted by the source can only dissipate to infinity in the form of de-wave, but not return from infinity in the infinite domain. At present, SBFEM has been applied to the analysis of wave problems in time domain and frequency domain and to the solution of boundary dynamic stiffness matrix of infinite foundation (Wolf and Song [19, 20]). Previous results show that the SBFEM is very accurate and effective in dealing with most problems of infinite medium, anisotropic medium, and inhomogeneous change of materials. Considering that the foundation soil is a saturated soil with two-phase coupling of water and soil, the dynamic consolidation of 3D infinite saturated soil is analyzed by the SBFEM, which has not been reported in previous literatures.

2. Governing Equation

Taking 3D saturated soil area V as the research object in Cartesian rectangular coordinates, the cross section is shown in Figure 1. If the field V is a finite field, the scale curvilinear coordinate system shown in Figure 2 is established for a unit V^e in the field, whose bottom surface is S^e and the cone surface is A^e. For convenient of expression, the scaled center point C coincides with the origin point O of the Cartesian coordinate system. When the SBFEM is used, elements similar to the FEM are discretized on the S^e boundary, which is on the bottom of the domain. η and ζ are the toroidal local coordinates of the elements on the S^e boundary in the surface coordinate system, and ξ is the radial coordinates perpendicular to the boundary. $\eta, \zeta = \pm 1$ represents the edge of bottom S^e. Radial coordinate $0 \leq \xi \leq 1$. When $\xi = 0$ or 1, it represents the scale center point and the bottom of the finite field, respectively. The bottom s of scaled center point and finite field V are represented, respectively. When the position of the scaled center is determined, a one-to-one conversion relationship is formed between the Cartesian rectangular coordinate system and the local scaled boundary coordinate system, which is called the scaled boundary transformation.

For the 3D infinite saturated soil shown in Figure 1(b), the scaled center point is selected outside the infinite domain. Similar to the finite field, the vertex of the element cone is the scaled center point C, and the bottom represents the interface (as shown in Figure 2). Then, the radial coordinates $\xi \geq 1$ and $\xi = 1$ correspond to the bottom of the infinite field. The whole infinite field is formed by assembling all the cones.

In the local coordinate system of the scaled boundary, any point on the bottom S^e of $\xi = 1$ can be expressed by n node coordinates of the discrete element on the bottom as follows:

$$
\begin{aligned}
x(\eta, \zeta) &= [N(\eta, \zeta)]\{x\} = [N]\{x\}, \\
y(\eta, \zeta) &= [N(\eta, \zeta)]\{y\} = [N]\{y\}, \\
z(\eta, \zeta) &= [N(\eta, \zeta)]\{z\} = [N]\{z\},
\end{aligned}
\tag{1}
$$

where the shape function is defined as $[N(\eta, \zeta)] = [N_1(\eta, \zeta) \ N_2(\eta, \zeta) \ N_3(\eta, \zeta) \ ,\dots]$.

(a)   (b)
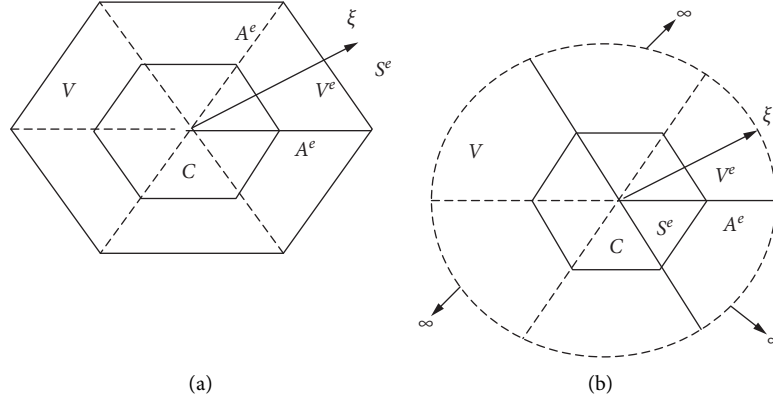
FIGURE 1: Cutaway view of three-dimensional saturated soil: (a) finite region and (b) unbounded media.
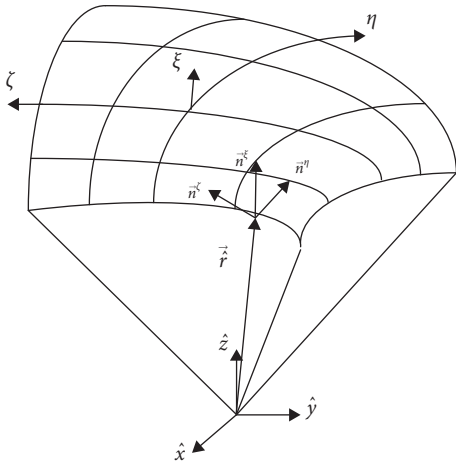
FIGURE 2: Transformation of global Cartesian coordinates to scaled boundary coordinates.

In the scaled coordinates, the relationship between point $\hat{r} = \hat{x}i + \hat{y}j + \hat{z}k$ in the computational element domain V^e and bottom S^e boundary point $r = xi + yj + zk$ can be expressed as follows:

$$\hat{x}(\xi, \eta, \zeta) = \xi x(\eta, \zeta),$$
$$\hat{y}(\xi, \eta, \zeta) = \xi y(\eta, \zeta),$$
$$\hat{z}(\xi, \eta, \zeta) = \xi z(\eta, \zeta). \tag{2}$$

Then,

$$\begin{Bmatrix} \dfrac{\partial}{\partial \hat{x}} \\[2ex] \dfrac{\partial}{\partial \hat{y}} \\[2ex] \dfrac{\partial}{\partial \hat{z}} \end{Bmatrix} = [\hat{J}]^{-1} \begin{Bmatrix} \dfrac{\partial}{\partial \xi} \\[2ex] \dfrac{\partial}{\partial \eta} \\[2ex] \dfrac{\partial}{\partial \zeta} \end{Bmatrix}, \tag{3}$$

where Jacobian matrix $[\hat{J}(\eta, \zeta)] = \begin{bmatrix} \hat{x}_\xi, \hat{y}_\xi, \hat{z}_\xi, \\ \hat{x}_\eta, \hat{y}_\eta, \hat{z}_\eta, \\ \hat{x}_\zeta, \hat{y}_\zeta, \hat{z}_\zeta, \end{bmatrix}$.

According to Biot's theory, the governing equations of consolidation of saturated soils include the dynamic equilibrium equation of soil skeleton and the continuous equation of fluid. In the Cartesian coordinate system $(\hat{x}, \hat{y}, \hat{z})$, the dynamic equilibrium equation expressed by the displacement ($\{u\} = \{u(\hat{x}, \hat{y}, \hat{z})\} = \{u_x\, u_y\, u_z\}^T$) of soil skeleton in frequency domain is as follows:

$$[L]^T\left(\{\sigma'\} + \{m\}p_f\right) + \rho\omega^2\{u\} + \rho\{b\} = 0, \tag{4}$$

where p_f is pore water pressure, ω is frequency, and $\rho = \rho_s + (1 - \phi)\rho_f$. ρ_s and ρ_f are soil skeleton and fluid density, ϕ is porosity, $\{b\} = \{b_x\, b_y\, b_z\}^T$, $\{\sigma'\} = \{\sigma'_x\, \sigma'_y\, \sigma'_z\, \tau_{yz}\, \tau_{xz}\, \tau_{xy}\}^T$ and $\{\sigma\} = \{\sigma'\} + \{m\}p_f$ are unit volume force, effective stress, and total stress, respectively. $\{m\} = \begin{bmatrix} 1 & 1 & 1 & 0 & 0 & 0 \end{bmatrix}^T$. Differential operator $[L]$ is defined as

$$[L] = \begin{bmatrix} \dfrac{\partial}{\partial \hat{x}} & 0 & 0 & 0 & \dfrac{\partial}{\partial \hat{z}} & \dfrac{\partial}{\partial \hat{y}} \\[2ex] 0 & \dfrac{\partial}{\partial \hat{y}} & 0 & \dfrac{\partial}{\partial \hat{z}} & 0 & \dfrac{\partial}{\partial \hat{x}} \\[2ex] 0 & 0 & \dfrac{\partial}{\partial \hat{y}} & \dfrac{\partial}{\partial \hat{y}} & \dfrac{\partial}{\partial \hat{x}} & 0 \end{bmatrix}^T. \tag{5}$$

The continuity equation of fluid motion in saturated soils in frequency domain is as follows:

$$-kp_{f,ii} + \omega^2 k\rho_f u_{i,j} + k\rho_f b_{i,j} + i\omega u_{i,j} + \dfrac{i\omega\phi p_f}{K_f} = 0, \tag{6}$$

where k and K_f are the permeability coefficient of soil and the bulk modulus of fluid, respectively.

For isotropic saturated soils, effective stress, strain, and displacement vector satisfy Hooke's law:

$$\{\sigma'\} = [D]\{\varepsilon\} = [D][L]\{u\}, \tag{7}$$

where $[D]$ is the elastic matrix of saturated soil material.

According to equation (3), in the scaled curvilinear coordinate system (ξ, η, ζ) shown in Figure 2, the differential operator $[L]$ is expressed as

$$[L] = [b^1]\frac{\partial}{\partial \xi} + \frac{1}{\xi}\left([b^2]\frac{\partial}{\partial \eta} + [b^3]\frac{\partial}{\partial \zeta}\right),$$

$$[b^1] = \frac{g^\xi}{|J|}\begin{bmatrix} n_x^\xi & 0 & 0 & 0 & n_z^\xi & n_y^\xi \\ 0 & n_y^\xi & 0 & n_z^\xi & 0 & n_x^\xi \\ 0 & 0 & n_z^\xi & n_y^\xi & n_x^\xi & 0 \end{bmatrix}^T,$$

$$[b^2] = \frac{g^\eta}{|J|}\begin{bmatrix} n_x^\eta & 0 & 0 & 0 & n_z^\eta & n_y^\eta \\ 0 & n_y^\eta & 0 & n_z^\eta & 0 & n_x^\eta \\ 0 & 0 & n_z^\eta & n_y^\eta & n_x^\eta & 0 \end{bmatrix}^T, \tag{8}$$

$$[b^3] = \frac{g^\zeta}{|J|}\begin{bmatrix} n_x^\zeta & 0 & 0 & 0 & n_z^\zeta & n_y^\zeta \\ 0 & n_y^\zeta & 0 & n_z^\zeta & 0 & n_x^\zeta \\ 0 & 0 & n_z^\zeta & n_y^\zeta & n_x^\zeta & 0 \end{bmatrix}^T,$$

where $n_x^\xi, n_y^\xi, n_z^\xi, n_x^\eta, n_y^\eta, n_z^\eta, n_x^\zeta, n_y^\zeta,$ and n_z^ζ are the components of the outer surface unit normal ($\mathbf{n}^\xi$, $\mathbf{n}^\eta$ and $\mathbf{n}^\zeta$) of the bottom S^e shown in Figure 2, respectively.

Equation (8) shows that $[b^1]$, $[b^2]$, and $[b^3]$ are independent of the radial coordinates ξ and satisfy the following formula:

$$\left(|J|[b^2]\right)_\eta + \left(|J|[b^3]\right)_\zeta = -2|J|[b^1]. \tag{9}$$

In the Cartesian coordinates $(\hat{x}, \hat{y}, \hat{z})$, the tangential force of a surface with a normal direction of $\mathbf{n} = \mathbf{n}_x i + \mathbf{n}_y j + \mathbf{n}_z k$ is

$$\{\tau\} = \begin{Bmatrix} \tau_x \\ \tau_y \\ \tau_z \end{Bmatrix} = \begin{bmatrix} n_x & 0 & 0 & 0 & n_z & n_y \\ 0 & n_y & 0 & n_z & 0 & n_x \\ 0 & 0 & n_z & n_y & n_x & 0 \end{bmatrix}\{\sigma\}. \tag{10}$$

From equations (3), (8), and (10), it can be seen that the tangential force on the surface (η, ζ), (ζ, ξ), and (ξ, η) of any given value ξ, η, and ζ is as follows:

$$\{t^\xi\} = \frac{|J|}{g^\xi}[b^1]^T\{\sigma\},$$

$$\{t^\eta\} = \frac{|J|}{g^\eta}[b^2]^T\{\sigma\}, \tag{11}$$

$$\{t^\zeta\} = \frac{|J|}{g^\zeta}[b^3]^T\{\sigma\}.$$

For the computational element domain V^e shown in Figure 2, the displacement and pore pressure of discrete nodes are expressed by a shape function similar to the coordinates of nodes on the bottom boundary S^e of $\xi = 1$. Then, on a surface S^ξ with any radial coordinate ξ, displacement and pore pressure can be expressed as

$$\{u\} = \{u(\xi, \eta, \zeta)\} = [N^u(\eta, \zeta)]\{u(\xi)\},$$
$$\{p_f\} = \{p_f(\xi, \eta, \zeta)\} = [N^p(\eta, \zeta)]\{p_f(\xi)\}. \tag{12}$$

From equations (7), (8), and (12), it can be seen that the effective stress in the scaled curvilinear coordinates is as follows:

$$\{\sigma'\} = [D]\left([b^1]^T\{u_\xi\} + \frac{1}{\xi}\left([b^2]^T\{u_\eta\} + [b^3]^T\{u_\zeta\}\right)\right)$$

$$= [D]\left([B_u^1]\{u(\xi)\}_\xi + \frac{1}{\xi}[B_u^2]\{u(\xi)\}\right), \tag{13}$$

$$\{\sigma'_\xi\} = [D]\left([B_u^1]\{u(\xi)\}_{\xi\xi} + \frac{1}{\xi}[B_u^2]\{u(\xi)\}_\xi - \frac{1}{\xi^2}[B_u^2]\{u(\xi)\}\right), \tag{14}$$

where $[B_u^1]^T = [b^1][N^u]$ and $[B_u^2] = [b^2][N^u]_{,\eta} + [b^3][N^u]_{,\zeta}$. Therefore, it can be concluded that $[B_u^1]$ and $[B_u^2]$ are only functions of circumferential coordinates, independent of radial coordinates η, ζ.

By using equations (3), (8), and (12), the differential equations (4) and (6) of saturated soil consolidation in Cartesian coordinate system $(\hat{x}, \hat{y}, \hat{z})$ can be transformed into the scaled curvilinear coordinates, and it can be expressed as follows:

$$[b^1]^T\left(\{\sigma'_\xi\} + \{m\}p_{f,\xi}\right) + \frac{1}{\xi}\left([b^2]^T\left(\{\sigma'_\eta\} + \{m\}p_{f,\eta}\right) + [b^3]^T\left(\{\sigma'_\zeta\} + \{m\}p_{f,\zeta}\right)\right) + \rho\omega^2\{u\} + \rho\{b\} = 0, \tag{15}$$

$$-k\{m\}^T\left([b^1]\dfrac{\partial}{\partial\xi}\left([b^1]^T\dfrac{\partial}{\partial\xi}+\dfrac{1}{\xi}\left([b^2]^T\dfrac{\partial}{\partial\eta}+[b^3]^T\dfrac{\partial}{\partial\zeta}\right)\right)+\dfrac{1}{\xi}[b^2]^T\dfrac{\partial}{\partial\eta}\left([b^1]^T\dfrac{\partial}{\partial\xi}+\dfrac{1}{\xi}\left([b^2]^T\dfrac{\partial}{\partial\eta}+[b^3]^T\dfrac{\partial}{\partial\zeta}\right)\right)\right.$$

$$+[b^3]^T\dfrac{\partial}{\partial\zeta}\left([b^1]^T\dfrac{\partial}{\partial\xi}+\dfrac{1}{\xi}\left([b^2]^T\dfrac{\partial}{\partial\eta}+[b^3]^T\dfrac{\partial}{\partial\zeta}\right)\right)\Big)\{m\}p_f+\omega^2k\rho_f\{m\}^T\left([b^1]^T\{u_\xi\}+\dfrac{1}{\xi}\left([b^2]^T\{u_\eta\}+[b^3]^T\{u_\zeta\}\right)\right)$$

$$+k\rho_f\{m\}^T[b^1]^T\{b_\xi\}\right)+\dfrac{1}{\xi}\left([b^2]^T\{b_\eta\}+[b^3]^T\{b_\zeta\}\right)\Big)+i\omega\{m\}^T\left([b^1]^T\{u_\xi\}+\dfrac{1}{\xi}\left([b^2]^T\{u_\eta\}+[b^3]^T\{u_\zeta\}\right)\right)+\dfrac{i\omega\phi p_f}{K_f}=0.$$

$$(16)$$

3. Application of Weighted Residual Method

Galerkin weighted residual method is adopted in computing unit domain V^e. For convenience of expression, the superscript e of the presentation unit is omitted. Interpolated shape functions of the same form as the displacement of discrete nodes are chosen for the weight function, such as $\{w^u\}=\{w^u(\xi,\eta,\zeta)\}=[N^u(\eta,\zeta)]\{w^u(\xi)\}$. For the dynamic equilibrium equation (12) of saturated consolidation soil, it can be obtained by the Galerkin method in the computational domain:

$$\int_V\left(\{w\}^T[b^1]^T\left(\{\sigma'_\xi\}+\{m\}p_{f,\xi}\right)\mathrm{d}V+\int_V\dfrac{1}{\xi}\{w\}^T\left([b^2]^T\left(\{\sigma'_\eta\}+\{m\}p_{f,\eta}\right)+[b^3]^T\left(\{\sigma'_\zeta\}+\{m\}p_{f,\zeta}\right)\right)\mathrm{d}V\right.$$

$$+\rho\omega^2\int_V\{w\}^T\{u\}\mathrm{d}V+\rho\int_V\{w\}^T\{b\}\Big)\mathrm{d}V=0.$$

$$(17)$$

For the second item in the above equation, by using the partial integral and substituting equations (9) and (11), we can obtain

$$I=\int_0^1\xi\left(\int_{\Gamma^\xi}\{w\}^T\left(\{t^\zeta\}g^\zeta\mathrm{d}\eta+\{t^\eta\}g^\eta\mathrm{d}\zeta\right)-\int_{S^\xi}-2\{w\}^T[b^1]^T+\{w_\eta\}^T[b^2]^T+\{w_\zeta\}^T[b^3]^T\right)\left(\{\sigma'\}+\{m\}p_f\right)|J|\mathrm{d}\eta\mathrm{d}\zeta\mathrm{d}\xi. \qquad (18)$$

By substituting equation (18) into equation (17), the following equation can be obtained:

$$\int_0^1\left(\xi^2\int_{S^\xi}\{w\}^T[b^1]^T\left(\{\sigma'_\xi\}+\{m\}p_{f,\xi}\right)|J|\mathrm{d}\eta\mathrm{d}\zeta+\xi\int_{\Gamma^\xi}\{w\}^T\left(\{t^\zeta\}g^\zeta d\eta+\{t^\eta\}g^\eta\mathrm{d}\zeta\right)\right.$$

$$-\xi\int_{S^\xi}\left(\left(-2\{w\}^T[b^1]^T+\{w_\eta\}^T[b^2]^T+\{w_\zeta\}^T[b^3]^T\right)\{\sigma'\}+\{m\}p_f\right)|J|\mathrm{d}\eta\mathrm{d}\zeta$$

$$+\rho\omega^2\xi^2\int_{S^\xi}\{w\}^T\{u\}|J|d\eta\ d\zeta+\rho\xi^2\int_{S^\xi}\{w\}^T\{b\}|J|\mathrm{d}\eta\mathrm{d}\zeta\mathrm{d}\xi=0.$$

$$(19)$$

Then, we substituted $\{w\}^T=\{w(\xi)\}^T[N^u]^T$ into the upper equation, and if equality is established for the upper equation in the whole integral domain, then

$$\{w\}^T \xi^2 \int_{S^\xi} [N^u]^T [b^1]^T \{\sigma'_\xi\} |J| d\eta d\zeta + \{w\}^T \xi^2 \int_{S^\xi} [N^u]^T [b^1]^T \{m\} [N^p] \{p_f(\xi)\}_\xi |J| d\eta d\zeta$$

$$+ \{w\}^T \xi \int_{S^\xi} \left(2[N^u]^T [b^1]^T - [N^u]_\eta^T [b^2]^T - [N^u]_\zeta^T [b^3]^T\right) \{\sigma'\} |J| d\eta d\zeta$$

$$+ \{w\}^T \xi \int_{S^\xi} \left(2[N^u]^T [b^1]^T - [N^u]_\eta^T [b^2]^T - [N^u]_\zeta^T [b^3]^T\right) \{m\} [N^p] \{p_f(\xi)\} |J| d\eta d\zeta \tag{20}$$

$$+ \{w\}^T \xi \int_{\Gamma^\xi} [N^u]^T \left(\{t^\zeta\} g^\zeta d\eta + \{t^\eta\} g^\eta d\zeta\right) + \{w\}^T \omega^2 \xi^2 \int_{S^\xi} [N^u]^T \rho [N^u] \{u(\xi)\} |J| d\eta d\zeta$$

$$+ \{w\}^T \rho \xi^2 \int_{S^\xi} [N^u]^T \{b\} |J| d\eta d\zeta = 0.$$

After multiplying $[\{w\}^T]^{-1}$ at both sides of the upper equation and substituting $[B_u^1]$ and $[B_u^2]$, we can obtain

$$\xi^2 \int_{S^\xi} [B_u^1]^T \{\sigma'_\xi\} |J| d\eta d\zeta + \xi^2 \int_{S^\xi} [B_u^1]^T \{m\} [N^p] \{p_f(\xi)\}_\xi |J| d\eta d\zeta$$

$$+ \xi \int_{S^\xi} \left(2[B_u^1]^T - [B_u^2]^T\right) \{\sigma'\} |J| d\eta d\zeta + \xi \int_{S^\xi} \left(2[B_u^1]^T - [B_u^2]^T\right) \{m\} [N^p] \{p_f(\xi)\} |J| d\eta d\zeta \tag{21}$$

$$+ \omega^2 \xi^2 \int_{S^\xi} [N^u]^T \rho [N^u] \{u(\xi)\} |J| d\eta d\zeta + \xi \{F^t(\xi)\} + \xi^2 \{F^b(\xi)\} = 0,$$

where $\{F^t(\xi)\} = \int_{\Gamma^\xi} [N^u(\eta,\zeta)]^T \left(\{t^\zeta\} g^\zeta d\eta + \{t^\eta\} g^\eta d\zeta\right)$ and $\{F^b(\xi)\} = \rho \int_{S^\xi} [N^u(\eta,\zeta)]^T \{b\} |J| d\eta d\zeta \circ.$

By using equations (13), (14), and (21), the following results can be obtained:

$$\xi^2 \int_{S^\xi} [B_u^1]^T [D] [B_u^1] |J| d\eta d\zeta \{u(\xi)\}_{\xi\xi} + \xi^2 \int_{S^\xi} [B_u^1]^T \{m\} [N^p] |J| d\eta d\zeta \{p_f(\xi)\}_\xi$$

$$+ \xi \int_{S^\xi} [B_u^1]^T [D] [B_u^2] |J| d\eta d\zeta \{u(\xi)\}_\xi + \xi \int_{S^\xi} \left(2[B_u^1]^T - [B_u^2]^T\right) [D] [B_u^1] |J| d\eta d\zeta \{u(\xi)\}_\xi$$

$$- \int_{S^\xi} [B_u^2]^T [D] [B_u^2] |J| d\eta d\zeta \{u(\xi)\} + \omega^2 \xi^2 \int_{S^\xi} [N^u]^T \rho [N^u] |J| d\eta d\zeta \{u(\xi)\} \tag{22}$$

$$+ \xi \int_{S^\xi} \left(2[B_u^1]^T - [B_u^2]^T\right) \{m\} [N^p] |J| d\eta d\zeta \{p_f(\xi)\} + \xi \{F^t(\xi)\} + \xi^2 \{F^b(\xi)\} = 0.$$

For the continuity equation of fluid in the consolidation equation of saturated soil, the weight function is expressed by the interpolation function which is the same as the pore pressure. Galerkin's method is used in the calculation domain. Similar to the above deduction, the following can be obtained from equation (16):

$$\int_V -k\{w\}^T \{m\}^T [b^1] [b^1]^T \{m\} p_{f,\xi\xi} + \frac{1}{\xi} \left([b^1] [b^2]^T \{m\} p_{f,\xi\eta} + [b^1] [b^3]^T \{m\} p_{f,\xi\zeta}\right)$$

$$- \frac{1}{\xi^2} \left([b^1] [b^2]^T \{m\} p_{f,\eta} + [b^1] [b^3]^T \{m\} p_{f,\zeta}\right) + \frac{1}{\xi} [b^2] \left([b^1]_\eta^T \{m\} p_{f,\xi} + [b^1]^T \{m\} p_{f,\xi\eta}\right)$$

$$+ \frac{1}{\xi} [b^3] \left([b^1]_\zeta^T \{m\} p_{f,\xi} + [b^1]^T \{m\} p_{f,\xi\zeta}\right) + \frac{1}{\xi^2} [b^2] \left([b^2]_\eta^T \{m\} p_{f,\eta} + [b^2]^T \{m\} p_{f,\eta\eta}\right)$$

$$
+ \frac{1}{\xi^2} [b^2] \left([b^3]_\eta^T \{m\} p_{f,\zeta} + [b^3]^T \{m\} p_{f,\eta\zeta} \right) + \frac{1}{\xi^2} [b^3] \left([b^2]_\zeta^T \{m\} p_{f,\eta} + [b^2]^T \{m\} p_{f,\eta\zeta} \right)
$$

$$
+ \frac{1}{\xi^2} [b^3] \left([b^3]_\zeta^T \{m\} p_{f,\zeta} + [b^3]^T \{m\} p_{f,\zeta\zeta} \right) + (i\omega + \omega^2 k \rho_f) \{w\}^T \{m\}^T [b^1]^T \{u_{,\xi}\}
$$

$$
+ \frac{1}{\xi} \left([b^2]^T \{u_\eta\} + [b^3]^T \{u_\zeta\} \right) + k \rho_f \{w\}^T \{m\}^T [b^1]^T \{b_\xi\}
$$

$$
+ \frac{1}{\xi} \left([b^2]^T \{b_\eta\} + [b^3]^T \{b_\zeta\} \right) + \frac{i\omega\phi \{w\}^T p_f}{K_f} dV = 0.
\tag{23}
$$

By using the partial integral and substituting $\{w^p\}^T = \{w^p(\xi)\}^T [N^p]^T$ into the upper equation, the following results can be obtained:

$$
- \xi^2 \{w\}^T \int_{S^\xi} [B_p^1]^T k [B_p^1] |J| d\eta d\zeta \{p_f(\xi)\}_{\xi\xi} + \xi \{w\}^T \int_{S^\xi} [B_p^1]^T k [B_p^2] |J| d\eta d\zeta \{p_f(\xi)\}_\xi
$$

$$
+ \xi \{w\}^T \left(\int_{\Gamma^\xi} [B_p^{2A}]^T k [B_p^1] |J| d\zeta + \int_{\Gamma^\xi} [B_p^{2B}]^T k [B_p^1] |J| d\eta \right) \{p_f(\xi)\}_\xi
$$

$$
+ 2\xi \{w\}^T \int_{S^\xi} [B_p^1]^T k [B_p^1] |J| d\eta d\zeta \{p_f(\xi)\}_\xi - \xi \{w\}^T \int_{S^\xi} [B_p^2]^T k [B_p^1] |J| d\eta d\zeta \{p_f(\xi)\}_\xi
$$

$$
+ \{w\}^T \left(\int_{\Gamma^\xi} [B_p^{2A}]^T k [B_p^2] |J| d\zeta + \int_{\Gamma^\xi} [B_p^{2B}]^T k [B_p^2] |J| d\eta \right) \{p_f(\xi)\}
$$

$$
- \{w\}^T \int_{S^\xi} [B_p^2]^T k [B_p^2] |J| d\eta d\zeta \{p_f(\xi)\} + \xi^2 (i\omega + \omega^2 k \rho_f) \int_{S^\xi} [N^p]^T \{m\}^T [B_u^1] |J| d\eta \, d\zeta \{u(\xi)\}_\xi
$$

$$
+ \xi (i\omega + \omega^2 k \rho_f) \left(\int_{\Gamma^\xi} [B_p^{2A}]^T [N^u] |J| d\zeta + [B_p^{2B}]^T [N^u] |J| d\eta \right) \{u(\xi)\} - \xi (i\omega + \omega^2 k \rho_f) \int_{S^\xi} [B_p^2]^T [N^u] |J| d\eta d\zeta \{u(\xi)\}
$$

$$
+ 2\xi (i\omega + \omega^2 k \rho_f) \int_{S^\xi} [N^p]^T \{m\}^T [B_u^1] |J| d\eta d\zeta \{u(\xi)\} + \xi^2 k \rho_f \int_{S^\xi} [B_p^1]^T \{b_\xi\} |J| d\eta d\zeta
$$

$$
+ 2\xi k \rho_f \int_{S^\xi} [B_p^1]^T \{b\} |J| d\eta d\zeta + \xi^2 i\omega \int_{S^\xi} \frac{\{w\}^T \phi}{K_f} [N^p] |J| d\eta d\zeta \{p_f(\xi)\} = 0,
\tag{24}
$$

where $[B_p^1] = [b^1]^T \{m\} [N^p]$, $[B_p^{2A}]^T = [N^p]^T \{m\}^T [b^2]$, $[B_p^2] = [b^2]^T \{m\} [N^p]_\eta + [b^3]^T \{m\} [N^p]_\zeta$, and $[B_p^{2B}]^T = [N^p]^T \{m\}^T [b^3]$.

The dynamic consolidation equation of saturated soil considering pore water pressure can be obtained by equations (22) and (24). The scaled boundary finite element equation expressed by pore water pressure and displacement is as follows:

$$
[E_0] \xi^2 \{u(\xi)\}_{\xi\xi} + [E_3] \xi^2 \{p_f(\xi)\}_\xi + (2[E_3] - [E_4]) \xi \{p_f(\xi)\} + (2[E_0] - [E_1] + [E_1]^T) \xi \{u(\xi)\}_\xi
$$

$$
- [E_2] \{u(\xi)\} + \omega^2 [M_0] \xi^2 \{u(\xi)\} + \xi^2 \{F^b(\xi)\} + \xi \{F^t(\xi)\} = 0,
\tag{25}
$$

$$
\begin{aligned}
&[E_5]\xi^2\{p_f(\xi)\}_{\xi\xi} + \left(2[E_5] - [E_6] + [E_6]^T + \{F^{t1}\}\right)\xi\{p_f(\xi)\}_\xi + \left(-[E_7] + \{F^{t2}\}\right)\{p_f(\xi)\} - i\omega[M_1]\xi^2\{p_f(\xi)\} \\
&\quad + \{F^{t1}\}\xi\{p_f(\xi)\}_\xi + \left(-[E_7] + \{F^{t2}\}\right)\times\{p_f(\xi)\} - i\omega[M_1]\xi^2\{p_f(\xi)\} - \left(i\omega + \omega^2 k\rho_f\right)[E_3]^T\xi^2\{u(\xi)\}_\xi \\
&\quad - \left(i\omega + \omega^2 k\rho_f\right)\left(2[E_3]^T - [E_8] + \{F^{t3}\}\right)\xi\{u(\xi)\} - k\rho_f\xi^2\{F^{b1}(\xi)\} + 2\xi\{F^{b2}(\xi)\} \\
&\quad - \xi\{F^{b3}(\xi)\} + \xi\{F^{b4}(\xi)\} = 0,
\end{aligned}
\tag{26}
$$

where

$$[M_0] = \int_{S^\xi} [N^u]^T \rho [N^u] |J| \mathrm{d}\eta\mathrm{d}\zeta,$$

$$[M_1] = \int_{S^\xi} \frac{[N^p]^T \phi}{K_f [N^p]} |J| \mathrm{d}\eta\mathrm{d}\zeta,$$

$$[E_0] = \int_{S^\xi} [B_u^1]^T [D]\left([B_u^1]|J|\mathrm{d}\eta\mathrm{d}\zeta\right),$$

$$[E_1] = \int_{S^\xi} [B_u^1]^T [D][B_u^1]|J|\mathrm{d}\eta\mathrm{d}\zeta,$$

$$[E_2] = \int_{S^\xi} [B_u^2]^T [D][B_u^2]|J|\mathrm{d}\eta\mathrm{d}\zeta,$$

$$[E_3] = \int_{S^\xi} [B_u^1]^T \{m\}[N^p]|J|\mathrm{d}\eta\mathrm{d}\zeta,$$

$$[E_4] = \int_{S^\xi} [B_u^2]^T \{m\}[N^p]|J|\mathrm{d}\eta\mathrm{d}\zeta,$$

$$[E_5] = \int_{S^\xi} [B_p^1]^T k[B_p^1]|J|\mathrm{d}\eta\mathrm{d}\zeta,$$

$$[E_6] = \int_{S^\xi} [B_p^2]^T k[B_p^1]|J|\mathrm{d}\eta\mathrm{d}\zeta,$$

$$[E_7] = \int_{S^\xi} [B_p^2]^T k[B_p^2]|J|\mathrm{d}\eta\mathrm{d}\zeta,$$

$$[E_8] = \int_{S^\xi} [B_p^2]^T [N^u]|J|\mathrm{d}\eta\mathrm{d}\zeta,$$

$$\{F^{b3}(\xi)\} = \int_{S^\xi} [B_p^2]^T \{b\}|J|\mathrm{d}\eta\mathrm{d}\zeta,$$

$$\{F^{b1}(\xi)\} = \int_{S^\xi} [B_p^1]^T \{b_\xi\}|J|\mathrm{d}\eta\mathrm{d}\zeta,$$

$$\{F^{b2}(\xi)\} = \int_{S^\xi} [B_p^1]^T \{b\}|J|\mathrm{d}\eta\mathrm{d}\zeta,$$

$$\{F^{b4}(\xi)\} = \int_{\Gamma^\xi} [B_p^{2A}]^T \{b\}|J|\mathrm{d}\zeta + [B_p^{2B}]^T \{b\}|J|\mathrm{d}\eta,$$

$$\{F^{t1}\} = \int_{\Gamma^\xi} [B_p^{2A}]^T k[B_p^1]|J|\mathrm{d}\zeta + \int_{\Gamma^\xi} [B_p^{2B}]^T k[B_p^1]|J|\mathrm{d}\eta,$$

$$\{F^{t2}\} = \int_{\Gamma^\xi} [B_p^{2A}]^T k[B_p^2]|J|\mathrm{d}\zeta + \int_{\Gamma^\xi} [B_p^{2B}]^T k[B_p^2]|J|\mathrm{d}\eta,$$

$$\{F^{t3}\} = \int_{\Gamma^\xi} \left([B_p^{2A}]^T [N^u]|J|\mathrm{d}\zeta + [B_p^{2B}]^T [N^u]|J|\mathrm{d}\eta\right).$$

$$\tag{27}$$

The displacement and pore pressure vectors are expressed by generalized displacement vectors $\{\mathbf{U}\} = \left\{\begin{array}{c} \{u(\xi)\} \\ \{p_f(\xi)\} \end{array}\right\}$.

The second-order differential equations can be obtained by equations (25) and (26):

$$
\begin{aligned}
&\xi^2 \begin{bmatrix} [E_0] & 0 \\ 0 & [E_5] \end{bmatrix} \{\mathbf{U}(\xi)\}_{\xi\xi} - \left(\xi^2 \begin{bmatrix} (i\omega + \omega^2 k\rho_f)[E_3]^T & 0 \\ 0 & -[E_3] \end{bmatrix} - \xi \begin{bmatrix} 2[E_0] - [E_1] + [E_1]^T & 0 \\ 0 & 2[E_5] - [E_6] + [E_6]^T + \{F^{t1}\} \end{bmatrix}\right)\{\mathbf{U}(\xi)\}_\xi \\
&\quad + \left(\xi^2 \begin{bmatrix} \omega^2[M_0] & 0 \\ 0 & -i\omega[M_1] \end{bmatrix} - \xi \begin{bmatrix} (i\omega + \omega^2 k\rho_f)(2[E_3]^T - [E_8] + \{F^{t3}\}) & 0 \\ 0 & [E_4] - 2[E_3] \end{bmatrix} - \begin{bmatrix} [E_2] & 0 \\ 0 & [E_7] - \{F^{t2}\} \end{bmatrix}\right)\{\mathbf{U}(\xi)\} \\
&= -\xi^2 \left\{\begin{array}{c} \{F^b(\xi)\} \\ -k\rho_f\{F^{b1}(\xi)\} \end{array}\right\} - \xi \left\{\begin{array}{c} \{F^t(\xi)\} \\ -k\rho_f(2\{F^{b2}(\xi)\} - \{F^{b3}(\xi)\} + \{F^{b4}(\xi)\}) \end{array}\right\}.
\end{aligned}
\tag{28}
$$
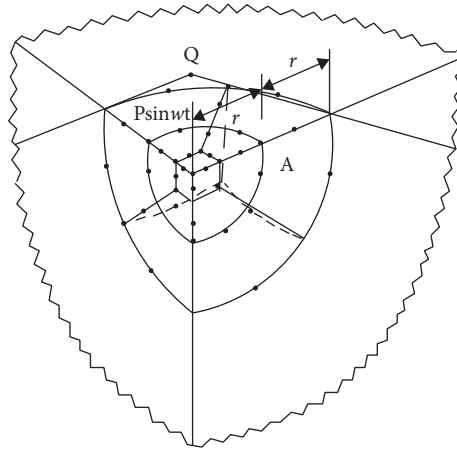
FIGURE 3: SBFEM discretization of 1/4 unbounded half-space.

(a)

(b)
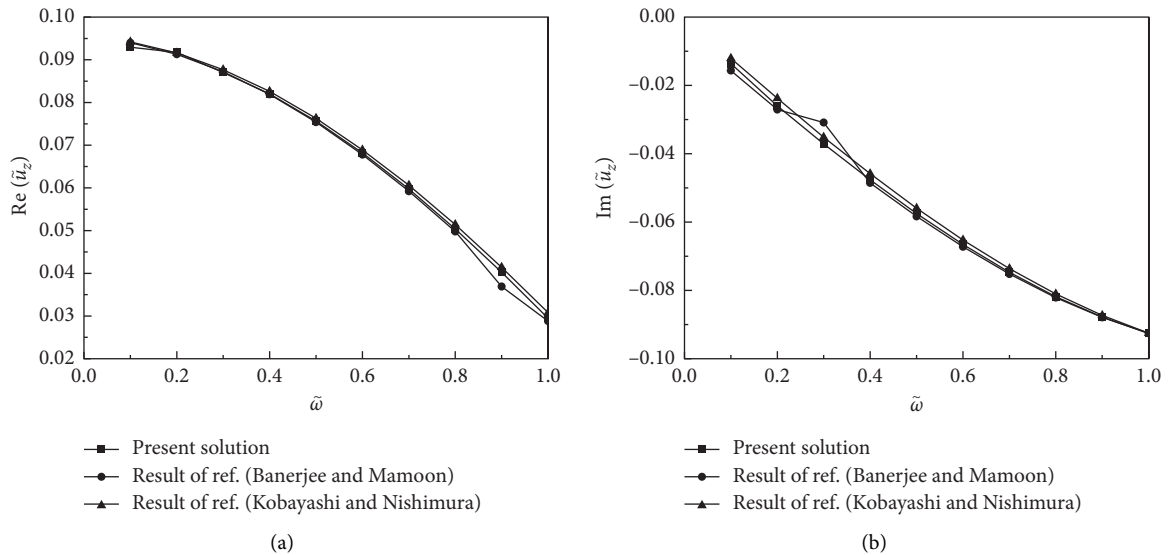
FIGURE 4: Compared present solutions with the reference's results: (a) real part of vertical displacement and (b) imaginary part of vertical displacement.

4. Numerical Analysis and Discussion

The displacement and pore pressure responses of 3D half-space surface subjected to vertical concentrated harmonic loads are investigated. In the calculation, the saturated soil layer is clay layer, and the relevant parameters in [16] are used. Some soil parameters adopted in the present study are obtained from field investigation and laboratory test, such as $\rho_s = 2000 \, \text{kg/m}^3$, $\rho_f = 1000 \, \text{kg/m}^3$, $\phi = 0.4$, $K_f = 2.0 \times 10^9 \, \text{N/m}^2$, $v = 0.4$, $k = 1.0 \times 10^{-9} \, \text{m/s}$, and $\mu = 1.0 \times 10^7 \, \text{Pa}$.

Using the method presented in this paper, the 3D half-space is divided into two parts. A hemisphere with a radius of 2R is a structure and the rest is a semi-infinite space. According to symmetry, 1/4 half space is taken for analysis, as shown in Figure 3. Two parts of 3D half-space are analyzed by scaled boundary finite element method. The structure half-space interface is discretized by three 8-node

two-dimensional elements, and the structure part is discretized by eighteen 8-node two-dimensional elements.

In order to verify the accuracy of this method, if $\rho_f = 0$ and $n = 0$, the two-phase medium degenerates into a single-phase medium. By using the method presented in this paper, the solution of the degenerate 3D linear elastic dynamic Boussinesq problem can be obtained. Figure 4 shows the relationship between vertical displacement $\tilde{u}_z = u_z r \mu / P$ and dimensionless frequency $\tilde{\omega} = \sqrt{\rho/\mu} \omega r$, where r is the horizontal distance between concentrated load P and surface calculation point. It can be seen from Figure 4(a) that the shape of the curve for the present solution is very similar to the solution in the literatures (Banerjee and Mamoon [21] and Kobayashi and Nishimura [22]). The maximum value of the solution in the present solution is 0.092, and the minimum value is 0.03, which is consistent with the solution in the literature. And, the difference between them is in the

-■- Result of 3D elastic half space
-●- Result of 3D saturated half space

(a)

-■- Result of 3D elastic half space
-●- Result of 3D saturated half space

(b)
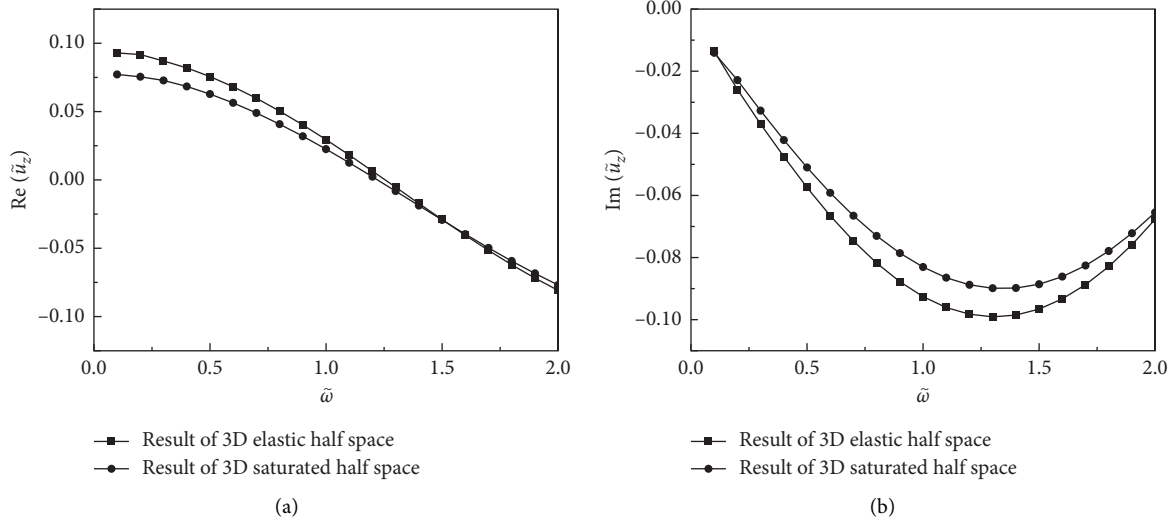
Figure 5: The vertical displacement for the 3D half-space varied with the frequency: (a) real part of vertical displacement and (b) imaginary part of vertical displacement.

-■- $k = 1.0 \times 10^{-11}$ m/s
-●- $k = 1.0 \times 10^{-9}$ m/s
-▲- $k = 1.0 \times 10^{-7}$ m/s

(a)

-■- $k = 1.0 \times 10^{-11}$ m/s
-●- $k = 1.0 \times 10^{-9}$ m/s
-▲- $k = 1.0 \times 10^{-7}$ m/s

(b)
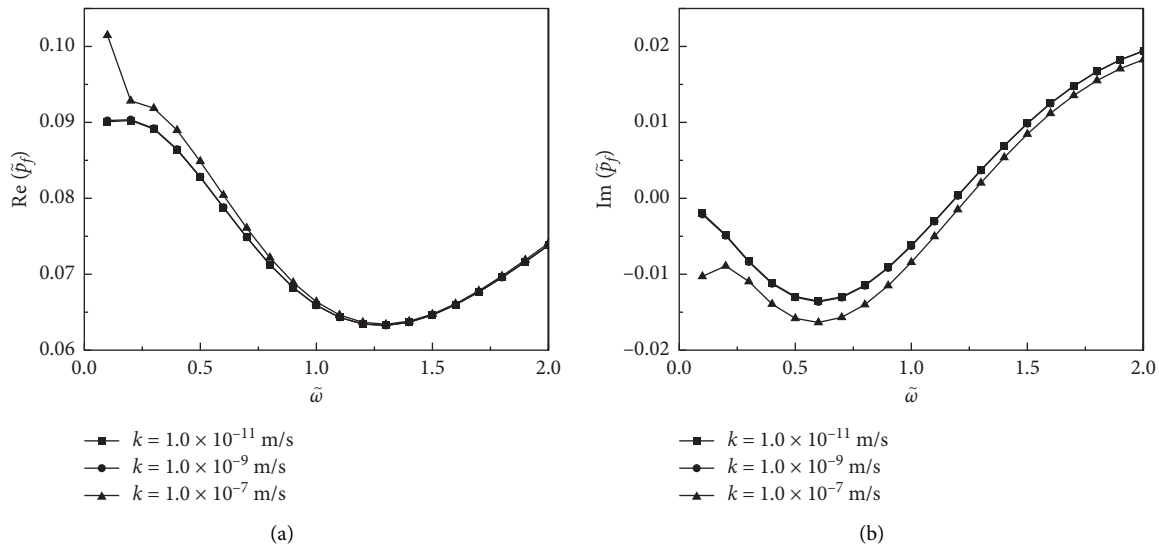
Figure 6: The pore pressure for the interface between the half spec and structure varied with the frequency: (a) real part of vertical displacement and (b) imaginary part of vertical displacement.

range of 0.002. It can be seen from Figure 4(b) that the solution in present solution has a decreasing trend, and the curve shape is relatively smooth. The maximum value decreased from −0.017 to −0.092. By comparing the present solution in this paper with that in the literature, it can be concluded that the fluctuation of the solution in present solution is relatively small. The numerical results in this paper are in good agreement with those in literature (Banerjee and Mamoon [21] and Kobayashi and Nishimura [23]), which verifies the accuracy of the proposed method.

Figure 5 shows the relationship between vertical displacement $\tilde{u}_z = u_z r\mu/P$ of saturated and elastic soils in 3D half space and dimensionless frequency $\tilde{\omega} = \sqrt{\rho/\mu}\omega r$. The results show that the dynamic responses of saturated soil and elastic soil are different at different frequencies. It can be seen from the figure

that, with the increase of $\tilde{\omega}$, the real part of the vertical displacement $\tilde{u}_z$ decreases, while the imaginary part of the vertical displacement $\tilde{u}_z$ appears at an extreme value near $\tilde{\omega} = 1.3$.

Figure 6 shows the relationship between pore pressure $\tilde{p}_f$ at point B on the structure-soil interface (2R away from the surface) and dimensionless frequency $\tilde{\omega}$ at different permeability coefficients $k = 1.0 \times 10^{-7}$ m/s, 1.0×10^{-9} m/s, and 1.0×10^{-11} m/s. It can be seen from the figure that the pore pressure amplitude increases with the increase of permeability coefficient of saturated soil.

5. Conclusion

In this paper, the scaled boundary element method for single-phase elastic media is extended to the dynamic

consolidation of 3D saturated soils with water-soil two-phase coupling. The application of scaled boundary element method in soil-structure interaction is extended. From the theoretical analysis in this paper, it can be seen that

(1) Not the same as single-phase media, the displacement and stress matrices are not only formed in the scaled boundary finite element equation of saturated soil consolidation but also the pore water pressure effect is coupled in the scaled boundary finite element matrix. According to Biot's theory, the governing differential equation of saturated soil consolidation is solved in Cartesian rectangular coordinate system, and the proportional boundary finite element equation in the form of pore pressure and displacement is obtained.

(2) The scaled boundary of dynamic consolidation of saturated soil also has unique advantages. The dimension of the analytical problem can be reduced by one dimension if only the boundary surface is discretized. In addition, similar to the boundary element method, it can automatically satisfy the radiation conditions at infinite distances. However, the method in this paper does not need to solve the fundamental solution and does not involve singular integrals.

(3) As a semi analytical method, the 3D scaled boundary finite element equation for dynamic consolidation of saturated soils is not only accurate in finite element sense but also convenient in mathematical processing. Especially, in dealing with complex structures and structural nonlinearity, it can simulate two-phase saturated soil-structure dynamic interaction in infinite and finite domain, which has important engineering practical value.

Data Availability

The data used to support the findings of this study are available from the corresponding author upon request.

Conflicts of Interest

The authors declare that they have no conflicts of interest.

Acknowledgments

References

[1] S. L. Chen and H. H. He, "Axisymmetric consolidation of a transversely isotropic single-layered soil," *Journal of Shanghai Jiaotong University*, vol. 39, no. 5, pp. 760–768, 2005.

[2] J. F. Lu, Y. Si, and J. H. Wang, "Interaction between superstructure, raft and layered viscoelasticsaturated soil," *Journal of Shanghai Jiaotong University*, vol. 35, no. 4, pp. 489–492, 2001.

[3] J. G. Jiang and H. T. Liang, "Analysis of internal forces of high-risesteel staggered truss under horizontal seismic considering soil-structure interaction," *Journal ofRailway Science and Engineering*, vol. 8, no. 2, pp. 17–20, 2011.

[4] X. L. Du and J. T. Wang, "Review of studies on the hydrodynamic pressure and its effects on the seismic response of dams," *Journal of Hydraulic Engineering*, vol. 32, no. 7, pp. 13–21, 2001.

[5] Z. F. Xia, G. L. Ye, J. H. Wang, B. Ye, and F. Zhang, "Fully coupled numerical analysis of repeated shake-consolidation process of earth embankment on liquefiable foundation," *Soil Dynamics and Earthquake Engineering*, vol. 30, no. 11, pp. 1309–1318, 2010.

[6] C. H. Zhang, *Structural-Foundation Dynamic Interaction Problem*, pp. 243–266, Hohai University Press, Nanjing, China, 1993.

[7] W. D. A. Smith, "non-reflecting plain boundary for wave propagationproblems," *Journal of Computational Physics*, vol. 15, no. 4, pp. 492–503, 1974.

[8] B. Engquist and A. Majda, "Absorbing boundary conditions for the numericalsimulationwaves," *Mathematics ofComputation*, vol. 31, no. 139, pp. 629–651, 1977.

[9] Z. P. Liao, K. L. Huang, and B. P. Yang, "Transmission boundary conditionsfor transient wave analysis," *Earthquake Engineering and Engineering Vibration*, vol. 2, no. 6, pp. 556–564, 1989.

[10] Z. P. Liao, Z. H. Zhou, and Y. H. Zhang, "Stable implementation of transmitting boundary in numerical simulation of wave motion," *Acta Geophysica Sinica*, vol. 45, no. 4, pp. 554–568, 2002.

[11] R. G. Keys, "Local Absorbing boundary conditions for acoustic media," *Geophysics*, vol. 60, no. 5, pp. 892–902, 1985.

[12] J. P. Wolf and C. H. Song, "Doubly asymptotic multidirectional transmitting boundary fordynamic unbounded medium-structure-interactionanalysis," *Earthquake Engineering andStructural Dynamics*, vol. 24, no. 2, pp. 175–188, 1995.

[13] C. Zhao and S. A. Valliappan, "Dynamic infinite element for three dimensional infinite domain wave problems," *International Journal for Numerical Methods in Engineering*, vol. 36, pp. 2567–2580, 1992.

[14] N. Khalili, S. Valliappan, J. Tabtabaie-Yazdi, and M. Yazdchi, "1D infinite element for dynamic problems in saturated porous media," *Communications in Numerical Methods in Engineering*, vol. 13, pp. 727–738, 1997.

[15] G. Bonnet, "Basic singular solutions for a poro-elastic medium in the dynamic range," *Journal of the Acoustical Society of America*, vol. 82, pp. 1758–1762, 1987.

[16] B. Xu, L. N. Gao, X. Y. Lei, M. Q. Xu, and L. Y. Liu, "Analysis of dynamic interaction between hole embedded in saturated soil and moving loads using 2.5D boundary element method," *Journal of Southwest Jiaotong University*, vol. 48, no. 4, pp. 659–665, 2013.

[17] M. Yazdchi, N. Khalili, and S. Valliappan, "Non-linear seismic behavior of concrete gravity dams using coupled finite element-boundary element method," *International Journal for Numerical Methods in Engineering*, vol. 44, no. 1, pp. 101–130, 1999.

[18] Q. K. Du, "The coupling of the natural boundary element and finite element methods for wave equation," *Journal of Huaibei Coal Industry Teachers College*, vol. 20, no. 2, pp. 1–10, 1999.

[19] J. P. Wolf and C. M. Song, "Dynamic-stiffness matrix in time domain of unbounded medium by infinitesimal finite-element cell method," *Earthquake Engineering andStructural Dynamics*, vol. 23, pp. 1181–1198, 1994.

[20] C. M. Song and J. P. Wolf, "The scaled boundary finite-element method alias consistent infinitesimal finite-element cell method," *Computer Methods in AppliedMechanics and Engineering*, vol. 147, no. 3-4, pp. 329–355, 1997.

[21] P. K. Banerjee and S. M. Mamoon, "A fundamental solution due to a periodic point force in the interior of an elastic half-space," *Earthquake Engineering and Structure Dynamics*, vol. 19, no. 1, pp. 91–105, 1990.

[22] S. Kobayashi and N. Nishimura, "Green's tensors for elastic half-space, an application of the boundary integral equation method," *Memoirs of the Faculty of Engineering, Kyoto University*, vol. 42, pp. 228–241, 1980.

[23] M. Li, H. Zhang, H. Guan, and G. Lin, "Three-dimensional investigation of wave–pile group interaction using the scaled boundary finite element method. Part I: theoretical developments," *Ocean Engineering*, vol. 63, pp. 174–184, 2013.

Research Article

Disturbance Effect of Pipe Jacking Group Adjacent Excavation on Surrounding Soil

Changbai Wang [ID],[1,2] **Jimin Liu** [ID],[1,2] **Hua Cheng** [ID],[1,2,3] **and Haibing Cai** [ID][1,2]

[1]*School of Civil Engineering and Architecture, Anhui University of Science and Technology, Huainan 232001, China*
[2]*State Key Laboratory of Mining Response and Disaster Prevention and Control in Deep Coal Mine,*
Anhui University of Science and Technology, Huainan, China
[3]*School of Resources and Environmental Engineering, Anhui University, Hefei 230601, China*

Correspondence should be addressed to Jimin Liu; jimliu@aust.edu.cn

Under the modern and complicated urban environment, clarifying the interaction mechanism and mutual influence mechanism between the urban tunnel and the surrounding environment is of considerable significance to the construction and operation of the tunnel. To understand and grasp the excavation-induced disturbance range and mechanism of adjacent pipeline jacking group on surrounding soils, this paper carries out relevant researches. Based on a case history of a three-hole parallel adjacent jacking pipeline in shallow overburden, a field test and assessment are performed. By setting monitoring points around the monitoring section, the earth pressure and water pressure under different buried depths and different spacing are monitored. For further discussion, the general law of soil disturbance around single-hole, double-hole, and three-hole jacking is investigated, the calculation method of lateral disturbance range and overlapping area range of pipe jacking group is deduced, and the degree of soil disturbance is evaluated as well. The results show that there will be different degrees of disturbance superposition in parallel multihole jacking due to the influence of the spacing, and the disturbance intensity is greatly affected by the parallel distance and buried depth.

1. Introduction

Pipe jacking technology is an underground pipeline construction method developed after shield tunnel. With its advantages of low comprehensive cost, high construction efficiency, and uninterrupted to urban traffic, it is widely used in municipal pipelines, underground pedestrian passageways, subways, and comprehensive pipe gallery. Due to the use of trenchless excavation technology, the surrounding soils are inevitably disturbed, which will lead to unloading or loading and other complex mechanical behaviors of the soil, resulting in changes in stress and strain of surrounding soils and even endangering the safety of adjacent buildings and underground pipelines, causing a series of environmental geotechnical problems. Therefore, the mechanism of soil disturbance caused by excavation has been the focus of

scholars and engineering applications [1–4]. In recent years, with the need for urban underground space development, pipe jacking through existing subway tunnels, foundation pits, railway, and other adjacent projects is gradually increasing [5–10], which puts forward new requirements and research directions for soil disturbance mechanism of pipe jacking. And the disturbance effect of pipe jacking adjacent excavation on surrounding soil has gradually aroused attention.

Some theoretical research studies, field tests, and laboratory tests on soil disturbance caused by pipe jacking excavation have been conducted, and the corresponding evaluation methods and indicators have been studied as well. During pipe jacking excavation, due to the extrusion of jacking force, cutting shear force of the microtunnel boring machine (MTBM) head, and vibration load, the soils near

the working face will have different degrees of disturbance in different areas. Fang et al. proposed the concept of soil disturbance zone division in pipe jacking construction [11]. Wei et al. expanded the soil disturbance zone to seven disturbance zones in combination with joint grouting and soil consolidation [12] and deduced the range of transverse and longitudinal disturbance zones caused by parallel pipe jacking [13]. Li and Miao studied the influence of grouting pressure and grouting amount on soil disturbance plastic zone based on the cavity expansion theory [14]. Chen et al. [15], Meng et al. [16], Xu et al. [17], and Lu et al. [18] had studied the evaluation index and method of disturbance based on laboratory tests. In the field test, according to the characteristics of the project, the field measurement, and analysis of the excavation disturbance of the surrounding soil of large-diameter circular pipe jacking [19, 20], rectangular pipe jacking [21], curved pipe jacking [22], and circular steel pipe jacking with flange plate [23] are carried out, and the relative research results are obtained.

Cavity expansion methods in geomechanics are a classic problem, which was widely used in stress-strain problems such as tunnel excavation, bolt support, shaft sinking, and in situ tests such as static CPT [24–27]. It is more significant that the cylindrical hole expansion theory under the isotropic initial stress state can also simulate the horizontal excavation construction process of urban underground pipeline and tunnel engineering, analyze the soil disturbance caused by horizontal excavation, and determine the maximum grouting pressure in the hole, which provides a practicable way for the research in this paper. Jia et al. [28] analyzed the expanded radius and internal expanding pressure of cylindrical hole and obtained the relationship between the plastic zone radius and the initial pore size and the expansion pressure based on the SMP criterion. With the help of FLAC numerical software, Han et al. [29] established a two-dimensional circular hole expansion model with pressure as the expansion boundary and analyzed the cavity shape and the distribution of the plastic zone.

At present, the research studies on soil disturbance mechanism mainly focus on single pipe jacking or parallel pipe jacking. The research on soil disturbance mechanism and field measurement of adjacent pipe jacking group is scarce. When there are more than two pipes excavating in sequence, what kind of disturbance effect will happen, whether there will be disturbance overlapping, and what is the relationship between the disturbance intensity and the center spacing of pipeline group and buried depth. These are the topics worthy of further study and discussion. Different from the previous researches, the disturbance effect of pipe jacking group adjacent excavation on surrounding soil would pay more attention to the soil disturbance perpendicular to the jacking direction, so the transverse disturbance range of soil will be focused on. Taking a practical three-hole parallel adjacent jacking in the drainage project of Meilan International Airport in Haikou as the engineering background, the disturbance effect of pipe jacking group adjacent excavation on surrounding soil is investigated, which would provide an engineering reference for similar projects.

2. Determination of Lateral Disturbance Range of Pipe Jacking Group Adjacent Excavation

For the convenience of the problem analysis, we make the following assumptions: (1) the material and section specification of the pipeline segment in the pipe jacking group are identical; (2) the jacking pipes of each hole are excavated in sequence, and the jacking speed is suitable and consistent; (3) the soil is homogeneous isotropic elastic-plastic cohesionless material, and the soil obeys the Mohr–Coulomb yield criterion. And the lateral disturbance range of single-hole excavation, double-hole excavation, three-hole excavation will be analyzed separately.

2.1. The Lateral Disturbance Range of Single-Hole Excavation. During single-hole pipe jacking, friction resistance is generated between the shell of MTBM and the surrounding soil, which makes the soil around the shell shear disturbance. At the same time, the horizontal excavation of pipe jacking will cause shear disturbance on the soil in the front of MTBM and excavation unloading on the soil upper front MTBM. Therefore, the horizontal excavation of single-hole pipe jacking will produce soil disturbance in a certain range perpendicular to the jacking direction.

Based on the field measurement and the theory of small hole expansion, the calculation method of the radius of plastic shear disturbance zone is given in the literature [30–34], but it is not suitable for shallow overburden engineering. Therefore, the shell shear disturbance zone will be further analyzed based on cavity expansion methods. And the pipe jacking in shallow overburden is regarded as cylindrical hole expansion in finite medium. The mechanical model is shown in Figure 1.

Referring to a_0 as the initial radius, the hole radius after expansion is called the expanding radius a. Referring to p_0 as the initial pressure of the hole, p is called the expansion pressure of the hole. When the uniformly distributed internal pressure changes from p_0 to p, the radius of the hole changes from a_0 to a. With the continuous increase of internal pressure, the soil around the hole begins to yield, from the original overall elastic state to the state containing both elastic and plastic regions. Therefore, the soil will be disturbed within the radius of plastic zone r_p, which is the radius of the shell shear disturbance zone R'.

The soils around the cylindrical hole satisfy the differential equation of stress balance according to the cavity expansion method:

$$\frac{\partial \sigma_r}{\partial r} + \frac{\sigma_r - \sigma_\theta}{r} = 0, \tag{1}$$

where σ_r and σ_θ are the radial and circumferential normal stresses, respectively, and r is the polar radius.

The geometric and physical equations in the elastic region can be expressed as
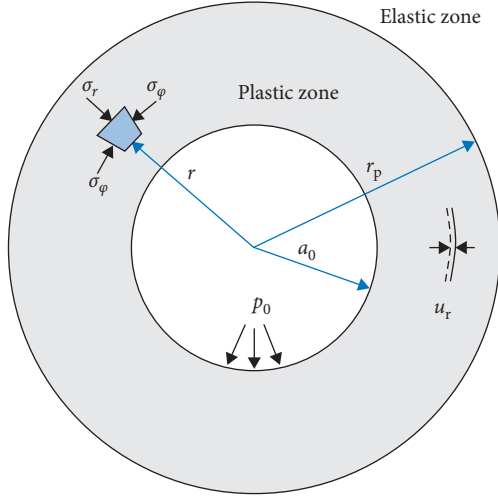
Figure 1: Mechanical model of cylindrical hole expansion.

$$
\begin{cases}
\varepsilon_r = -\dfrac{du_r}{d_r}, \\[3mm]
\varepsilon_\theta = -\dfrac{u_r}{r},
\end{cases}
\tag{2}
$$

$$
\begin{cases}
\varepsilon_r = \dfrac{1-\nu^2}{E}\left(\sigma_r - \dfrac{\nu}{1-\nu}\sigma_\theta\right), \\[3mm]
\varepsilon_\theta = \dfrac{1-\nu^2}{E}\left(\sigma_\theta - \dfrac{\nu}{1-\nu}\sigma_r\right),
\end{cases}
\tag{3}
$$

where ε_r and ε_θ are the radial and circumferential strain, respectively, E is the elastic modulus, and ν is Poisson's ratio.

Combining equations (1)–(3), the stress and displacement field of soils in elastic zone satisfy the following:

$$
\begin{cases}
\sigma_r = p_0 + \left(p_y - p_0\right)\left(\dfrac{r_p}{r}\right)^2, \\[3mm]
\sigma_\theta = p_0 - \left(p_y - p_0\right)\left(\dfrac{r_p}{r}\right)^2,
\end{cases}
\tag{4}
$$

$$
u_r = \frac{p_y - p_0}{2G}\left(\frac{r_p}{r}\right)^2 r,
\tag{5}
$$

where G is the shear modulus of soil and p_y is the expanding pressure at elastoplastic interface.

According to the basic assumption 3, the soil outside the hole obeys the Mohr–Coulomb criterion without considering the cohesion, and its yield criterion can be expressed as

$$
\frac{\sigma_r}{\sigma_\theta} = R_{ps} = \frac{1+\sin\varphi}{1-\sin\varphi},
\tag{6}
$$

where φ is the internal friction angle of soil, R_{ps} is the ratio of large principal stress to small principal stress, and it is also the ratio of radial force to circumferential force.

The stress in the plastic zone satisfies both the differential equation of stress equilibrium and the Mohr-Coulomb criterion. Substituting equation (6) into equation (1), we get

$$
\sigma_r = A\left(\frac{1}{r}\right)^{1-\left(1/R_{ps}\right)},
\tag{7}
$$

where A is the integral constant.

In the meanwhile, the soil in elastic zone also satisfies the Mohr–Coulomb criterion, by substituting the yield condition (6) into the stress field equation (4), the expansion pressure of the cylindrical hole at the beginning of yielding can be obtained, and it is also the radial stress at the radius of the plastic zone:

$$
p_y = \sigma_r|_{r=r_p} = \frac{2R_{ps}p_0}{1+R_{ps}}.
\tag{8}
$$

The integral constant A can be obtained by simultaneous equations (7) and (8):

$$
A = \frac{2R_{ps}p_0}{1+R_{ps}} r_p^{\,1-\left(1/R_{ps}\right)}.
\tag{9}
$$

Then, the radial stress in the plastic zone is

$$
\sigma_r = \frac{2R_{ps}p_0}{1+R_{ps}}\left(\frac{r_p}{r}\right)^{1-\left(1/R_{ps}\right)},
\tag{10}
$$

and the radius of the shell shear disturbance zone is

$$
r_p = \left(\frac{1+R_{ps}}{2R_{ps}p_0}\right)^{R_{ps}/\left(R_{ps}-1\right)} ap^{R_{ps}/\left(R_{ps}-1\right)}.
\tag{11}
$$

Therefore, the radius of the shell shear disturbance zone is

$$
R' = r_p = \left(\frac{1+R_{ps}}{2R_{ps}p_0}\right)^{R_{ps}/\left(R_{ps}-1\right)} ap^{R_{ps}/\left(R_{ps}-1\right)}.
\tag{12}
$$

As jacking excavation, soil output, driving machine jacking, and other processes, the pipe jacking excavation will continue to disturb the surrounding soil along a certain angle to the ground. The complete boundary line on both sides will form a junction with the ground; thus, a lateral disturbance area forms, which is shown in Figure 2.

According to the limit equilibrium principle, the boundary of the disturbance zone should be tangent to the shear disturbance zone, and the horizontal elevation angle of the boundary line is equal to the active earth pressure angle

$$
\alpha = 45° + \frac{\varphi}{2},
\tag{13}
$$

where φ is the internal friction angle of the soil.

Therefore, the range of horizontal disturbance caused by single-hole pipe jacking is

$$
L = 2ht g\left(45° - \frac{\varphi}{2}\right) + 2\frac{R'}{\cos\left(45° - (\varphi/2)\right)},
\tag{14}
$$
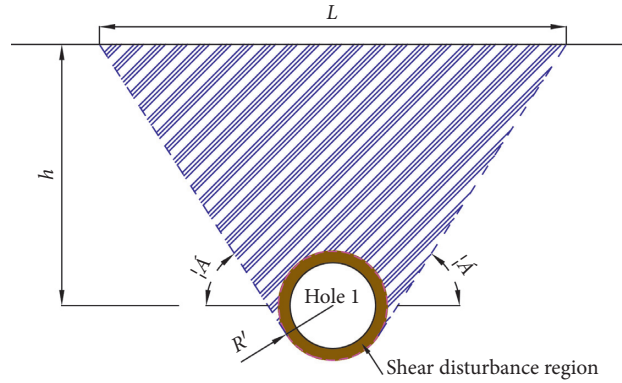
FIGURE 2: Schematic diagram of lateral disturbance range of single-hole jacking.

where h is the vertical distance between the center of pipe segment and ground surface, φ is the internal friction angle of soil, and R' is the radius of the shell shear disturbance zone, which can be determined by formula (12).

2.2. The Lateral Disturbance Range of Double-Hole Excavation and Disturbance Superposition.

When the second jacking pipe excavates in sequence, the double-hole jacking pipeline will be formed. At this time, the influence of horizontal center spacing should be considered. If the center spacing between two holes is large, the second hole only produces soil disturbance near itself, and its lateral disturbance range is the same as that of single-hole jacking. If the center spacing between two holes is small, disturbance superposition will occur near the junction center of the two holes. Assuming that the center spacing of pipeline is B, it satisfies

$$B > 2hctg\alpha + \frac{2R'}{\sin\ \alpha}. \tag{15}$$

The lateral disturbance range of the double hole is shown in Figure 3(a). The center spacing of the double hole is small and satisfies

$$B < 2hctg\alpha + \frac{2R'}{\sin\ \alpha}. \tag{16}$$

The lateral disturbance range of the double hole is shown in Figure 3(b). And the lateral overlapping area range is

$$L' = 2hctg\alpha - B + \frac{2R'}{\sin\ \alpha}. \tag{17}$$

2.3. The Lateral Disturbance Range of Three-Hole Excavation and Disturbance Superposition.

When the third hole excavates in parallel, the influence of the lateral disturbance range is the same as that of double-hole jacking, but the jacking position of the third hole should be considered. If the third hole is jacked outside the previous two holes, it is consistent with the superposition effect of double-hole jacking, as shown in Figures 4(a) and 4(b). If the third hole is jacked in the middle of the previous two holes, it will be further overlapped in the previous two-hole overlapped area, as shown in Figures 4(c) and 4(d). The lateral disturbance

zone of the third hole jacking and the lateral overlapping area range are the same as formulas (14) and (17).

3. Case Description

3.1. Overview.

To effectively discharge the rainy season precipitation and municipal sewage around Meilan International Airport and the surrounding areas in Haikou, the construction method combining large-diameter adjacent pipe jacking group underground excavation with large-diameter box culvert open excavation is adopted. This project locates outside the red line of Meilan Airport phase II expansion project and passes through the nursery, industrial plants, and urban roads. The aerial view of the project is shown in Figure 5. Among them, a three-hole parallel jacking pipeline group is adopted in the area from No. 4 shaft to No. 5 shaft. The total length of pipe jacking group is 1470 meters, the horizontal center spacing of the pipe jacking group is 3.18 meters, and the average cover depth of the pipe section is about 3.93 meters. It started in October 2019 and finished in April 2020. The construction of No. 1 hole, No. 3 hole, and No. 2 hole has been carried out successively and the cross section of the pipe jacking group is the same, which is shown in Figure 6.

Each ring of the jacking pipeline adopts circular prefabricated reinforced concrete segments with a width of 0.32 m. The inner diameter of the segment is 3.5 m and the length is 2.5 m. To effectively bore through the soft soil layer, the MTBM is used in this project, whose whole length is 5.71 m and the outer shell diameter is 4.16 m. In the meanwhile, the grouting system of synchronous grouting at the head and follow-up grouting at the pipe is adopted to ensure the jacking quality.

3.2. Geological Conditions.

The strata at the construction site can be divided into three main layers and the soft subsoil is about 13.5 m thick. The water table is located at a depth of 2.3 m below the ground. The basic physical parameters and depth for these soils are given in Table 1. Plain fill (layer ①) is located on the surface, and the silty clay (layer ②) and coarse sand (layer ③) are underneath, respectively. The main strata of pipe jacking are silty clay and coarse sand.

(a)

(b)
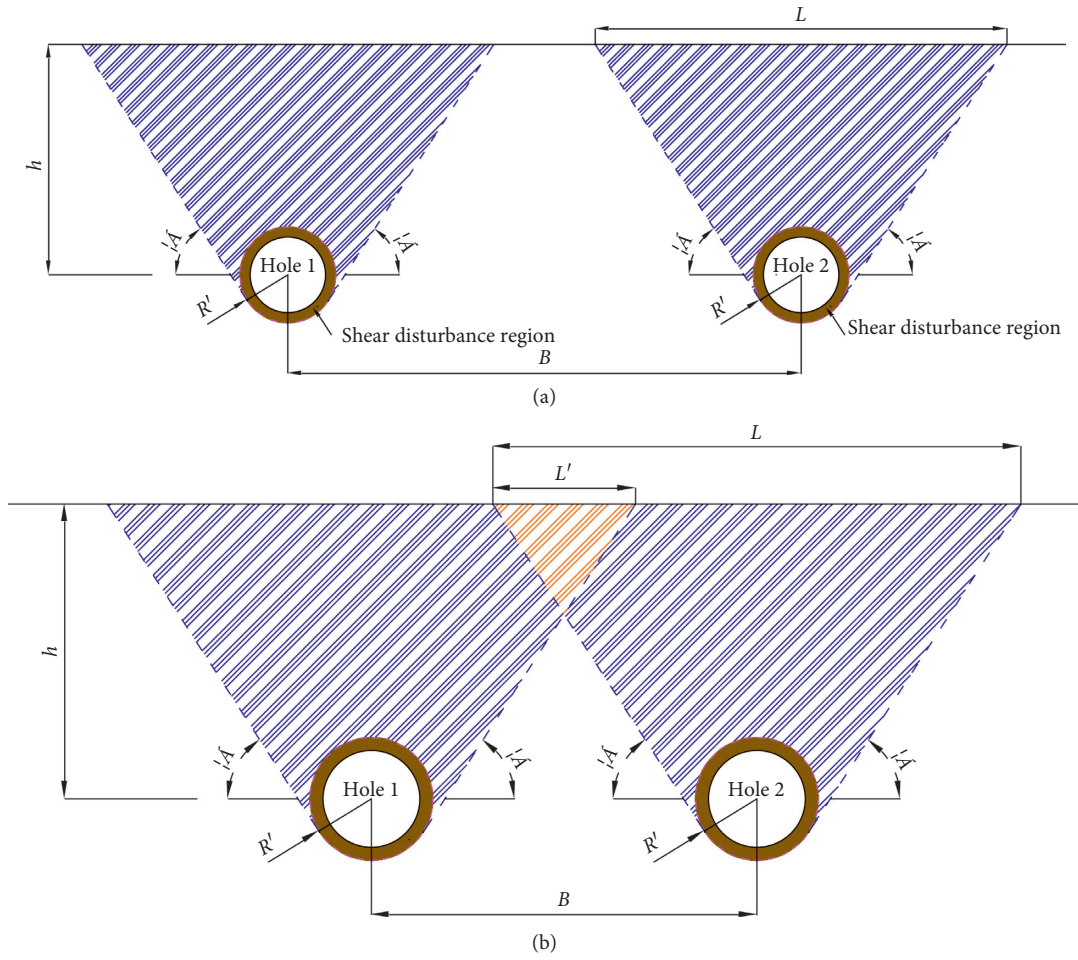
FIGURE 3: Schematic diagram of lateral disturbance range of double-hole jacking. (a) The center spacing is large in double-hole excavation. (b) The center spacing is small in double-hole excavation.

(a)

FIGURE 4: Continued.

(b)

(c)
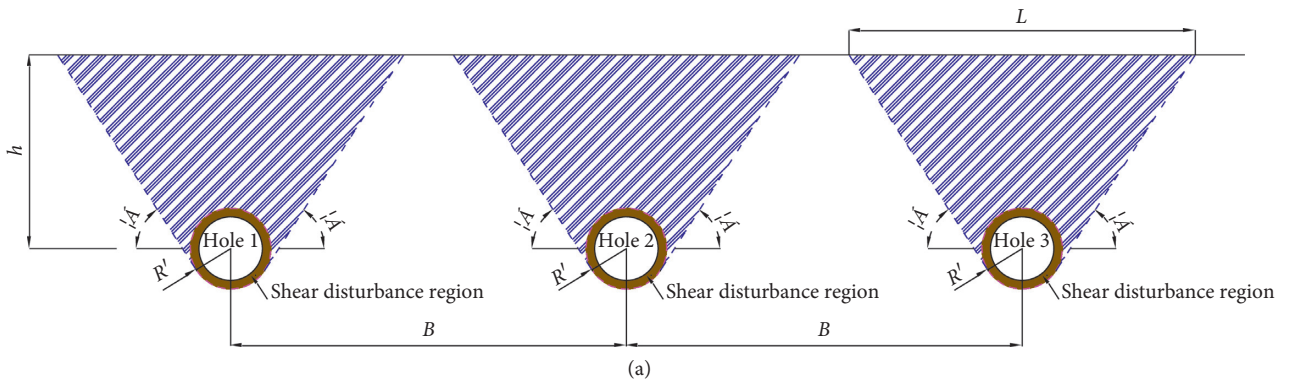
(d)
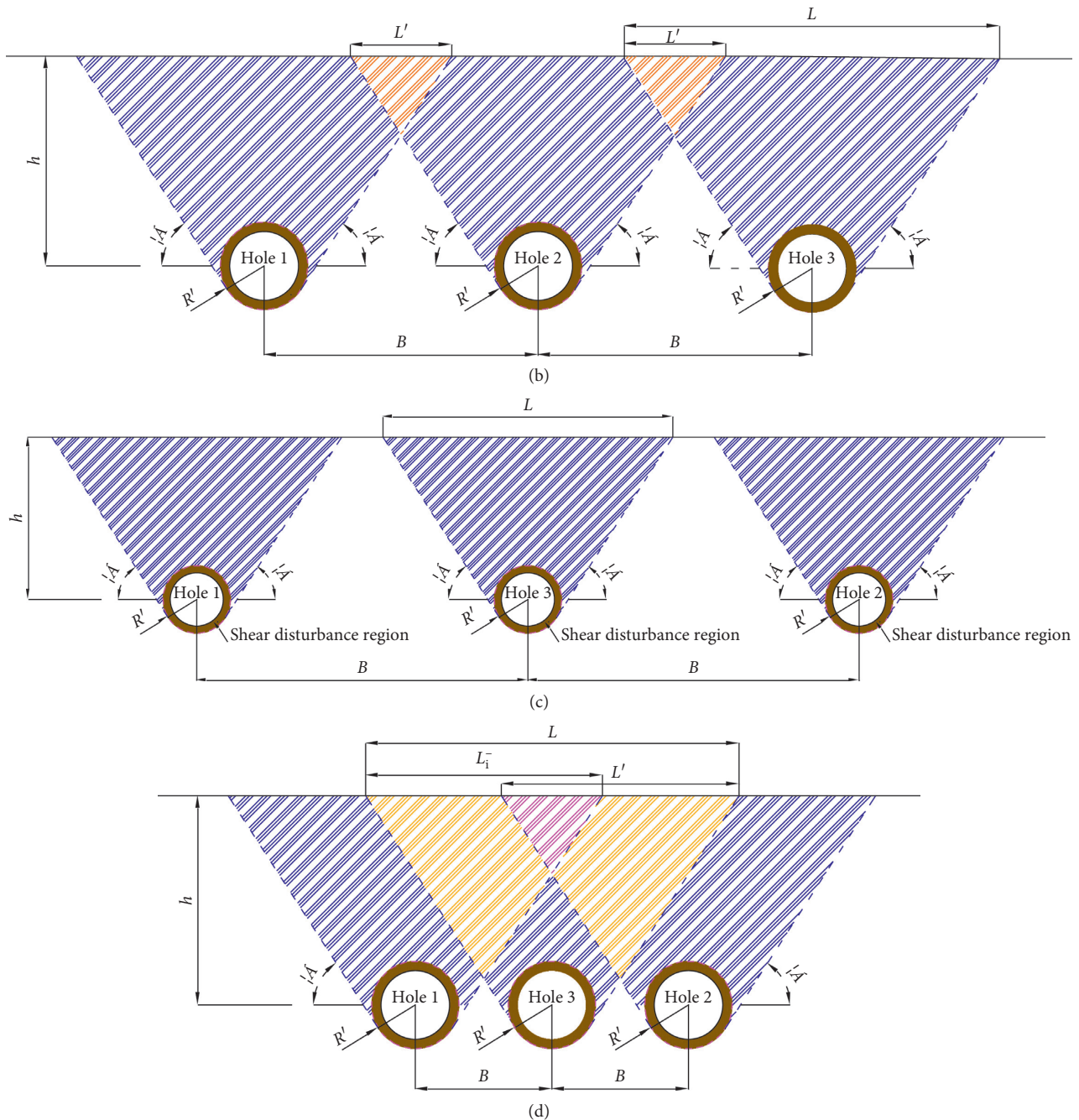
FIGURE 4: Schematic diagram of lateral disturbance range of three-hole pipeline jacking. (a) The third hole is located on the outside of the previous two holes and the center spacing is large. (b) The third hole is located on the outside of the previous two holes and the center spacing is small. (c) The third hole is located in the middle of the previous two holes and the center spacing is large. (d) The third hole is located in the middle of the previous two holes and the center spacing is small.

4. Field Test Scheme

4.1. Test Content and Layout of Monitoring Points.

The field monitoring contents include the earth pressure and pore water pressure of the soil around the pipe jacking group. According to the site construction and environmental conditions, the monitoring section is arranged at 4 + 368.9 mileage between No. 4 shaft and No. 5 shaft. To investigate the soil disturbance around the pipe jacking group to the greatest extent, seven monitoring holes are set on the monitoring section. Among them, No. 2, No. 4, and No. 6 monitoring holes are located directly above Hole 1, Hole 2, and Hole 3, respectively. No. 3 and No. 5 monitoring holes are located at the middle of the center spacing, and No. 1 and No. 7 monitoring holes are located at the double center spacing of Hole 1 and Hole 3. Two monitoring points are set at No. 2, No. 4, and No. 6 monitoring holes, and five monitoring points are set at No. 1, No. 3, No. 5, and No. 7
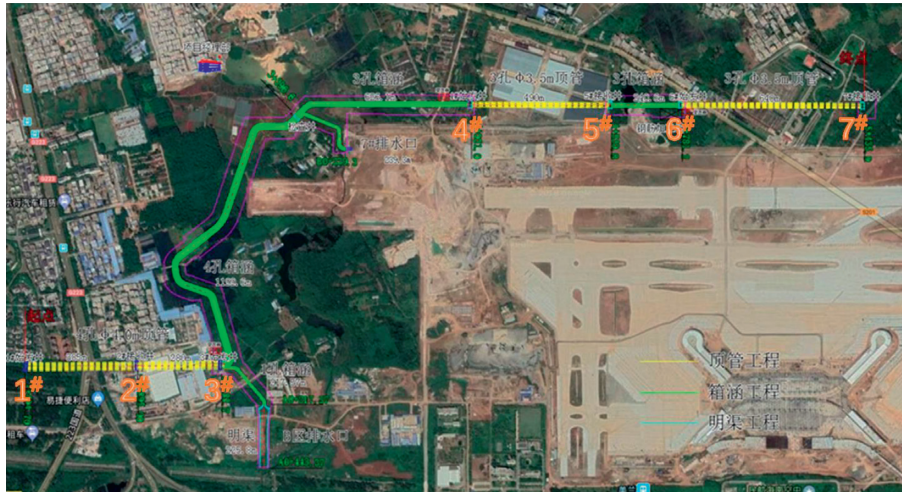
FIGURE 5: Aerial view of the project.
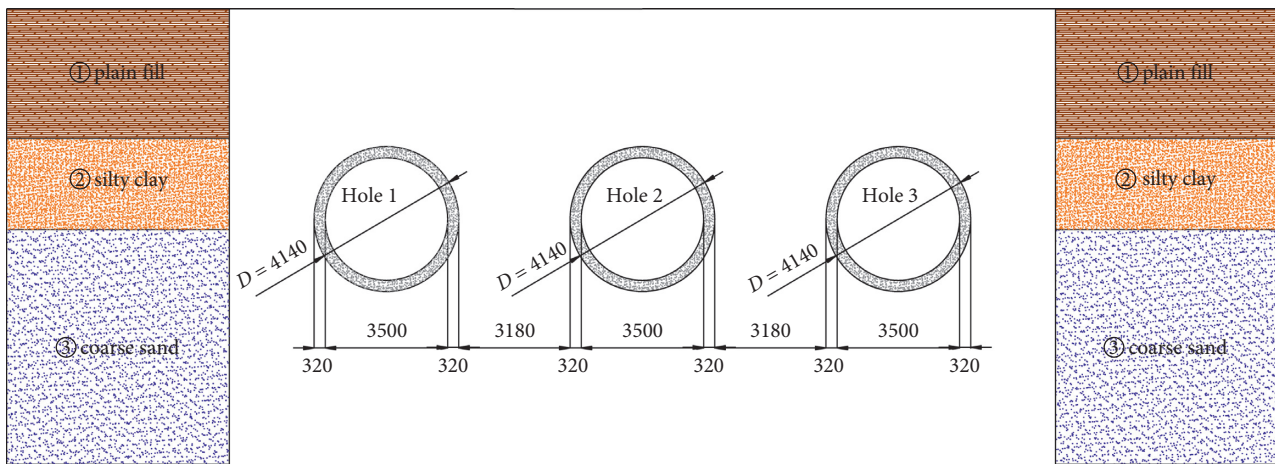
FIGURE 6: Cross section of pipe jacking group.

TABLE 1: Main geotechnical parameters of soils at the construction site.

Soil layer	Depths (m)	Water content (%)	Void ratio	Cohesion (kPa)	Internal friction angle (°)
①plain fill	0–3.98	30.4	0.865	27.9	16.8
②silty clay	3.98–6.58	25.03	0.81	14.91	15.42
③coarse sand	6.58–13.28			8	

monitoring holes. Earth pressure and pore water pressure gauges are arranged above and below at each monitoring point, so there are 7 monitoring holes, 26 monitoring points, and 52 stress gauges in total. The layout of the earth pressure gauge and pore water pressure gauge measuring points is shown in Figure 7. Figure 8 describes the erection and burying of on-site monitoring.

4.2. Test Monitoring Elements and Data Collection. JTM-V2000 vibrating wire earth pressure gauge and JTM-V3000 vibrating wire pore water pressure gauge are used as monitoring elements. Its working principle is that the high sensitivity induction membrane produces deflection under the action of load and changes the excited frequency of the

metal string of the induction membrane. The load on the earth pressure box and pore water pressure gauge is calculated by using the sensor calibration coefficient. In this project, data acquisition adopts the combination of a 32-channel JTM-MV20A data acquisition box and hand-held JTM-10A vibrating wire sensor reader. JTM-MV20A data acquisition box monitors and records the vibration frequency of the metal string every 6 seconds, and ZLY-V1.0 intelligent acquisition cloud platform management system software transmits data online and monitors the scene.

5. Analysis of Test Results

5.1. Analysis of Soil Disturbance during the First Hole Excavation. From Nov. 10 to 21, 2019, Hole 1 passed through
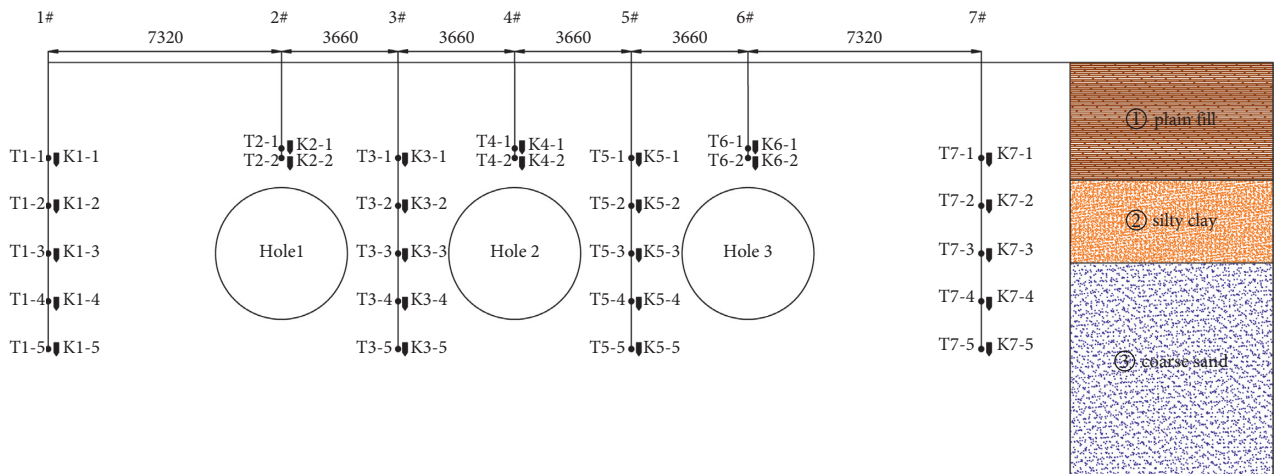
FIGURE 7: Distribution map of monitoring points.

(a)

(b)

(c)

(d)
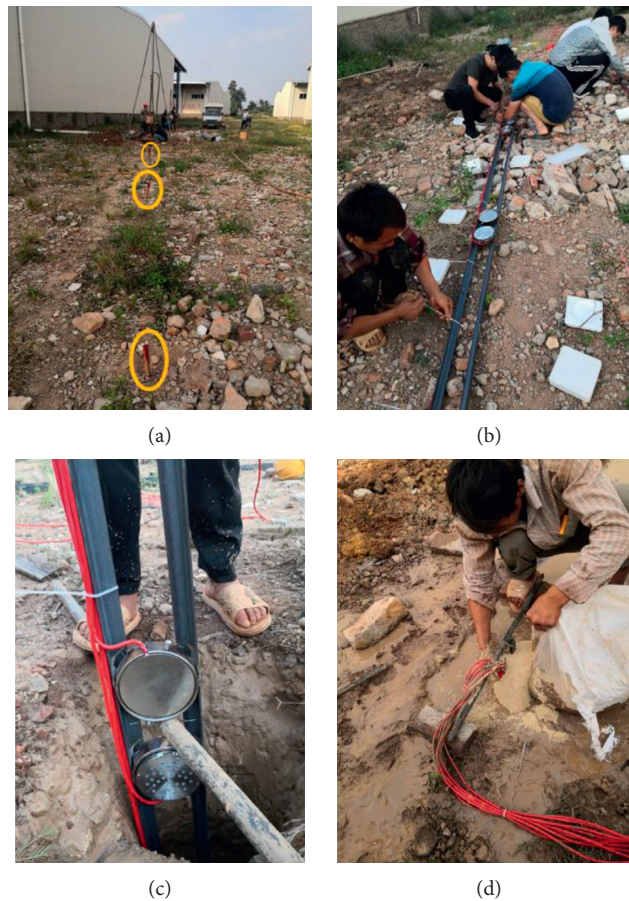
FIGURE 8: Diagram of monitoring elements erection and burying.

the monitoring section. The earth pressure and pore water pressure of No. 1, 2, 3, and 4 monitoring holes at different depths are recorded in Figures 9 and 10, respectively. And the earth pressure and pore water pressure of Nos. 5, 6, and 7 monitoring holes are unchanged.

It can be seen from Figures 9 and 10 that (1) the pore water pressure and earth pressure of No. 1, 2, 3, and 4 monitoring

holes are gradually decreasing. Since Nov. 10, 2019, when field monitoring starts, the tail of MTBM has just left the monitoring section, and the outer diameter of the MTBM is larger than the outer diameter of the first segment, which would form a gap on the outer wall of the segment. At this time, the thixotropic slurry injected from the tail and segment joint has just been injected into the gap, and the hoop supporting has not yet been
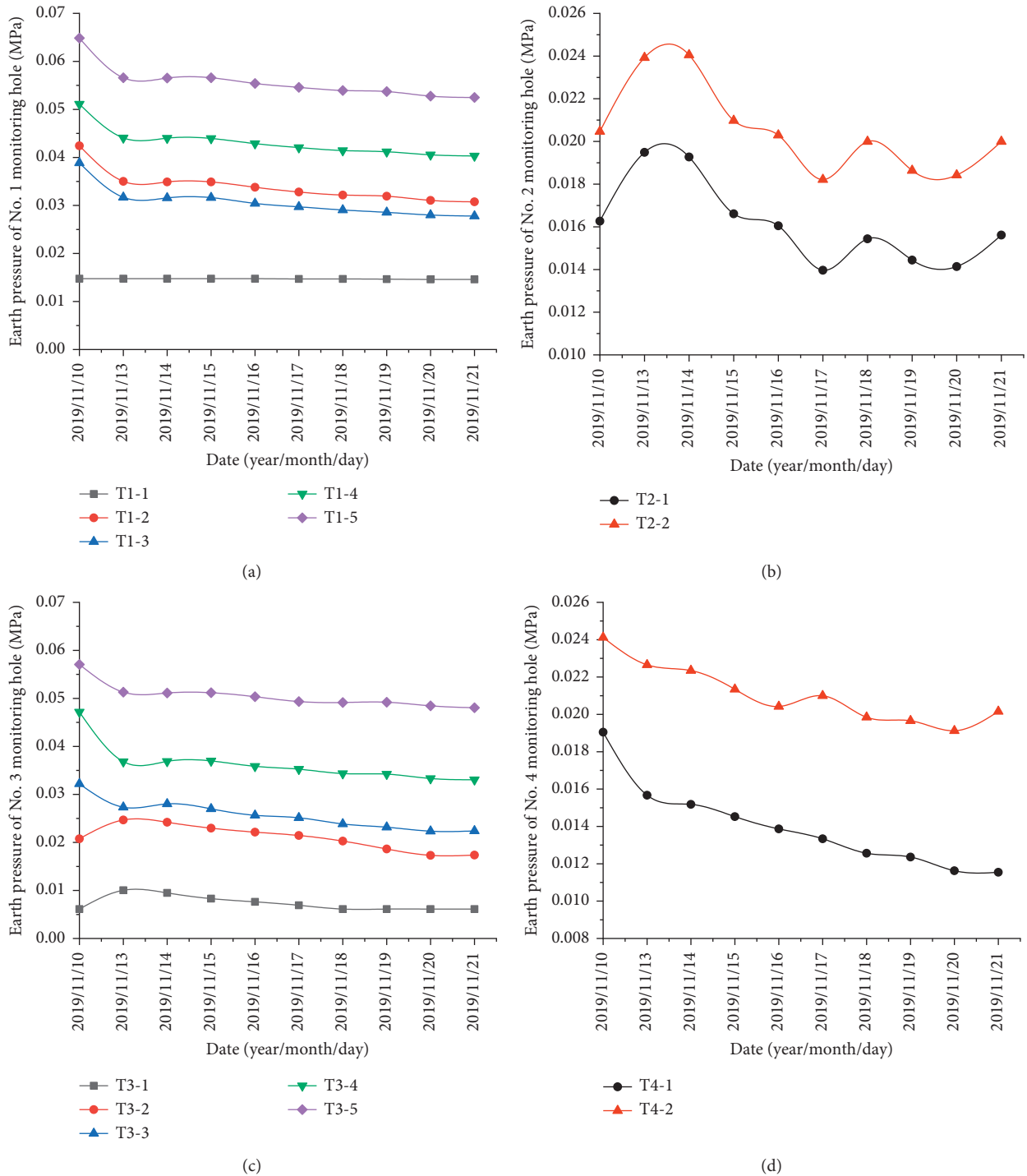
FIGURE 9: Variation diagram of earth pressure during Hole 1 jacking. (a) Earth pressure of No. 1 monitoring hole. (b) Earth pressure of No. 2 monitoring hole. (c) Earth pressure of No. 3 monitoring hole. (d) Earth pressure of No. 4 monitoring hole.

formed. After the tail of the MTBM comes out, the soil has no capacity to support itself and self-stabilization and fill the void quickly, resulting in the release of soil stress and the dissipation of pore water pressure gradually. (2) The decline level of the earth pressure and pore water pressure of No. 1, No. 2, No. 3, and No. 4 monitoring holes is different. And the pressure reduces to zero between No. 4 and No. 5 monitoring holes.

5.2. Analysis of Soil Disturbance during the Second Hole Excavation. From Dec. 27 to 31, 2019, Hole 3 passed through the monitoring section. The earth pressure and pore water pressure of Nos. 4, 5, 6, and 7 monitoring holes at different depths are recorded in Figures 11(a) and 12, respectively. And the earth pressure and pore water pressure of Nos. 1, 2, and 3 monitoring holes are basically unchanged.
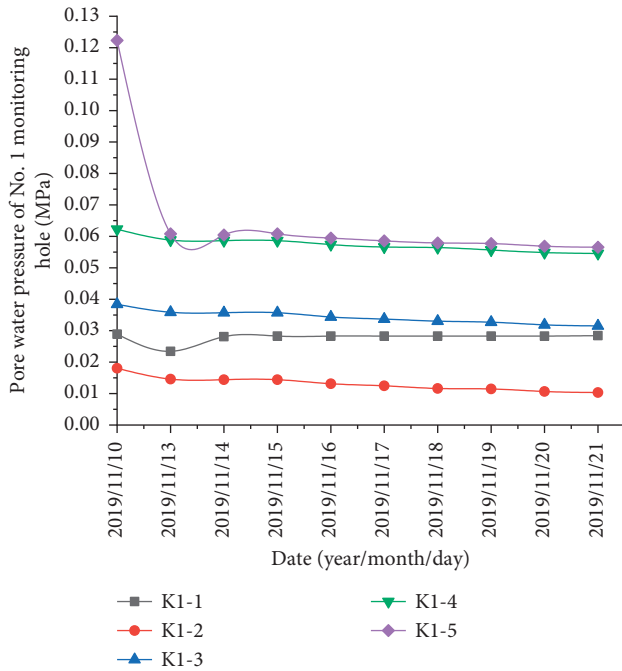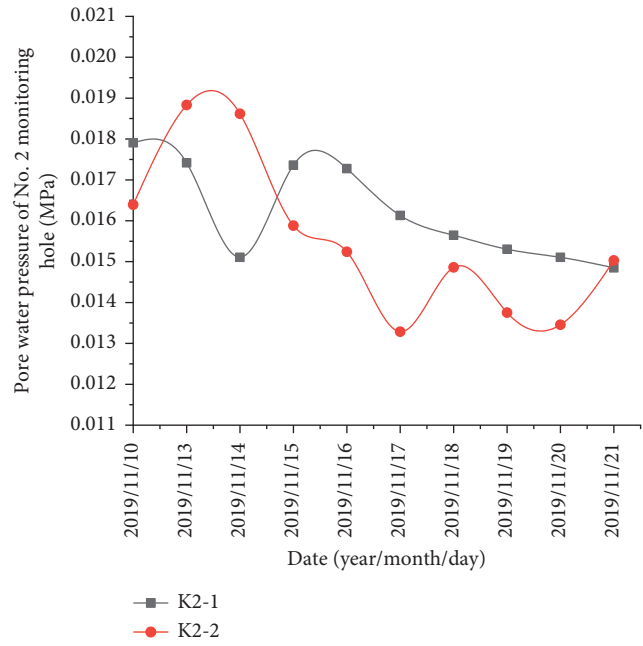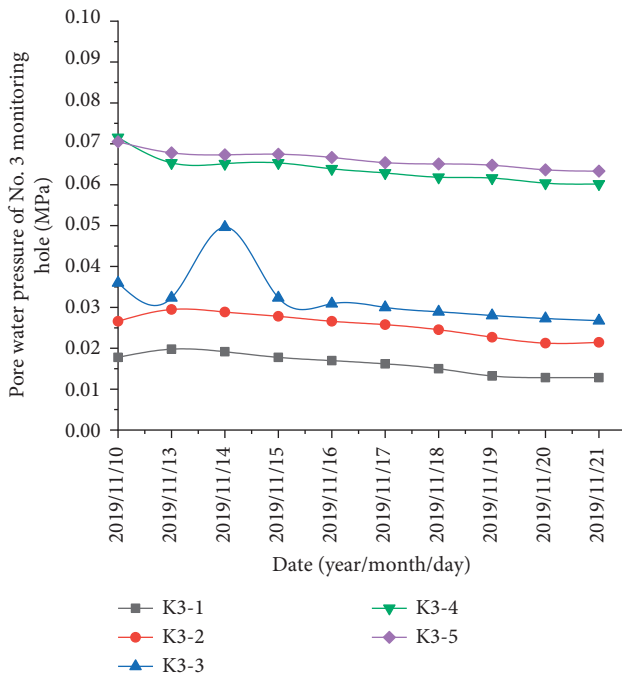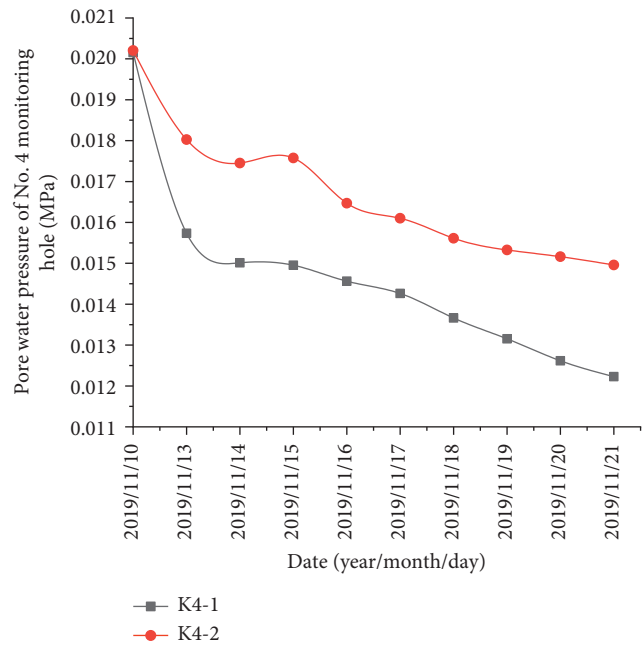
Figure 10: Variation diagram of pore water pressure during Hole 1 jacking. (a) Pore water pressure of No. 1 monitoring hole. (b) Pore water pressure of No. 2 monitoring hole. (c) Pore water pressure of No. 3 monitoring hole. (d) Pore water pressure of No. 4 monitoring hole.

It can be seen from Figures 11 and 12 that (1) the earth pressure and pore water pressure of Nos. 4, 5, 6, and 7 monitoring holes have changed clearly. Taking No. 6 monitoring hole which is shown in Figure 8(c) as an example, the pressure basically remains unchanged for a long time before it arrives at the monitoring section ahead of 15 m. When it arrives at the monitoring section ahead of 15 m, the pressure begins to increase sharply. When it reaches the monitoring section, the pressure is still fluctuating, but slightly gentle than before. After leaving the monitoring section for 10 m, the pressure decreases slowly. (2) The range and intensity of variation of earth pressure and pore water pressure in No. 4, No. 5, No. 6, and No. 7 monitoring holes are different. Between No. 3 and No. 4 monitoring holes, the pressure value decays clearly.

(a)

(b)

(c)

(d)
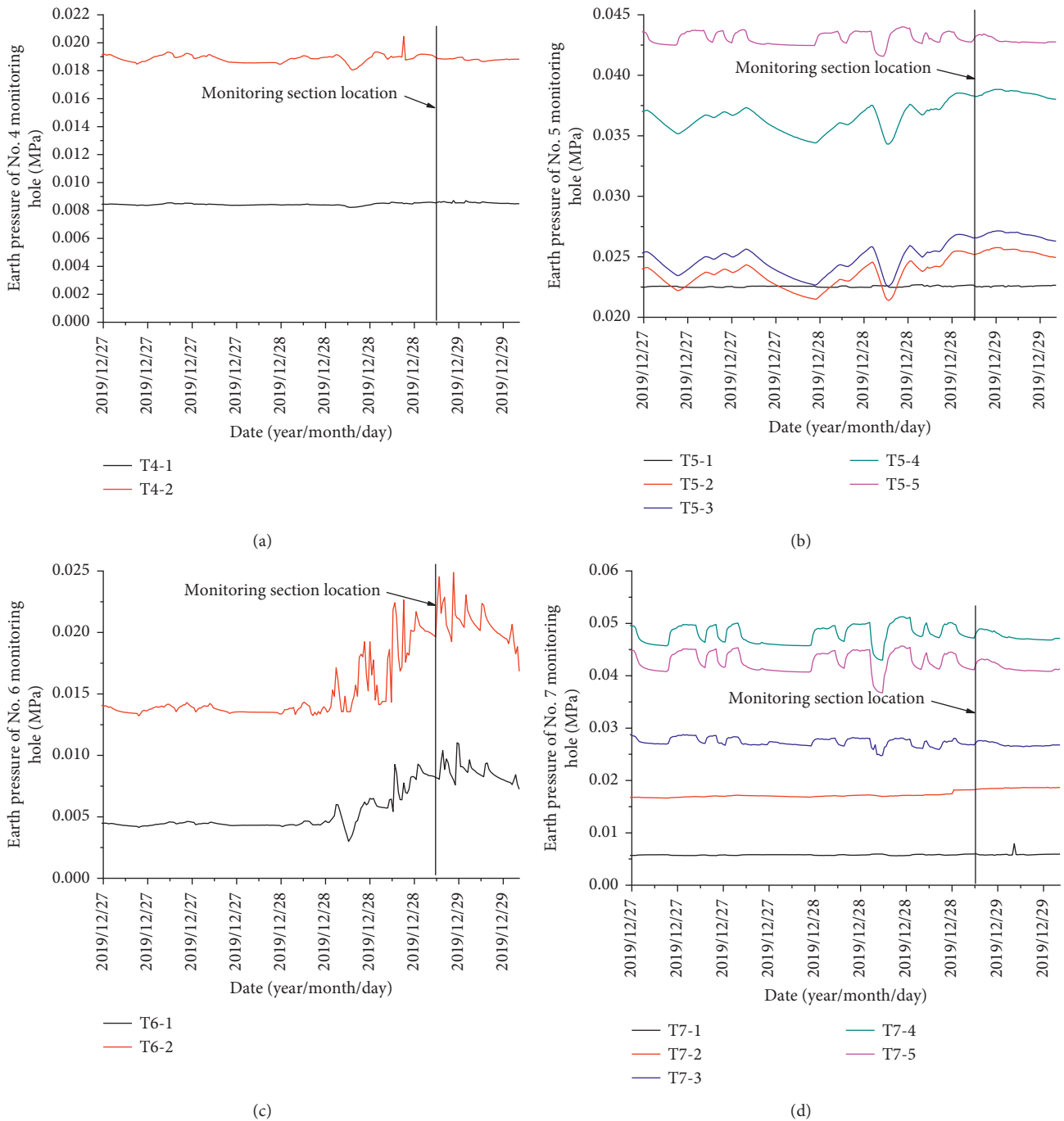
FIGURE 11: Variation diagram of earth pressure during Hole 3 jacking. (a) Earth pressure of No. 4 monitoring hole. (b) Earth pressure of No. 5 monitoring hole. (c) Earth pressure of No. 6 monitoring hole. (d) Earth pressure of No. 7 monitoring hole.

5.3. Analysis of Soil Disturbance during the Third Hole Excavation.
From Apr. 10 to 15, 2020, Hole 2 passed through the monitoring section. The earth pressure and pore water pressure of Nos. 2, 3, 4, 5, and 6 monitoring holes at different depths are recorded in Figures 13 and 14, respectively. And the earth pressure and pore water pressure of Nos. 1 and 7 monitoring holes are basically unchanged.

It can be seen from Figures 13 and 14 that (1) the earth pressure and pore water pressure of Nos. 2, 3, 4, 5, and 6 monitoring holes have some changes before and after reaching the monitoring section. And its disturbance law near the monitoring section with the change of horizontal jacking distance is basically the same as that of Hole 3. (2) The amplitude and intensity of variation of soil pressure and pore water pressure in No. 2, 3, 4, 5, and 6 monitoring holes are different. Between No. 1 and No. 2 monitoring holes and between No. 6 and No. 7 monitoring holes, the pressure decays clearly.
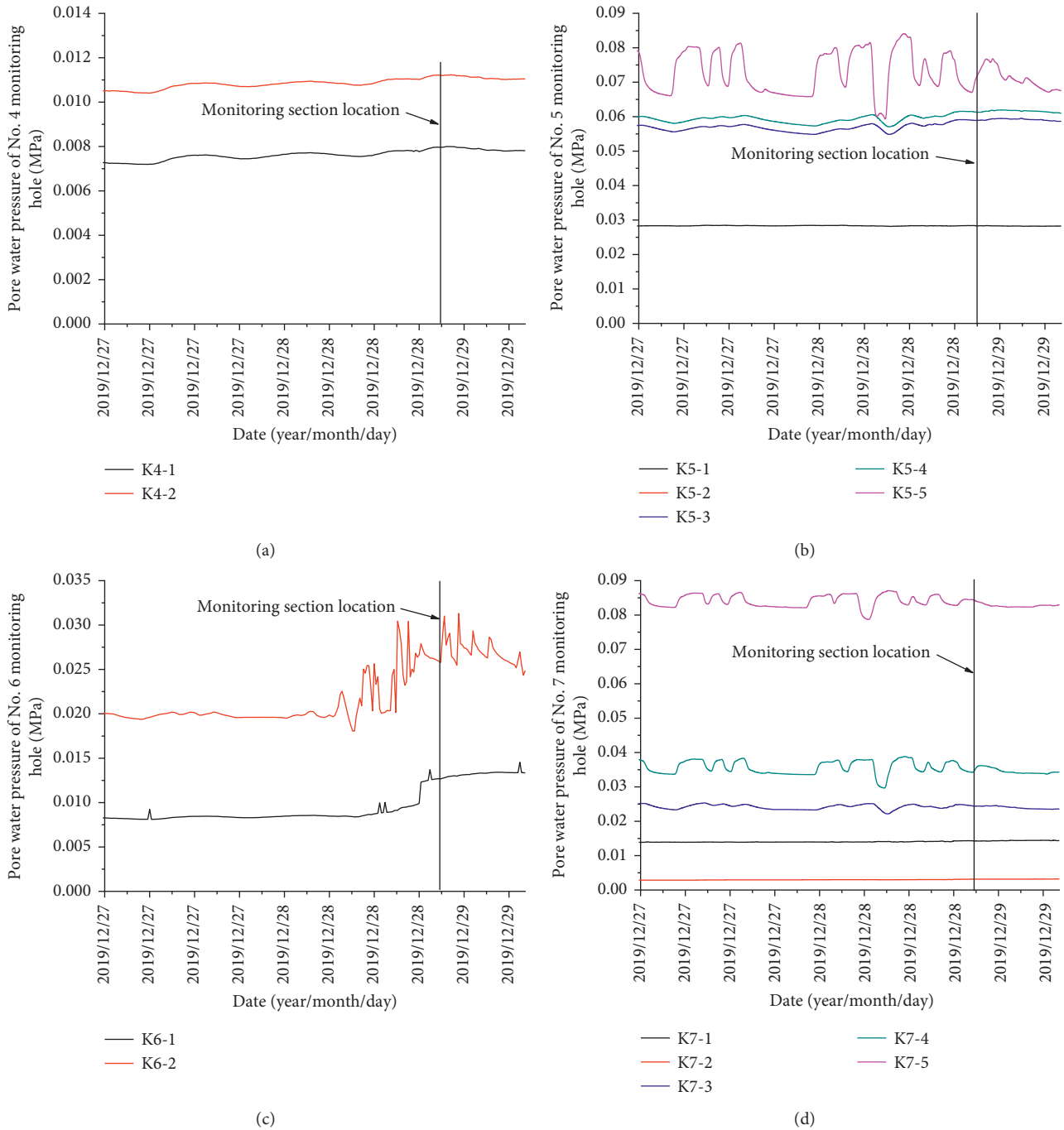
Figure 12: Variation diagram of pore water pressure during Hole 3 jacking. (a) Pore water pressure of No. 4 monitoring hole. (b) Pore water pressure of No. 5 monitoring hole. (c) Pore water pressure of No. 6 monitoring hole. (d) Pore water pressure of No. 7 monitoring hole.

From the field test data, it can be seen that when the head of MTBM excavates through the monitoring section in sequence, the stress field of soil around the monitoring section fluctuates in varying degrees with the change of the horizontal jacking distance, and the change laws of soil pressure and pore water pressure are completely consistent. The horizontal jacking distance affect not only the soil disturbance but also the spacing of pipeline group and buried depth. Therefore, it is necessary to deeply analyze the lateral soil disturbance range and the soil disturbance degree of single-hole, double-hole, and three-hole jacking.

5.4. Analysis of the Lateral Disturbance Range and Disturbance Superposition. In this project, the pipeline group excavates in sequence, and the third hole excavates in the middle of the previous two holes, whose construction sequence is the same as that in Figure 4(d). Ignoring the

(a)

(b)
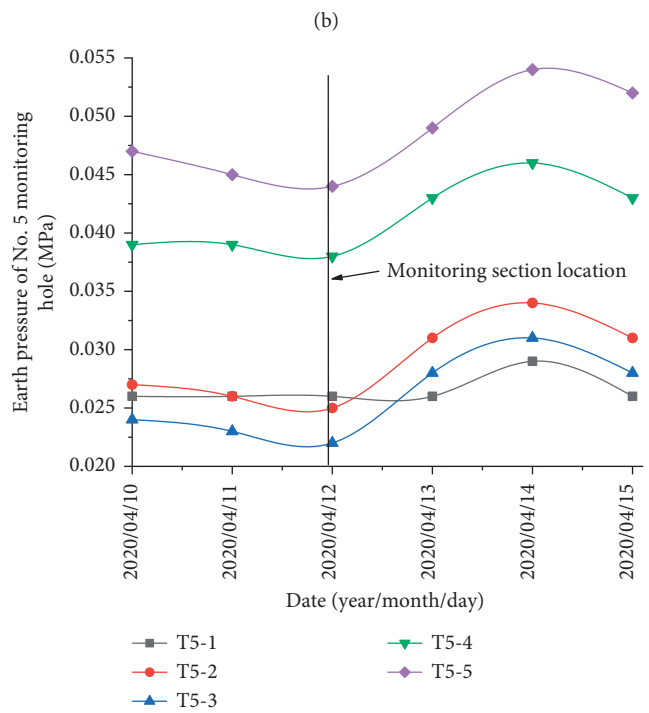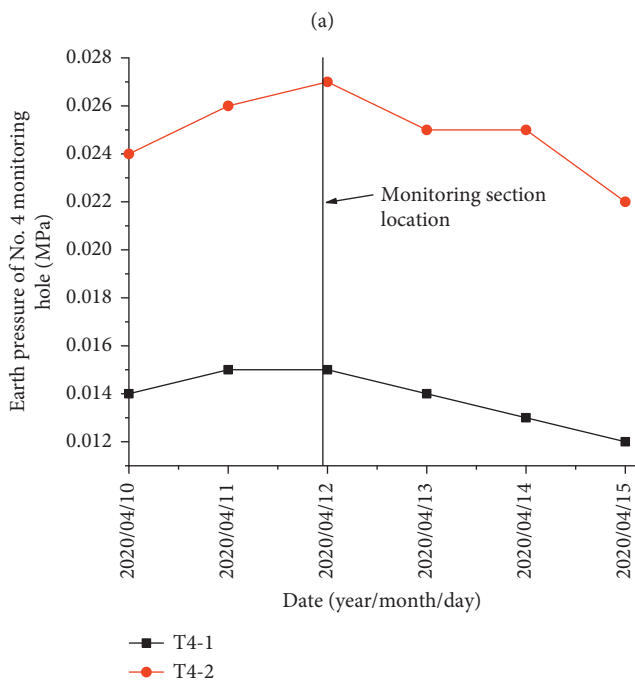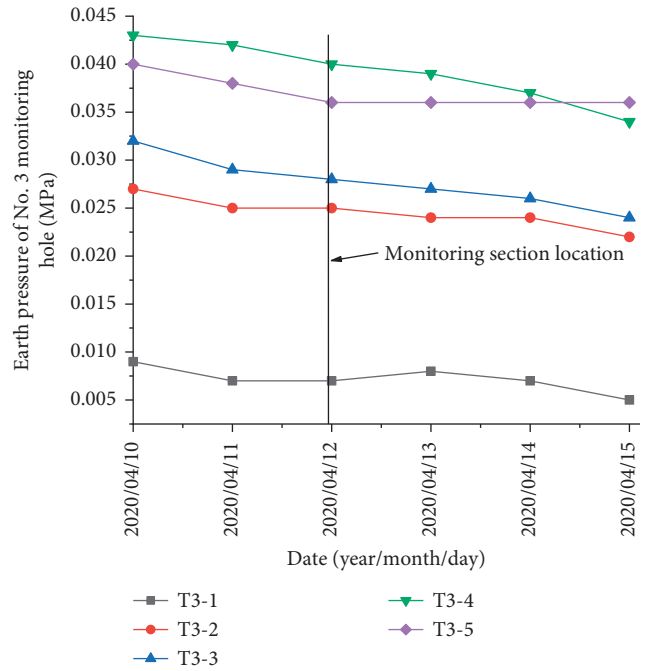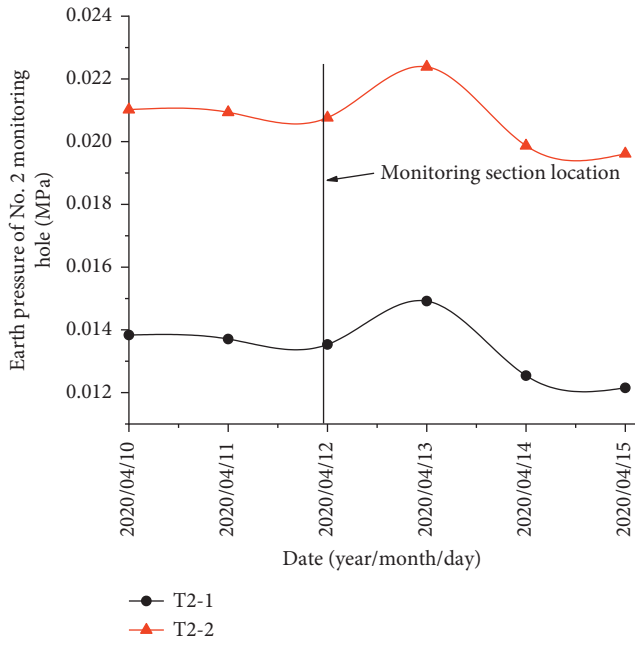
(c)

(d)

Figure 13: Continued.

(e)
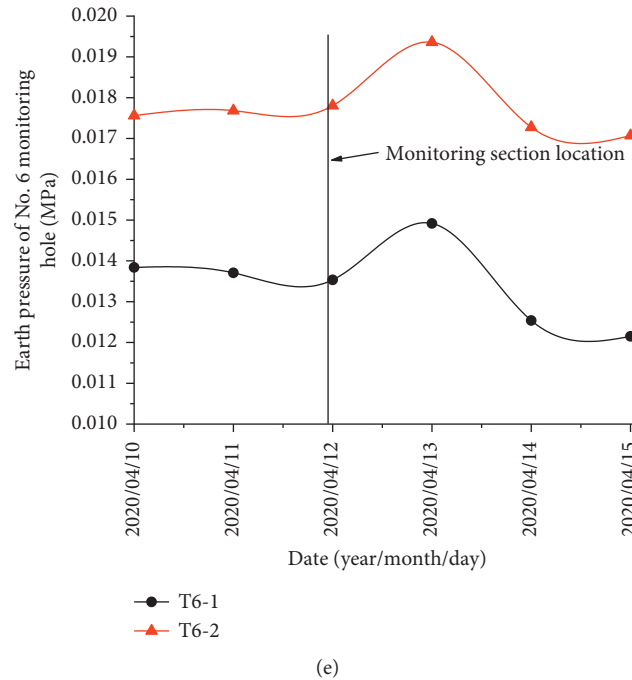
FIGURE 13: Variation diagram of earth pressure during Hole 2 jacking. (a) Earth pressure of No. 2 monitoring hole. (b) Earth pressure of No. 3 monitoring hole. (c) Earth pressure of No. 4 monitoring hole. (d) Earth pressure of No. 5 monitoring hole. (e) Earth pressure of No. 6 monitoring hole.

influence of soil structure, jacking speed, and other factors, the lateral disturbance range and disturbance overlapping area of single-hole, double-hole, and three-hole jacking can be determined, respectively. The calculation results are shown in Table 2 and Figure 15.

It can be seen from the table and figure that when Hole 1 excavates, its lateral disturbance range is 15.4 m and its disturbance can affect the earth pressure and pore water pressure at No. 1, 2, 3, and 4 monitoring holes, when Hole 3 excavates, its lateral disturbance range is 15.4 m and its disturbance can affect the earth pressure and pore water pressure at Nos. 4, 5, 6, and 7 monitoring holes, and when Hole 2 excavates, disturbance overlapping appears due to the small center spacing, its overlapping area range is 8.08 m, and its disturbance can affect the earth pressure and pore water pressure at Nos. 2, 3, 4, 5, and 6 monitoring holes. And the theoretical calculation results are consistent with the above field test data.

6. Evaluation of Soil Disturbance Degree

Based on the field test data, with the help of disturbance evaluation method, the disturbance degree of soil can be analyzed [34, 35], and the influence of lateral spacing perpendicular to the jacking direction, the buried depth, and disturbance overlap effect on soil disturbance can be deeply investigated. In this paper, the evaluation of soil disturbance

degree based on pore water pressure is adopted. The stress disturbance degree of soil can be expressed as

$$\lambda_d = 1 - \frac{u}{u_0}, \tag{18}$$

where λ_d is the degree of soil disturbance and u_0 and u are the pore water pressure before and after disturbance.

6.1. Evaluation of the Influence of the Lateral Spacing Perpendicular to the Jacking Direction on the Disturbance Degree. When the three holes excavate in turn, the monitoring points under the same buried depth are taken to analyze the soil disturbance degree of different lateral spacing, and the results are shown in Figure 16. When Hole 1 excavates, the soil disturbance of No. 2 monitoring hole is the most obvious, followed by No. 3 monitoring hole, and No. 4 and No. 1 monitoring holes are the least. When Hole 3 excavates, the soil disturbance of No. 6 monitoring hole is the most obvious, followed by No. 5 monitoring hole, and No. 4 and No. 7 monitoring holes are the minimum. When Hole 2 excavates, the soil disturbance of No. 4 monitoring hole is the most obvious, followed by No. 3 and No. 5 monitoring holes, and No. 2 and No. 6 monitoring holes are the least. This shows that the closer to the pipe, the more obvious the soil disturbance during the single-hole, double-hole, and three-hole jacking. Moreover, the soil disturbance on the top of pipe jacking is more obvious than that on the side due to the loose structure of the overlying soil.

(a)

(b)

(c)

(d)
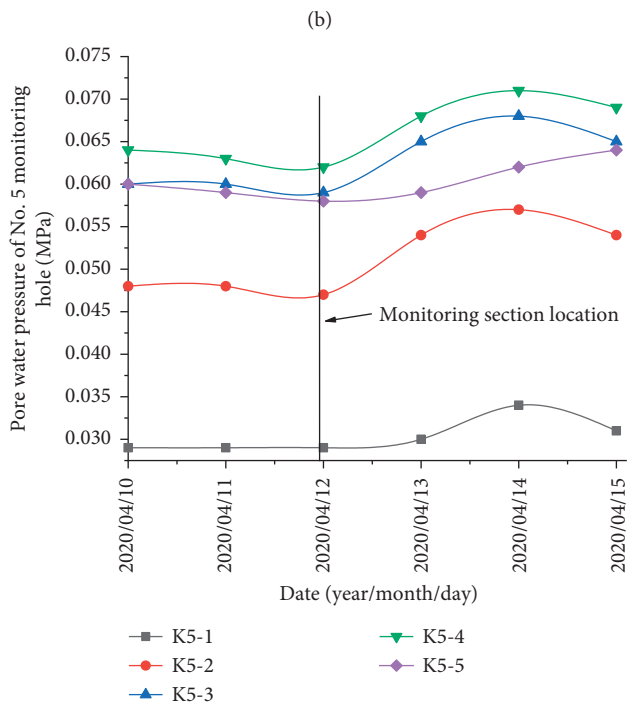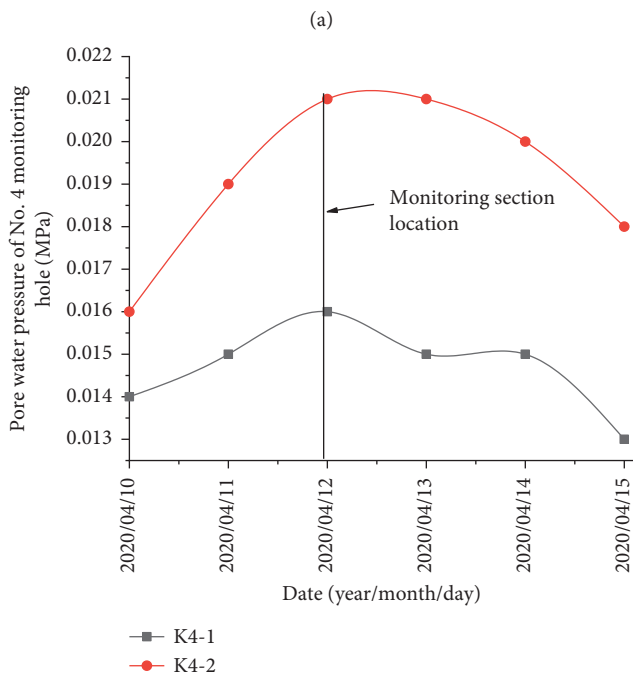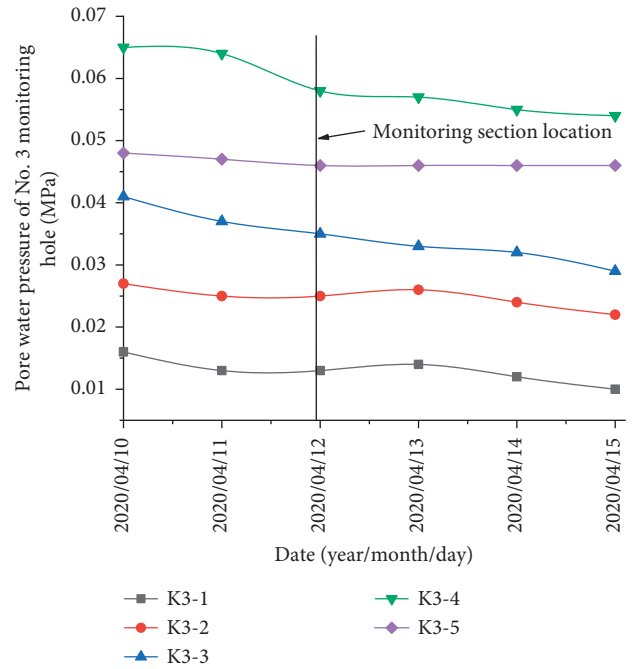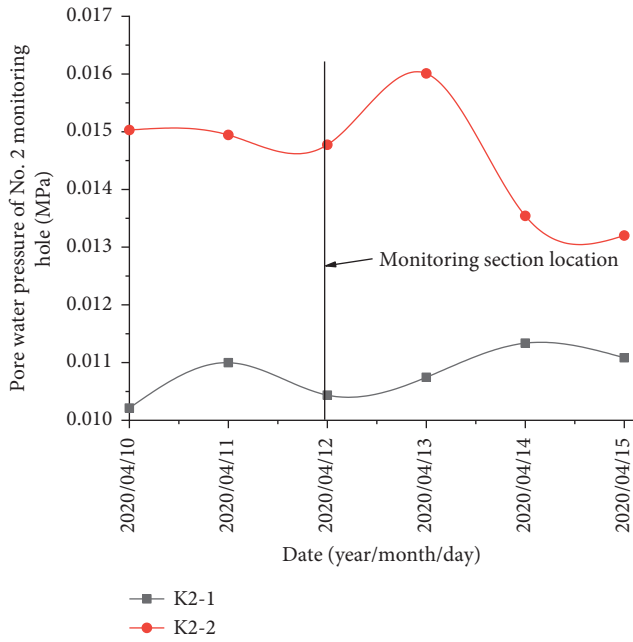
FIGURE 14: Continued.
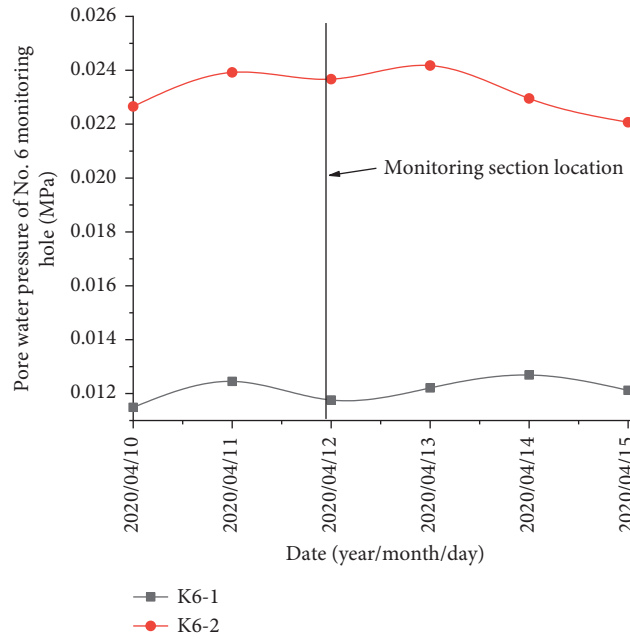
(e)

FIGURE 14: Variation diagram of pore water pressure during Hole 2 jacking. (a) Pore water pressure of No. 2 monitoring hole. (b) Pore water pressure of No. 3 monitoring hole. (c) Pore water pressure of No. 4 monitoring hole. (d) Pore water pressure of No. 5 monitoring hole. (e) Pore water pressure of No. 6 monitoring hole.

TABLE 2: Calculation table of lateral disturbance range and overlapping range.

Jacking sequence	Weighted value of internal friction angle	The horizontal elevation angle of the boundary line (°)	The radius of disturbance zone (m)	Disturbance criteria	Lateral disturbance rang (m)	Overlapping area range (m)
Hole 1					$L_1 = 15.4$	$L_1' = 0$
Hole 3	16.8	52	2.47	$B > 2hctg\alpha + (2R'/\sin \alpha)$	$L_2 = 15.4$	$L_2' = 0.76$
Hole 2				$B < 2hctg\alpha + (2R'/\sin \alpha)$		$L_3' = 8.08$

6.2. Evaluation of the Influence of the Buried Depth on the Disturbance Degree. Take the soil disturbance degree analysis of No. 4 monitoring hole under different buried depths, and the results are shown in Figure 17. After comparison, it is found that the larger the buried depth is, the closer it is to the top

surface of the pipelines, the higher the degree of soil disturbance is, and the more severe the soil disturbance is.

6.3. Evaluation of the Influence of Overlap on the Disturbance Degree. Comparing the soil disturbance degree of
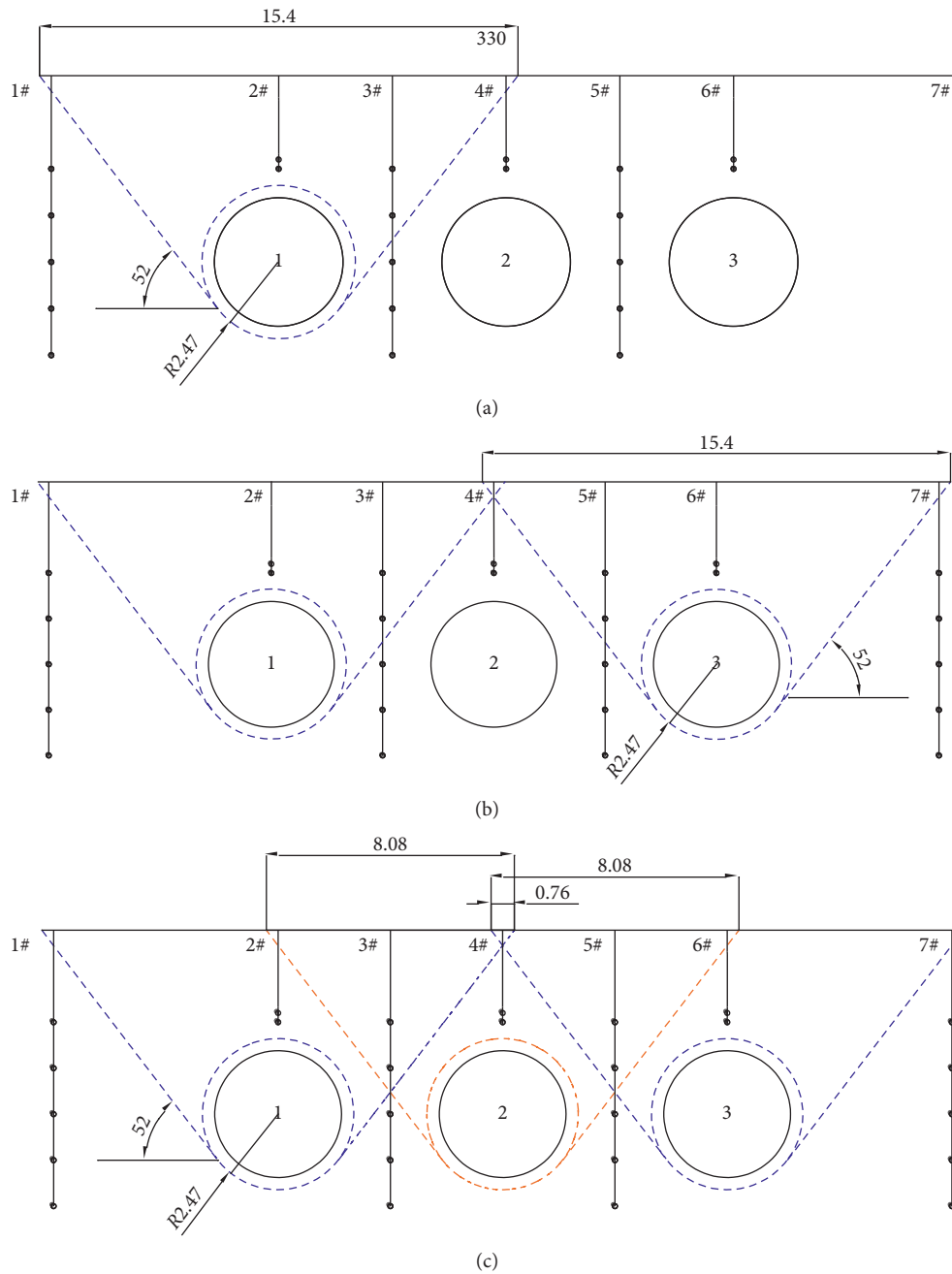
Figure 15: Calculation map of lateral disturbance range and overlapping range. (a) Hole 1 excavates. (b) Hole 3 excavates. (c) Hole 2 excavates.

monitoring point 3-1 when Hole 1 and Hole 2 excavate through, respectively, the disturbance overlap effect of double-hole jacking can be obtained, and the result is shown in Figure 18.

It can be seen that, in the double-hole disturbance overlap area, the soil disturbance caused by the second hole is larger than that caused by the first hole, but the disturbance intensity is smaller. This is because the soil structure is more loose when the second hole excavates, and the disturbance caused by the loading and unloading of the soil during jacking is less obvious than that of the original soil before.

(a)

(b)

(c)
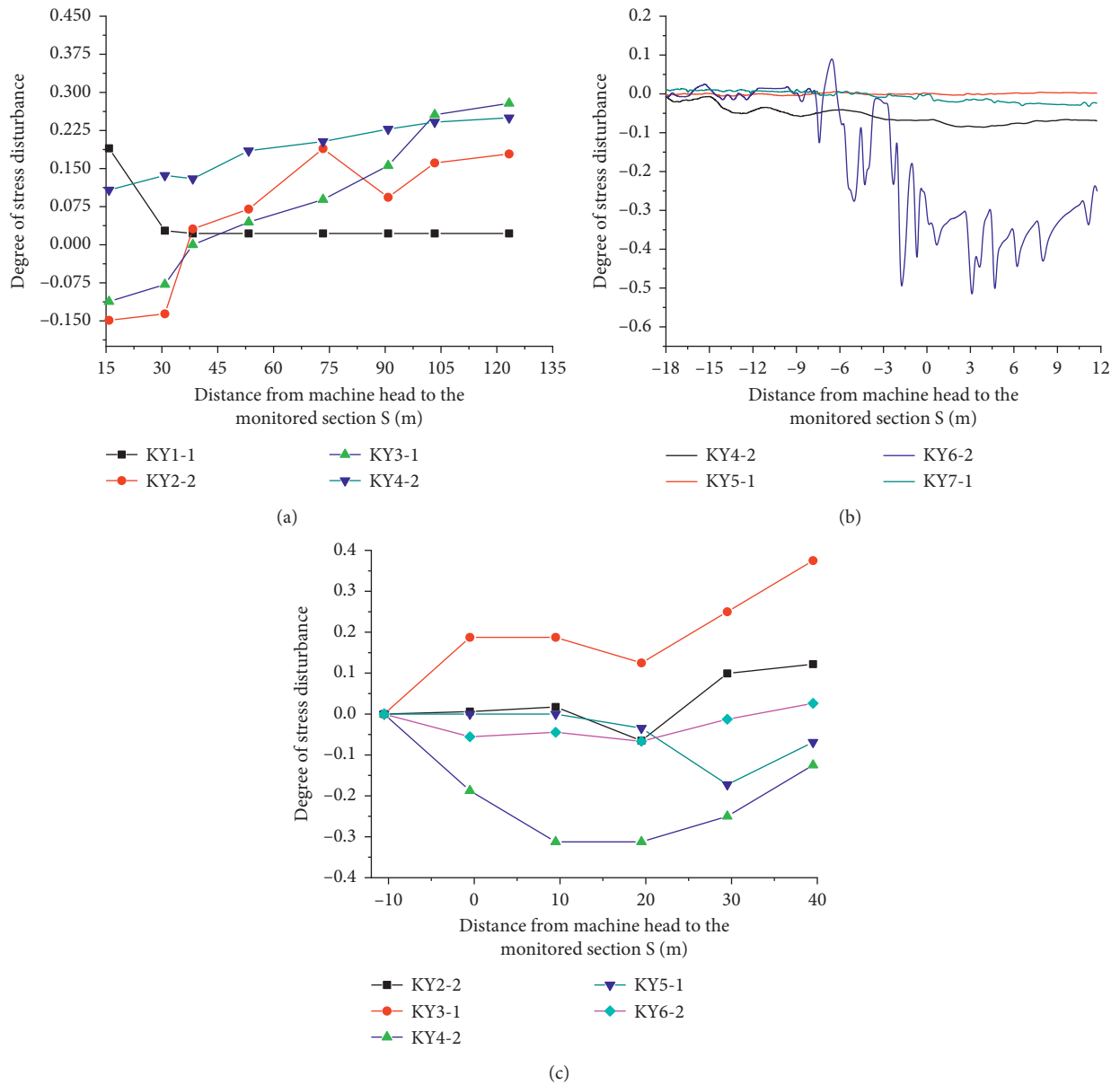
FIGURE 16: Degree of soil disturbance under different lateral spacing. (a) Hole 1 excavates. (b) Hole 3 excavates. (c) Hole 2 excavates.
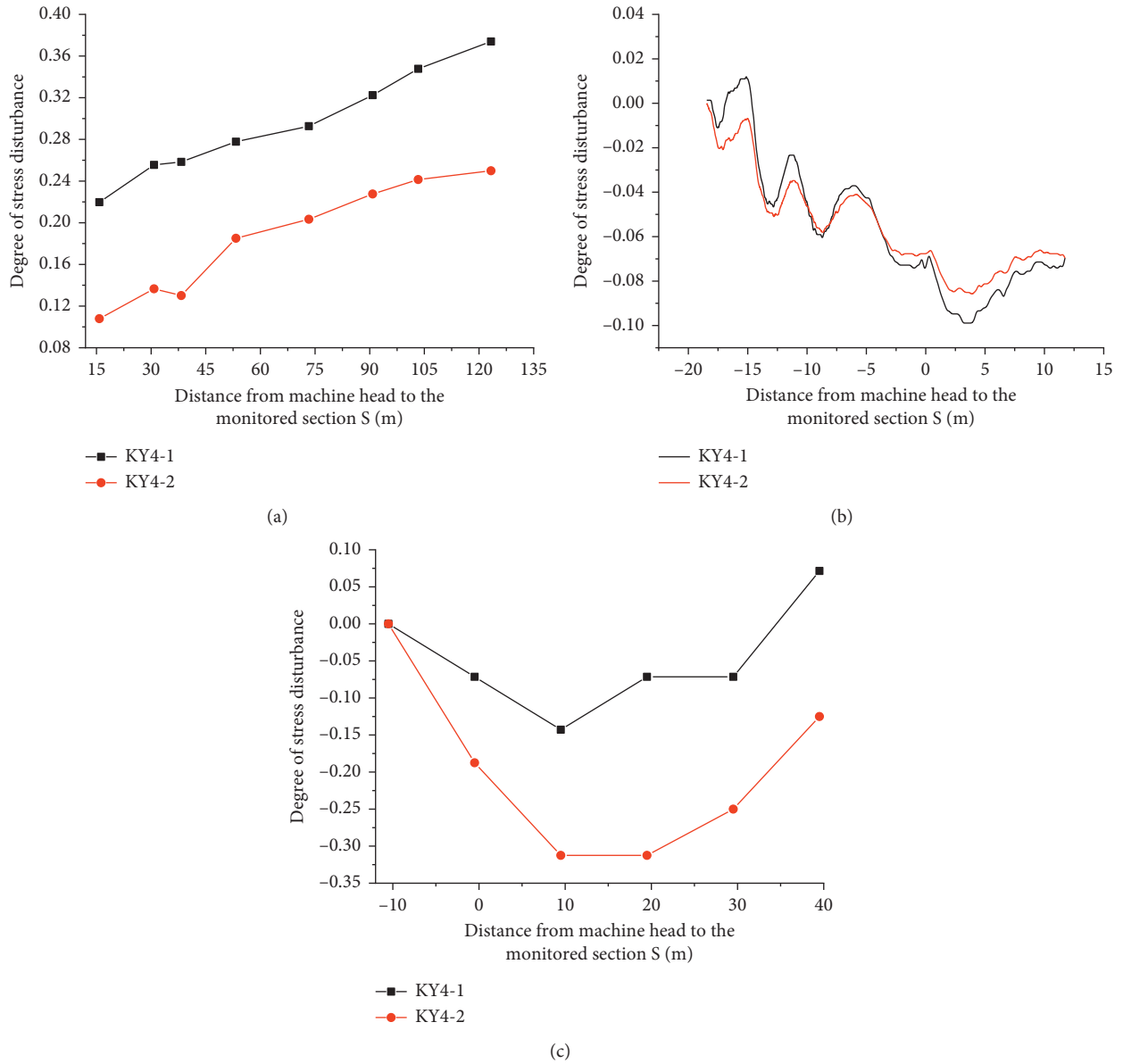
Figure 17: Degree of soil disturbance under different buried depth. (a) Hole 1 excavates. (b) Hole 3 excavates. (c) Hole 2 excavates.
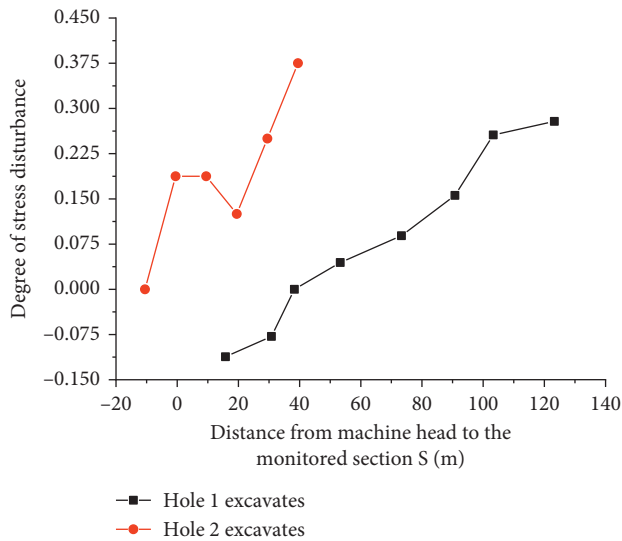
FIGURE 18: Analysis chart of double-hole overlap disturbance degree.

7. Conclusions

Combining theory analysis with field test, the effect of soil disturbance in the vertical direction of pipe jacking group and its interaction are mainly discussed in this paper. Based on the actual project, the following conclusions are obtained:

(1) The horizontal jacking of pipe jacking is regarded as the problem of cavity expansion in finite medium in this paper. Based on the cylindrical hole expansion model, the calculation formula of the plastic zone disturbance radius of soil is deduced. Furthermore, according to the limit equilibrium principle, the calculation formula of the transverse disturbance range caused by single-hole jacking construction is established.

(2) The influence of center spacing between two holes and the jacking position on the lateral disturbance range of soil in double-hole and three-hole jacking construction is analyzed and discussed. If the center spacing is large, the soil disturbance only occurs around the plastic disturbance area of each pipe. If the center distance is small, the disturbance superposition will occur. The calculation formulas of the critical value of the center spacing and the lateral overlapping area range in double-hole and three-hole jacking are established.

(3) The disturbance superposition mechanism of three-hole excavation is the same as that of double-hole excavation, but the influence of jacking position should be considered. When the third hole is located outside the previous two holes, its disturbance superposition effect is the same as that of double-hole excavation. When the third hole is located in the center of the two holes, if the center distance is small, there will be secondary disturbance superposition. The conclusion of theoretical analysis is the same as

that of field test, which proves the rationality of theoretical solution effectively.

(4) With the help of the pore water pressure measured in the field test, the disturbance degree of the soil during the multihole jacking is further analyzed. From the analysis results, in the case of single-hole, double-hole, and three-hole jacking, the deeper the buried depth and the closer to the pipe, the greater the soil disturbance. At the same time, affected by the soil structure, the disturbance degree of the soil on the top of the pipe jacking is larger than that on the side, and the disturbance degree of the second hole is larger than that of the first hole, but the degree is not as severe as before.

Data Availability

The field data in this paper are collected and sorted by field measurement, which is mainly used to verify the theoretical prediction. All data generated or analyzed during this study are included in this article.

Conflicts of Interest

The authors declare that there are no conflicts of interest regarding the publication of this paper.

Acknowledgments

References

[1] D. M. Zhang, X. Zong, and H. W. Huang, "Longitudinal deformation of existing tunnel due to underlying shield tunneling," *Rock and Soil Mechanics*, vol. 35, pp. 2659–2666, 2014.

[2] Y.-F. Chen, H.-K. Zheng, M. Wang, J.-M. Hong, and C.-B. Zhou, "Excavation-induced relaxation effects and hydraulic conductivity variations in the surrounding rocks of a large-scale underground powerhouse cavern system," *Tunnelling and Underground Space Technology*, vol. 49, pp. 253–267, 2015.

[3] T. Siren, P. Kantia, and M. Rinne, "Considerations and observations of stress-induced and construction-induced excavation damage zone in crystalline rock," *International Journal Of Rock Mechanics and Mining Sciences*, vol. 73, pp. 165–174, 2015.

[4] Z. Zhang, M. Zhang, and Q. Zhao, "A simplified analysis for deformation behavior of buried pipelines considering disturbance effects of underground excavation in soft clays," *Arabian Journal of Geosciences*, vol. 8, no. 10, pp. 7771–7785, 2015.

[5] R. Liang, T. Xia, M. Huang, and C. Lin, "Simplified analytical method for evaluating the effects of adjacent excavation on shield tunnel considering the shearing effect," *Computers and Geotechnics*, vol. 81, pp. 167–187, 2017.

[6] Z. Gang, X. Y. Yang, H. Z. Zhou, Y. M. Du, J. Y. Sun, and X. X. Yu, "A Simplified Prediction method for evaluating

tunnel displacement induced by laterally adjacent excavations," *Computers and Geotechnics*, vol. 95, pp. 119–128, 2017.

[7] P. Lueprasert, P. Jongpradist, P. Jongpradist, and S. Suwansawat, "Numerical investigation of tunnel deformation due to adjacent loaded pile and pile-soil-tunnel interaction," *Tunnelling and Underground Space Technology*, vol. 70, pp. 166–181, 2017.

[8] H. Fu, M. Zhang, F. Wang, T. H. Ling, and X. L. Yang, "The failure mechanism of surrounding rock around an existing shield tunnel induced by an adjacent excavation," *Computers and Geotechnics*, vol. 117, pp. 103–126, 2020.

[9] B. Liu, D. W. Zhang, S. Y. Liu, and Y. J. Qin, "Numerical simulation and field monitoring on a large cross-section pipe-jacking underpass traversing existing metro tunnels," *Chinese Journal of Rock Mechanics and Engineering*, vol. 36, pp. 2850–2860, 2017.

[10] V. K. Dang, D. Dias, N. A. Do, and T. H. Vo, "Impact of blasting at tunnel face on an existing adjacent tunnel," *International Journal of Geomate*, vol. 15, pp. 22–31, 2018.

[11] Y. H. Fang, H. O. Mo, and C. Y. Zhang, "Theoretical and testing analysis of soild deformation in the area of disturbance caused by pipe jacking," *Chinese Journal of Rock Mechanics and Engineering*, vol. 22, pp. 601–605, 2003.

[12] G. Wei, R. Q. Xu, and W. Tu, "Testing study and analysis on soil disturbance induced by pipe jacking construction," *Chinese Journal of Rock Mechanics and Engineering*, vol. 23, pp. 476–482, 2004.

[13] G. Wei, X. J. Wei, and Y. M. Tu, "Analysis on site monitoring of ground deformation induced by parraler pipe jacking construction," *Chinese Journal of Rock Mechanics and Engineering*, vol. 25, pp. 3299–3304, 2006.

[14] C. L. Li and L. C. Miao, "Determination of the range of shield tunneling-induced soil disturbance," *Rock and Soil Mechanics*, vol. 37, pp. 759–766, 2016.

[15] B. Chen, S. W. Xu, F. L. Peng, Q. F. Li, and W. M. Ye, "Experimental study of indices for evaluating small disturbance in underground crossing construction," *Chinese Journal of Rock Mechanics and Engineering*, vol. 30, pp. 2682–2689, 2011.

[16] F.-y. Meng, R.-p. Chen, and X. Kang, "Effects of tunneling-induced soil disturbance on the post-construction settlement in structured soft soils," *Tunnelling and Underground Space Technology*, vol. 80, pp. 53–63, 2018.

[17] Y. Xu, D. a. Sun, J. Sun, D. Fu, and P. Dong, "Soil disturbance of Shanghai silty clay during EPB tunnelling," *Tunnelling and Underground Space Technology*, vol. 18, no. 5, pp. 537–545, 2003.

[18] T. Lu, S. Liu, G. Cai, K. Wu, and W. Xia, "Investigation of soft soil disturbance and recompression settlement induced by excavation," *Rock and Soil Mechanics*, vol. 41, 2021.

[19] H. N. Feng, X. G. Wen, G. Wei, C. Liu, Z. X. Yang, and X. N. Gong, "In-situ test research on influence of pipe jacking on soil," *Rock and Soil Mechanics*, vol. 24, pp. 781–785, 2003.

[20] Y. Zheng, W. Q. Ding, and L. S. Chen, "Study of measured data and soil disturbance influenced by pipe Jacking Construction," *Chinese Journal Of Underground Space And Engineering*, vol. 6, pp. 1015–1020, 2010.

[21] J. Guo, B. S. Ma, Y. S. Zhao, X. H. Chen, and H. X. Ji, "Soil disturbance measurement and analysis of large section rectangular pipe-jacking construction," *Special Structure*, vol. 36, pp. 1–7, 2019.

[22] P. Zhang, B. S. Ma, C. Zen, and X. Y. Wang, "Site monitoring analysis of contact pressure during steel curved pipe jacking with larger buried depth," *Journal of Huazhong University Of Science and Technology (natural Science Edition)*, vol. 44, pp. 93–97, 2016.

[23] W. Zhao, B. F. Jiang, P. J. Jia, J. C. Dong, and Y. Zhao, "Theoretical analysis on soil disturbance induced by densely packed circular pipes with Fringes," *Chinese Journal of Underground Space and Engineering*, vol. 15, pp. 1734–1740, 2019.

[24] A. S. Vesic, "Expansion of cavities in infinite soil mass," in *Proceedings of the ASCE*, Vancouver, Canada, July 1972.

[25] H. S. Yu, *Cavity Expansion Methods in Geomechanics*, Kluwer Academic Publishers, Amsterdam, Netherlands, 2000.

[26] X.-L. Yang and J.-F. Zou, "Cavity expansion analysis with non-linear failure criterion," *Proceedings of the Institution of Civil Engineers-Geotechnical Engineering*, vol. 164, no. 1, pp. 41–49, 2011.

[27] S. L. Chen and Y. N. Abousleiman, "Exact drained solution for cylindrical cavity expansion in modified Cam Clay soil," *Geotechnique*, vol. 63, pp. 510–517, 2013.

[28] S. H. Jia, C. F. Zhao, and C. Zhao, "Analysis of expanded radius and internal expanding pressure of cylindrical hole," *Chinese Journal of Rock Mechanics and Engineering*, vol. 34, pp. 182–188, 2015.

[29] W. J. Han, S. Y. Liu, D. W. Zhang, and C. Y. Gu, "Numerical simulation of pressure-controlled cavity expansion," *Rock and Soil Mechanics*, vol. 31, pp. 405–411, 2010.

[30] A. Hedayat and J. Weems, "The elasto-plastic response of deep tunnels with damaged zone and gravity effects," *Rock Mechanics and Rock Engineering*, vol. 52, no. 12, pp. 5123–5135, 2019.

[31] Y. Xiang and S. Feng, "Theoretical prediction of the potential plastic zone of shallow tunneling in vicinity of pile foundation in soils," *Tunnelling and Underground Space Technology*, vol. 38, pp. 115–121, 2013.

[32] B. Azari, B. Fatahi, and H. Khabbaz, "Assessment of the elastic-viscoplastic behavior of soft soils improved with vertical drains capturing reduced shear strength of a disturbed zone," *International Journal of Geomechanics*, vol. 16, pp. 4001–4011, 2016.

[33] C.-F. Tsang, F. Bernier, and C. Davies, "Geohydromechanical processes in the Excavation Damaged Zone in crystalline rock, rock salt, and indurated and plastic clays-in the context of radioactive waste disposal," *International Journal of Rock Mechanics and Mining Sciences*, vol. 42, no. 1, pp. 109–125, 2005.

[34] J. M. Kranabetter, S. Haeussler, and C. Wood, "Vulnerability of boreal indicators (ground-dwelling beetles, understory plants and ectomycorrhizal fungi) to severe forest soil disturbance," *Forest Ecology and Management*, vol. 402, pp. 213–222, 2017.

[35] D. J. Yuan, F. Yin, H. W. Wang, Q. F. Huang, and H. Xiao, "Study of soil disturbance caused by super-large diameter slurry shield tunneling," *Chinese Journal of Rock Mechanics and Engineering*, vol. 28, pp. 2074–2080, 2009.